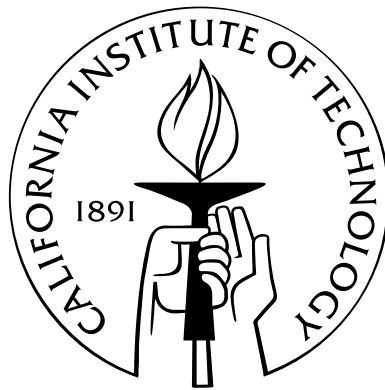


Monitoring Earth Surface Dynamics With Optical Imagery

Thesis by
Sébastien Leprince

In Partial Fulfillment of the Requirements
for the Degree of
Doctor of Philosophy



California Institute of Technology
Pasadena, California

2008
(Defended 16 May 2008)

© 2008

Sébastien Leprince

All Rights Reserved

Acknowledgements

First and foremost, I would like to thank my advisor, Jean-Philippe Avouac, for his continuous support and unconditional enthusiasm. He has inspired me in many ways, and I value the time he has always allocated for our discussions, even on days when his schedule was already unreasonably booked. His approachable attitude has created a friendly and efficient environment, which has encouraged collaborations, and has provided work conditions that everyone could hope for.

Pursuing graduate studies in Electrical Engineering while being immersed in the Geological and Planetary Science Division has not always been a simple task. I still remember attending the tecto-lunch group meetings, lost among Earth scientists discussing subjects as weird as rock dating, subduction zones, convergence rates, exhumation rates, etc..., while hoping that someone would just start talking about “normal” topics, such as Fourier analysis. Those were the years when Martine Simoes was trying to teach me tectonics, and when Laurent Demanet was offering me, during our frequent dinners, the stimulating discussions on Fourier analysis I had hoped for earlier during the day. I thank them both to have complementarily impacted my research’s views.

To defend this thesis, I have gathered professors from several disciplines in Electrical Engineering and in Earth Sciences, and my gratitude goes to Mark Simons, Pietro Perona, P. P. Vaidyanathan, and Charles Elachi, for serving on my committee.

I am indebted to Renaud Binet and to Rémi Michel who have introduced me, during my visits to the Laboratoire de Détection et de Géophysique, CEA, France, to their pioneering work on subpixel correlation. The early work with Sylvain Barbot has also proved to be essential, and I am glad that he is now among the regular users of COSI-Corr. The release and the ease of use of the COSI-Corr software would have never been achieved without the work of François Ayoub. His contribution has been determinant in developing the aerial modules as well as the extensions to satellite sensors other than SPOT, such as the ASTER

sensor. Discussions with Pablo Musé have been extremely fruitful. His numerous feedbacks toward the end of my thesis have been invaluable and will definitely impact my future work. Our racquetball games helped to release stress and to brainstorm new ideas, and despite the distance, I hope we will continue our collaboration internationally.

I would like to thank all the COSI-Corr users who place their trust in us to derive measurements of ground displacements from optical images. The comments and feedbacks of the early, or even the very early, adopters, have been tremendously useful to better understand the problems our technique could help address. The collaborations with Yann Klinger, Etienne Berthier, Dirk Scherler, Mike Taylor, Ivana Barisin, Barry Parsons, and Cara Schiek, have shed light on many aspects that may have been overlooked otherwise.

Attention has been directed to my research thanks to Elisabeth Nadin who proofread the EOS article of Chapter 2 and who published a remarkable press release during the AGU fall meeting of December 2007.

The many post-docs of the group have contributed to its warm atmosphere and my sincere thoughts go to Mohamed Chlieh, who has been an unforgettable officemate, and also to Frederic Herman, Laurent Bollinger, Gweltaz Maheo, and Oliver Beyssac. Heather Steele, our assistant, has been part of this wonderful team and has efficiently taken care of all the daily problems so that we could all be dedicated to our research.

Laurent Mathevet helped me co-direct the Caltech Francophile Club, and the memory of the long lines in front of our “crêpes” cooking stand for International Weeks will stay strong.

My application to Caltech was influenced by my undergraduate lab partner, i.e., my “binôme” Stéphane Provost, who transferred to Harvey Mudd College. He certainly motivated me to go to Caltech, which has opened me to a whole different world.

Education starts with family and my parents have always been supportive of my choices, even in going abroad several times for long periods. I have certainly learned from my mother that to love is to let people do what they should to be happy. Many thoughts go to my grandfather for giving me the taste for sciences and engineering at an early age.

Last but not least, my sweetest thoughts go to Susan for her continuous love and support over the last few years. The short lines here cannot give her enough credit, but her attention in trying to smooth out the “Frenchness” of my writing has considerably improved my English fluency.

Abstract

Despite the increasing availability of high-quality optical satellite images, continuous monitoring of Earth's surface changes is still of limited use due to technical limitations. To overcome these limitations, this thesis presents a processing chain to accurately orthorectify and co-register sets of satellite and aerial images, which, associated with a precise correlation technique, allow for the measurement of horizontal ground deformations with accuracy better than 1/10 of the pixel size. The irregular resampling problem is addressed to avoid introducing aliasing in the orthorectified images. Image registration and correlation is achieved with an iterative, unbiased processor that estimates the phase plane in the Fourier domain for sub-pixel shift detection. Errors due to the imaging system are calibrated and modeled, topography artifacts are characterized and solutions are proposed to compensate or to filter them.

A software package implementing these procedures, Co-registration of Optically Sensed Images and Correlation (COSI-Corr), is available from the Caltech Tectonics Observatory website. The procedure is validated in several different contexts, and applied to seismotectonics and glaciology studies.

Accurate measurements of horizontal co-seismic displacements in the near fault zone allow unambiguous imaging of surface ruptures. It is shown that measurements of surface ruptures from optical aerial and satellite images compare well with field measurements, and that in addition they have the potential of densely measuring the fault perpendicular component, and the off-fault distributed slip. When combined with seismic waveform modeling, fault geometry and surface offsets add crucial constraints to describe in details the seismic faulting process.

Dense maps of glacier velocity are reported for several glaciers in Europe and in the Himalayas. Optical image correlation proves robust even in challenging mountainous areas, allowing accurate measurements of glacier flow velocity. Seasonal variations of glacier flow

velocity are well identified, suggesting that such measurements can be used to better study the effects of climate change, and to refine the tuning of numerical glacier models.

Contents

Acknowledgements	iii
Abstract	v
1 Introduction	1
1.1 Context of the Thesis	1
1.2 Structure of the Manuscript	3
2 Monitoring Earth Surface Dynamics With Optical Imagery	7
2.1 Increase of Data Set Availability	8
2.2 COSI-Corr Software Package	9
2.3 Coseismic Deformation	9
2.4 Ice Flow	10
2.5 “Slow” Landsliding	12
2.6 A Technique Ready for Operational Use	12
3 Automatic and Precise Orthorectification, Co-Registration, and Sub-Pixel Correlation of Satellite Images, Application to Ground Deformation Measurements	17
3.1 Introduction	18
3.2 Pushbroom Geometry and Orthorectification Models	21
3.2.1 The Direct Orthorectification Model	21
3.2.2 The Inverse Orthorectification Model	26
3.3 Image Resampling	29
3.3.1 Resampling Regularly Spaced Data: Changing the Sampling Rate .	30
3.3.2 Resampling on an Irregular Grid	31

3.3.3	Inverse Resampling Results	33
3.4	Correlation of Optical Images	36
3.4.1	Statement of the Problem	36
3.4.2	Phase Correlation Methods	37
3.4.3	Phase Correlation Properties	39
3.4.4	Discrete Fourier Transform of Finite Length Signals	42
3.4.5	Finding the Images Phase Difference	43
3.4.6	Image Correlation, Complete Algorithm	51
3.4.7	Correlation Tests and Results	53
3.5	The Processing Chain	55
3.5.1	Corrected Orthorectification	57
3.5.2	Look Directions Optimization from Precise GCPs Generation	60
3.5.3	The Complete Processing Chain	63
3.6	Tests and Results	65
3.6.1	Measuring a Null Displacement Field from SPOT 5 Images	65
3.6.2	The 1999 Hector Mine Earthquake Imaged From SPOT	75
3.7	Conclusion and Future Work	82
4	Measuring Coseismic Ground Deformation from Aerial Photographs Using COSI-Corr	85
4.1	Introduction	86
4.2	Technique Overview	88
4.3	Orthorectification	88
4.3.1	Interior Orientation	90
4.3.2	Exterior Orientation	90
4.3.3	Mapping Process	91
4.4	Resampling	91
4.5	GCPs Selection and Co-Registration Optimization	91
4.5.1	GCPs Selection	91
4.5.2	Co-Registration Optimization	93
4.6	Correlation	94
4.7	Application Case	95

4.8	DEM Artifacts	102
4.9	Scan	108
4.9.1	Scan Artifacts	108
4.9.2	Scan Resolution	111
4.10	GCPs	111
4.10.1	GCPs—Absolute Accuracy	111
4.10.2	GCPs—Tectonic Signal Distortions	112
4.11	Conclusion	115
5	Co-Registration of Optically Sensed Images and Correlation (COSI-Corr): an Operational Methodology for Ground Deformation Measurements	119
5.1	Introduction	120
5.2	COSI-Corr Methodology	121
5.3	The 2005, Mw 7.6 Kashmir Earthquake from ASTER Images	122
5.4	The 1992, Mw 7.3 Landers Earthquake from Aerial Photographs	125
5.5	Conclusion	126
6	In-Flight CCD Distortion Calibration for Pushbroom Satellites Based on Subpixel Correlation	129
6.1	Introduction	130
6.2	Previous Work	133
6.2.1	Benefiting from the Dual Acquisition System HRV1 and HRV2 on SPOT Satellites	133
6.2.2	Along-Track Subtraction of Stacked Profiles	133
6.3	Proposed Methodology	134
6.3.1	Assumptions and Notations	134
6.3.2	Methodology	136
6.4	Results	145
6.5	Discussion and Conclusion	147
7	The 2005, Mw 7.6 Kashmir Earthquake: Sub-Pixel Correlation of ASTER Images and Seismic Waveforms Analysis	151
7.1	Introduction	152

7.2	Remote Sensing Analysis	154
7.3	Seismological Analysis	157
7.4	The 2005 Kashmir Earthquake in Its Neotectonic Setting	167
7.5	Discussion	169
7.5.1	Performance of the Sub-Pixel Correlation of Optical Images	169
7.5.2	Characteristics of the Seismic Rupture	169
7.5.3	Relation to Known Active Faults and Geological Structures	170
7.5.4	Importance of Out-of-Sequence Thrusting for Seismic Hazard Along the Himalayan Arc	172
7.5.5	Return Period of Major Earthquakes Across the Himalaya of Kashmir and Himachal Pradesh	172
7.6	Conclusion	173
8	Glacier-Surface Velocities in Alpine Terrain from Optical Satellite Imagery— Accuracy Improvement and Quality Assessment	175
8.1	Introduction	176
8.2	Remote Sensing of Glacier-Surface Velocities	177
8.3	Methods and Data	179
8.3.1	Orthorectification, Co-Registration, and Sub-Pixel Correlation of Satel- lite Images Using COSI-Corr, Application to Mountain Glaciers	182
8.3.2	Post-Processing Procedures	183
8.3.3	Data Filtering	185
8.3.4	Quality Assessment and Validation Techniques	187
8.4	Study Area	188
8.5	Results	189
8.5.1	Case Study 1: Khumbu Himal, Nepal	189
8.5.2	Case Study 2: Garhwal Himalaya, India	197
8.6	Discussion	205
8.6.1	Measurement Errors	205
8.6.2	Comparison with Field-Based Velocity Measurements	206
8.6.3	Comparison with SAR-Derived Velocity Measurements	207
8.6.4	Other Optical Sensors	208

8.6.5	Implications for Glacier Monitoring	209
8.7	Conclusions	211
9	Conclusion	213
9.1	Advances	213
9.2	Limitations and Perspectives	215
9.2.1	Limitations Due to Image Content	215
9.2.2	Limitations Due to Ancillary Data Quality	216
9.2.3	Limitations Due to Image Quality	217
9.2.4	Limitations Due to Chosen Processing Strategy	219
A	Direct Model Orthorectification, Using a DEM	223
B	TPSS Algorithm Applied to the Inverse Orthorectification Problem	225
C	TPSS Algorithm Applied to the Phase Correlation Minimization Problem	227
D	Application to ASTER Images	229
E	Determining the Overlap Between the Slave and the Reference Images	231
	Bibliography	233

List of Figures

2.1	North/south component of the coseismic displacement field due to the 1999 Hector Mine earthquake, California	11
2.2	Amplitude of the horizontal displacement over the Mer de Glace area from 23 August 2003 to 18 September 2003, obtained from two panchromatic 2.5-meter-resolution SPOT 5 images	13
2.3	Absolute horizontal displacement and displacement vectors of the La Valette landslide, as imaged from the correlation of two 2.5-meter SPOT 5 images . .	14
3.1	The look direction and the look angles	22
3.2	Orbital coordinate system and attitude variations	23
3.3	Inverse orth-rectification model principle	27
3.4	General regular resampling scheme	30
3.5	Raw image	33
3.6	Orthorectified image	33
3.7	Distribution of local resampling distances	34
3.8	Raw image log-spectrum	35
3.9	Orthorectified image log-spectrum	35
3.10	Modeling of the acquisition systems	41
3.11	Log-spectrum and corresponding mask of SPOT 5 THR 2.5 m resolution images	48
3.12	Log-spectrum and corresponding mask of SPOT 5 HRG 5 m resolution images	49
3.13	Evolution of the mean bias and standard deviation of the correlation measurements with varying parameters	54
3.14	Histograms of the correlation measurements for a constant offset	55

3.15	Mean correlation bias and standard deviation with respect to the relative displacement between images. The simplest form of the algorithm is characterized here	56
3.16	Mean correlation bias and standard deviation with respect to the relative displacement between images. The complete form of the algorithm is characterized here	56
3.17	Evolution, with respect to the iterations of the look directions correction algorithm, of the mis-registration of the GCPs to be generated	67
3.18	Histograms of the relative offsets between the two orthorectified SPOT 5 images	69
3.19	North/South component of the SPOT 5 / SPOT 5 correlation	70
3.20	East/West component of the SPOT 5 / SPOT 5 correlation	71
3.21	SPOT 5 / SPOT 5 SNR map assessing the quality of the measurements . . .	72
3.22	Section across the power spectral density of the N-S correlation image	74
3.23	North/South component of the SPOT 4 / SPOT 2 correlation	76
3.24	East/West component of the SPOT 4 / SPOT 2 correlation	77
3.25	SNR of the SPOT 4 / SPOT 2 correlation	78
3.26	Profile from the SPOT 4 / SPOT 2 North/South correlation image	80
3.27	Right lateral slip from SPOT measurements	81
4.1	Geometry of an aerial photograph acquisition	89
4.2	Shaded DEM of the study area	97
4.3	North/South component of the Landers 1989/1995 correlation map	98
4.4	Profile from Fig. 4.3	99
4.5	East/West component of the Landers 1989/1995 correlation map	100
4.6	SNR component of the Landers 1989/1995 correlation map	101
4.7	East/West component of the Landers 1995/2002 correlation map	103
4.8	North/South component of the Landers 1995/2002 correlation map	104
4.9	Geometry of the orthorectification and correlation measure in case of a unique DEM	105
4.10	East/West component of the Landers 1989/1995 correlation map corrected for artifacts due to a single DEM use	106

4.11	Profile BB' of the uncorrected (Fig. 4.5) and corrected (Fig. 4.10) East/West correlation map	107
4.12	Line component of the MD/USGS scan correlation map	109
4.13	Profile CC' (Fig. 4.12) showing scan artifacts	110
4.14	North/South component of the 1989/2002 correlation map of Hector Mine earthquake	113
4.15	North/South component of the denoised SPOT correlation map of Hector Mine earthquake	114
4.16	North/South component of the 1989/2002 correlation map of Hector Mine earthquake with long wavelength distortions removed	116
4.17	GCPs correction brings a 2nd-order polynomial correction	117
5.1	Northward component of the coseismic offset field from the 2005 Kashmir earthquake seen from ASTER images	123
5.2	Subtracting attitude variations from Fig. 5.1	124
5.3	Northward component of the coseismic offset field from the 1992, Mw 7.3 Landers earthquake of California	127
6.1	Linear artifacts, running in the satellites along-track direction, betray the unmodeled distortions of the CCD arrays of each satellite	132
6.2	Distorted optical system	135
6.3	CCD element pointing direction	136
6.4	East-West component of the disparity field measured from sub-pixel correlation of a SPOT 5 5 m and a SPOT 4 10 m image	137
6.5	Measured distortions, in pixel, in the focal plane of the SPOT 4- HRV1 panchromatic sensor	141
6.6	Polar representation of the differences between calibrated and uncalibrated interior orientation look directions	142
6.7	Same experiment as in Fig. 6.4, but the derived CCD correction model has been accounted for during orthorectification	144
6.8	Same experiment as in Fig. 6.1, but the derived CCD correction model for both SPOT 4 and SPOT 2 images have been accounted for during orthorectification	146

6.9	Comparison of the right lateral slip along the fault trace estimated from the correlation analysis from Fig. 6.1 and from Fig. 6.8	147
7.1	Tectonic setting of the October 8 2005 Kashmir earthquake	153
7.2	Northward ground displacements measured from sub-pixel correlation of ASTER images	155
7.3	E-W ground displacements measured from sub-pixel correlation of ASTER images	156
7.4	Example of decorrelation due to landsliding	158
7.5	Northward ground displacements determined from the correlation of ASTER images from April 30, 2001, and from November 19, 2005	159
7.6	Surface fault trace mapped from the discontinuity of the offset field	160
7.7	Surface fault slip	161
7.8	Modeling of teleseismic waveforms (P waves) using the source model derived from the joint inversion of waveforms and surface slip	163
7.9	Slip distribution derived from the seismic waveforms and surface slip distribution	164
7.10	Slip distribution derived from the modeling of seismic waveforms without constraints on surface slip	166
7.11	Slip distribution derived from the seismic waveforms and surface slip distribution assuming an epicenter 12 km northwest of that determined by the USGS	167
7.12	Comparison of ruptured fault trace with bedrock geology	171
8.1	Processing chain of the applied method to derive accurate glacier surface velocities	181
8.2	Effect of DEM error on displacement measurements	184
8.3	Ortho-image and displacement map from the Mount Everest region, Nepal .	190
8.4	Correction of attitude effects and sensor distortions	191
8.5	Velocity field of the central part of Khumbu glacier	193
8.6	Stacked displacement profiles from the lower part of Khumbu glacier	195
8.7	Longitudinal, transverse, and shear strain rate maps over Khumbu glacier . .	196
8.8	Continuous velocity profile of Khumbu glacier	198
8.9	Uncorrected and corrected E-W displacement map over the Gangotri glacier group	201

8.10	Topography bias as a function of slope angle and aspect	202
8.11	Recent velocity history of the lower part of Gangotri glacier	204
8.12	Comparison of GPS-derived and ASTER-derived velocity measurements . . .	207
9.1	Loss in correlation precision by introduction of aliasing	218

List of Tables

3.1	Relevant parameters for the SPOT scenes	66
4.1	Data references. Scans were obtained from the USGS and from a microdensitometer (MD) nominally designed for astronomy. CIR: Color Infra-Red. . .	95
4.2	USGS scans artifacts amplitude measured in row and column direction . . .	110
8.1	List of the ASTER scenes used in this study	180
8.2	Details on the error evolution during post-processing	186

Chapter 1

Introduction

1.1 Context of the Thesis

To assess seismic hazard, understanding the mechanics of earthquake rupture is crucial. Predicting earthquakes is still considered the Holy Grail of seismo-tectonics, and many doubt that it will ever be possible. However, some aspects of earthquake rupture could be anticipated if the earthquake rupture process could be better understood. Seismic hazard is therefore not assessed by trying to answer the question “when will the next earthquake strike?”, but rather by asking related questions such as “where, or on which fault, can an earthquake happen?” and “if an earthquake can happen there, how strong could the ground shaking be, and how large could the damage area be?” Potential earthquake location is investigated through geological field studies to identify active faults, and potential magnitudes are estimated based on historical account or paleoseismological investigations. Some aspects of future earthquakes might also be forecasted through mechanical modeling based on fault geometry, past history of ruptures, and mechanical properties. Recommendations for infrastructure construction are based on such studies to mitigate seismic hazard, placing our understanding of earthquake rupture mechanics at the center of seismic hazard assessment. Our understanding of earthquake mechanics, i.e, the ability of our mechanical models to accurately reproduce past events, therefore relies heavily on the observations of these events.

The rupture dynamics of past earthquakes is studied through models that are constrained by a combination of observations including seismograms and measurements of ground displacements from GPS, radar interferometry, and field surveys. Measurements from field surveys are of particular importance because thus far they have been the only

data to reliably constrain the geometry and the slip distribution of fault ruptures. A fundamental source of information for earthquake modeling, field measurements of surface rupture involve sending teams of geologists to where an earthquake has struck (sometimes in barely accessible terrain) to find the fault trace (with the risk of missing it) and to measure the ground displacement induced by the earthquake. Although such measurements have been an invaluable source of information, the difficulty of the task has greatly diminished its quantitative potential. For example, field measurements of surface ruptures can only be made on a limited number of locations where clear offset piercing points are observable (roads or terrace risers), and the fault-perpendicular component is generally not measurable. In addition, zones of distributed strain are generally not observable in the field. Field observations are therefore completed by other measurements, but because seismic and GPS stations generally sparsely cover, if at all, the near fault zone of seismic ruptures, they can only provide large-scale information on the rupture dynamics. Radar interferometry techniques provide denser details on the ground displacement induced by earthquakes, but saturate around rupture zones where the ground displacement gradient exceeds the dimensionless ratio of the radar pixel size by the radar wavelength. The key information that is needed to adequately constrain mechanical models of seismic ruptures is then only accessible through field measurements. According to the context described, providing dense and detailed information on the near fault coseismic displacement field therefore seems out of reach, along with the design and calibration of accurate models describing seismic ruptures.

The first advance emerged in 2000 [1], when it was shown that the correlation of optical satellite images could, under some restrictive conditions, provide quantitative measurements of horizontal coseismic displacement fields in the near fault zone. My thesis work started in 2003 in this context, and at that time, the technique was delivering hardly reproducible results. It was already recognized that images, usually acquired at different view angles, should be reprojected onto some common reference frame to be compared, but the effects of lack of resolution in topography, camera modeling uncertainties, and satellite attitude uncertainties on ground displacement measurements were unclear. Biases due to resampling problems had also been acknowledged, but no formulation had been proposed to avoid them. Correlation methods that worked well had been proposed, but measurement robustness was still lacking, and measurement accuracy was unpredictable. Because no specific processing chain existed, the impact of all the variables had not been characterized, and the general

technique of correlating optical satellite images to measure ground deformation was lacking formalization at all stages. Reliable use of the technique was therefore out of reach. The primary goal of this work was to identify, understand, and overcome these major limitations to propose a more mature technology that could potentially be used on an operational basis in case of large disasters.

As will be demonstrated in the pages of this manuscript, these initial goals have been reached, proposing a general processing chain to retrieve horizontal ground displacement fields from optical satellite imagery. Deeper investigations have also extended the technique to a variety of optical sensors, and to a variety of surface processes, having impact well beyond the original field of seismo-tectonics. The principal claim defended in this thesis is that optically sensed imagery, in addition and in complement to all the other techniques currently in use, can provide accurate monitoring of a myriad of Earth surface dynamics phenomena.

1.2 Structure of the Manuscript

This thesis exposes the processing methods, the limitations, and some key applications of the correlation of optical satellite and aerial images in, but not limited to, seismo-tectonics and glaciology. The manuscript is composed of papers that have been either published or submitted during this thesis work and are:

- Chapter 2: S. Leprince, E. Berthier, F. Ayoub, C. Delacourt, and J.P. Avouac, “Monitoring Earth Surface Dynamics with Optical Imagery,” *Eos Transactions, American Geophysical Union*, vol. 89, January 1st, 2008.
- Chapter 3: S. Leprince, S. Barbot, F. Ayoub, and J.P. Avouac, “Automatic and Precise Ortho-rectification, Co-registration and Sub-Pixel Correlation of Satellite Images, Application to Ground Deformation Measurements,” *IEEE Transactions on Geoscience and Remote Sensing*, vol. 45, no. 6, pp. 1529–1558, 2007.
- Chapter 4: F. Ayoub, S. Leprince, and J.P. Avouac, “Measuring Coseismic Ground Deformation from Aerial Photography Using COSI-Corr,” *International Society for Photogrammetry and Remote Sensing (ISPRS)*, (submitted), 2007.

- Chapter 5: S. Leprince, F. Ayoub, Y. Klinger, and J.P. Avouac, “Co-Registration of Optically Sensed Images and Correlation (COSI-Corr): an Operational Methodology for Ground Deformation Measurements,” *International Geoscience and Remote Sensing Symposium (IGARSS)*, vol. 6, Barcelona, Spain, July 2007, pp. 2700–2702.
- Chapter 6: S. Leprince, P. Musé, and J.P. Avouac, “In-Flight CCD Distortion Calibration for Pushbroom Satellites Based on Subpixel Correlation,” *IEEE Transactions on Geoscience and Remote Sensing*, (in press), 2008.
- Chapter 7: J.P. Avouac, F. Ayoub, S. Leprince, O. Konca, and D. V. Helmberger, “The 2005, Mw 7.6 Kashmir earthquake, rupture kinematics from sub-pixel correlation of ASTER images and seismic waveforms analysis,” *Earth and Planetary Science Letters*, vol. 249, no. 3–4, pp. 514–528, 2006.
- Chapter 8: D. Scherler, S. Leprince, and M. R. Strecker, “Glacier-Surface Velocities in Alpine Terrain from Optical Satellite Imagery—Accuracy Improvement and Quality Assessment”, *Remote Sensing of Environment*, (submitted), 2008.

Two additional papers illustrating how the correlation of optical satellite images can complement geological and seismological observations have also been prepared, but do not appear in this thesis. However, the reader is invited to consult them. They are:

- M. Taylor, S. Leprince, J.P. Avouac, and K. Sieh, “Detecting Co-seismic Displacements in Glaciated Regions: An Example from the Great November 2002 Denali Earthquake Using SPOT Horizontal Offsets,” *Earth and Planetary Science Letters*, (in press), 2008.
- A. O. Konca, S. Leprince, J.P. Avouac, and D. V. Helmberger, “Rupture process of 1999, Mw 7.1 Duzce Earthquake from Joint Analysis of SPOT, GPS, InSAR, Strong-motion and Teleseismic data,” *Bulletin of the Seismological Society of America*, (submitted), 2008.

Chapter 2 is a short non-technical paper targeting a large audience and used here as a brief overview of the work accomplished and of the ideas developed in the following chapters. Chapter 3 is the fundamental paper of this thesis, presenting the processing chain that allows for precise orthorectification, co-registration and sub-pixel correlation of pushbroom

satellite images. Chapter 4 presents the extension of Chapter 3 to the processing of aerial frame photographs and pinpoints the specificities of these sensors. Chapter 5 demonstrates that the technique from Chapter 3 can be indifferently applied to different pushbroom satellites, and that satellite and aerial images of different resolutions can be combined to analyze coseismic displacement fields at different scales. Chapter 6 tackles the recurring problem of in-flight sensor calibration for pushbroom satellites. A general procedure that suppresses systematic biases in ground displacement measurements is exposed. Chapter 7 demonstrates how dense measurement of the near fault zone coseismic displacements from satellite imagery benefits earthquake rupture modeling, and how this information, coupled with seismic waveform analysis, could help in early damage assessment of large earthquakes. Chapter 8 presents the particular use of optical satellite image correlation to derive glacier flow velocities, and particularities to high mountainous terrains are discussed. Finally, Chapter 9 concludes this thesis and discusses the major advances, as well as the perspectives, of the work described in this manuscript.

Chapter 2

Monitoring Earth Surface Dynamics With Optical Imagery

By Sébastien Leprince¹, Etienne Berthier², François Ayoub¹, Christophe Delacourt³, and Jean-Philippe Avouac¹

¹ Tectonics Observatory, Geology and Planetary Science Division, California Institute of Technology, Pasadena, California, USA

² CNRS-LEGOS, 14 av. Ed. Belin, 31400 Toulouse, France

³ Domaines Ocaniques, UMR 6538, IUEM, Université de Bretagne Occidentale, Plouzané, France

Foreword— This chapter has been published under the reference S. Leprince, E. Berthier, F. Ayoub, C. Delacourt, and J.P. Avouac, “Monitoring Earth Surface Dynamics with Optical Imagery,” *Eos Transactions, American Geophysical Union*, vol. 89, January 1st, 2008. In this thesis, it is referred to as reference [2]. The image analysis has been performed by S. Leprince, demonstrating the generality and broad applicability of the technique developed in Chapter 3. This chapter has benefited from the expertise in glaciology of E. Berthier, the expertise in landslide hazards of C. Delacourt, and the expertise in tectonics of J.P. Avouac. E. Berthier and C. Delacourt have also permitted low-cost access to the images. The Mer de Glace and Barcelonnette SPOT 5 images were acquired thanks to the Incitation à l’Utilisation Scientifique des Images SPOT (ISIS) program. SPOT 5 images copyright Centre National d’Etudes Spatiales. The

efficient packaging of the COSI-Corr software by F. Ayoub allowed the image analysis algorithms to run within a reasonable amount of time.

The increasing availability of high-quality optical satellite images should allow, in principle, continuous monitoring of Earth’s surface changes due to geologic processes, climate change, or anthropic activity. For instance, sequential optical images have been used to measure displacements at Earth’s surface due to coseismic ground deformation [1], ice-flow [3,4], sand dune migration [5], and landslides [6, 7].

Surface changes related to agriculture, deforestation, urbanization, and erosion—which do not involve ground displacement—might also be monitored, provided that the images can be registered with sufficient accuracy. Although the approach is simple in principle, its use is still limited, mainly because of geometric distortion of the images induced by the imaging system, biased correlation techniques, and implementation difficulties.

These obstacles have been overcome thanks to recent methodological advances and the development of a user-friendly software package called Co-Registration of Optically Sensed Images and Correlation (COSI-Corr) [8]. The software makes it possible to coregister images and to measure surface displacements with unprecedented ease and accuracy. This article describes some applications of the technique and pinpoints some key thematic questions that can benefit from this approach.

2.1 Increase of Data Set Availability

The application of the technique depends primarily on the availability of high-quality optical images, for which there exists considerable archived data to mine. Aerial surveys by the U.S. Geological Survey have covered the United States since the 1950s, the Institut Géographique National has surveyed the French territory since the 1940s, and similar archives exist across the world. Multiple satellite programs have delivered worldwide coverage such as Landsat since 1972, Satellite pour l’Observation de la Terre (SPOT) since 1986, and the Advanced Spaceborne Thermal Emission and Reflection Radiometer (ASTER) instrument, on board the NASA satellite Terra, since 1999. Many high-resolution satellites have been launched more recently, including IKONOS, QuickBird, OrbView, EROS, and FORMOSAT.

Images acquired by these programs have been essential in assessing temporal changes induced by large-scale natural disasters like earthquakes, tsunamis, floods, and volcanic eruptions. However, precisely quantifying temporal changes between series of images, possibly acquired by different instruments and at different resolutions, remains a considerable challenge.

2.2 COSI-Corr Software Package

The COSI-Corr software package allows for automatic and precise orthorectification, co-registration, and sub-pixel correlation of satellite and aerial images [8]. The procedure does not require external information such as GPS measurements of ground control points, and it is based solely on topographic knowledge and on the ancillary data provided with the observing platform.

In particular, the software package takes advantage of the availability of accurate digital elevation models with global coverage (Shuttle Radar Topography Mission). Sub-pixel change detection (i.e., correlation) is then applied to the set of orthoimages produced. COSI-Corr makes it possible to measure local displacements between temporal series of images, possibly acquired by different instruments and at different resolutions, with measurement accuracy of the order of a small fraction of the nominal images' resolution.

A plug-in for Environment for Visualizing Images (ENVI) remote sensing software, COSI-Corr is freely available from the California Institute of Technology's Tectonics Observatory (<http://www.tectonics.caltech.edu>).

2.3 Coseismic Deformation

Coseismic deformation is generally studied through field surveys of surface ruptures or geodetic or interferometric synthetic aperture radar (InSAR) measurements. However, these techniques often fail to provide detailed maps of the near-field surface strain, which may consist of a complex of surface ruptures and cracks within a fault zone of finite width. Consequently, InSAR and field measurements are not efficient approaches to estimating the total slip across a fault zone and its along-strike variability.

The distribution of slip, which is critical to understanding earthquake dynamics and

the damaging near-field seismic waves, might be best assessed from correlating optical images. Optical-image correlation has proven to be efficient in mapping fault ruptures and in measuring both the fault-parallel and fault-perpendicular components of coseismic displacements [9]. Several studies indicate success in correlating images from the same sensor and with nearly equal incidence views, e.g., [1, 10, 11].

COSI-Corr now allows the processing of images acquired by different systems and with different incidence views, considerably broadening the technique’s potential. Fig. 2.1 shows one component of the coseismic displacement field induced by the 1999 Mw 7.1 Hector Mine earthquake, California, measured by correlating a 10-meter SPOT 4 image with a 15-meter ASTER image. Although the deformation field is not as well resolved as the one measured by correlating two SPOT images with 10-meter resolution [8], the fault trace is effortlessly delineated and the fault slip vectors can be measured from the surface displacement discontinuities. A secondary branch of the rupture that accounts for a right lateral displacement of about 1 meter is also visible. This example also demonstrates the sub-pixel capabilities of COSI-Corr. Even with images from different sensors, uncertainties on the fault slip measurements are very low: 0.15 meter to 0.8 meter.

2.4 Ice Flow

In the current climatic context, monitoring continental ice and better understanding glacier dynamics are crucial. Rignot and Kanagaratnam, [12], recently detected that the rapid increase in ice velocities is the major cause of mass reduction of polar ice sheets, but the seasonal and interannual variability of glacier flow remains poorly known. Cross correlation of optical imagery can address these issues [4, 6]. Fig. 2.2 shows horizontal displacements in the Mer de Glace area (Alps) over 26 days (23 August to 18 September 2003), derived from 2.5-meter-resolution SPOT 5 images. Our study reveals details of the ice velocity field with exceptional accuracy. Very few areas of decorrelation are observed, and when such areas are present, they result mainly from changes in length and orientation of mountain shadows between the two dates. Around the main glaciers, many small, disconnected regions (subkilometric size) have measurable motion. This complete and homogeneous ice flow field measured with COSI-Corr is valuable to validating and calibrating ice flow models, which can then be used to predict the fate of mountain glaciers and ice sheets under global warming

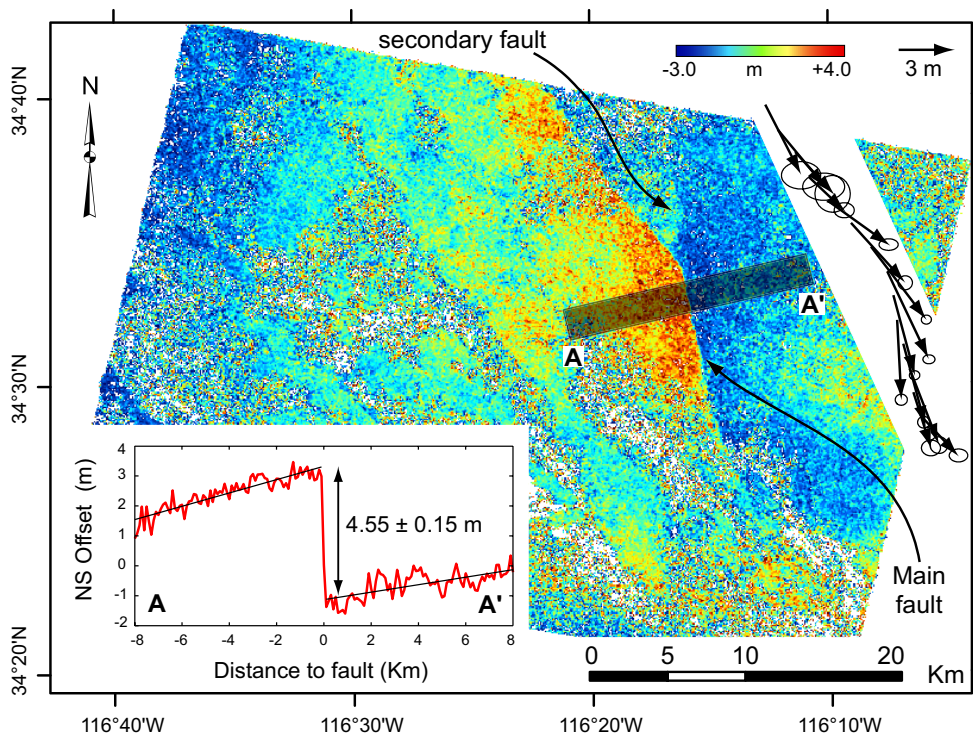


Figure 2.1: North/south component (northward positive) of the coseismic displacement field due to the 1999 Hector Mine earthquake, California. The pre-earthquake image (10-meter SPOT 4 acquisition from 17 August 1998) and the post-earthquake image (15-meter ASTER acquisition from 10 May 2000) were orthorectified and coregistered on a 10-meter-resolution grid, and offsets were measured from subpixel correlation between sliding windows. No measurement is assigned to white points where the correlation is too weak. The main fault rupture is a linear discontinuity in the data. Horizontal fault slip vectors are measured from linear least-square adjustment on each side of the fault and on each N-S and E-W component of profiles running perpendicularly to the fault. Profiles are stacked over a width of 2 km. This produces the vector plot of the displacement at fault, showing right-lateral strike-slip motion. Ellipses represent the 95% confidence interval. The standard deviation on individual measurements is around 1.3 meters.

scenarios.

2.5 “Slow” Landsliding

The mechanics of slowly moving landslides, a common phenomenon in mountainous areas, also remains poorly understood. The dynamics are complex and highly sensitive to climatic factors [13], making it difficult to assess how slow landslides evolve with time. Conventional geodetic measurements (tacheometry, leveling, kinematic GPS) are commonly used to monitor the temporal evolution of landslides, but they cannot capture the spatial heterogeneities of mass movement, which may be best assessed with multitemporal images.

Fig. 2.3 shows cumulative horizontal displacement over about 11 months, measured from the sub-pixel correlation of two 2.5-meter-resolution SPOT 5 images. This displacement field is consistent with InSAR measurements [14], but it provides better spatial resolution. Interestingly, the velocity field does not coincide with the geomorphic expression of the landslide and is highly heterogeneous. A network of benchmarks had been installed for repeated geodetic measurements. Although the targets were correctly placed according to the morphology of the landslide, they missed the most active areas. These areas were revealed by our technique and may otherwise have remained undetected.

2.6 A Technique Ready for Operational Use

Investigating and monitoring Earth’s surface evolution through co-registration and correlation of multitemporal and multisensor images is promising, especially given the existing archives of satellite and aerial images, the increasing number of satellite imagery systems, and their improving resolution. The COSI-Corr methodology corrects pointing inaccuracies in both push-broom satellites and aerial images to achieve sub-pixel image co-registration. In addition, the sub-pixel correlation of precisely co-registered images allows for the accurate estimation of displacement fields between multitemporal images.

The accuracy of the technique may be limited by the following: availability of accurate digital elevation models, especially in mountainous areas; the quality of ancillary data provided with the images (attitude records should be well sampled); radiometric noise, sensor saturation, and aliasing; shadow length and orientation differences between images;

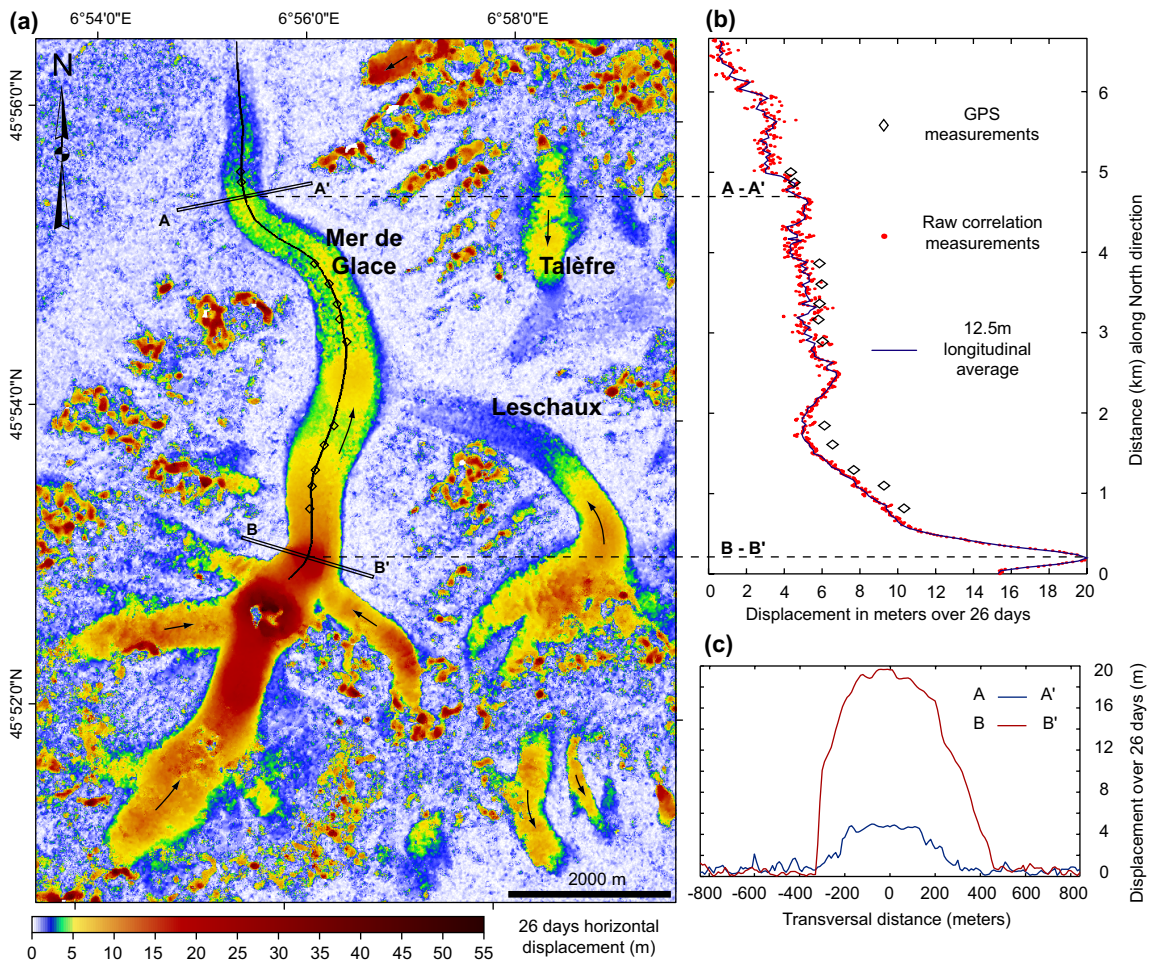


Figure 2.2: (a) Amplitude of the horizontal displacement over the Mer de Glace area from 23 August 2003 to 18 September 2003, obtained from two panchromatic 2.5-meter-resolution, SPOT 5 images. Arrows indicate the flow direction. Displacements below the images resolution appear in blue. Displacements as high as 55 meters (about 800 m/yr) are recorded over this 26-day period. (b) Displacements along a central flow line of the Mer de Glace measured from SPOT 5 images and from campaign GPS. The time period covered by the GPS (12 August 2003 to 3 September 2003) starts slightly earlier in the summer and includes the August 2003 European heat wave, which explains the faster velocities observed over this period [4]. (c) Displacement along transverse profiles AA' and BB'.

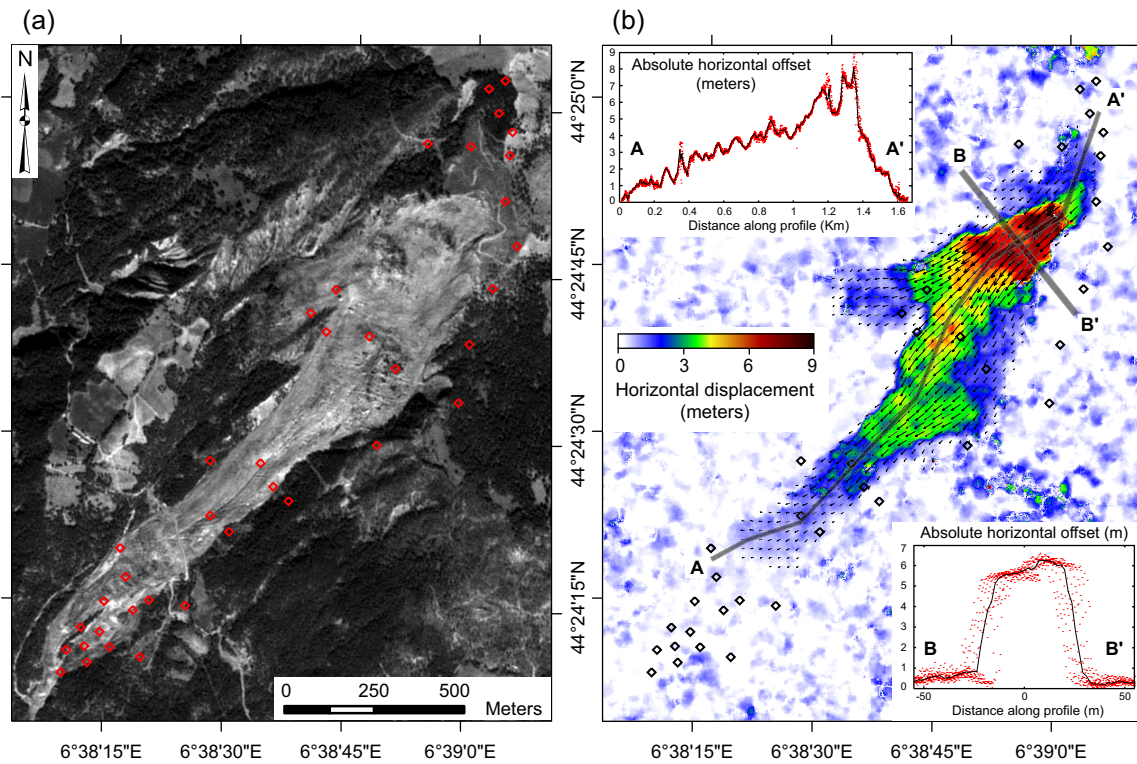


Figure 2.3: (a) Orthorectified SPOT image of the La Valette landslide (Ubaye Valley, French Alps). The red diamonds show the geodetic benchmarks for field survey. (b) Absolute horizontal displacement and displacement vectors as imaged from the correlation of two 2.5-meter SPOT 5 images acquired on 19 September 2003 and 22 August 2004. The maximum displacement is 9 meters. Longitudinal and transversal profiles, along AA' and BB', respectively, show the raw data (red dots) and the average over a 15-meter-wide swath (black line). The black diamonds indicate the geodetic benchmarks. The displacement field revealed from the correlation would not have been noticed in the geodetic measurements.

variations in snow, cloud, or vegetation cover; or man-made changes such as new buildings.

Despite these limitations, COSI-Corr is an efficient and versatile tool for investigating a variety of geomorphic and seismotectonic processes such as faulting, the mechanics of ice flow and the effects of climate, and landslides.

This approach has myriad potential applications: For instance, it has also been used to accurately measure sand dune migration. Correlation of optical images is a valuable complement to InSAR to measure displacements at Earth's surface because it directly provides the two components of the horizontal displacement field, it is more robust against decorrelation, and it does not saturate if there is a large displacement gradient. Furthermore, because COSI-Corr also allows for accurate co-registration of multispectral bands, applications that require high-quality band-to-band co-registration, such as vegetation monitoring, can also be investigated.

Chapter 3

Automatic and Precise Orthorectification, Co-Registration, and Sub-Pixel Correlation of Satellite Images, Application to Ground Deformation Measurements

By Sébastien Leprince¹, Sylvain Barbot², François Ayoub², and Jean-Philippe Avouac²

¹ Electrical Engineering Department, California Institute of Technology, Pasadena, California, USA

² Division of Geological and Planetary Sciences, California Institute of Technology, Pasadena, California, USA

Foreword— This chapter is an updated version of a previously published paper under the reference S. Leprince, S. Barbot, F. Ayoub, and J. P. Avouac, “Automatic and Precise Ortho-rectification, Co-registration and Sub-Pixel Correlation of Satellite Images, Application to Ground Deformation Measurements,” *IEEE Transactions on Geoscience and Remote Sensing*, vol. 45, no. 6, pp. 1529–1558, 2007. In this thesis, it is referred to as reference [8]. This chapter constitutes the fundamental part of this thesis, identifying and formulazing the processing steps necessary to make quantitative measurements of ground dis-

placements using optical satellite images. All studies in this thesis take root from this chapter. S. Leprince is responsible for the theoretical work, design, and tests of the algorithms described, while S. Barbot and F. Ayoub have contributed in editing and packaging these algorithms. This packaging work has made possible the release of the Co-registration of Optically Sensed Images and Correlation (COSI-Corr) software package. J.P. Avouac is the project principal investigator.

We describe a procedure to accurately measure ground deformations from optical satellite images. Precise orthorectification is obtained thanks to an optimized model of the imaging system where look directions are linearly corrected to compensate for attitude drifts, and sensor orientation uncertainties are accounted for. We introduce a new computation of the inverse projection matrices for which a rigorous resampling is proposed. The irregular resampling problem is explicitly addressed to avoid introducing aliasing in the orthorectified images. Image registration and correlation is achieved with a new iterative, unbiased processor that estimates the phase plane in the Fourier domain for sub-pixel shift detection. Without using supplementary data, raw images are wrapped onto the digital elevation model, and co-registered with a $\frac{1}{50}$ pixel accuracy. The procedure applies to images from any pushbroom imaging system. We analyze its performance using SPOT images in the case of a null test (no coseismic deformation) and in the case of large coseismic deformations due to the Mw 7.1 Hector Mine, California, earthquake of 1999. The proposed technique would also allow precise co-registration of images for the measurement of surface displacements due to ice-flow or geomorphic processes, or for any other change detection applications. A complete software package, COSI-Corr, is available for download from the Caltech Tectonics Observatory website.

3.1 Introduction

Earth surface changes can be determined by comparing pairs of optical satellite images acquired on different dates. Precise image co-registration is a prerequisite in such applications and this critical step is often a major source of limitation [15], [16]. For instance,

a registration accuracy of less than $\frac{1}{5}$ of a pixel is required to achieve a change detection error of less than 10% in Landsat Thematic Mapper images, [17]. As to the measurement of Earth surface displacements, which is the driving motivation of this study, most applications require a measurement accuracy of less than 1 meter. This implies the images' co-registration accuracy must be even less, significantly smaller than the pixel size of most currently available optical satellite images. Examples of such applications include the measurement of coseismic ground deformations [1], [18], [10], [19], of ice flow [4], and of sand dune migrations [5].

Difficulties in accurately co-registering satellite images arise from the non-ideal characteristics of the optical systems, the changing attitude of the spacecraft during the scanning operation of the images, digital elevation model (DEM) errors, and inaccurate resampling. The accuracy of the measurements of ground displacements in addition depends on the performance of the correlation technique. Despite these difficulties, encouraging results were obtained in a number of studies. It should be noted however that they were all carried on using data from only one imaging system and under restrictive conditions such as similar viewing angles and satellite tracks [1], [20], [21], or using external information from GPS measurements [10]. Precise co-registration of images with viewing angle differing by more than 3° also seems out of reach [21], [1]. The operational use of such a technique, in particular to monitor coseismic deformations, would benefit from a more generic approach allowing cross correlation of images from different imaging systems with different viewing angles, and without the need for information other than what is extracted from the satellite ancillary data and the topography.

To be co-registered, remotely sensed images need to be projected and resampled onto some common reference system. One method consists of fixing one image as the reference image, the master image. Its viewing geometry defines the common reference system, and other images, the slave images, are projected and resampled onto this reference system. Analysis of images' discrepancies is carried out in this reference frame by applying the desired change detection algorithm. This approach is commonly used in processing pairs of radar images to produce differential interferograms [22]. Examples with optical images are found in [18] and [4]. A second method is to project and resample each image onto a reference system that is independent of the satellite viewing geometry, such as a ground projection. The technique thus consists of projecting images onto the ground according

to their viewing geometry, change detection analysis being performed on the set of ground images generated. This approach is illustrated in [1], [10], and [19]. Here we prefer this second method. It is the most flexible way to co-register images from different acquisition systems (e.g. pushbroom images, aerial photographs, etc...) and the production of ground projected images provides a georeferenced by-product suitable for many other needs.

This paper describes an automatic processing chain to accurately and rigorously co-register and compare a set of optical satellite images. The processing chain is composed of four fundamental processes: the first process projects each pixel from the satellite focal plane onto a ground reference system. This operation utilizes knowledge from both the imaging system and the ground topography. The second process performs the resampling of the acquired image according to the projection mapping previously calculated. This yields ground projected images, called orthorectified images. Cumulative uncertainties on both the imaging system and the topography lead to distortions and mis-registrations between the pairs of orthorectified images to be compared. The processing chain is therefore augmented with a third process optimizing the satellite viewing parameters with respect to some reference frame. This reference frame will be either a shaded version of the topography model or another image previously orthorectified. Mis-registrations to be corrected are measured from the fourth process, a correlation.

In this study we focus on images from the SPOT (Satellite pour l'Observation de la Terre) satellite systems principally because raw images are delivered with all the acquisition parameters (ephemeris, attitude components during the imaging process, CCD look directions, etc...) provided in ancillary data [23]. We also use panchromatic (PAN) images rather than multi-spectral images because of their higher ground resolution, which is a major advantage for the measurement of ground deformations. PAN images of the SPOT satellites 1,2,3,4 have a ground resolution of 10 m. 5 m and 2.5 m ground resolution are available from SPOT 5. The technique presented can be applied to any multi-spectral images, making it appropriate for any change detection applications. Images from other pushbroom systems also can be processed from our methodology, as explained for ASTER (Advanced Spaceborne Thermal Emission and Reflection Radiometer) images in Appendix D. An application is given in [9].

The first three sections of the paper present, respectively, the orthorectification mapping computation, the resampling scheme, and the correlation-registration algorithm. The fourth

section describes the global optimization mechanism and the processing chain that allows for accurate image orthorectification and co-registration. Finally, the last section assesses the quality of the whole process and presents an application to the measurement of a coseismic displacement field.

3.2 Pushbroom Geometry and Orthorectification Models

A rigorous way to register satellite images is to determine the orthorectification parameters for each image such that precise registration is achieved. We therefore first examine the modeling of the SPOT satellites' viewing geometry. SPOT satellites are pushbroom imaging systems, meaning that all optical parts remain fixed during the images acquisition and the scanning is accomplished by the forward motion of the spacecraft. Each line in the image is then acquired at a different time and submitted to the variations of the platform. Since the pushbroom acquisition system of all SPOT satellites are modeled by the same set of equations (see Appendix D for the case of ASTER images), it is possible to derive a common orthorectification scheme.

3.2.1 The Direct Orthorectification Model

The direct orthorectification model computes the geographic location on the ground where each pixel in the raw image, i.e. the focal plane of the instrument, has to be projected. Notations are derived from the SPOT satellite geometry handbook [24].

3.2.1.1 Navigation Reference Coordinate System and Look Directions

The Navigation Reference Coordinate System (O_1, X_1, Y_1, Z_1) is the spacecraft body fixed reference system. O_1 is the satellite center of mass and the axes are defined such that, at nominal attitude when the satellite roll, pitch and yaw are null angles, if \vec{P} and \vec{V} are the satellite position and velocity vectors, we have:

$$\begin{cases} \vec{Y}_1 // \vec{V} \\ \vec{Z}_1 // \vec{P} \\ \vec{X}_1 = \vec{Y}_1 \wedge \vec{Z}_1. \end{cases} \quad (3.1)$$

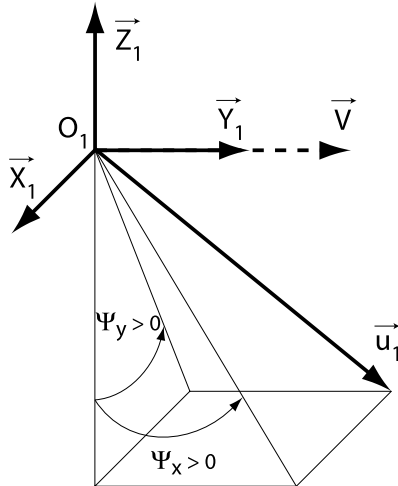


Figure 3.1: Definition of the look direction \vec{u}_1 from the look angles Ψ_x and Ψ_y in the Navigation Reference Coordinate System

The SPOT satellites' (1,2,3,4, and 5) positions and velocities are given in Cartesian coordinates with reference to the ITRF (International Terrestrial Reference Frame) [25]. In the past years, the WGS 84 geodetic system has been gradually aligned to the successive ITRF realizations. For our study, we can consider that the WGS 84 and the different ITRF realizations are undistinguishable, and we then express all coordinates in the WGS 84 reference system.

The SPOT satellites sensor consists of a Charge Coupled Device (CCD) line array responsible for the image pushbroom scanning operation. Expressed in the Navigation Reference Coordinate System, the look directions are modeling the equivalent pointing direction of each CCD element. Constant during the image acquisition, they provide the internal camera model accounting for the mirror rotation, optical distortions, and calibration parameters resulting from on-ground post-processing. The look directions are provided in ancillary data in the form of a two-angle rotation, (Ψ_x, Ψ_y) , around the satellite body fixed system axes (Fig. 3.1). Hence, for all columns c and for all rows r in the raw image, the look directions \vec{u}_1 are given by:

$$\vec{u}_1(c, r) = \frac{\vec{u}'_1(c, r)}{\|\vec{u}'_1(c, r)\|_2}, \quad \text{for all } c, r = 1, \dots, N \quad (3.2)$$

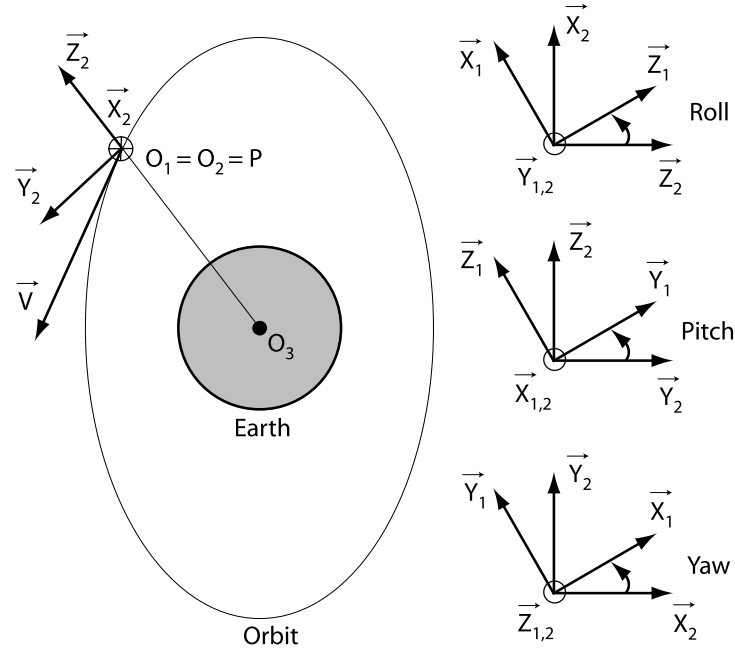


Figure 3.2: Orbital coordinate system and attitude variations

with

$$\vec{u}_1'(c, r) = \begin{pmatrix} -\tan \Psi_y(c) \\ \tan \Psi_x(c) \\ -1 \end{pmatrix}, \text{ for all } r,$$

where N is the number of CCD elements in the line array. Theoretically, these look directions should be attached to the optical center of the imaging system. Here, we assume that they are attached to the center of mass O_1 , since to our knowledge, no model linking the optical center to the center of mass is available. However, the non linear distortions induced by this approximation account for much less than a millimeter on the ground and are neglected here. Furthermore, the static error is absorbed from the parameters optimization, Section 3.5.1.2.

3.2.1.2 Orbital Coordinate System and Attitude Variations

The Orbital Coordinate System (O_2, X_2, Y_2, Z_2) is centered on the satellite ($O_2 = O_1$) and its orientation is based on the spacecraft's position in space (Fig. 3.2). Roll, pitch, and yaw

variations are given as rotation angles around the Y_2 , X_2 , and Z_2 axes defined by:

$$\begin{cases} \vec{Z}_2(t) = \frac{\vec{P}(t)}{\|\vec{P}(t)\|_2} \\ \vec{X}_2(t) = \frac{\vec{V}(t) \wedge \vec{Z}_2(t)}{\|\vec{V}(t) \wedge \vec{Z}_2(t)\|_2} \\ \vec{Y}_2(t) = \vec{Z}_2(t) \wedge \vec{X}_2(t), \end{cases} \quad (3.3)$$

where $\vec{P}(t)$ and $\vec{V}(t)$ are the instantaneous position and velocity of the satellite.

For historical reasons, SPOT attitudes data are expressed within the inverted Navigation Reference Coordinate System [24]. Applying this convention and given $a_p(t)$, $a_r(t)$, $a_y(t)$, the absolute rotation angles around the pitch, roll, and yaw axes at time t , the satellite look directions $\vec{u}_2(c, r)$ in the Orbital Coordinate System for all CCD elements are given, for all $c, r = 1, \dots, N$, by:

$$\vec{u}_2(c, r) = R_p(r) \cdot R_r(r) \cdot R_y(r) \cdot \vec{u}_1(c), \quad (3.4)$$

with

$$R_p(r) = \begin{bmatrix} 1 & 0 & 0 \\ 0 & \cos a_p(r) & \sin a_p(r) \\ 0 & -\sin a_p(r) & \cos a_p(r) \end{bmatrix},$$

$$R_r(r) = \begin{bmatrix} \cos a_r(r) & 0 & -\sin a_r(r) \\ 0 & 1 & 0 \\ \sin a_r(r) & 0 & \cos a_r(r) \end{bmatrix},$$

$$R_y(r) = \begin{bmatrix} \cos a_y(r) & -\sin a_y(r) & 0 \\ \sin a_y(r) & \cos a_y(r) & 0 \\ 0 & 0 & 1 \end{bmatrix},$$

where $R_r(r)$, $R_p(r)$, and $R_y(r)$ are the roll, pitch, and yaw rotation matrices at the time of acquisition of image row r .

3.2.1.3 Look Directions in Terrestrial Coordinate System

For each pixel in the raw image, the corresponding look direction \vec{u}_3 expressed within the Terrestrial Coordinate System is then

$$\vec{u}_3(c, r) = \begin{bmatrix} X_{2_x}(r) & Y_{2_x}(r) & Z_{2_x}(r) \\ X_{2_y}(r) & Y_{2_y}(r) & Z_{2_y}(r) \\ X_{2_z}(r) & Y_{2_z}(r) & Z_{2_z}(r) \end{bmatrix} \cdot \vec{u}_2(c, r). \quad (3.5)$$

3.2.1.4 Location on Earth Model

The corresponding ground location M of the raw image pixel (c, r) is determined by calculating the intersection between $\vec{u}_3(c, r)$ and the Earth ellipsoid model. For any such pixel we are then to find the point $M(x_M, y_M, z_M)$ that verifies

$$\begin{aligned} \overrightarrow{O_3M}(c, r) &= \overrightarrow{O_3P}(r) + \mu \cdot \vec{u}_3(c, r), \quad \text{for } \mu > 0 \\ \text{and } \frac{x^2 + y^2}{A^2} + \frac{z^2}{B^2} &= 1, \quad \text{with } \begin{cases} A = a + h \\ B = b + h \end{cases}, \end{aligned} \quad (3.6)$$

where O_3 is the Earth Cartesian center and a and b are, respectively, the semi-major and semi-minor axis of the ellipsoid. h is the approximated elevation above the ellipsoid at the ground location M . For any pixel (c, r) , μ is determined such that

$$\left[\frac{u_{3_x}^2 + u_{3_y}^2}{A^2} + \frac{u_{3_z}^2}{B^2} \right] \mu^2 + 2 \left[\frac{P_x u_{3_x} + P_y u_{3_y} + P_z u_{3_z}}{A^2} + \frac{P_z u_{3_z}}{B^2} \right] \mu + \left[\frac{P_x^2 + P_y^2}{A^2} + \frac{P_z^2}{B^2} \right] = 1,$$

where $\overrightarrow{O_3P}(r) = (P_x, P_y, P_z)$ and $\vec{u}_3(c, r) = (u_{3_x}, u_{3_y}, u_{3_z})$. The smallest solution, μ_1 , is to be kept (the largest one intersecting with the other side of the ellipsoid) and used in eq. (3.6) to obtain the geocentric coordinates $M(x_M, y_M, z_M)$ of the pixel (c, r) .

Using a DEM, the intersection with the topographic surface is computed by locally and successively approximating the topography with a wider ellipsoid (Appendix A).

3.2.1.5 Direct Model Transformation Matrices

All the pixels in the raw image are associated with Cartesian geocentric coordinates, which can be converted into geodetic coordinates, and then into UTM (Universal Transverse Mer-

cator) coordinates [26], expressed in meters, like the ground displacements to be measured. These ground coordinates are stored in two matrices, N and E , representing the Northing and Easting components. The pixel of coordinates (c, r) in the raw image will then have the ground coordinates $\{E(c, r), N(c, r)\}$. The transformation matrices provide necessary information to resample the raw image and to produce an orthorectified image.

However, this approach contains an important drawback: it projects the regular pixel grid from the instrument focal plane to an irregular grid on the ground. On a large scale, irregularities result from the global rotation between the raw and orthorectified images due to the satellite orbit inclination. On a more local scale, irregularities are due to changes in the satellite attitudes and to the topography roughness. For specific applications in seismotectonics, coseismic displacements are typically of a sub-pixel scale. The resampling of the images therefore needs particular attention to preserve sub-pixel information from the raw images; resampled images have to respect the Shannon-Nyquist sampling criterion to avoid aliasing (Section 3.3.1).

3.2.2 The Inverse Orthorectification Model

To facilitate the rigorous resampling of the images to orthorectify, we determine the non-integer pixel coordinates in the raw image of a predefined regular grid on the ground. This operation, called the inverse orthorectification model, has been investigated in several studies [27], [28], [29]. However, they are all based on the collinearity equations stating that a point in the focal plane, the optical center, and the imaged point on the ground are all aligned. This assumption is no longer valid in the presence of aberrations or distortions from the imaging system. Modern satellites, such as SPOT satellites, provide look directions as a complete physical model of the imaging system [24]. We therefore propose a new inverse orthorectification scheme, which fully exploits the information from the ancillary data, by inverting the direct orthorectification model.

Our scheme assumes that any given point on the ground lying inside or in the close vicinity of the imaged area has one and only one corresponding point in the image plane or in its close vicinity. We extend the assumption to the close vicinity of the image because we extrapolate attitude and sensor values outside the image plane. In practice this assumption is satisfied when dealing with a stable imaging system, and can be verified a posteriori. We have never encountered limitations due to this assumption.

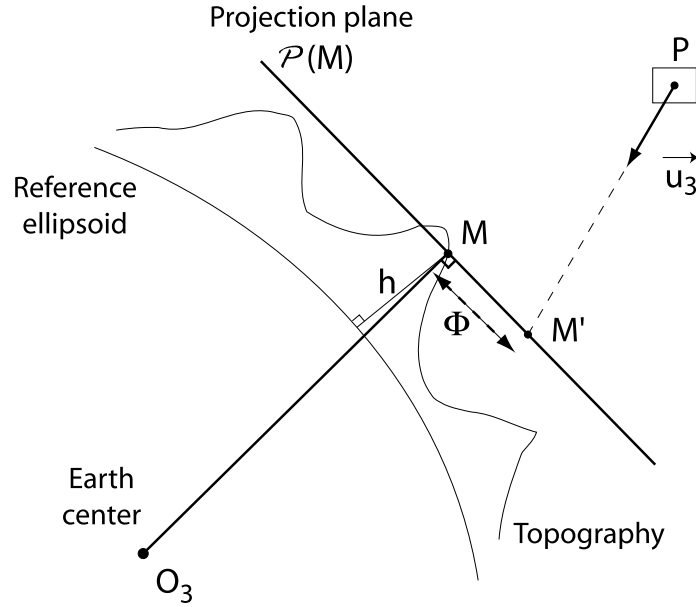


Figure 3.3: Inverse ortho-rectification model principle

3.2.2.1 The Orthorectification Grid

To compare a set of co-registered images, all images have to be rectified onto a common grid. The orthorectification grid is therefore defined as the smallest rectangular grid that includes the image footprint, and whose starting coordinates (UTM) are a multiple of the desired image resolution. Comparable images (ortho-rectified at the same resolution) will then not suffer from grid misalignment. The image footprint is determined by application of the direct orthorectification model to the four corners of the raw image.

3.2.2.2 Inverse Ortho-Rectification Principle

Given a point M on the ground (on the orthorectification grid) its elevation is determined from bi-cubic interpolation of the DEM and its coordinates converted into the Earth-centered Cartesian WGS 84 system [26].

Eq. (3.5) gives the look directions $\vec{u}_3(c, r)$ for all $c, r = 1, \dots, N$. Now we consider a continuous version of the look directions with the notation $\vec{u}_3(x, y)$ and $(x, y) \in \mathbf{R}^2$. Finding the pixel coordinates (x, y) in the raw image that are associated with a given point $M(x_M, y_M, z_M)$ on the ground is equivalent of finding $(x, y) \in \mathbf{R}^2$ that minimize the function

$$\Phi(x, y) = \|\overrightarrow{O_3 M} - \overrightarrow{O_3 M'(x, y)}\|_2^2, \quad (3.7)$$

where $M'(x, y)$ should be the point on the ground seen from the look direction $\vec{u}_3(x, y)$. Let $\vec{O}_3\vec{P} = (P_x, P_y, P_z)$ be the satellite position for the look angle \vec{u}_3 . Assuming a rectilinear propagation of light through the atmosphere, the line of sight implied by $\vec{u}_3 = (u_{3_x}, u_{3_y}, u_{3_z})$ is $\vec{s} = \vec{O}_3\vec{P} + t \cdot \vec{u}_3$, for some $t > 0$. If M' lies at the intersection between \vec{s} and the topography, determining its coordinates is extremely tedious and the non-linearities of the topography may cause the minimization of Φ to fail. For both simplicity and efficiency, we construct a projection plane for each point M on the orthorectification grid, on which M' actually lies. The projection plane $\mathcal{P}(M)$ is the plane passing through M and perpendicular to $\vec{O}_3\vec{M}$ (Fig. 3.3). Since $M \in \mathcal{P}(M)$, the solution of the minimization of Φ is unchanged but the straightforward computation of M' and the near quadratic regularity of Φ are now ensured. All points $M'(\alpha, \beta, \gamma)$ in $\mathcal{P}(M)$ must satisfy $\vec{O}_3\vec{M} \cdot \vec{MM}' = 0$. Hence the projection plane is explicitly defined by

$$x_M\alpha + y_M\beta + z_M\gamma - (x_M^2 + y_M^2 + z_M^2) = 0. \quad (3.8)$$

\vec{s} then intersects $\mathcal{P}(M)$ for

$$t = t^* = \frac{d - x_M P_x - y_M P_y - z_M P_z}{x_M u_{3_x} + y_M u_{3_y} + z_M u_{3_z}}, \quad (3.9)$$

with $d = x_M^2 + y_M^2 + z_M^2$.

The solution of the inverse orthorectification problem, (x^*, y^*) , is therefore obtained by minimizing the function

$$\Phi(x, y) = \|\vec{O}_3\vec{M} - \vec{O}_3\vec{M}'(x, y)\|_2^2, \quad (3.10)$$

with

$$\vec{O}_3\vec{M}'(x, y) = \vec{O}_3\vec{P}(y) + t^* \cdot \vec{u}_3(x, y), \quad (3.11)$$

for all points M in the orthorectification grid.

3.2.2.3 Minimizing Φ

By projecting M' onto the plane surface $\mathcal{P}(M)$, the non-linearities of Φ are now only due to the satellite optical distortions and changing attitudes, which are smoothly varying in the vicinity of the solution. The problem of minimizing Φ is then quasi linear and the

near-quadratic regularity of Φ makes an unconstrained gradient minimization approach appropriate.

The algorithm requires that Φ be a continuous function for all $x, y \in \mathbf{R}$, while it is only given at integer pixel locations. Satellite velocities, positions, attitudes, and sensor orientations are then linearly interpolated between pixels and linearly extrapolated beyond the image limits (to satisfy the unconstrained minimization process). The linear extrapolation should preserve the continuity of the values as well as the global motion of the satellite. We have chosen extrapolated points to lie on the line joining the values at the image limits in both x and y directions.

Several classical gradient minimization procedures were tested, namely the quasi-Newton, the steepest descent, and the conjugate gradients algorithms, but we occasionally experienced convergence problems when the initialization guess was not accurate. The two-point step size (TPSS) gradient algorithm [30] proved to be more robust and efficient. Implementation details are provided in Appendix B.

3.2.2.4 Inverse Model Transformation Matrices

Outputs of the minimization are stored into two matrices with dimensions determined by the orthorectification grid. x^* values are stored in the X matrix, y^* values in the Y matrix. If the ground coordinates of the upper-left-corner grid element are (E_0, N_0) and the grid resolution is r , then at the ground location $(E_0 + i \cdot r, N_0 - j \cdot r)$ the pixel of coordinates $(X(i, j), Y(i, j))$ in the raw image has to be projected. This inverse orthorectification model is used next to resample raw images and to produce precise orthorectified images.

3.3 Image Resampling

In the image processing literature the nearest-neighborhood, bi-linear, and bi-cubic resampling methods are the most commonly used [31]. These methods have been designed with the constraint of keeping a small kernel size to minimize the computational cost inherent to any convolution process. These resampling methods can be seen as a zeroth-, first-, and third-order polynomial approximations of the theoretical resampling kernel, the sinc function. Unlike the sinc function, approximating kernels introduce a certain amount of aliasing in the resampled images [31], which may reduce the accuracy of any correlation

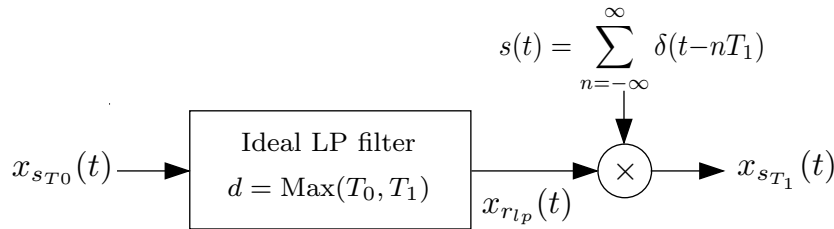


Figure 3.4: General regular resampling scheme

process, hence any registration process. For example, systematic correlation biases have been observed when images were resampled from these methods [1]. Moreover, it will be shown next that an explicit formulation of the irregular resampling problem is required to avoid addition of aliasing while constructing orthorectified images.

3.3.1 Resampling Regularly Spaced Data: Changing the Sampling Rate

Consider the continuous band-limited low-pass signal $x_c(t)$ sampled at the Nyquist rate $\frac{2\pi}{T_0}$ (with T_0 the sampling period). The sampled signal is called $x_{s_{T_0}}(t)$. Resampling a given sampled signal can be done by sampling its reconstructed continuous version at a new rate $\frac{2\pi}{T_1}$.

If $T_1 > T_0$, appropriate low-pass filtering of the reconstructed signal, which is equivalent of reconstructing a lower band-limited version of $x_c(t)$, is needed to avoid aliasing in the resampled signal $x_{s_{T_1}}(t)$. From the Shannon-Nyquist sampling theorem [32], a general ideal reconstruction filter is written as:

$$h_{r_d}(t) = \begin{cases} \frac{\sin\left(\frac{\pi t}{d}\right)}{\frac{\pi t}{d}}, & \text{for } t \neq 0 \\ 1, & \text{for } t = 0, \end{cases} \quad (3.12)$$

where d can be seen as the effective reconstruction period. A general resampling scheme that allows for up-sampling as well as for down-sampling regularly spaced data is designed by setting the parameter $d = \text{Max}(T_0, T_1)$, Fig. 3.4. It is of note that up-sampling does not add information and that $x_{s_{T_1}}(t)$ is then oversampled.

3.3.2 Resampling on an Irregular Grid

We present an aliasing-free resampling scheme where the original signal is regularly sampled and has to be irregularly resampled, which is the problem posed by the inverse orthorectification modeling.

For simplification, we assume that sampling irregularities account for a small fraction of the mean sampling period. Denote by T_0 the sampling period of the signal to be resampled and by $\{T_1\}$ the set of sampling periods of the resampled signal. It is supposed that $\mu(\{T_1\}) \gg \sigma(\{T_1\})$. $\mu(\cdot)$ represents the mean operator and $\sigma(\cdot)$ the standard deviation operator. $\mu(\{T_0\}) = T_0$ and $\sigma(\{T_0\}) = 0$ for regularly sampled signals. Therefore, the parameter d of a general reconstruction filter for irregularly spaced data is such that

$$d = \max(T_0, \{T_1\}). \quad (3.13)$$

This ensures the resampled signal to be aliasing free. However, it is locally subjected to oversampling since this scheme is equivalent of reconstructing the signal at its lower regularly sampled resolution. As it will be shown later, this non-optimality is not a problem for most applications.

3.3.2.1 The Two-Dimensional Resampling Kernel

For simplicity and computational efficiency, we concentrate on separable resampling kernels. The reconstruction filter is an ideal low-pass filter of the form:

$$h_{r_{d_x, d_y}}(x, y) = \begin{cases} \frac{\sin(\frac{\pi x}{d_x})}{\frac{\pi x}{d_x}} \cdot \frac{\sin(\frac{\pi y}{d_y})}{\frac{\pi y}{d_y}}, & \text{for } x, y \neq 0, \\ 1, & \text{for } x, y = 0, \end{cases}$$

where d_x, d_y are called the ‘‘resampling distances’’. They represent the maximum distance between adjacent samples in the x and y directions.

Practically, a finite length approximation is derived from weighting by a non rectangular window that tapers close to the edges, the Kaiser window. This helps in minimizing the maximum reconstruction error [32] that mostly manifests itself as ringing in the reconstructed image (Gibbs phenomenon). Setting the kernel length to $2N + 1$ samples, the 2D

separable Kaiser window is defined by:

$$w_{K_{d_x, d_y}}(x_n, y_n) = \begin{cases} \frac{I_0(\beta_x(1 - (\frac{x_n}{Nd_x})^2)^{\frac{1}{2}})}{I_0(\beta_x)} \cdot \frac{I_0(\beta_y(1 - (\frac{y_n}{Nd_y})^2)^{\frac{1}{2}})}{I_0(\beta_y)}, & \text{for } \begin{cases} -Nd_x \leq x_n \leq Nd_x \\ -Nd_y \leq y_n \leq Nd_y, \end{cases} \\ 0, & \text{otherwise,} \end{cases}$$

where $I_0(\cdot)$ represents the zeroth-order modified Bessel function of the first kind and β the shape parameter. Practically, the shape parameters are set to $\beta_x = \beta_y = 3$ and $N = 12$ samples. This set up is a reasonable compromise between the mean square reconstruction error measured on a set of SPOT images and the computational cost.

If we call i_0 the image to be resampled and i_1 the resampled image, then i_1 is obtained by the following two-dimensional discrete convolution:

$$i_1[x, y] = \frac{1}{c(x, y)} \sum_{x_n \in D_x} \sum_{y_n \in D_y} i_0[x_n, y_n] h_{r_{d_x, d_y}}(x - x_n, y - y_n) w_{K_{d_x, d_y}}(x - x_n, y - y_n), \quad (3.14)$$

with

$$c(x, y) = \sum_{x_n \in D_x} \sum_{y_n \in D_y} h_{r_{d_x, d_y}}(x - x_n, y - y_n) w_{K_{d_x, d_y}}(x - x_n, y - y_n),$$

where $D_x = [x - Nd_x, x + Nd_x]$ and $D_y = [y - Nd_y, y + Nd_y]$. $\{x_n, y_n\}$ are the original data samples and $\{x, y\}$ are the resampled data points.

3.3.2.2 Resampling Using Inverse Transformation Matrices

The inverse transformation matrices map a regular grid on the ground onto an irregular grid in the raw image. This is equivalent of considering $T_0 = 1$ (raw image sampled at every pixel) regular and $\{T_1\}$ irregular, both expressed in pixels since they are defined in the raw image space. We define d_x and d_y , which must each verify:

$$d = \max(T_0, \{T_1\}). \quad (3.15)$$

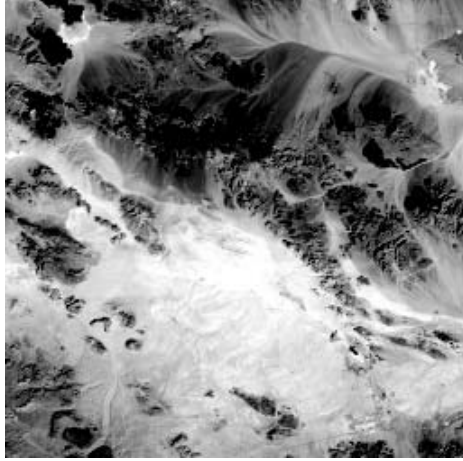


Figure 3.5: Raw image

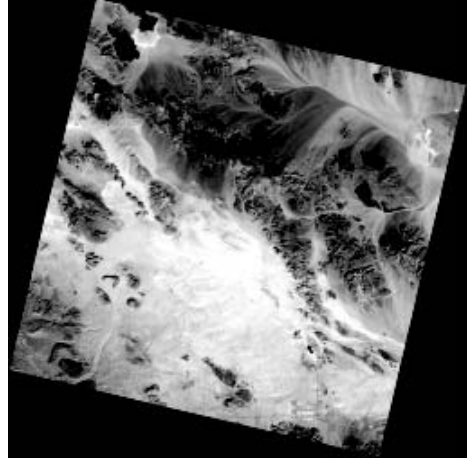


Figure 3.6: Orthorectified image

If we denote by d_{i,j_x} the local distances of the X matrix, then:

$$d_{i,j_x} = \max \begin{pmatrix} |X_{i,j} - X_{i-1,j-1}|, |X_{i,j} - X_{i,j-1}|, \\ |X_{i,j} - X_{i-1,j}|, |X_{i,j} - X_{i+1,j-1}|, \\ |X_{i,j} - X_{i+1,j+1}|, |X_{i,j} - X_{i,j+1}|, \\ |X_{i,j} - X_{i-1,j+1}|, |X_{i,j} - X_{i+1,j}| \end{pmatrix}, \quad (3.16)$$

for all points (i, j) in the matrix X whose coordinates $X(i \pm 1, j \pm 1)$ are within the raw image. Then, to avoid aliasing, one should choose $d_x = \max(1, \max(\{d_{i,j_x}\}))$. d_y is determined using the same procedure applied to the Y matrix. Resampling is now straightforward because the points to be resampled are defined within the regular data set of the raw image.

3.3.3 Inverse Resampling Results

We present some results from an image that has been processed using the inverse orthorectification model and the inverse resampling procedure. The raw image is a SPOT 5 PAN image of the Hector Mine area in California with a nominal ground resolution of 5 m and scene orientation of 13.6° . It is orthorectified at a ground resolution of 10 m on a UTM projection. The computed resampling distances are $d_x = 2.501$ pixels and $d_y = 2.413$ pixels. The raw and the orthorectified images are presented in Fig. 3.5 and Fig. 3.6.

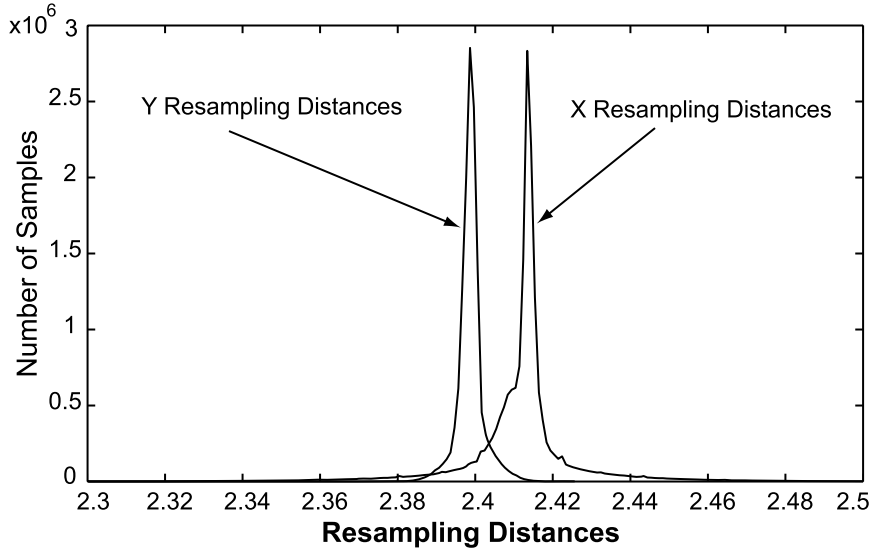


Figure 3.7: Distribution of local resampling distances (in pixels) for each transformation matrix

3.3.3.1 Resampling Distances

The rescaling factor is $\frac{1}{2}$ (the resolution is lowered by a factor of 2). The resampling distances should then be $d_x = d_y = 2$ pixels. The rotation angle corresponds to the scene orientation $\alpha = 13.6^\circ$. Geometrically, if we take a square of side length a , rotating it by an angle α , then the smallest non-rotated square that will contain the rotated one will have a side length $d = a\sqrt{2} \cos(\frac{\pi}{4} - \alpha)$. Taking $a = 2$ pixels, the first-order approximation of the resampling distances is then $d_x = d_y = 2.414$ pixels. Accounting for local distortions due to topography and satellite attitude variations, the resampling distances computed from the transformation matrices differ slightly from this estimate. This validates the resampling distance computation. Moreover, this computation is done with no a priori knowledge on the scene orientation, making this resampling scheme suitable for all optical imaging systems.

Fig. 3.7 shows that the irregularities of the sampling periods are much smaller than the average sampling periods, as assumed above. In this particular case $\mu(\{d_{i,j_x}\}) = 2.41$ pixels with $\sigma(\{d_{i,j_x}\}) = 0.020$ pixel, and $\mu(\{d_{i,j_y}\}) = 2.40$ pixels with $\sigma(\{d_{i,j_y}\}) = 0.036$ pixel.

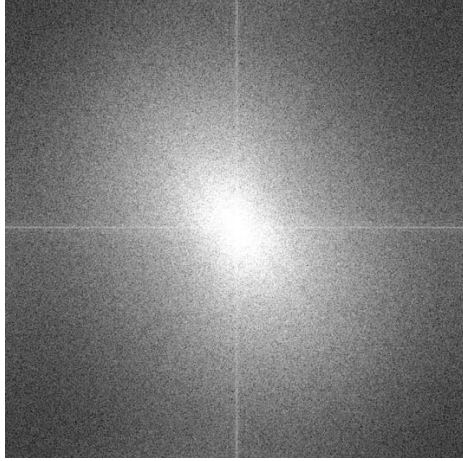


Figure 3.8: Raw image log-spectrum

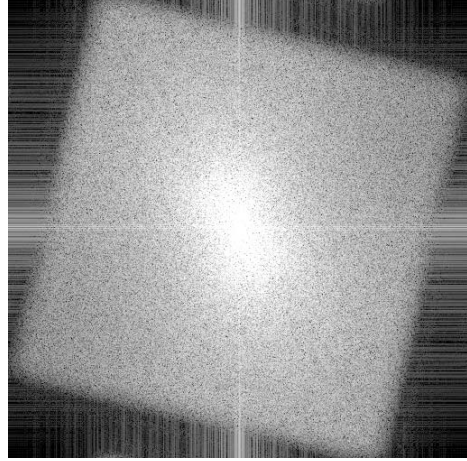


Figure 3.9: Orthorectified image log-spectrum

3.3.3.2 Fourier Spectrum of Orthorectified Images

Fig. 3.8 and Fig. 3.9 represent the Fourier spectrum of the raw and orthorectified images. These spectrums have been computed over small corresponding areas. The zero frequency is at the center of the images.

The rotation seen in the orthorectified image spectrum reflects the general rotation applied to the raw image, [33], when producing the orthorectified image. However, distortions due to the local topography are here producing a shear effect. The truncation of the spectrum is visible since it fits within the bandwidth defined by the Nyquist resampling frequency. As no aliasing (no frequency folding on the edges) is noticed in the orthoimage spectrum, we conclude that resampling distances are correctly computed. The dark areas of the orthorectified spectrum denote over-sampling, making this resampling scheme not optimum: even though the image is being resampled on a 10 m grid, the frequency content is the one of an image that would be “optimally” resampled at a resolution of approximately 12.5 m. An objective sense of “optimal” resampling is defined from the sampling efficiency.

Sampling efficiency. *The sampling efficiency η of a sampling scheme that allows no aliasing is defined as the ratio between the area S , support for the information (where the spectrum is not zero) within the Fourier elementary cell, and the area of the Fourier elementary cell. We call the Fourier elementary cell the cell that periodically tiles the Fourier plane of a discrete signal.*

Applying in the Fourier domain the formula we used in 3.3.3.1 to deduce the smallest size of a square containing a rotated square, the efficiency of the resampling scheme presented is therefore:

$$\eta(\alpha) = \frac{1}{2 \cos^2(\frac{\pi}{4} - \alpha)}, \quad \text{for } \alpha \in [0, \frac{\pi}{4}], \quad (3.17)$$

where α is the scene orientation. Hence for a general application $\eta \in [\frac{1}{2}, 1]$, at most. In this particular example, this gives $\eta_{SPOT} \approx 0.69$ (η is a decreasing function of α).

3.3.3.3 Possible Improvements

The main limitation of this resampling scheme comes from the separability of the kernel. Ideally, the resampling kernel would be locally rotated, so that it would be aligned with the grid defined by the resampling points in the raw image. Consequently, the vanishing high-frequency points in the Fourier spectrum will all correspond to the Nyquist frequency, the spectrum will not be rotated anymore, and the scene orientation will not induce over-sampling. The rotation of the resampling grid could be estimated from the local rotations in the inverse transformation matrices.

Another improvement would be to use locally adaptive resampling distances. In areas of steep topography, the resampling distances take high values while lower values correspond to areas of flatter relief. By imposing the maximum resampling distances to be used for the whole image, over-sampling is introduced in flatter topography areas, limiting the image effective resolution in those regions. This could be the main limiting sampling efficiency factor with high-resolution images. These possible improvements would ensure the sampling efficiency of the orthorectified image to come close to unity.

3.4 Correlation of Optical Images

3.4.1 Statement of the Problem

We discuss a technique to accurately and robustly measure the relative displacement between two images of the same resolution, one being the shifted version of the other. The problem to solve is an image registration problem [34] that we have chosen to tackle with correlation methods: two similar images are said to be registered when their cross-correlation attains its maximum. The relative displacement is then deduced from the position of best

registration.

The registration/correlation algorithm needs to meet several requirements:

- We are primarily interested in measuring coseismic displacements from pre- and post-earthquake images. For SPOT 1, 2, 3, 4 images, the finest resolution available is 10 m. Commonly, horizontal coseismic displacements are less than 10 m. The correlation algorithm must then allow for sub-pixel measurements with an accuracy of a few tens of centimeters. The required accuracy is therefore at least $\frac{1}{20}$ of a pixel.
- During the image co-registration process, correlation is needed to measure the mis-registration to be corrected even though it can be large. The correlation should then also give precise measurements at the multi-pixel scale, typically half the correlation window size. The image co-registration accuracy should be better than the coseismic displacement measurement accuracy.
- The spatial resolution of the coseismic offset field measured depends on the size of the sliding correlation window. We therefore seek a method that is reliable on small correlation windows, typically 32×32 pixels.
- Correlation should be as insensitive as possible to temporal decorrelations, data quantization, or other noise sources.
- For general use, the parameters of the algorithm should not depend on the window size.
- This algorithm has to be general so that it can process any digital images. We saw that the Fourier spectrum of the orthorectified images may be quite peculiar. The algorithm should then adapt to any given spectrum. When extending the global coseismic offset measurement technique to other optical devices (other satellite systems or aerial photographs), this correlation scheme should remain valid.

3.4.2 Phase Correlation Methods

We focus on particular correlation methods, the phase correlation methods, which have already shown good results for similar applications [1], [20], [10], [19]. All phase correlation methods rely on the Fourier Shift Theorem [32]: the relative displacement between a pair

of similar images is retrieved from the phase difference of their Fourier transform. Let i_1 and i_2 be two images that differ only by a displacement (Δ_x, Δ_y) such that

$$i_2(x, y) = i_1(x - \Delta_x, y - \Delta_y). \quad (3.18)$$

Denoting by I_1 and I_2 their Fourier transform, from the Fourier Shift Theorem we have the relation

$$I_2(\omega_x, \omega_y) = I_1(\omega_x, \omega_y)e^{-j(\omega_x\Delta_x + \omega_y\Delta_y)}, \quad (3.19)$$

where ω_x and ω_y are the frequency variables in column and row. The normalized cross-spectrum of the images i_1 and i_2 is then

$$C_{i_1 i_2}(\omega_x, \omega_y) = \frac{I_1(\omega_x, \omega_y)I_2^*(\omega_x, \omega_y)}{|I_1(\omega_x, \omega_y)I_2^*(\omega_x, \omega_y)|} = e^{j(\omega_x\Delta_x + \omega_y\Delta_y)}, \quad (3.20)$$

where $*$ denotes the complex conjugate. The images' relative displacement can thus be estimated from the two-dimensional slope of the cross-spectrum's phase. Applying the inverse Fourier transform, \mathcal{F}^{-1} , to eq. (3.20), we have the correlation function

$$\mathcal{F}^{-1}\{e^{j(\omega_x\Delta_x + \omega_y\Delta_y)}\} = \delta(x + \Delta_x, y + \Delta_y). \quad (3.21)$$

The images' relative displacement can then alternatively be estimated from the coordinates of the correlation peak. In case of sub-pixel displacements, this peak is not a Dirac delta function anymore, but a downsampled version of a Dirichlet kernel [35]. Further processing is then required to recover the image shift.

These approaches show that phase correlation methods fall into two categories. In the first category, the relative images' shift is recovered by explicitly estimating the linear phase of the images' cross-spectrum [1], [36], [37]. In the second category, the relative displacement is calculated by determining the exact location of the correlation peak [35].

In [35], images to be correlated are supposed to be sampled with a sampling efficiency $\eta = 1$. This is generally not the case when images have been resampled for orthorectification. Also, to avoid correlation bias, frequency masking should be applied to only select parts of the cross-spectrum where the phase information is valid (images may be corrupted by aliasing or optical aberrations). For these reasons, a correlation algorithm whose main

scheme belongs to the first category will be described, adaptive masking being applied on the cross-spectrum.

3.4.3 Phase Correlation Properties

We review some properties of the phase correlation methods, and evaluate the sensitivity to additive white noise and blur, two common phenomena [38]. We also discuss the range of measurable image shifts.

3.4.3.1 Image Blur

The image i_1 of a natural scene u_1 , acquired by an imaging device using incoherent illumination, is modeled as

$$i_1(x, y) = u_1(x, y) * |h_1(x, y)|^2, \quad (3.22)$$

where h_1 is the instrument point spread function (PSF) [39] and $*$ denotes the continuous time convolution. The optical transfer function (OTF) of the device is

$$H_1(\omega_x, \omega_y) = \mathcal{F}\{|h_1(x, y)|^2\}, \quad (3.23)$$

where \mathcal{F} denotes the forward Fourier transform. Then

$$I_1(\omega_x, \omega_y) = U_1(\omega_x, \omega_y)H_1(\omega_x, \omega_y), \quad (3.24)$$

where $U_1(\omega_x, \omega_y) = \mathcal{F}\{u_1(x, y)\}$. If the same scene is acquired at a different time with possibly another instrument of OTF H_2 , considering the two scenes displaced by (Δ_x, Δ_y) such that $u_2(x, y) = u_1(x - \Delta_x, y - \Delta_y)$, then eq. (3.20) becomes

$$C_{i_1 i_2}(\omega_x, \omega_y) = e^{j(\omega_x \Delta_x + \omega_y \Delta_y)} \frac{H_1(\omega_x, \omega_y)H_2^*(\omega_x, \omega_y)}{|H_1(\omega_x, \omega_y)H_2^*(\omega_x, \omega_y)|}. \quad (3.25)$$

If both images are acquired by the same instrument, then $H_1 = H_2$, $C_{i_1 i_2}(\omega_x, \omega_y) = e^{j(\omega_x \Delta_x + \omega_y \Delta_y)}$, and the measurement of (Δ_x, Δ_y) is not biased. If the two optical devices are different (e.g., SPOT and aerial camera, or SPOT-4 and SPOT-5), $H_1 \neq H_2$ and the measurement is potentially biased. From eq. (3.23), it follows that for an aberration-free and diffraction-limited optical system, the OTF is always real and nonnegative. In such

cases, $C_{i_1 i_2}(\omega_x, \omega_y)$ is therefore not biased. However, aberrations can cause the OTF to have negative values in certain bands of frequencies [39]. For SPOT satellites, only $\frac{3}{5}$ of the spectral bandwidth is aberration-free [38]. Hence this motivates the masking of high frequencies to achieve a bias-free correlation. It thus turns out that the sub-optimality of the resampling efficiency does not appear to be a serious drawback, since oversampling contributes in masking possible aberrations.

3.4.3.2 Phase Correlation and Noise

From the Wiener-Khintchine Theorem [40], the inter-spectral density, $S_{xy}(\omega)$, of two jointly wide sense stationary (WSS) random processes, $x(t)$ and $y(t)$, is defined as the Fourier transform of their cross-correlation function:

$$S_{xy}(\omega) \triangleq \mathcal{F}\{R_{xy}(\tau)\}, \quad (3.26)$$

with $R_{xy}(\tau) = E\{x(t)y^*(t-\tau)\}$, and $E\{\cdot\}$ denotes the expectation over all possible outcomes of x and y . It can be shown that the relation (3.25) also holds if we consider the images as random stationary processes [38], [41]:

$$\frac{S_{i_1 i_2}(\omega_x, \omega_y)}{|S_{i_1 i_2}(\omega_x, \omega_y)|} = C_{i_1 i_2}(\omega_x, \omega_y). \quad (3.27)$$

Consider two theoretical images, u_1 and u_2 with no noise, such that $u_2(x, y) = u_1(x - \Delta_x, y - \Delta_y)$. Assume that the noises from the scenes (temporal decorrelation, atmospheric noise, topographic effects, shadows, etc...) and from the sensor (quantization, thermal fluctuations, etc...) are all white and additive. The complete acquisition system is sketched in Fig. 3.10, where $n_i(x, y)$ and $n_{ii}(x, y)$ are white noises, thus WSS by definition. The inter-spectral density of the acquired images i_1 and i_2 , is then given by [38], [41]:

$$S_{i_1 i_2}(\omega_x, \omega_y) = H_1(\omega_x, \omega_y) e^{j(\omega_x \Delta_x + \omega_y \Delta_y)} H_2^*(\omega_x, \omega_y).$$

Under the assumption of additive white noises, the displacement of the scenes is only altered by optical aberrations. In the case of aberration-free imaging systems, or when it can be

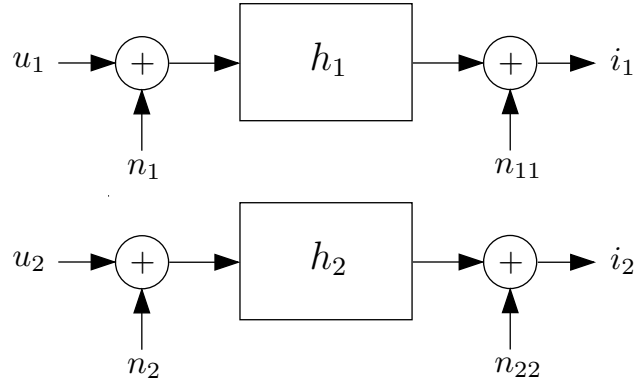


Figure 3.10: Modeling of the acquisition systems

assumed from some appropriate frequency masking, then:

$$\frac{S_{i_1 i_2}(\omega_x, \omega_y)}{|S_{i_1 i_2}(\omega_x, \omega_y)|} = e^{j(\omega_x \Delta_x + \omega_y \Delta_y)}. \quad (3.28)$$

Hence the measurement of ground displacements is not biased by either additive white noise or blurring, or a combination of the two phenomena.

3.4.3.3 Solution Periodicity and Largest Measurements

Define two discrete images of size $N \times N$ pixels such that

$$i_2[x, y] = i_1[x - \Delta_x, y - \Delta_y]. \quad (3.29)$$

The discrete normalized cross-spectrum is given by

$$C_{i_1 i_2}[k_x, k_y] = e^{j \frac{2\pi}{N} (k_x \Delta_x + k_y \Delta_y)}, \quad (3.30)$$

for $k_x, k_y = 0, \dots, N - 1$. Now examine the case where images are shifted by $(\Delta_x, \Delta_y) + (n_x, n_y)N$ samples so that

$$i'_2[x, y] = i'_1[x - \Delta_x + n_x N, y - \Delta_y + n_y N],$$

for $(n_x, n_y) \in \mathbf{Z}^2$. The cross-spectrum becomes

$$\begin{aligned} C_{i_1' i_2'}[k_x, k_y] &= e^{j\frac{2\pi}{N}(k_x(\Delta_x + n_x N) + k_y(\Delta_y + n_y N))} \\ &= e^{j2\pi k_x n_x} e^{j2\pi k_y n_y} e^{j\frac{2\pi}{N}(k_x \Delta_x + k_y \Delta_y)} \\ &= C_{i_1 i_2}[k_x, k_y]. \end{aligned}$$

Therefore, if (Δ_x, Δ_y) is a solution of the $i_1, i_2, N \times N$ pixels image translative registration problem, then $(\Delta_x + n_x N, \Delta_y + n_y N)$ is also a solution, for any $(n_x, n_y) \in \mathbf{Z}^2$. We have a periodic set of solutions.

We will call physical solutions the solutions for which the two images to be correlated share a common area when overlapped. The physical solution must be unique, and attained for $n_x = 0$ and $n_y = 0$. From any solution in the solution set, the physical solution can be uniquely determined if and only if $|\Delta_x| < \frac{N}{2}$ and $|\Delta_y| < \frac{N}{2}$. Otherwise, there is ambiguity: two different physical solutions in each x and y directions may exist, and wrapping of the solution set occurs. Therefore, to avoid measurement ambiguity, displacements to be measured should be constrained to the range $-\frac{N}{2}$ to $\frac{N}{2}$ pixels, if the correlation window is of size $N \times N$ pixels.

3.4.4 Discrete Fourier Transform of Finite Length Signals

From the point of view of the discrete Fourier transform, infinite periodic images whose period corresponds to the finite extent of the selected image patches are being analyzed [32]. Periodicity creates sharp discontinuities, introducing “cross pattern” artifacts in the Fourier transform (Fig. 3.8 and Fig. 3.9). In [1], it has then been chosen to mask the low frequencies. However, we previously showed that the low frequencies are the less likely to be corrupted by optical aberrations or aliasing. These artifacts are importantly attenuated by weighting the image patches with a Blackman window so that image discontinuities are smoothed out [37], but it removes a significant amount of the signal energy [36]. The raised-cosine window achieves a good compromise between reducing both the frequency artifacts and the image loss of information. In one dimension, the raised-cosine window of length N , N even,

is given by:

$$w_{rc}(x) = \begin{cases} \cos^2\left(\frac{\pi}{2\beta N}\left(|x| - N\left(\frac{1}{2} - \beta\right)\right)\right), & \text{for } N\left(\frac{1}{2} - \beta\right) \leq |x| \leq \frac{N}{2}, \\ 1, & \text{for } |x| < N\left(\frac{1}{2} - \beta\right), \\ 0, & \text{otherwise,} \end{cases}$$

where β , called the roll-off factor, ranges from 0 to $\frac{1}{2}$. The two-dimensional window is constructed assuming a separable window. For $\beta = 0$, it is equivalent to the rectangle window. For $\beta = \frac{1}{2}$, it is equivalent to the Hanning window.

3.4.5 Finding the Images Phase Difference

3.4.5.1 Previous Work

Several approaches have been thought of to find the best approximation to the phase difference between two images, one being a shifted version of the other. According to eq. (3.20), the phase of the normalized cross-spectrum is a linear function of the displacement vector, namely:

$$\varphi(\omega_x, \omega_y) = \omega_x \Delta_x + \omega_y \Delta_y, \quad (3.31)$$

where ω_x and ω_y are radian frequencies, ranging from $-\pi$ to π . The phase slope might be estimated by least-square adjustment with possibly some weighting to filter out the effect of noise and aliasing at high frequencies [37]. However this is a valid approach only when the phase is not wrapped, i.e. under the condition $|\varphi(\omega_x, \omega_y)| \leq \pi$. This condition is always satisfied when $|\Delta_x| \leq 0.5$ and $|\Delta_y| \leq 0.5$. Hence only displacements less than half the pixel size are measurable. This technique needs to be complemented with another one to solve for multi-pixel displacements. These might be estimated from the coordinates of the correlation peak, eq. (3.21). However, accurate sub-pixel measurement could not be obtained from this technique, thus providing only nearest integer pixel estimation. The domains of validity of these two successive approaches are then non-overlapping. As a result, a two-step method consisting of first estimating the displacement at the multi-pixel scale and then at the sub-pixel scale from plane fitting is not stable when the displacements to be measured are close to half the pixel size.

In [36], a more robust approach has been proposed to evaluate the images phase differ-

ence. The normalized cross-spectrum matrix $C(\omega_x, \omega_y)$ is theoretically a rank one matrix since C is separable, i.e., $C(\omega_x, \omega_y) = e^{j(\omega_x \Delta_x + \omega_y \Delta_y)} = e^{j\omega_x \Delta_x} e^{j\omega_y \Delta_y} = c_1(\omega_x) c_2(\omega_y)$. From the Eckart-Young-Mirsky theorem [42], the best low-rank approximation \hat{X} to a $N \times M$ matrix X with $\text{rank}\{X\} = r$ with respect to both the Frobenius and the L_2 norms, is obtained from the Singular Value Decomposition (SVD). If $X = U\Sigma V^T = \sum_{i=1}^r \mathbf{u}_i \sigma_i \mathbf{v}_i^T$ with singular values $\sigma_1 \geq \sigma_2 \geq \dots \geq \sigma_r \geq 0$, then the best low-rank k approximation \hat{X} is given by

$$\hat{X} = \sum_{i=1}^k \sigma_i \mathbf{u}_i \mathbf{v}_i^T, \quad (3.32)$$

where $k \leq r$. The Frobenius norm of a matrix X is defined as

$$\|X\|_F = \sqrt{\sum_{i=1}^N \sum_{j=1}^M |x_{ij}|^2}. \quad (3.33)$$

The idea in [36] is therefore to determine the best rank one approximation to the normalized cross-spectrum matrix. The displacement vector is recovered by calculating the slope of the unwrapped phase of the two singular vectors \mathbf{u}_1 and \mathbf{v}_1^T . This method has proven a strong robustness against noise. However there are two main drawbacks remaining: first, it is also subjected to phase wrapping. Even though this approach involves only one dimensional unwrapping, it still remains a sensitive step. The second drawback, which is the main concern, is that the whole normalized cross-spectrum matrix (or a rectangular subset of it) has to be used to compute the best rank one approximation. This computation is potentially biased with corrupted phase values. A solution would be to use a weighted SVD, but most of these algorithms require the weight matrix to be positive definite symmetric [43]. Frequency weights with no a priori constraint on the spectrum orientation or separability should be applied.

In [1] another approach is proposed based on the Hermitian inner product of two functions f and g defined as:

$$\langle f, g \rangle = \int_{-\infty}^{\infty} f(x) g^*(x) dx. \quad (3.34)$$

Define the theoretical normalized cross-spectrum of the images by $C(\omega_x, \omega_y) = e^{j(\omega_x \Delta_x + \omega_y \Delta_y)}$, and the one actually computed by $Q(\omega_x, \omega_y)$. The projection of Q onto the continuous space

defined by the theoretical cross-spectrums is defined as:

$$\begin{aligned} P_{Q,C}(\Delta_x, \Delta_y) &= \sum_{\omega_x} \sum_{\omega_y} Q(\omega_x \omega_y) C^*(\omega_x, \omega_y) \\ &= \sum_{\omega_x} \sum_{\omega_y} Q(\omega_x \omega_y) e^{-j(\omega_x \Delta_x + \omega_y \Delta_y)}. \end{aligned} \quad (3.35)$$

The values of Δ_x and Δ_y that maximize the norm of this projection are the ones that are the most likely to solve the registration problem. It is then proposed to find (Δ_x, Δ_y) that maximizes the modulus $|\text{MP}_{Q,C}(\Delta_x, \Delta_y)|$, where

$$\text{MP}_{Q,C}(\Delta_x, \Delta_y) = \sum_{\omega_x} \sum_{\omega_y} M(\omega_x, \omega_y) Q(\omega_x, \omega_y) e^{-j(\omega_x \Delta_x + \omega_y \Delta_y)},$$

and $M(\omega_x, \omega_y)$ is a binary mask to filter out some frequencies. This technique is effective and insensitive to phase wrapping. Therefore it is suitable for both large and small displacement measurements. However, the resolution method proposed, based on a dichotomy, is computationally inefficient. Also, as previously mentioned, the frequency masking is not properly set.

3.4.5.2 Proposed Method

We propose to minimize, with respect to the Frobenius norm, the weighted residual matrix between the computed normalized cross-spectrum and the theoretical one. This approach allows us to explicitly solve the phase wrapping ambiguity, yielding accurate and robust displacement measurements at both sub-pixel and multi-pixel scales. This scheme also allows for flexibility on the frequency weighting.

$Q(\omega_x, \omega_y)$ denotes the normalized cross-spectrum computed from the images, and $C(\omega_x, \omega_y)$ the theoretical one. Define the function

$$\phi(\Delta_x, \Delta_y) = \sum_{\omega_x=-\pi}^{\pi} \sum_{\omega_y=-\pi}^{\pi} W(\omega_x, \omega_y) |Q(\omega_x, \omega_y) - e^{j(\omega_x \Delta_x + \omega_y \Delta_y)}|^2,$$

where W is some weighting matrix with positive entries. We are looking for (Δ_x, Δ_y) that minimize ϕ . Let

$$\varphi_{\Delta}(\omega_x, \omega_y) = W(\omega_x, \omega_y) |Q(\omega_x, \omega_y) - C(\omega_x, \omega_y)|^2. \quad (3.36)$$

We can write

$$\begin{aligned}\varphi_{\Delta}(\omega_x, \omega_y) &= W(\omega_x, \omega_y) [Q(\omega_x, \omega_y) - C(\omega_x, \omega_y)] \cdot [Q(\omega_x, \omega_y) - C(\omega_x, \omega_y)]^* \\ &= 2W(\omega_x, \omega_y) [1 - Q_R(\omega_x, \omega_y) \cos(\omega_x \Delta_x + \omega_y \Delta_y) - \\ &\quad Q_I(\omega_x, \omega_y) \sin(\omega_x \Delta_x + \omega_y \Delta_y)],\end{aligned}$$

by setting $Q(\omega_x, \omega_y) = Q_R(\omega_x, \omega_y) + jQ_I(\omega_x, \omega_y)$ and by noticing that $Q_R^2(\omega_x, \omega_y) + Q_I^2(\omega_x, \omega_y) = 1$, by definition of Q .

So far it can be noted that minimizing ϕ is equivalent to maximizing $\Re\{\text{MP}_{Q,C}(\Delta_x, \Delta_y)\}$ if $M = W$, $\Re\{\cdot\}$ is the real part operator. We have the relation:

$$\phi(\Delta_x, \Delta_y) = 2 \sum_{\omega_x} \sum_{\omega_y} W(\omega_x, \omega_y) - 2\Re\{\text{MP}_{Q,C}(\Delta_x, \Delta_y)\}.$$

Considering ideal noiseless measurements and for a null expected translation between image patches we approximate ϕ by $\tilde{\phi}$ such that:

$$\tilde{\phi}(\Delta_x, \Delta_y) \propto \left(ab - \frac{\sin(a\Delta_x)}{\Delta_x} \frac{\sin(b\Delta_y)}{\Delta_y} \right), \quad (3.37)$$

for (Δ_x, Δ_y) in the physical solution set. Here, the frequency masking is modeled as an ideal rectangular low-pass filter with cut-off frequencies $\Omega_x = a$ and $\Omega_y = b$. Without masking, $a = b = \pi$. With appropriate initialization, a gradient descent algorithm to find (Δ_x, Δ_y) that minimizes ϕ can be considered. The TPSS algorithm [30], already introduced in Section 3.2.2.3, is used. It is robust and converges rapidly, in typically less than 10 iterations. Details of the algorithm are provided in Appendix C. The initialization of the algorithm is described in Section 3.4.5.5.

The proposed minimization algorithm is unconstrained and may provide a non-physical solution. Assuming that no displacement exceeds half the correlation window size, the physical displacement is given by:

$$\Delta_{\varphi} = \Delta - \left\lceil \frac{\Delta}{N} \right\rceil N, \quad (3.38)$$

where Δ is the optimum displacement returned by the algorithm, N is the one-dimensional correlation window size, and $\lceil \cdot \rceil$ is the rounding to the nearest integer operator.

3.4.5.3 Adaptive Frequency Masking

A bias-free correlation can be achieved through frequency masking (Sections 3.4.3.1 and 3.4.3.2). Although any weighting matrix W with positive entries would be possible, we set the values $W(\omega_x, \omega_y)$ to be either 0 (for corrupted frequencies) or 1 (for noncorrupted frequencies). As previously mentioned, high frequencies are the most likely to be corrupted due to optical aberrations and aliasing. The power spectrum of natural scenes is exponentially decreasing with frequency [44] [45] [46]. In the Fourier domain, the modulus of a white noise remains constant, and assuming that the images are degraded with some additive white noise, the phase information is then most likely to be biased in the high frequencies. We also want to filter out frequencies that correspond to the zeros of the resampling transfer function used for orthorectification (Section 3.3.3.2). Thus, all frequencies where the phase information is the most likely to be corrupted share the same property: the magnitude of the cross-spectrum is much lower at these frequencies than at those where the phase is less likely to be corrupted. The mask is therefore defined by retaining only the frequencies where the magnitude of the cross-spectrum exceeds some threshold.

One of the initial requirements listed was that correlation parameters, hence the mask pattern, must not depend on the image correlation size. A possible solution is to define:

$$\begin{cases} \text{LS}_{i_1 i_2}(\omega_x, \omega_y) = \log_{10} |I_1(\omega_x, \omega_y) I_2^*(\omega_x, \omega_y)|, \\ \text{NLS}_{i_1 i_2}(\omega_x, \omega_y) = \text{LS}_{i_1 i_2}(\omega_x, \omega_y) - \max\{\text{LS}_{i_1 i_2}(\omega_x, \omega_y)\}, \end{cases}$$

where I_1 and I_2 are the Fourier transform of the images to be correlated. LS stands for “Log-Spectrum” and NLS for “Normalized Log-Spectrum”. The frequency mask is then defined according to the parameter m such that:

$$W_{i_1 i_2}(\omega_x, \omega_y) = \begin{cases} 0, & \text{if } \text{NLS}_{i_1 i_2}(\omega_x, \omega_y) \leq m \cdot \mu\{\text{NLS}_{i_1 i_2}(\omega_x, \omega_y)\} \\ 1, & \text{otherwise.} \end{cases}$$

A value of m close to unity gives satisfactory results for most of the images.

The log-spectrum and corresponding mask of a level 1A SPOT 5, THR 2.5 m resolution image is presented in Fig. 3.11. The 2.5 m resolution image is characterized by its quincunx sampling scheme [47], leading to a diamond shape spectrum. The mask figure shows that

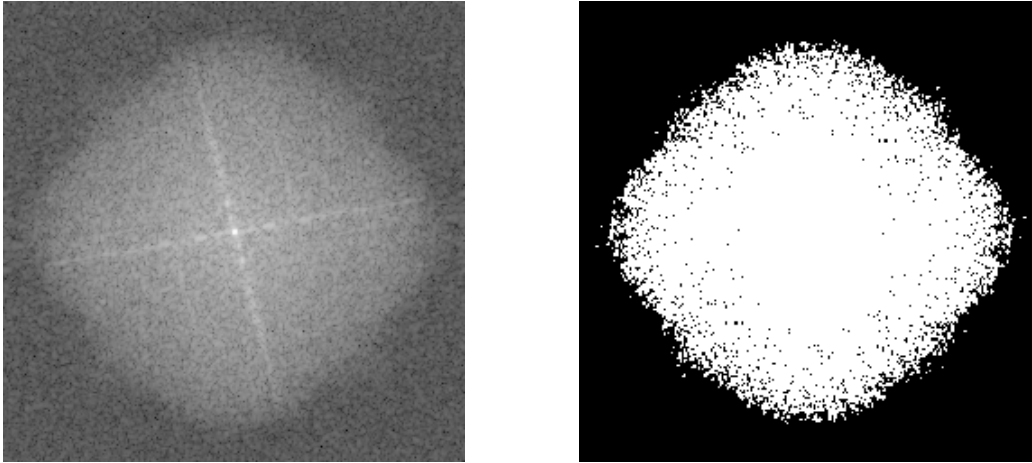


Figure 3.11: Log-spectrum (left) of 256×256 pixels 1A-SPOT 5, THR 2.5 m resolution image, weighted by a raised-cosine window with $\beta = 0.5$. The tilted cross results from the original image features. Corresponding mask (right) for $m = 1.0$. White represents unity weights and black null weights.

only the frequencies that are the most likely to be corrupted are filtered out. In Fig. 3.12, the log-spectrum and the corresponding masks of an orthorectified SPOT 5 HRG, 5 m resolution image are presented. Frequencies within the bandwidth of the resampling kernel are accurately selected and the mask pattern remains unchanged as the window size changes. These characteristics warrant unbiased correlation and ensure flexibility of the algorithm.

3.4.5.4 Adding Robustness, Resampling in Frequency and Fine Tuning of Frequency Mask

The robustness and accuracy of the algorithm are improved by iterating it. Denote by (Δ_x^0, Δ_y^0) the displacement measured after the first convergence of the algorithm and by $Q^0(\omega_x, \omega_y)$ the normalized cross-spectrum measured from the images to correlate. Once (Δ_x^0, Δ_y^0) have been obtained, it is possible to compute (Δ_x^1, Δ_y^1) from $Q^1(\omega_x, \omega_y)$ defined as:

$$Q^1(\omega_x, \omega_y) = Q^0(\omega_x, \omega_y) e^{-j(\omega_x \Delta_x^0 + \omega_y \Delta_y^0)}. \quad (3.39)$$

If the sequence $\{(\Delta_x^i, \Delta_y^i)\}$ converges toward zero, then the uncertainty on the measurement decreases. It is seen as a successive resampling of the images, done in the frequency domain, by compensating the shift measured.

The frequency mask is similarly adjusted. One may assign less weight to frequencies

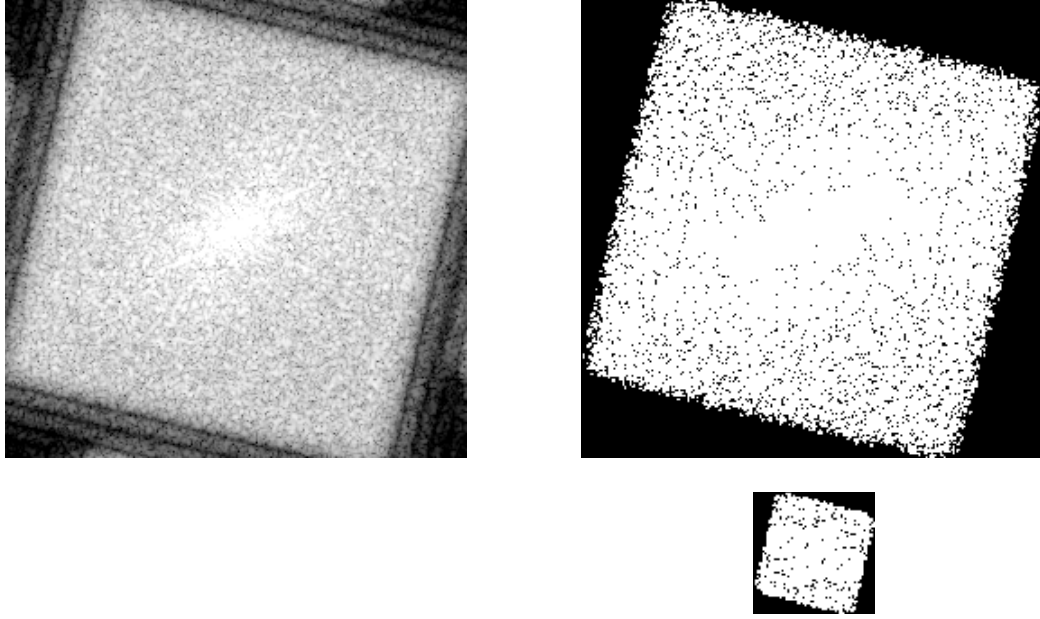


Figure 3.12: Log-spectrum (upper left) of 256×256 pixels orthorectified SPOT 5, HRG 5 m resolution image, weighted by a raised-cosine window with $\beta = 0.5$ and corresponding masks for 256×256 pixels window, $m = 1.0$ (upper right). Computed mask on 64×64 pixels window and $m = 1.0$ (lower right).

that have an original weight equal to unity but whose fit to the theoretical cross-spectrum is poor. Since Q and C are normalized, $|Q(\omega_x, \omega_y) - C(\omega_x, \omega_y)| \leq 2$. Hence, if $0 \leq W(\omega_x, \omega_y) \leq 1$, $\varphi_\Delta(\omega_x, \omega_y) \in [0, 4]$. Denote by $C^0(\omega_x, \omega_y) = e^{j(\omega_x \Delta_x^0 + \omega_y \Delta_y^0)}$ the best match for the normalized cross-spectrum that has been first deduced from minimization. The residual per frequency after the first minimization is

$$\varphi_\Delta^0(\omega_x, \omega_y) = W^0(\omega_x, \omega_y) |Q^0(\omega_x, \omega_y) - C^0(\omega_x, \omega_y)|^2,$$

where W^0 is the original weighting matrix. A new weighting matrix is then defined as

$$W^1(\omega_x, \omega_y) = W^0(\omega_x, \omega_y) \left(1 - \frac{\varphi_\Delta^0(\omega_x, \omega_y)}{4} \right)^n. \quad (3.40)$$

We have chosen $n = 6$. This scheme forces the algorithm to converge toward a solution which is close to the first solution obtained, but it adds more robustness against noise in practice.

Based on these principles we define the robustness iterations as follows:

$$\begin{cases} Q^{i+1}(\omega_x, \omega_y) = Q^i(\omega_x, \omega_y)e^{-j(\omega_x\Delta_x^i + \omega_y\Delta_y^i)} \\ \varphi_{\Delta}^i(\omega_x, \omega_y) = W^i(\omega_x, \omega_y)|Q^i(\omega_x, \omega_y) - C^i(\omega_x, \omega_y)|^2 \\ W^{i+1}(\omega_x, \omega_y) = W^i(\omega_x, \omega_y) \left(1 - \frac{\varphi_{\Delta}^i(\omega_x, \omega_y)}{4}\right)^n. \end{cases}$$

The global shift between the two images is then given by:

$$\begin{cases} \Delta_x = \sum_i \Delta_x^i \\ \Delta_y = \sum_i \Delta_y^i. \end{cases} \quad (3.41)$$

The robustness iterations can stop when the sequence of $\{(\Delta_x^i, \Delta_y^i)\}$ becomes lower than some prescribed threshold. In practice we prefer imposing a fixed number of iterations (up to 4). It achieves good noise and bias reduction in the measurements while maintaining a reasonable computational cost.

From the quantities calculated above, the signal-to-noise ratio (SNR) of the measurement is given by:

$$\text{SNR}^i = 1 - \frac{\sum_{\omega_x} \sum_{\omega_y} \varphi_{\Delta}^i(\omega_x, \omega_y)}{4 \sum_{\omega_x} \sum_{\omega_y} W^i(\omega_x, \omega_y)}. \quad (3.42)$$

It quantifies the quality of the correlation and ranges from 0 (no correlation) to 1 (perfect correlation).

3.4.5.5 Initializing the Minimization Algorithm

The minimization algorithm needs to be initialized with some displacement $(\Delta_{x_0}, \Delta_{y_0})$. According to eq. (3.37), a gradient descent algorithm should be initialized with $(\Delta_{x_0}, \Delta_{y_0}) = (\Delta_x^* \pm 1, \Delta_y^* \pm 1)$ to converge toward the solution (Δ_x^*, Δ_y^*) . $\phi(\Delta_x, \Delta_y)$ could then be scanned with steps $\Delta_x < 1$ pixel and $\Delta_y < 1$ pixel in the physical solution set, the scanning point minimizing ϕ being used as initialization. However, this solution is computationally expensive, in particular for large image patches. We therefore rather use the peak correlation method defined by eq. (3.21) to approximate the solution. Providing that the displacement to be measured is less than half the correlation window size, this directly provides the physical solution.

Designate by (x_0, y_0) the integer coordinates of the correlation peak. According to eq. (3.21), in case of a pure integer shift we should have $(\Delta_{x_0}, \Delta_{y_0}) = (-x_0, -y_0)$. Denote by $p_{x_i y_j}$ the amplitude of the correlation at coordinates (x_i, y_i) . We obtain a better estimate by setting:

$$\begin{cases} \Delta_{x_0} = -\frac{\sum_{i=-1}^1 \sum_{j=-1}^1 x_i p_{x_i y_j}}{\sum_{i=-1}^1 \sum_{j=-1}^1 p_{x_i y_j}} \\ \Delta_{y_0} = -\frac{\sum_{i=-1}^1 \sum_{j=-1}^1 y_i p_{x_i y_j}}{\sum_{i=-1}^1 \sum_{j=-1}^1 p_{x_i y_j}}. \end{cases} \quad (3.43)$$

This approximation is computationally efficient and is used to initialize the minimization algorithm.

3.4.6 Image Correlation, Complete Algorithm

Denote by i_1 a reference image (the master image) and by i_2 (the slave image) an image representing the same scene shifted by a translation. It is assumed that i_1 and i_2 share the same resolution. Let p_1 and p_2 be two overlapping patches extracted from i_1 and i_2 . Let p_1 and p_2 be of size $2^M \times 2^M$ pixels with M such that 2^M is larger than twice the largest translation to be estimated.

The SNR, thus the correlation accuracy, is higher when the overlapping area of patches to correlate is maximum. Patches to correlate are then iteratively relocated to compensate for their relative displacement. These iterations (usually at most two) are done from the peak correlation method to lower the computational cost. This method has been found as robust against noise as the minimizing algorithm for pixel scale measurements. The minimization algorithm is performed last on relocated patches.

- **Step 1:** Define two raised-cosine windows of size $2^M \times 2^M$. w_{rc_1} with $\beta_1 = 0.35$ and w_{rc_2} with $\beta_2 = 0.5$.
- **Step 2:** Let $p_2^0 = p_2$. Correlate $p_1(x, y)w_{rc_1}(x, y)$ with $p_2^0(x, y)w_{rc_1}(x, y)$ using the peak correlation method (and applying the sub-pixel approximation as defined by eq. (3.43)). The estimated translation is given by $(\tilde{\Delta}_x^0, \tilde{\Delta}_y^0)$. Let $(t_x^0, t_y^0) = ([\tilde{\Delta}_x^0], [\tilde{\Delta}_y^0])$ where $[.]$ is the rounding to the nearest integer operator. Define $p_2^1(x, y) = p_2^0(x + t_x^0, y + t_y^0)$. Iterate **step 2** until $t_x^i \leq 1$ and $t_y^i \leq 1$. If convergence is not reached, then **stop** and set SNR= 0. Else, let $n + 1$ be the number of iterations needed to achieve

convergence. Then define $(\Delta_{x_0}, \Delta_{y_0}) = (\tilde{\Delta}_x^n, \tilde{\Delta}_y^n)$ and set

$$\begin{cases} T_x = \sum_{i=0}^n t_x^i \\ T_y = \sum_{i=0}^n t_y^i. \end{cases}$$

- **Step 3:** Taking $(\Delta_{x_0}, \Delta_{y_0})$ as initialization values, correlate, using the phase minimization algorithm the patches $p_1(x, y)w_{rc_2}(x, y)$ and $p_2^n(x, y)w_{rc_2}(x, y)$. Set m close to unity. If the minimization does converge, let $(\Delta_{x_\varphi}, \Delta_{y_\varphi})$ be the physical solution derived. Otherwise **stop** and set SNR= 0.

If $|\Delta_{x_\varphi}| > 1.5$ or $|\Delta_{y_\varphi}| > 1.5$ then **stop** and set SNR= 0.

- **Step 4 [optional]:** Set $T_x = T_x + \Delta_{x_\varphi}$ and $T_y = T_y + \Delta_{y_\varphi}$. Using sinc interpolation with resampling distances $d_x = d_y = 1$ pixel, interpolate p_2 such that $p_2^n(x, y) = p_2^0(x + T_x, y + T_y)$. Set $(\Delta_{x_0}, \Delta_{y_0}) = (0, 0)$. Then go back to **step 3**, only once.

- **Step 5:** Return:

$$(\Delta_x, \Delta_y, \text{SNR}) = (T_x + \Delta_{x_\varphi}, T_y + \Delta_{y_\varphi}, \text{SNR}).$$

In **step 2**, the convergence within 0.5 pixel between two image patches cannot always be achieved. The correlation peak method exhibits some bias and in noisy images, if a displacement of 0.5 pixel is to be measured, it can be systematically overestimated. Therefore, if a stopping condition such that $t_x^i = 0$ and $t_y^i = 0$ were set, displacements that could effectively be recovered in **step 3** would be lost. This situation has been encountered in practice. The consequence is that in **step 3**, offsets theoretically up to 1.5 pixels have to be measured.

Step 4, which consists in precisely relocating the patch p_2 to maximize the overlap with the patch p_1 , is optional. Precise relocation is achieved from sinc interpolation. A larger patch has to be considered to avoid edge effects in the interpolated patch. The resampling kernel is of size 25×25 pixels. Only one iteration of this optional step is applied since improvements on subsequent iterations are insignificant.

3.4.7 Correlation Tests and Results

We have produced a set of test images from raw, SPOT 5 HRG, 5 m resolution images. Translated images have been generated from sinc resampling. To simulate orthorectified images, or oversampled images such as the SPOT 5 THR 2.5 m resolution images, the test images have been oversampled by 33% by setting the resampling distances to $d_x = d_y = 1.5$ pixels. We used a resampling kernel of size 25×25 pixels.

We have consistently verified that the larger the correlation window, the lower the correlation uncertainty and bias. Therefore, only cases with small, 32×32 pixel, correlation windows are presented. Correlation windows scan the test images with a constant step of 16 pixels in each dimension. The test images, subsets of the SPOT full scene, are composed of 3000×3000 pixels. 32400 correlation measures are gathered at each test. Correlation quality is assessed by examining the distribution of these measurements when the offset introduced between the test images is varying. Since results in both x and y directions are nearly identical, only variations along the x axis are presented.

3.4.7.1 Masking Test

We consider the correlation algorithm with no **step 4**, no frequency masking and no robustness iterations. If the test images are shifted by 0.5 pixel, the distribution of the measurements, Fig. 3.14, yields $\mu\{\Delta_x\} = -0.42$ pixel and $\sigma\{\Delta_x\} = 0.017$ pixel. In this case, the correlation is neither precise (the error is 8% of the pixel size) nor very accurate. Let now examine the distribution of the correlation measures when the masking parameter m is varying, Fig. 3.13(a). The solid black line represents the mean bias $B = \Delta_{x_{th}} - \mu\{\Delta_x\}$, where $\Delta_{x_{th}}$ is the theoretical displacement to be evaluated, and the shaded area represents the 2-sigma ($\pm\sigma\{\Delta_x\}$) deviation of the measurements. Measurements are biased toward the nearest integer pixel. When $m \geq 1.4$ the masking effect no longer exist. When $m \leq 0.7$ the mask is discarding too much information and the correlation loses precision and accuracy. An optimum value is attained for $m = 0.75 - 0.9$. Setting $m = 0.9$, Fig. 3.14, it is now measured $\mu\{\Delta_x\} = -0.47$ pixel and $\sigma\{\Delta_x\} = 0.010$ pixel.

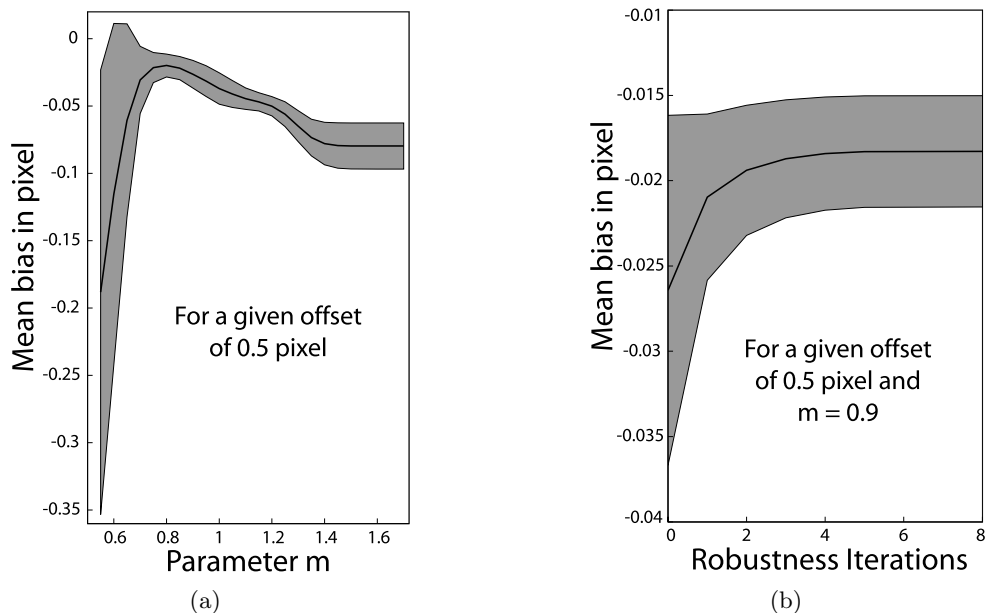


Figure 3.13: (a) Evolution of the mean bias (black line) and standard deviation (shaded area) of the correlation measurements when the masking parameter m is varying. No robustness iterations are applied. Measurements are given for a half-pixel offset. (b) Evolution of the mean bias and standard deviation of the correlation measurements when adding robustness. Measurements are given for a half-pixel offset and $m = 0.9$.

3.4.7.2 Robustness Iterations

With the robustness iterations, the frequency mask is adapted at each iteration. The algorithm is then initialized with a suboptimal value of the masking parameter, typically $m = 0.9$. Fig. 3.13(b) represents the evolution of the mean bias and error deviation of the correlation measurements when the robustness iterations are increasing. The maximum improvement is reached after 4 iterations. More iterations do not degrade the results. If the algorithm is initialized with $m \leq 0.75$, the robustness iterations have no significant effect on the correlation. The histogram of the measurements for $m = 0.9$ with 4 robustness iterations is presented in Fig. 3.14. Precision and accuracy of the correlation are greatly improved. We measure $\mu\{\Delta_x\} = -0.48$ pixel and $\sigma\{\Delta_x\} = 0.003$ pixel.

3.4.7.3 Global Performances, Simplest Form

We consider the simplest form of the algorithm, with no **step 4**. Due to the convergence condition imposed in **step 2**, measurements fall within the range of -2 to +2 pixels. Fig. 3.15 shows the mean bias and the measurements standard deviation with respect to the offsets

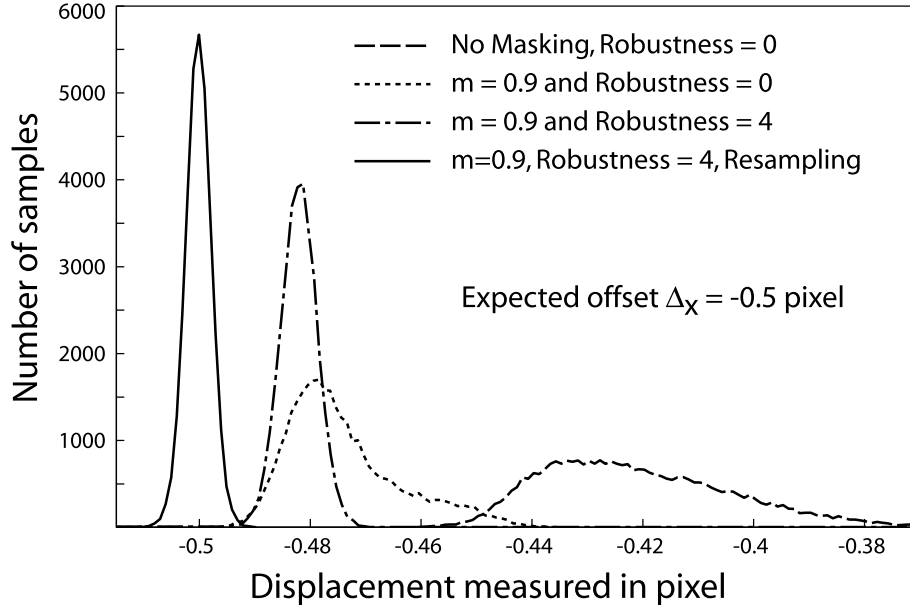


Figure 3.14: Histograms of the correlation measurements for a constant offset $\Delta_x = -0.5$ pixel. A constant bin size of $\frac{1}{1000}$ pixel is used. Bias and error are characterized for 4 configurations of the algorithm. Suggested improvements such as masking, robustness iterations, and sinc interpolation allow for precise and accurate correlation, even with small image patches.

to be estimated. For 32×32 pixel windows, the maximum error is about of $\frac{1}{20}$ of the pixel size.

3.4.7.4 Global Performances, Extended Form

We consider the extended form of the algorithm, including **step 4**. Fig. 3.16 shows the mean bias and measurements standard deviation with respect to the offsets to be estimated. This step increases the processing time by almost a factor of 10, but the correlation bias is significantly reduced by a factor of 10. The maximum uncertainty, considering 32×32 pixel windows, is only about $\frac{1}{200}$ of the pixel size.

3.5 The Processing Chain

From the technical data related to the SPOT 1,2,3,4 satellites [48], the absolute location error when no ground control points (GCP) are used, considering a flat terrain, is less than 350 m. It is at most 50 m on SPOT 5. Registration errors are then up to 700 m when co-registering SPOT 1–4 images and up to 100 m when co-registering SPOT 5 images.

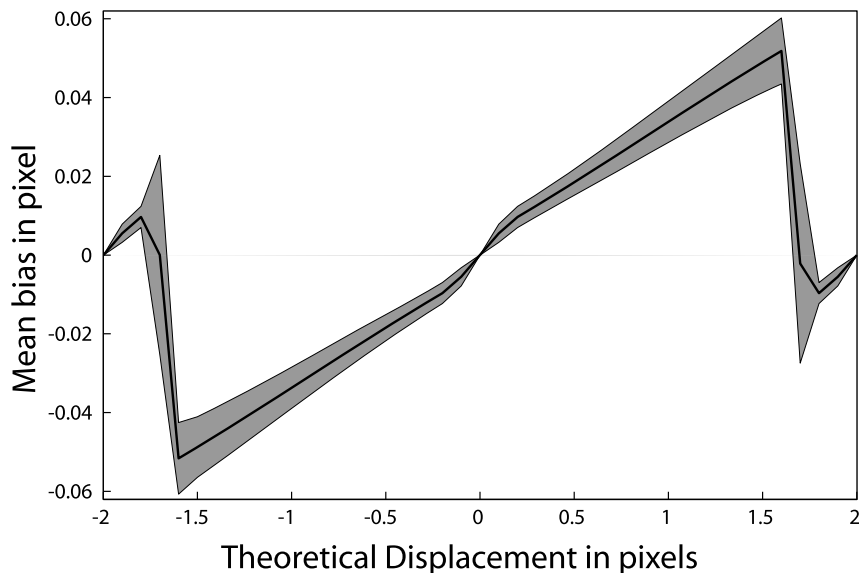


Figure 3.15: Mean correlation bias (black line) and standard deviation (shaded area) are plotted with respect to the relative displacement between the test images. The simplest form of the algorithm is characterized here, without **step 4**. $m = 0.9$ and 4 robustness iterations are applied. The correlation measurements exhibit a nearly linear bias with respect to the offsets to be estimated. The sharp discontinuities around ± 1.5 pixels are due to the patches relocation to the nearest integer pixel. They highlight the convergence condition in **step 2**.

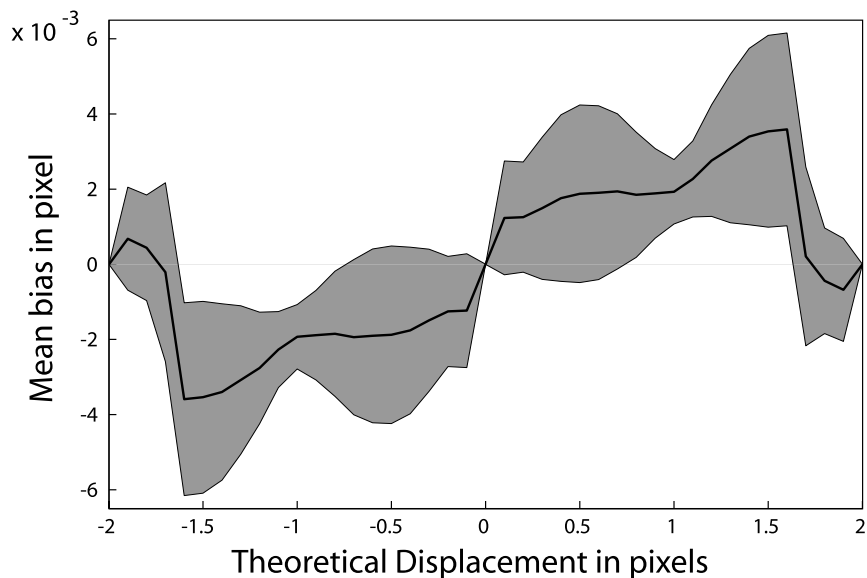


Figure 3.16: Mean correlation bias (black line) and standard deviation (shaded area) are plotted with respect to the relative displacement between the test images. The complete form of the algorithm that includes **step 4** is characterized here. $m = 0.9$ and 4 robustness iterations are applied. Considering the optional step in the algorithm allows for a reduction of the mean bias by a factor of 10. The maximum measurement uncertainty is about $\frac{1}{200}$ pixel for patches of size 32×32 pixels.

For our application, we need to co-register the images with an accuracy of a few tens of centimeters by optimizing the orthorectification parameters. To remain of general use, this technique should not involve additional information other than that from the satellite and the topography.

3.5.1 Corrected Orthorectification

3.5.1.1 Problem Modeling

For an ideal topographic model, image mis-registrations result from cumulative errors on the satellite viewing parameters, i.e., errors on the satellite look angles \vec{u}_1 that are modeling the optical system, the attitude variations of the platform given by the roll, pitch, and yaw angles, the spacecraft position, and velocity. On SPOT systems, information on the satellite trajectory (position and velocity) is sampled every 30 s while the image acquisition time is around 9 s. However, these data are recorded with a very high accuracy thanks to the on-board DORIS (Doppler Orbitography and Radio-positioning Integrated by Satellite) receiver system [49]. RMS error on the satellite position is less than 70 cm in each of the three satellite reference axes [24], and compared with the 830 km satellite altitude, it appears negligible. This high position accuracy combined with a very smooth trajectory of the satellite allow for a precise estimation of the satellite trajectory during the time of the image acquisition. Major uncertainties on the viewing parameters are therefore not likely to come from erroneous positions and velocities.

All the remaining parameters that are composing the viewing geometry, i.e., optical model and attitude variations, are combined in the global look directions \vec{u}_3 , eq. (3.5). The various sources of errors on each individual parameter might then be considered to contribute only to a global error on the resulting look directions. From this perspective, the strict constraint on the trajectory accuracy is loosened since an error in position can be modeled from different imaging parameters [50]. For example, changes on the altitude can be compensated for by changes on the instrument focal length, which is a constituting parameter of the instrument modeling vectors \vec{u}_3 .

3.5.1.2 Look Directions Correction

Assume that the exact ground coordinates where a particular pixel has to be projected are known; say the pixel $p(x_0, y_0)$ in the raw image is associated with the ground point M_0 . The set $\{p(x_0, y_0), M_0\}$ is called a GCP. Theoretically, the associated look direction $\vec{u}_{3_{th}}(x_0, y_0)$ is determined by:

$$\overrightarrow{O_3M_0} = \overrightarrow{O_3P}(y_0) + t \cdot \vec{u}_{3_{th}}(x_0, y_0), \quad \text{for some } t > 0.$$

Hence this gives

$$\vec{u}_{3_{th}}(x_0, y_0) = \frac{\overrightarrow{O_3M_0} - \overrightarrow{O_3P}(y_0)}{\|\overrightarrow{O_3M_0} - \overrightarrow{O_3P}(y_0)\|_2}, \quad (3.44)$$

where $\overrightarrow{O_3P}(y_0)$ is the given satellite position at the time when the line y_0 was being acquired. Call $\vec{u}_3(x_0, y_0)$ the look direction at the pixel $p(x_0, y_0)$, derived from the satellite ancillary data. The discrepancy with the theoretical look direction is

$$\begin{aligned} \vec{d}u_3(x_0, y_0) &= \vec{u}_{3_{th}}(x_0, y_0) - \vec{u}_3(x_0, y_0), \\ &= \frac{\overrightarrow{O_3M_0} - \overrightarrow{O_3P}(y_0)}{\|\overrightarrow{O_3M_0} - \overrightarrow{O_3P}(y_0)\|_2} - \vec{u}_3(x_0, y_0). \end{aligned} \quad (3.45)$$

If three GCPs are given, the three discrepancies $\vec{d}u_3(x_n, y_n)$ computed for $n = 0, 1, 2$ can be linearly extrapolated in each of the three dimensions to correct all the look directions $\vec{u}_3(x, y)$ in the image. This correction compensates for any linear drift along the satellite trajectory, including linear drifts of the roll, pitch, and yaw angles. It yields a non-linear correction in terms of ground coordinates, in particular due to the topography.

If more than three GCPs are available, higher-order corrections can be applied. Here, we determine the best linear correction in the least-square sense. Given N pixels $p(x_n, y_n)$ associated to N ground coordinates M_n , N discrepancies $\vec{d}u_3(x_n, y_n)$ for $n = 0, \dots, N-1$ are computed:

$$\vec{d}u_3(x_n, y_n) = \vec{d}u_3(n) = \begin{pmatrix} du_3^0(n) \\ du_3^1(n) \\ du_3^2(n) \end{pmatrix}, \quad \text{for } n = 1, \dots, N.$$

We assign a confidence level to each GCP through some weights w_n . Three corrective planes, each best approximating in the Weighted Least-Square (WLS) sense the set of discrepancies $\vec{du}_3(n)$ in all three dimensions must be computed. We are then to find the coefficients (a^i, b^i, c^i) for $i = 0, 1, 2$ such that

$$\epsilon^i = \sum_{(x_n, y_n)} [w_n(a^i x_n + b^i y_n + c^i - du_3^i(n))]^2, \text{ for } i = 0, 1, 2,$$

is minimum. The solution is obtained by equating the partial derivatives of ϵ^i to zero.

Define the constants:

$$\begin{aligned} \alpha_1 &= \sum_{n=1}^N w_n^2 x_n^2 & \beta_2 &= \sum_{n=1}^N w_n^2 y_n^2 \\ \alpha_2 &= \sum_{n=1}^N w_n^2 x_n y_n & \beta_3 &= \sum_{n=1}^N w_n^2 y_n \\ \alpha_3 &= \sum_{n=1}^N w_n^2 x_n & \gamma_3 &= \sum_{n=1}^N w_n^2. \end{aligned} \quad (3.46)$$

Then, for each dimension i of \vec{u}_3 , compute:

$$\begin{aligned} \delta_1^i &= \sum_{n=1}^N w_n^2 x_n du_n^i, \\ \delta_2^i &= \sum_{n=1}^N w_n^2 y_n du_n^i, \\ \delta_3^i &= \sum_{n=1}^N w_n^2 du_n^i. \end{aligned} \quad (3.47)$$

Hence the sets of coefficients are determined by:

$$\begin{bmatrix} a^i \\ b^i \\ c^i \end{bmatrix} = \begin{bmatrix} \alpha_1 & \alpha_2 & \alpha_3 \\ \alpha_2 & \beta_2 & \beta_3 \\ \alpha_3 & \beta_3 & \gamma_3 \end{bmatrix} \cdot \begin{bmatrix} \delta_1^i \\ \delta_2^i \\ \delta_3^i \end{bmatrix}, \text{ for } i = 0, 1, 2.$$

A global correction matrix \mathbf{C} is thus defined as:

$$\mathbf{C} = \begin{bmatrix} a^0 & b^0 & c^0 \\ a^1 & b^1 & c^1 \\ a^2 & b^2 & c^2 \end{bmatrix}. \quad (3.48)$$

At any pixel (x, y) in the raw image, the approximated look direction discrepancy is therefore given by:

$$\vec{du}_{3_{app}}(x, y) = \mathbf{C} \begin{bmatrix} x \\ y \\ 1 \end{bmatrix}. \quad (3.49)$$

Assuming N GCPs to be known prior to orthorectification, calculating \mathbf{C} is a pre-processing step. During the orthorectification, once the look direction $\vec{u}_3(x, y)$ has been determined from the ancillary data, eq. (3.5), it is corrected by the corresponding approximated look direction discrepancy such that the new corrected look direction becomes

$$\vec{u}_{3_{cor}}(x, y) = \vec{u}_3(x, y) + \vec{du}_{3_{app}}(x, y). \quad (3.50)$$

The orthorectification process is then pursued following the standard procedure. In case of a non-corrected orthorectification or if no GCPs are provided, entries of \mathbf{C} are set to zero. Then $\vec{u}_{3_{cor}}(x, y) = \vec{u}_3(x, y)$.

3.5.2 Look Directions Optimization from Precise GCPs Generation

Instead of optimizing the viewing parameters from a given set of GCPs, we describe a global scheme that iteratively refines a rough selection of GCPs such that the look directions correction implied allows for precise image georeferencing and co-registration. This general principle is described next, followed by its particular application to image georeferencing and then to image co-registration.

3.5.2.1 Acquiring Precise Ground Control Points, Principle

Given a raw image, selected patches are roughly orthorectified using only the satellite ancillary data. GCPs are then determined from the mis-registration, measured from correlation, between these image patches and a ground reference image. A global methodology is as follows:

1. Select a set of at least three pixels in the raw image. Call this set of pixels $\{p(x_i, y_i)\}$, with x_i, y_i integers, the Image Control Points (ICP). They have been designated to become the future GCPs.

2. From the satellite ancillary data and a given set of GCPs, $\{GCP^0\}$, deduce the correction matrix \mathbf{C}^0 .
3. From the satellite ancillary data and the matrix \mathbf{C}^0 , project on the ground the ICPs. The direct corrected model orthorectification is applied here (section 3.2.1). All ICPs $p(x_i, y_i)$ are associated with ground coordinates $(\lambda_i^0, \varphi_i^0, \tilde{h}_i^0)$, then forming approximated GCPs.
4. Locate in the reference image the closest integer pixels to the points of coordinates $(\lambda_i^0, \varphi_i^0)$. Call these pixels $p_{ref_i}^0$. In the reference image, select $N \times N$ pixels patches, $\mathbf{P}_{ref_i}^0$, centered on the pixels $p_{ref_i}^0$.
5. According to the ground grids defined by the patches $\mathbf{P}_{ref_i}^0$ (ground resolution and coordinates), orthorectify onto the same grids, using the inverse model orthorectification method and the correction implied by \mathbf{C}^0 , the raw image. It produces the roughly orthorectified patches $\tilde{\mathbf{P}}_i^0$.
6. Correlate the reference patches $\mathbf{P}_{ref_i}^0$ with the patches $\tilde{\mathbf{P}}_i^0$. Deduce the North/South and the East/West geographical shifts, $(\Delta\lambda_i^0, \Delta\varphi_i^0)$, between the patches. Signal to noise ratios of the correlations are designated by SNR_i^0 .
7. From the DEM, determine from bi-cubic interpolation the elevations h_i^0 of the ground points $(\lambda_i^0 + \Delta\lambda_i^0, \varphi_i^0 - \Delta\varphi_i^0)$. Define the new set of GCPs such that $\{GCP_i^1\} = \{(\lambda_i^0 + \Delta\lambda_i^0, \varphi_i^0 - \Delta\varphi_i^0, h_i^0, \text{SNR}_i^0)\}$.
8. Go back to **2** and iterate the global process by providing the set of refined GCPs, $\{GCP_i^1\}$, as a priori knowledge for the next round. The signal-to-noise ratio on the GCPs is used as a confidence weight to determine the new correction matrix \mathbf{C}^1 .

This process is repeated until both the mean and the standard deviation of the ground misregistrations $(\Delta\lambda_i, \Delta\varphi_i)$, weighted by the SNR and taken over all GCPs, become stable. When this procedure is stopped, we are left with an accurate set of GCPs: $\{GCP_i^{k+1}\} = \{(x_i, y_i, \lambda_i^k + \Delta\lambda_i^k, \varphi_i^k - \Delta\varphi_i^k, h_i^k, \text{SNR}_i^k)\}$ if $k + 1$ is the total number of iterations. This set of GCPs is then utilized to orthorectify the raw image from the inverse corrected orthorectification scheme.

The algorithm is initialized by the GCP set $\{GCP^0\}$, from which \mathbf{C}^0 is calculated. This initial correction ensures a significant overlap of the patches to correlate, even though the satellite parameters may be largely biased. This initial correction is not needed when processing SPOT 5 images. The set $\{GCP^0\}$ is then empty and $\mathbf{C}^0 = \mathbf{0}$. However when dealing with SPOT 1,2,3,4 images, the initial mis-registration between patches may be quite large (only attitude angular velocities are provided, so that attitude angles are known up to a constant). The set $\{GCP^0\}$ can then consist of 3 GCPs, manually selected.

3.5.2.2 Georeferencing with precise GCPs and Statistical Correlation

Georeferencing consists in associating pixels to absolute ground coordinates. In the context of processing satellite images the georeferencing is seen as the co-registration of the images with a ground truth, a topographic model in our case. The absolute georeferencing error is therefore from the DEM.

The accurate registration of a set of images with the topographic model aims at limiting artifacts due to parallax when comparing images. The process of precise orthorectification therefore starts with a precise GCP generation according to the topography. A shaded DEM is generated from the scene sun elevation and azimuth during acquisition, provided in ancillary data [23]. This shaded topography model is used as the first reference image for the GCPs optimization procedure.

GCPs are derived from a correlation algorithm that measures the mis-registration between orthorectified image patches and a reference image. Comparing satellite images with a shaded topography is a valid approach thanks to the large swath of imaging satellites (60 km for SPOT and ASTER satellites). Some topographic features in the raw image are then very likely to be recognized in the shaded relief image. However the nature of the two images to be correlated is quite different. The satellite image is acquired by an optical sensor and the relief image is a synthetic image. Their Fourier transform is therefore hardly comparable and at this point, rather than the correlation algorithm presented in Section 3.4.6, we use a simpler, less accurate but more robust method: the statistical correlation. The statistical correlation is defined as the absolute value of the correlation coefficient taken between a roughly orthorectified patch and the corresponding reference patch [51], [52]. This computation is carried out on patches surrounding the reference patch such that a statistical correlation matrix is built. The estimated mis-registration, expressed in pix-

els, is found from quadratic approximation, separately in each x and y dimensions, of the maximum of the correlation matrix. We chose a C_1 -continuous approximating quadratic B-spline [53] for its simplicity and because it was showing little biases at the sub-pixel scale. The signal-to-noise ratio is computed from the average of the two approximated maxima in each dimension.

Over 30 GCPs, the optimization algorithm converges toward an uncertainty on the set of the generated GCPs that is smaller than the topography resolution (typically within half the resolution at $1-\sigma$).

3.5.2.3 Co-registration with Precise GCPs and Frequency Correlation

Starting with a set of raw images, designate a particular image to be orthorectified and co-registered with the topography. This orthorectified image next becomes the new reference. Correlation between comparable satellite images is more accurate than between the satellite images and the relief image. New ICPs, chosen in the remaining raw images, are then optimized to become GCPs relative to the reference image. The frequency correlator described in Section 3.4.6 is used to optimize the GCPs. The optional **step 4** is not needed since the iterative resampling is implicit in the GCPs generation scheme. Only a few ICPs are necessary in this process.

Ultimately the goal of this study is to retrieve the horizontal coseismic displacement field from pre- and post-earthquake images. If we assume the pre-earthquake image to be co-registered according to the topography, the orthorectified pre-earthquake image becomes the registration reference for the post-earthquake image. In this case, ICPs on the raw post-earthquake image should be chosen as far away as possible from the zone of ground deformation. Co-seismic displacements could otherwise be partly compensated and biased from the look directions correction.

3.5.3 The Complete Processing Chain

We summarize the procedure to accurately orthorectify and co-register a set of pushbroom satellite images, and to retrieve coseismic displacements from pre- and post-earthquake images. It is assumed that ancillary data on the satellite viewing geometry are available with the raw images. It is also assumed that a topographic model whose resolution is close to the ground resolution of the images is provided.

1. One image of the set is chosen to be the reference image. A shaded version of the topographic model is generated as described above. If the satellite viewing parameters for this particular image are largely biased, three GCPs are visually selected from the shaded topographic model. On visually recognizable topographic features, ICPs are selected from the raw image, and GCPs are generated using statistical correlation on the shaded topography.
2. From the set of GCPs obtained, the mapping of the raw image onto the ground is computed with the inverse orthorectification model. Two inverse transformation matrices, one for each of the two dimensions of the image, are created.
3. The reference image is resampled according to the transformation matrices.
4. Another raw image of the set is chosen. Three GCPs are manually selected from the first orthorectified image, if needed. ICPs are chosen from the raw image and GCPs are generated using frequency correlation on the reference image.
5. The raw image is orthorectified according to the set of GCPs devised. It is then resampled. An accurately orthorectified and co-registered image is produced. Steps 4 and 5 are repeated if more than two images of the same area have to be co-registered.
6. The image ground projection grids have been designed so that they all align exactly. Any change detection algorithm can then be applied on overlapping areas. In the case of coseismic deformation measurements, correlation using the frequency correlation detailed in Section 3.4.6 is performed between sliding windows scanning the pre- and post-earthquake images. Each correlation results in a measure of displacement along the lines (East/West displacements) and along the columns (North/South displacements) of the orthoimages.

The correlation grid is defined from three parameters: the correlation window size, the step size (defining the correlation image pixel size) and the coordinates in the master image where the correlation starts. The starting pixel is the closest to the upper left master image corner whose ground coordinates are multiple of both the image resolution and the correlation step size. Doing so allows us to mosaic or stack correlation images without further resampling.

3.6 Tests and Results

Tests of the performance and limitations of the technique are carried on cloudless pairs of SPOT images acquired above the Hector Mine area in California, where a Mw 7.1 earthquake occurred in 1999. The SRTM DEM [54] with a ground resolution of 1 arc-second (30 m) is used. It has an absolute height accuracy of 16 m and a relative height accuracy of 10 m. The absolute horizontal accuracy is 20 m and the relative horizontal accuracy is 15 m. These accuracies are quoted at 90% level.

The SRTM mission initially measured ground positions in Cartesian coordinates but delivers orthometric heights, expressed with respect to the EGM 96 geoid. According to the orthorectification procedures described, ground elevations should be expressed with respect to the WGS 84 ellipsoid and the DEM should be compensated by adding the geoid undulations. However, for the EGM 96 geoid, the shortest wavelength resolved is of 111 km and corresponds to the spherical harmonic of degree 360 [55]. Neglecting the deflection of vertical, the difference between the ellipsoid and geoid heights is then considered constant at the scale of an image footprint (60×60 km), and the DEM is not compensated for. This constant height offset is then absorbed during the GCPs optimization.

Two experiments are done. First the orthorectification and the co-registration are examined from a set of two images acquired after the earthquake. Second, a set of two images bracketing the 1999 Mw 7.1 Hector Mine earthquake, are considered.

3.6.1 Measuring a Null Displacement Field from SPOT 5 Images

This experiment involves the co-registration of two orthorectified SPOT 5 images, denoted by image 1 and image 2. Table 3.1–case A displays their general characteristics. Acquired 6 months apart, they share a nominal ground resolution of 5 m. In addition, they have very similar incidence angles so that geometric artifacts, if presents, should be negligible. Although they were acquired at the same time of the day, the shadows are quite different due to the seasonal difference of the sun elevation. These two images were acquired by two different instruments HRG 1 and HRG 2, which are theoretically identical.

The Hector Mine area is a desert region, and over a period of 6 months, landscape modifications due to vegetation changes or man-made constructions were very limited. No major seismic activity was reported in this area between the acquisition of these two images [56].

Table 3.1: Relevant parameters for the SPOT scenes

Parameters	Case A		Case B	
	Image 1	Image 2	Image 1	Image 2
Satellite	SPOT 5	SPOT 5	SPOT 4	SPOT 2
Instrument	HRG 1-A	HRG 2-A	HRV 1	HRV 1
Date	26/7/2002	24/1/2003	17/8/1998	10/8/2000
UTC Time	18:38:18	18:39:45	18:38:18	18:41:09
K-J Location	545-280	545-281	545-281	545-281
Spectral Mode	PAN	PAN	PAN	PAN
Resolution	5 m	5 m	10 m	10 m
Scene Orientation	13.61°	13.60°	10.3°	11.1°
Incidence Angle	-1.726°	-1.642°	- 2.9°	+ 5.2°
Sun Azimuth	127.72°	158.15°	137.4°	136.1°
Sun Elevation	68.27°	33.38°	63.9°	65.8°
Pre-proc. Level	1A	1A	1A	1A

Additionally, the Hector Mine earthquake did not produce any measurable afterslip at the surface [57], so there should be no terrain change in this dataset.

In all, these images have nearly identical characteristics, and are as similar as two satellite images, acquired at different periods of time, can be.

3.6.1.1 Processing Steps

The first processing step is to co-register image 1 to the topography. Since we are using SPOT 5 images, no manually selected GCPs are needed.

To minimize the resolution difference between the DEM (30 m) and the image (5 m), the DEM is resampled on a 10 m UTM grid. A sinc kernel (theoretically C^∞) is used to later avoid gridding artifacts in the shaded relief image. This interpolation is not required but it has been found to improve the GCPs accuracy by up to 15–20%. The sun elevation and azimuth of image 1 are used to construct the shaded image.

35 ICPs are chosen in the raw image on visually recognizable topographic features. The GCPs optimization is carried out through statistical correlation with the shaded DEM on patches of 300×300 pixels corresponding to 3×3 km on the ground. Several iterations of the algorithm are performed and at each round, the average and the standard deviation of

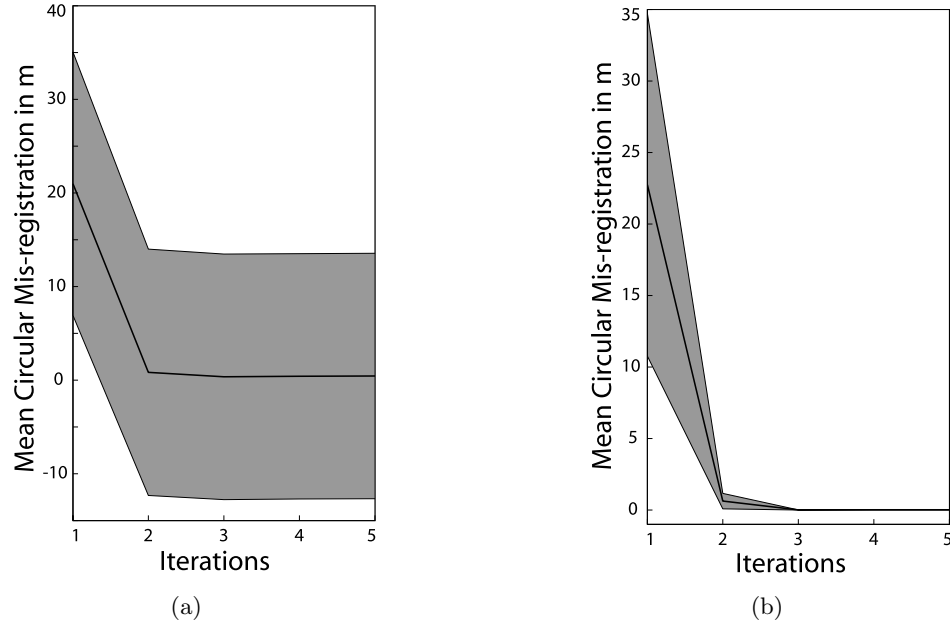


Figure 3.17: Evolution, with respect to the iterations of the look directions correction algorithm, of the mis-registration of the GCPs to be generated. The mean bias (black line) and the standard deviation (shaded area) are calculated from the local mis-registration of each GCP, weighted by their relative SNR. (a) Convergence of the GCPs between the raw image 1 and the shaded relief image. (b) Convergence of the GCPs between the raw image 2 and the orthorectified image 1.

the mis-registrations are measured over all GCPs, Fig. 3.17(a). The initial mis-registration measured ($\mu = 20.97$ m and $\sigma = 14.07$ m) is within the SPOT specifications; the global error is less than 50 m. Convergence of the algorithm is reached after 3 iterations. The average residual mis-registration is evaluated to 40 cm while the standard deviation residual is estimated to 13.1 m. This last uncertainty is consistent with the 15 m relative horizontal accuracy of the SRTM DEM. This shows clearly that the DEM resolution and accuracy limits the use of such approach. The georeferencing quality is therefore limited by that of the DEM.

Using this set of GCPs, image 1 is orthorectified onto a UTM grid with a 5 m resolution. It is then resampled. The resampling distances are $d_x = 1.26$ pixels and $d_y = 1.21$ pixels, consistent with the scene orientation of 13.61° (theoretical resampling distances are $d_{th} = 1.20$ pixels: Section 3.3.3.1, $a = 1$ pixel).

Image 2 is then co-registered with the orthoimage 1. No manual GCPs are needed. 3 ICPs distant from each other are chosen from the raw image 2. These points are optimized from frequency correlation on the orthoimage 1 and a set of 3 GCPs is generated.

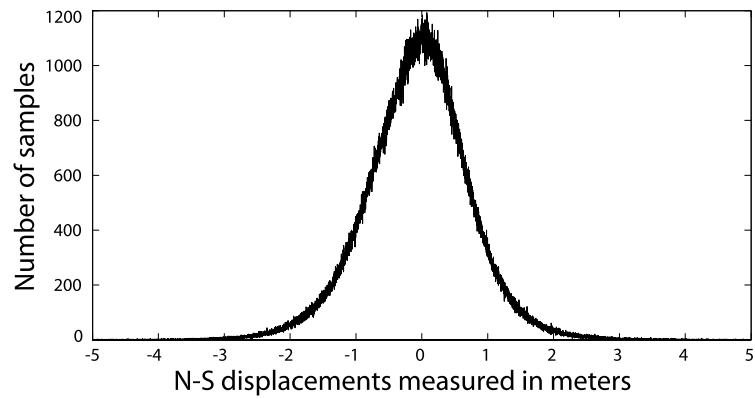
Correlation patches of size 512×512 pixels corresponding to 2.56×2.56 km on the ground are chosen. The correlation mask parameter is set to $m = 0.9$ and two robustness iterations are performed for each correlation. The mis-registration residuals on the GCPs with respect to the number of iterations are presented in Fig. 3.17(b). Once again, with no a priori knowledge the average and the standard deviation of the initial mis-registrations are within the SPOT 5 specifications. It is measured $\mu = 22.74$ m and $\sigma = 11.98$ m. Convergence is reached after three iterations. The average residual mis-registration measured is $\mu = 1.2$ cm for a standard deviation $\sigma = 1.6$ cm. Since a linear correction based upon three GCPs is applied, this small co-registration error reflects the maximum accuracy of the correlation given the correlation patches size and the noise contained within the patches. This proves the convergence of the process. When increasing the number of GCPs, the co-registration accuracy commonly stays below $\frac{1}{50}$ of a pixel. The image 2 is orthorectified and resampled on a 5 m UTM grid using these 3 GCPs. The computed resampling distances are $d_x = 1.26$ pixel and $d_y = 1.21$ pixel.

Correlation between sliding windows is performed on the overlapping orthorectified images. The frequency correlation from Section 3.4.6 is used. Correlation is executed on 32×32 pixel windows (160×160 m on the ground) and with a sliding step of 8 pixels (40×40 m on the ground). The mask parameter is set to $m = 0.9$ and four robustness iterations are applied.

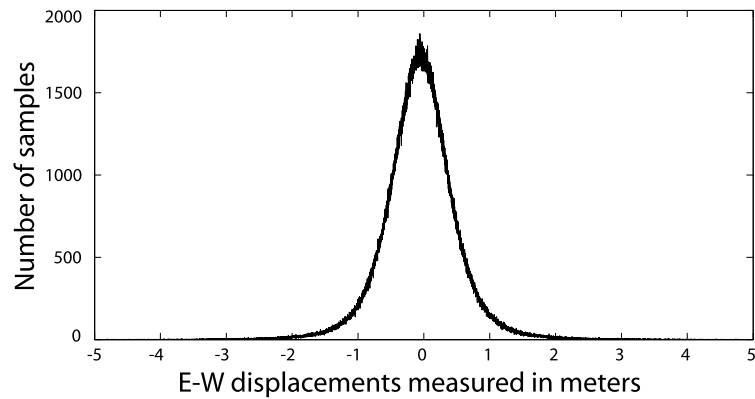
3.6.1.2 Results Analysis

The result of the correlation process is presented in Fig. 3.19 and Fig. 3.20, where each image represents one component of the horizontal ground displacement field. Fig. 3.21 shows the SNR image associated with the measurements. Here, only the simplest form of the correlation algorithm is presented since the extended form failed to show any improvement. Offsets measured with the two approaches agree within less than 10 cm. The relative noise between the two images induces a measurement uncertainty that overwhelms a possible correlation bias. The correlation images, composed of 1748×1598 measurements, need 3.25 hours to be computed using the algorithm's simplest form on a PC with a 3.6 GHz Xeon CPU. On the same computer, the extended algorithm needs 26.3 hours. Only the simplest form of the correlation process is considered hereafter.

Although images 1 and 2 are very similar, decorrelation areas are present. Decorrelation



(a)



(b)

Figure 3.18: Histograms of the relative offsets between the two orthorectified SPOT 5 images. 32×32 pixels correlation window have been used. Decorrelation points are discarded. (a) It is measured $\mu\{\Delta_{NS}\} = -0.058$ m and $\sigma\{\Delta_{NS}\} = 0.80$ m. (b) It is measured $\mu\{\Delta_{EW}\} = -0.051$ m and $\sigma\{\Delta_{EW}\} = 0.57$ m.

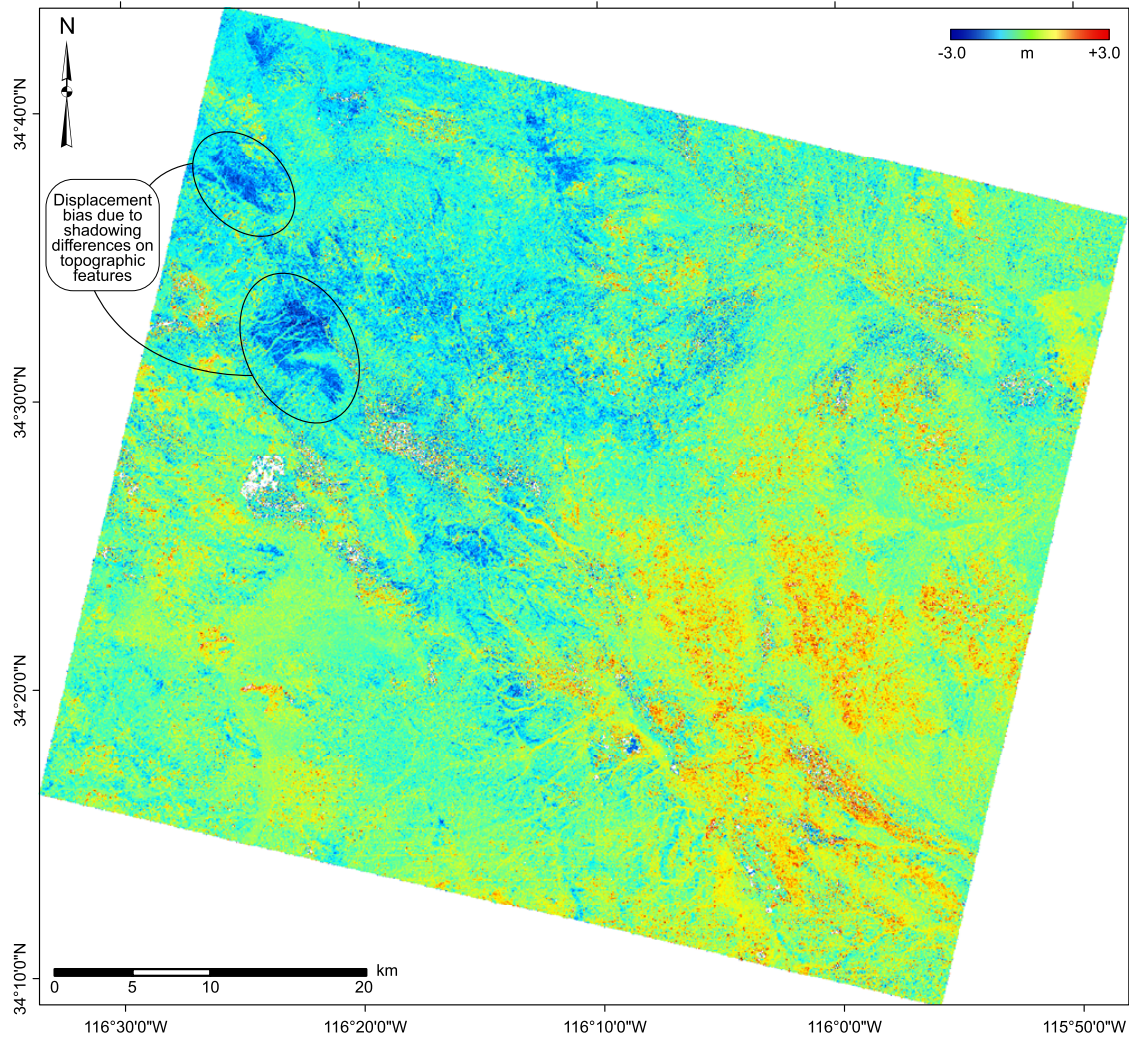


Figure 3.19: North/South component of the SPOT 5 / SPOT 5 correlation. Displacements are positive toward the North. Shadowing biases are mostly visible in this component since the Sun azimuth of the two images is mostly North/South oriented (127.72° and 158.15°). Decorrelation points are discarded and appear in white.

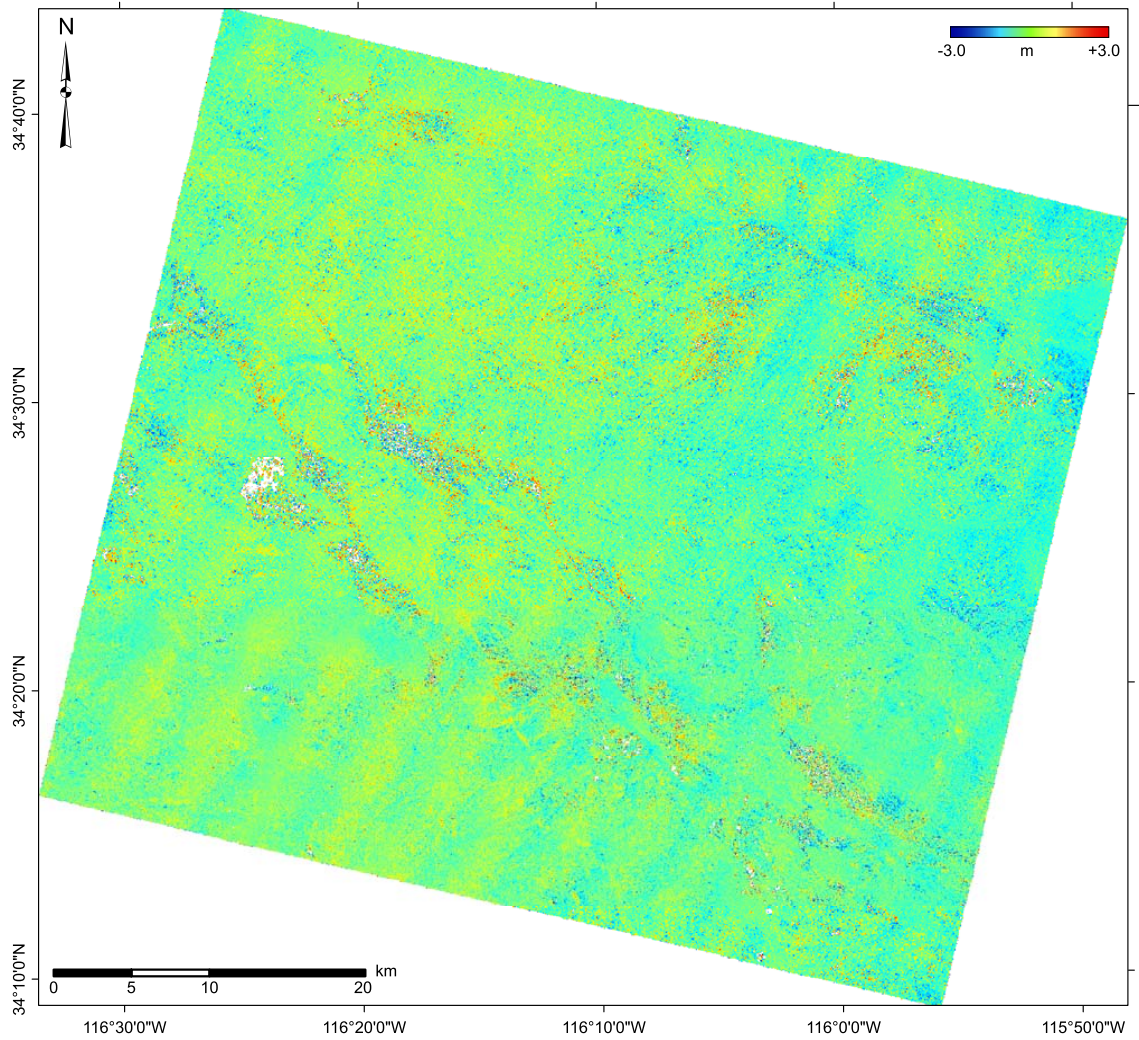


Figure 3.20: East/West component of the SPOT 5 / SPOT 5 correlation. Displacements are positive toward the East. No shadowing bias is noticed along this direction. An unexplained wave artifact of a period of 5 km and with an amplitude of 40 cm on the ground is seen. Decorrelation points are discarded and appear white.

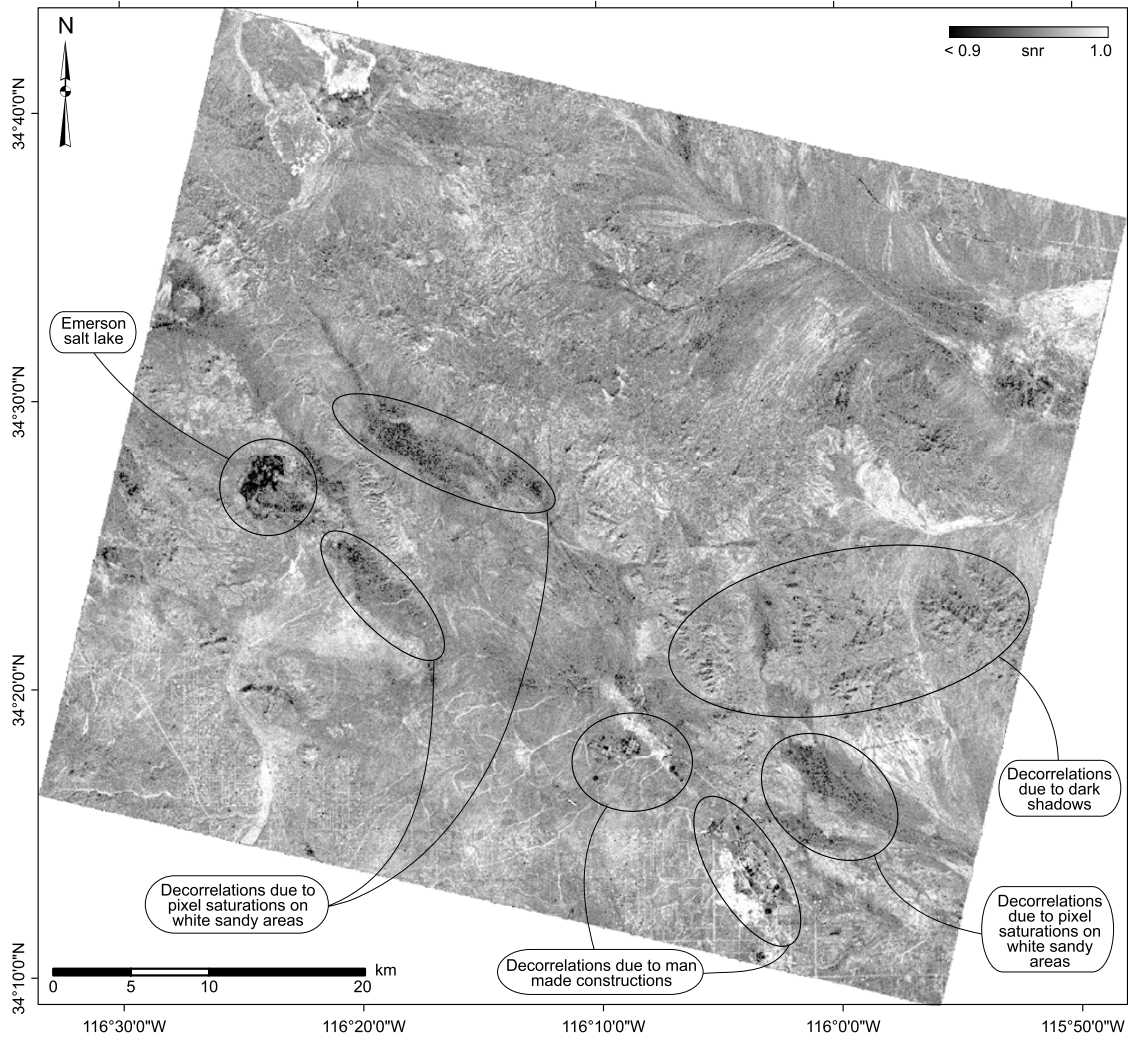


Figure 3.21: SNR map assessing the quality of the measurements. SNR values range from 0 to 1 but it is only shown ranging from 0.9 to 1 since most of the values are very close to 1. Decorrelation areas are shown in black. Examples of the typical decorrelation situations are indicated. Cloud cover or vegetation changes are not an issue in this desert region.

is the loss of correlation, characterized by a low or null (if the correlation algorithm does not converge) SNR, or by extremely large unphysical measurements (> 5 m here). These decorrelation points represent here 0.1% of the total number of measurements. Inspection of the decorrelation areas shows that correlation is lost in three major circumstances. First, temporal decorrelation occurs when windows to correlate contain drastic changes. These changes may be caused by lateral surface processes, mainly due to alluvions. This is particularly clear in the surrounding of Emerson Lake, a salt lake located on the West side of the scene, Fig. 3.21. Vegetation changes, clouds, or snow are not a matter of concern in this desert region. New buildings or large man-made modifications are also a source of temporal decorrelation. The second source of decorrelation is the shadowing difference. The scene 2 was acquired in winter when the sun elevation was much lower (33.38°) than when the scene 1 was acquired during summer (68.27°). In image 2, this results in topographic shadows where information is lost, along with the correlation. The third source of decorrelation involves ground features that are, at the correlation window scale, translation invariant. The algorithm is not capable of proposing a stable registration point between the windows to correlate and does not converge. For instance, this phenomenon occurs in areas of constant radiometry. The interior of the Emerson Lake is an example. Large water basins, on the South-East side, are another example. Straight and isolated roads are also cases where correlation is lost along the road direction.

After filtering out these decorrelation points, histograms in each dimension are given in Fig. 3.18. They show an average displacement of 7.8 cm. Therefore, on average, a registration better than $\frac{1}{50}$ of the nominal image resolution (5 m) is achieved. The spread of the histograms is Gaussian and can be seen as reflecting the noise on the measurements. However it does not characterize the noise level of the correlation technique, which should be much lower as shown in Section 3.4.7.3, but rather the “natural” noise of the scenes. The noise is indeed not distributed evenly as a function of the spatial wavelength and is thus not white. The largest displacements forming the tails of the histograms are found on topographic features and alluvions. In alluvions and deposits areas, measured displacements are up to 1.5 m with more typical values around 60–70 cm. These measurements are most likely to be physical. On topographic features, displacements up to 2.5 m are observed. Visual inspection of the images reveals that they are artifacts resulting from shadowing differences. Given the close incidence angles of the two images, topographic bias can only

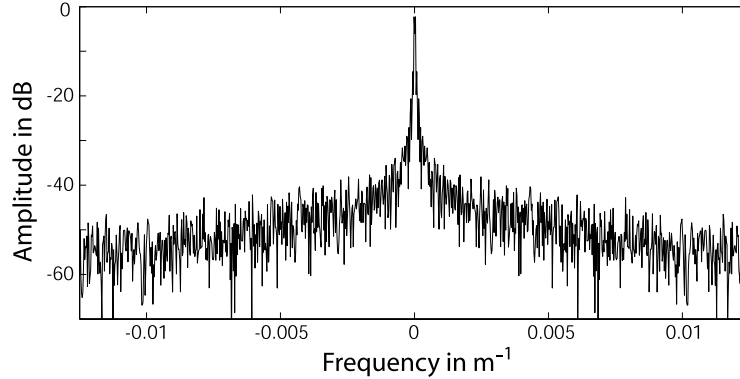


Figure 3.22: Section across the power spectral density of the North/South correlation image

account for at most a few centimeters. The large difference in the sun elevation then largely contributes in biasing the correlation measurements on topographic features. Also, the spread of the correlation histograms is larger in the sun azimuth direction.

Looking at the East/West displacement field, a sinusoidal artifact that covers the whole image is visible. The amplitude is estimated around 40 cm with a period of 5 km. We have not yet found a definitive explanation for this artifact. If we exclude areas where measurements are obviously biased, meaning away from shading artifacts, alluvions, or decorrelation areas, the measurements' standard deviation is about 25 cm. Using 32×32 pixel correlation windows the intrinsic noise of the correlation is therefore estimated at $\frac{1}{20}$ pixel. This performance is much lower than the theoretical one stated in Section 3.4.7. Real scene images actually contain aliasing from the optical system and are subjected to radiometric noise and quantization. Reducing the effects of these noise sources then appears as a priority to further improve the performance of the technique.

The measurement of disparities between a set of satellite images is thus subjected to several kind of noises. The decorrelation noise is modeled as a zero mean impulse noise: some measurements take random values within the range allowed by the correlation window size (\pm half the correlation window size). Another component of the noise has been described as the “natural” noise of the scene. It is additive, Gaussian and zero mean with a standard deviation typically around 1 m. On average, it determines the minimum displacement that can confidently be retrieved from a set of images. This noise has itself two additive components. It has a low frequency component that characterizes artifacts induced from the lack of topographic resolution, shadowing, or satellite-induced artifacts (due to at-

titudes or sensor uncertainties). It has also a high-frequency component, modeled as white additive and Gaussian. This noise accounts for the measurement uncertainty induced by slight scene changes, aliasing, quantization, noise of the sensors and intrinsic correlation accuracy. Fig. 3.22 shows a section across the power spectral density of the North/South correlation image. The superposition of the noises clearly appears. A white noise with lower power is superposed to a higher-power low-frequency noise. More confidence on the displacements measured can therefore be obtained if these two noise sources can be unambiguously isolated. The low-frequency noise tends to be more localized in the correlation images.

3.6.2 The 1999 Hector Mine Earthquake Imaged From SPOT

In this last example we analyze SPOT 4 and SPOT 2 images bracketing the 1999, Mw 7.1, Hector Mine earthquake. The SPOT 4 image, acquired in August 1998, is referred to as image 1. The SPOT 2 image, acquired in August 2000, is referred to as image 2. Principal characteristics of these images are reviewed in Table 3.1–case B.

This test is an opportunity to assess the performance of the technique to measure coseismic ground deformation. It also allows us to test the registration quality when images show a significant difference in their incidence angle. As stated in the introduction, most of the techniques currently in use fail to achieve precise image co-registration when incidence angle difference exceeds 3° . It is here 8.1° .

3.6.2.1 Processing Steps

We follow the same procedure as in the previous example, and the same 10 m sinc interpolated DEM obtained from the 1 arc-second SRTM DEM, is used. The only difference is that 3 GCPs are visually selected between the raw image 1 and the shaded DEM to initiate the GCPs optimization. The initial mis-registration corresponds to the uncertainty on the three GCPs manually selected, $\mu_{init} = 32.72$ m and $\sigma_{init} = 23.6$ m. Convergence is reached after three iterations and $\mu_{final} = 0.25$ m and $\sigma_{final} = 11.43$ m. The raw image 1 is orthorectified and resampled, according to the GCPs generated, onto a 10 m UTM grid. Computed resampling distances are $d_x = 1.29$ pixel and $d_y = 1.16$ pixel. Three GCPs are visually selected from the raw image 2 with respect to the orthoimage 1, and three ICPs are chosen from the raw image 2 such that they are distant from each other and they do not belong

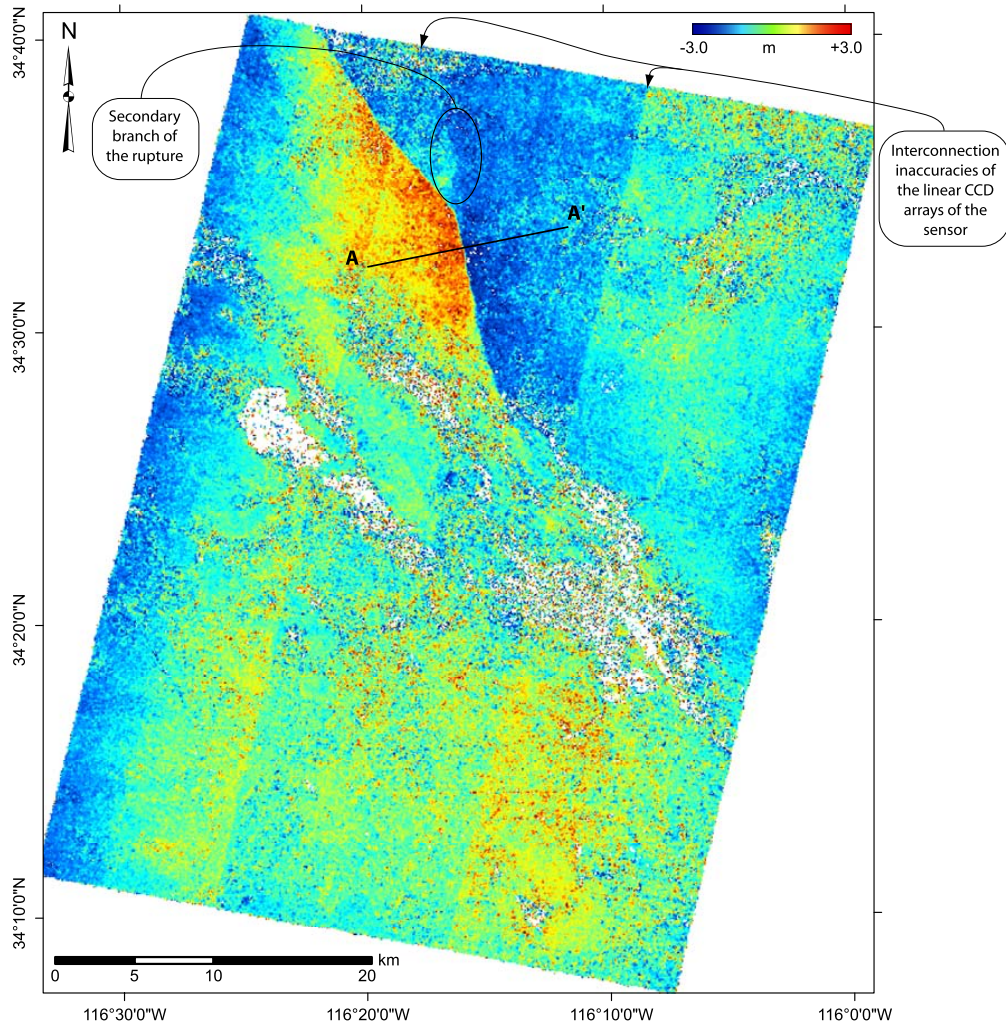


Figure 3.23: North/South component of the SPOT 4 / SPOT 2 correlation. Displacements are positive toward the North. The fault rupture is visible going from the North-West corner to the center of the image. The maximum displacement on the fault along the North-South direction is of 6 m. A secondary branch is also noticed. Sensor artifacts lead to linear distortions in the satellite along track direction. Decorrelation points are discarded and appear in white. The profile AA' is reported in Fig. 3.26.

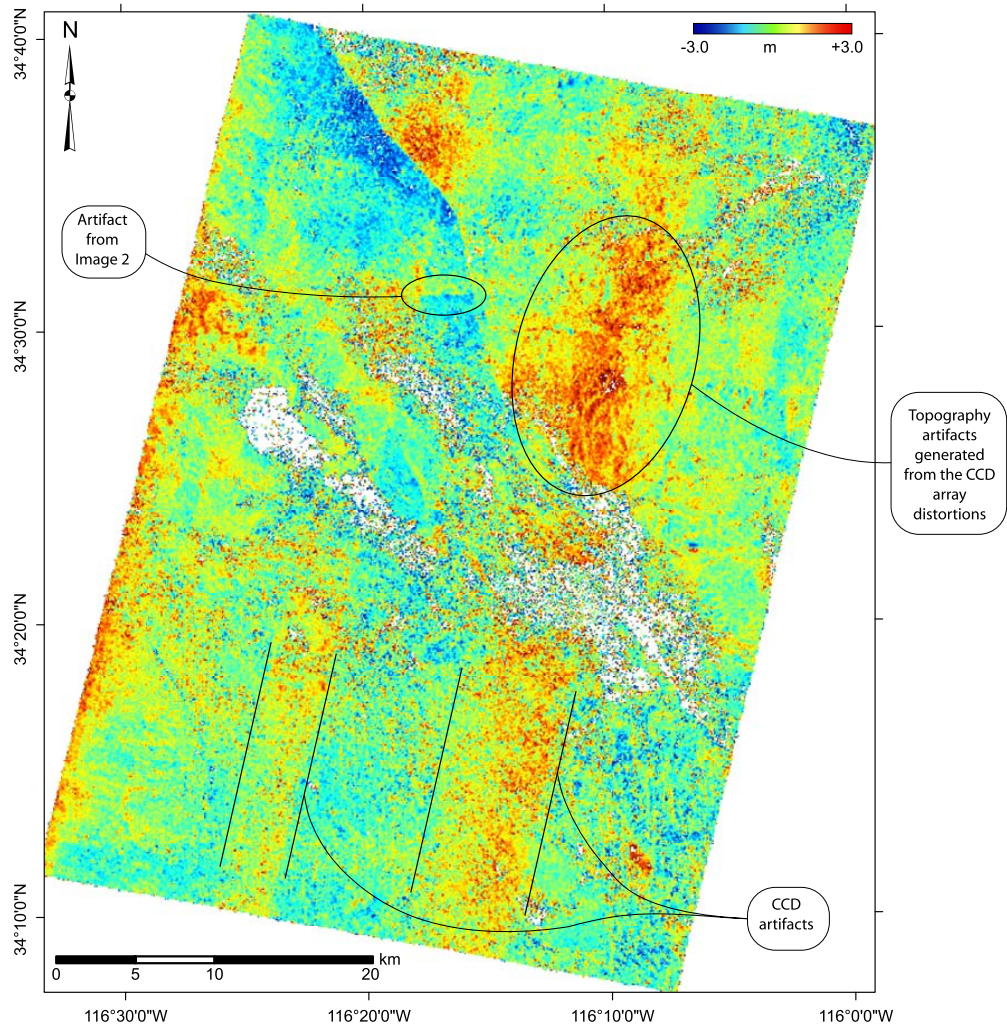


Figure 3.24: East/West component of the SPOT 4 / SPOT 2 correlation. Displacements are positive toward the East. The fault rupture is visible going from the North-West corner to the center of the image. The maximum East-West component of the fault slip is estimated to 3.5 m. Sensor distortions are inducing linear artifacts and parallax effects on topographic features. Decorrelation points are discarded and appear in white.

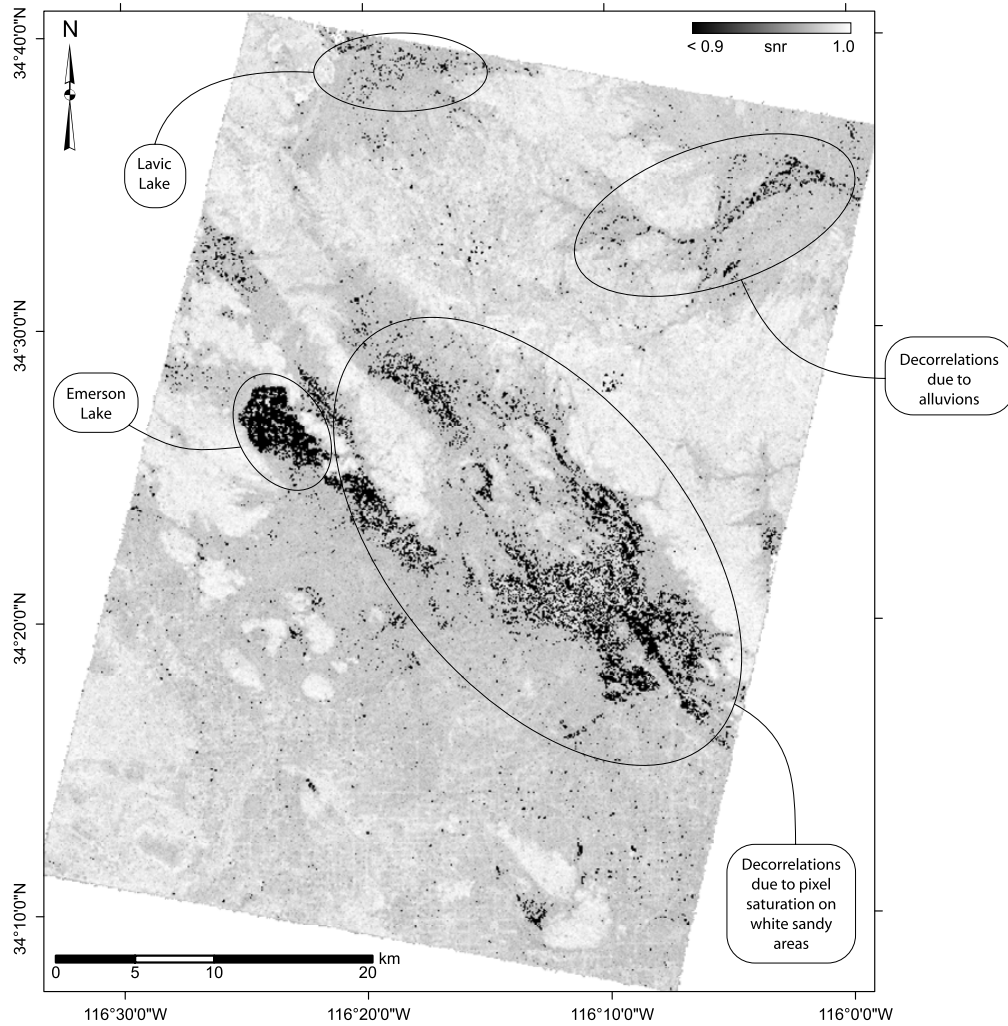


Figure 3.25: SNR of the SPOT 4 / SPOT 2 correlation. The SNR ranges from 0 to 1 but it is only shown ranging from 0.9 to 1 since most of the values are close to 1. Decorrelation areas are shown in black. In this particular case, decorrelations are mainly due to sensor saturation and alluvions.

to the near fault deformation zone. Optimization is achieved through frequency correlation of 256×256 pixel patches (2.56×2.56 km). Convergence is reached after three iterations and the average residual mis-registration is below 1.5 mm with a standard deviation below 2 mm. Using only 3 ICPs, the convergence only reflects the accuracy of the correlation. In this case, we notice a significant improvement, in comparison to the previous test, because the shadowing of the scenes is similar. The raw image 2 is orthorectified and resampled, according to this set of three GCPs generated, onto a 10 m UTM grid. Computed resampling distances are $d_x = 1.32$ pixel and $d_y = 1.17$ pixel. The resampling distance d_x increases as the incidence angle increases: the foreshortening effect becomes more important in the satellite across track direction.

Overlapping areas of orthoimages 1 and 2 are cropped and correlation is performed with 32×32 pixel (320×320 m) sliding windows and with a step of 8 pixels (80 m). The mask parameter is set to $m = 0.9$ and 4 robustness iterations are applied. The simplest form of the correlation algorithm is used.

3.6.2.2 Results Analysis

Fig. 3.23 and Fig. 3.24 represent, respectively, the displacements along the North/South and the East/West directions. Fig. 3.25 shows the SNR associated with the measurements.

The ground deformation induced by the earthquake is clearly visible. The surface rupture appears as a discontinuity in the displacement field that is traced from the North-West corner to the center of the correlation images. The horizontal slip vector is measured from profiles taken perpendicular to the fault trace, Fig. 3.26. Horizontal coseismic displacement measured on the fault is up to 6 m in the North/South direction and up to 3.5 m in the East/West direction. In the North/South correlation image, a secondary rupture branches to the North where the main rupture bends. The coseismic displacement measured on this secondary branch is up to 1 m. The location of the fault trace and the surface fault slip recovered from the SPOT images compare well with the surface ruptures and fault slip measured in the field [58], and from SAR images [59], [57], [60]. We observe in Fig. 3.27 that the fault slip measured from the SPOT images is generally close to the maximum slip measured in the field and varies smoothly along strike. The horizontal coseismic fault slip at the surface is therefore accurately and densely (every 80 m) recovered from the proposed technique. The nominal image resolution being 10 m, all the measurements are in

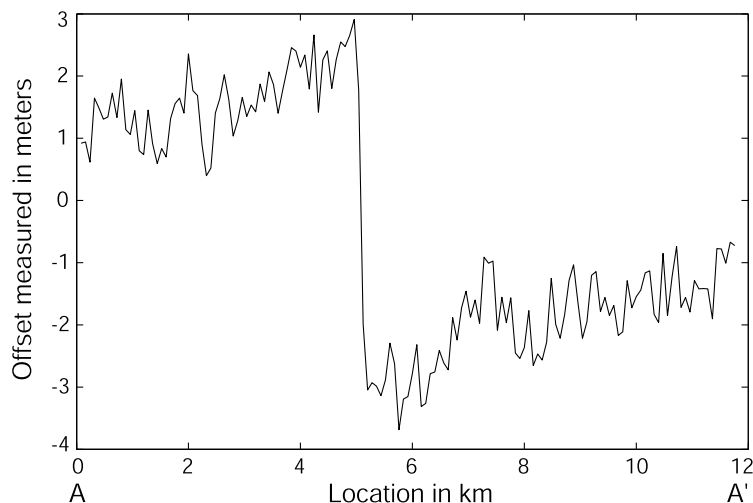


Figure 3.26: Profile AA' from the SPOT 4 / SPOT 2 North/South correlation image. This profile shows the maximum displacement of 6 m measured in the N/S direction. The high-frequency noise is clearly visible and accounts for about 85 cm.

the sub-pixel range, within ± 3 m. Several sources of decorrelation, noise or artifacts are noticed.

Decorrelation areas are visible and explicitly shown in the SNR image. Some of them are the consequence of drastic surface changes that occurred during the two years separating the images acquisition. Decorrelation is easily identifiable on the Emerson salt Lake and the Lavic salt Lake areas. Large decorrelation areas going from the center of the correlation images and toward the East are due to sensor saturation: white sandy areas appear too bright on the post-earthquake image. Non-recorded high radiometric contrasts induce a loss of correlation.

Filtering out the decorrelation areas and away from the major discontinuities, the displacements show a Gaussian distribution centered on $\mu_{NS} = -4.4$ cm in the North/South direction and on $\mu_{EW} = 23.3$ cm in the East/West direction. On average, the registration of the images is on the order of $\frac{1}{40}$ of the nominal image resolution. The standard deviations are respectively 62.2 cm and 85.6 cm in the North/South and East/West components. This noise level is consistent with the previous example, given the longer time period between the images and their lower resolution.

Linear artifacts in the satellite along track direction that are biasing the mean displacements are visible. They are due to the SPOT 4 and SPOT 2 CCD arrays mis-alignments. The panchromatic SPOT 1,2,3 and 4 satellite sensors are indeed composed of four CCD

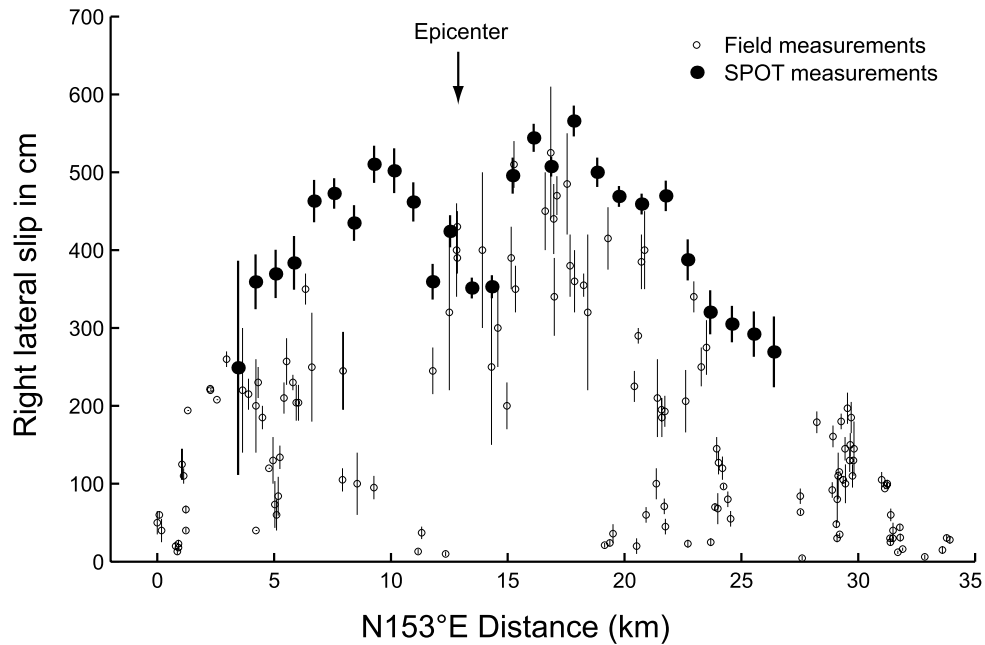


Figure 3.27: Right lateral slip is determined by projecting the horizontal slip vectors along the fault strike. Horizontal slip vectors are measured from linear least-square adjustment, on each side of the fault and on each NS and EW images, of stacked profiles running perpendicularly to the rupture. Profiles are stacked over a width of 880 m and a length of 8 km. Slip vectors further North (0–4 km) do not fall within the image extent, and further South (beyond 27 km) are corrupted by decorrelations. The overall envelop of the lateral slip reported from SPOT measurements is in good agreement with the field survey, although field measurements are under-estimated: in many portions of the rupture, cultural features of sufficient linearity were lacking to properly estimate the distributed shear, that may account for up to 40% of the total right lateral deformation [58]. Origin of the measurements is located at the UTM point 566880 E, 3828400 N.

linear sensors of 1500 pixels each, aligned together to form the complete 6000 pixel sensor [23]. Discontinuities measured range from 30 cm to 70 cm (0.03 to 0.07 pixel). This is in agreement with the sensor discontinuities and distortions reported in [50] and [1].

In the East/West component, a small horizontal linear offset is present around the location $34^{\circ}31'N$, $116^{\circ}17'W$. Unexplained at this time, it is identified as an artifact from image 2. This offset is indeed not present when correlating the SPOT 4, 1998 and SPOT 5, 2002 images, while it does appear in the correlation of the SPOT 2, 2000 and SPOT 5, 2002 images.

The distortions of the CCD arrays (relative tilt between CCD arrays as seen in [50]) also produce local look direction distortions along the satellite across track direction. Some parallax effects are therefore noticed in the East/West component of the disparity field when these distortions occur on areas of rough topography. Beside this small parallax effect due to the CCD distortions, no other topographic artifacts are seen in the East/West correlation images. The North/South correlation image is free of topographic artifacts. No shadowing differences are biasing the measurements since the SPOT images have been acquired at the same period of the year. This test demonstrates the performance of our procedure to co-register satellite images with important incidence angle difference. It also indicates that, when the DEM ground resolution and height accuracy are “precise enough”, shadowing differences and CCD distortions are the main sources of artifacts.

3.7 Conclusion and Future Work

This chapter has presented a complete procedure for automatic and precise orthorectification and co-registration of optical satellite images. The approach has been validated using SPOT images and SRTM DEM, without any external information such as GPS. In the test cases analyzed, the co-registration accuracy is on the order of $\frac{1}{50}$ of the image nominal resolution, and the absolute georeferencing precision is similar to that of the digital elevation model used.

The orthorectification takes into account the imaging system distortions and the satellite attitude variations during the image acquisition. Thanks to the inverse orthorectification model, the raw images are rigorously resampled to produce orthorectified images without adding aliasing. The rigorous resampling has proven to be key for our application and we

advocate for the use of near theoretical resampling kernels for applications requiring geodesic accuracy. Based on our analysis of the frequency correlation methods, improvements have been suggested to improve accuracy, robustness and flexibility. Displacements smaller than $\frac{1}{20}$ of a pixel, using 32×32 pixel correlation windows, are accurately measured from real noisy images. The test cases show that our procedure does not introduce any bias on the measurements of ground displacements. Thanks to our precise georeferencing and correlation techniques we have found evidence for artifacts and biases of the imaging systems at the sub-pixel scale. Sensor discontinuities and distortions on the SPOT 2 and SPOT 4 satellites have been identified and measured. Similarly, biased displacements induced by shadowing differences have been quantified. It is up to a few meters in the example considered, exceeding topographic artifacts due to parallax effects. Image acquisition dates and times should therefore be carefully considered in change detection applications. Correlation noise results from three additive components: decorrelation, due to severe ground changes or lack of information between the scenes is modeled as an impulse noise; topographic artifacts, shadowing differences, uncorrected satellite attitudes and sensor distortions are modeled as a localized low-frequency noise; slight changes in the scenes, radiometric quantization, aliasing, sensor noise and correlation uncertainties are modeled as an additive white Gaussian noise. The last two components constitute the “natural” noise and determine the smallest ground motion that can accurately be measured. The standard deviation of this noise is typically around 1 m but the low-frequency component, mostly localized in the images, accounts for the largest errors. This is why the ground displacement discontinuities are accurately measured with an uncertainty ranging from 20 cm to 80 cm in each of the North/South and East/West directions. This technique is a powerful complement to differential radar interferometry [22], which can provide much more accurate measurements of ground displacements in the range direction, but generally fails in the near fault zone due to a loss of coherence or a fringe rate in excess of one fringe per pixel [61].

Some limiting factors have also been identified, suggesting directions for further improvements. The resampling method proposed ensures the production of aliasing-free orthoimages, but is suppressing some of the image high-frequencies. An adaptive resampling kernel would increase the resampling efficiency. The frequency correlation technique is very versatile but its sensitivity to aliasing or quantization has not been analyzed yet. The information provided on each CCD on the form of a look direction is essential in correct-

ing optical biases. This information is fully available on SPOT 5 images which has made it possible to accurately model sensor artifacts. For high-precision instruments, on-board calibration of all the sensor CCD elements should be generalized. The accuracy or the sampling of the on board gyroscopes may not allow the recording of too small or too fast attitude variations. We have encountered some cases, not shown in this study, where long wavelength variations due to pitch oscillations were visible in the correlation images. These small unrecorded variations had an amplitude of 1.5 m on the ground with a periodicity of 4.2 km. This sets the accuracy limit of the SPOT gyroscopes. A linear correction is therefore not always sufficient and higher-order or trigonometric corrections may be investigated.

The processing techniques described allow co-registering optical satellite images, possibly acquired from different satellite systems, with unprecedented accuracy. This should be helpful in reducing or eliminating measurement uncertainties and biases for any change detection applications.

The algorithms described in this study have been implemented in a software package, COSI-Corr (Co-registration of Optically Sensed Images and Correlation), developed with IDL (Interactive Data Language) and integrated under ENVI. It allows for precise orthorectification, co-registration and correlation of SPOT and ASTER satellite images as well as aerial photographs. It is available from the Caltech Tectonics Observatory website (<http://www.tectonics.caltech.edu/>).

Chapter 4

Measuring Coseismic Ground Deformation from Aerial Photographs Using COSI-Corr

By François Ayoub¹, Sébastien Leprince², and Jean-Philippe Avouac¹

¹ Division of Geological and Planetary Sciences, California Institute of Technology, Pasadena, California, USA

² Electrical Engineering Department, California Institute of Technology, Pasadena, California, USA

Foreword— This chapter is an updated version of a previously submitted paper under the reference F. Ayoub, S. Leprince, and J. P. Avouac, “Measuring co-seismic ground deformation from Aerial Photography using COSI-Corr,” *International Society for Photogrammetry and Remote Sensing (ISPRS)*, (submitted), 2007. In this thesis, it is referred to as reference [62]. In this work, F. Ayoub is responsible for developing, packaging, and testing the algorithms that are specific to aerial photography processing. F. Ayoub and S. Leprince worked jointly to adapt the satellite image processing tools from Chapter 3 to aerial photography processing, i.e., ground control points optimization, resampling, and correlation. In particular, this joint work has enabled the definition of a general core for the COSI-Corr software package, which has gained flexibility and that has benefited from extended series of tests. J.P. Avouac is the project principal investigator.

We describe and test a procedure to accurately measure ground deformations from multi-temporal aerial images. For the purpose of this study we have adapted photogrammetry techniques from a procedure initially designed for satellite images. The algorithms were implemented in a software package, COSI-Corr (available from the Caltech Tectonics Observatory website). The technique is validated by several case examples. First we measure coseismic ground deformations due to the 1992, Mw 7.3, Landers, California, earthquake from 1-m-resolution aerial photography of the National Aerial Photography Program (United States Geological Survey). The fault ruptures are clearly detected, including small kilometric segments with fault slip as small as a few tens of centimeters. We also obtained similar performance from images of the fault ruptures produced by the 1999 Mw 7.1 Hector Mine, California, earthquake. The measurements are shown to be biased due to the inaccuracy of the Digital Elevation Model, film distortions, scanning artifacts, and uncertainty of ground displacements at the location of the tie points used to co-register the multi-temporal images. We show that some of these artifacts can be identified and corrected.

4.1 Introduction

Large earthquakes generally produce ground ruptures which are an important source of information for earthquake mechanics in complement to geodetic and seismological measurements. Field measurements suffer from a numerous limitations: fault ruptures have a complex geometry and the zone of anelastic co-seismic strain is sometimes distributed and difficult to detect in the field; fault slip can generally be measured only on a limited number of locations where clear offset piercing points are observable such as roads or terrace risers for example; the fault-perpendicular component is generally not measurable in the field. It has been shown that optical satellite imagery can help overcome most of these limitations; the principle of the approach is that surface deformation can be measured by comparing images acquired before and after an earthquake [1]. The technique has proven effective in a number of studies [9, 10, 19, 20, 63, 64] and has been implemented in a software for Co-Registration of Optically Sensed Images and Correlation (COSI-Corr) [8], available from the Caltech Tectonics Observatory. However, the resolution of satellite images (e.g., 2.5–10 m for SPOT, 15 m for ASTER) is sometimes insufficient to measure subtle ground deformations, especially where fault displacement is less than 1 m [8], which is typically the

case for earthquakes with magnitude M_w less than 7. In addition, satellite images, with appropriate geometric accuracy and ground resolution, are only rarely available for past earthquakes which are known to have produced surface ruptures. The use of aerial photography with sub-metric ground resolution would extend the applicability of the technique to earthquakes too small to be measured from satellite images, or for which good quality satellite images are unavailable. Encouraging experiments have been conducted in [65] on the 1992 Landers earthquake using aerial photography from the United States Geological Survey (USGS). Motivated by this result, we have adapted to aerial images the procedure designed in [8] for the processing of satellite images. Hereafter, we describe this adaptation and assess the performance and limitations of the technique. Our study is focused on applications in seismotectonics but the method described here is also applicable to measure ice flow [4, 66] or landslides [7], for example.

Retrieving accurate ground deformation of sub-resolution amplitude requires a number of processing steps. Prior to comparison, images must be finely co-registered. This is achieved by reconstructing the images on a common projection while accounting for acquisition distortion, scaling difference, and parallax effect due to topography. The reconstruction also has to preserve the original information contained in the images and special care needs to be paid to resampling. Ultimately, the correlation of the reconstructed images provides a map of the horizontal ground displacements. The performance and accuracy of the technique depends on the quality of the correlation and of the co-registration.

Hereafter, we detail the various processing steps: reconstruction mapping; resampling; co-registration optimization, and correlation. We next show an example of application to the 1992, M_w 7.3, Landers, California, earthquake. The technique is validated and sources of artifacts due to scanning quality and topographic distortions are identified and investigated. We next show an application to the 1999, M_w 7.1, Hector Mine, California, earthquake to illustrate that, in the case of the co-seismic deformation measurements, some ambiguity between real ground displacement and misregistration can arise, and we show how this ambiguity can be removed.

4.2 Technique Overview

Our technique requires the digitization of the film-based photographs. A scanner with high spatial and radiometric resolution is generally necessary. Digital photography is not considered in this study as the aerial photography archive is mainly film-based. However, the technique described in this paper could be used with digital frame camera as well.

To be co-registered, images are reconstructed on a common reference system. We chose the UTM ground projection as it presents several advantages. First, it provides a support independent from the acquisition system, allowing pairing of images from different devices, e.g., satellite and aerial images. Second, the relative displacements between reconstructed images is directly measured in length unit. Third, the reconstructed images are cartographically correct, a possibly useful by-product.

The reconstruction, called orthorectification, is done in two steps. The first step defines the transformation necessary to orthorectify the images, using photogrammetry techniques. The aim is to associate ground projection coordinates to pixel coordinates in the raw image. This mapping accounts for the image acquisition parameters (camera geometry, attitude, and position of the focal plane), and the topography with the help of a Digital Elevation Model (DEM). The second step consists in resampling the image.

Cumulative uncertainties on both the acquisition parameters and topography lead to distortions and mis-registrations between the pairs of orthorectified images to be compared. The co-registration is therefore improved by optimizing the second image's acquisition parameters, the slave, with respect to the first orthorectified image, the master.

Orthorectified and finely co-registered images are then correlated from sliding windows. At each step, horizontal offsets along East/West and North/South directions are measured and stored.

4.3 Orthorectification

A relation between ground coordinates and their imaged locations in the raw image must be established to project a raw image onto a predefined ground grid. This relation is defined using classical photogrammetry techniques [67].

Fig. 4.1 represents the acquisition geometry of an aerial photograph. R_g is the ground reference system with \vec{X} pointing to the East, \vec{Y} pointing to the North, and \vec{Z} vertical

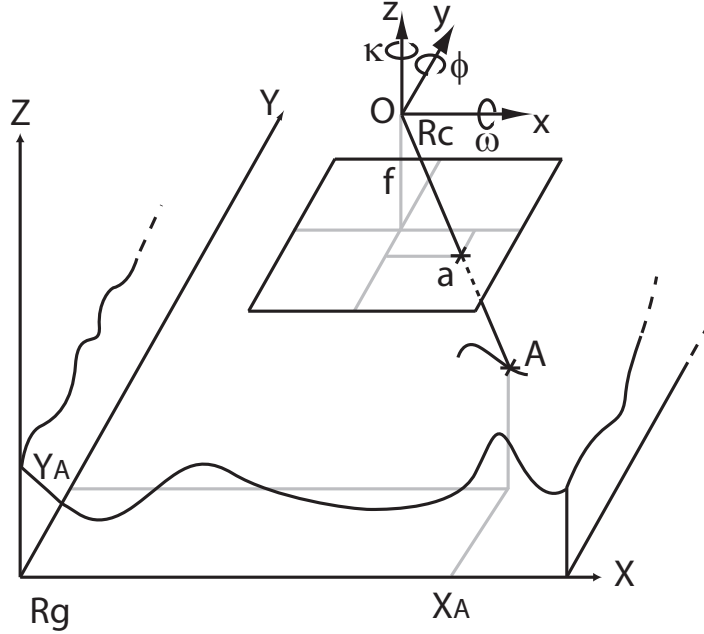


Figure 4.1: Geometry of an aerial photograph acquisition

pointing upwards. A point P whose coordinates are (X, Y, Z) in the ground reference system R_g is noted $P(X, Y, Z)_{R_g}$. R_c is the camera reference system, centered on the optical center O , with (\vec{x}, \vec{y}) parallel to the focal plane. The distance between O and the focal plane is the focal length f of the camera. For convenience, we also define the digitized image 2D reference system R_i (not represented on Fig. 4.1), with the origin located at the image top left pixel, and axes oriented along the column and line directions.

A ground point $A(X, Y, Z)_{R_g}$ (Fig. 4.1) is imaged on the focal plane (where the film lies), at $a(x, y, -f)_{R_c}$, and its pixel coordinates in the image are $(c, l)_{R_i}$.

The mapping function relates the ground point coordinates $(X, Y, Z)_{R_g}$ to its imaged pixel location $(c, l)_{R_i}$ and is expressed as a composition of three functions f_1, f_2, f_3 with:

$$(X, Y, Z)_{R_g} \xrightarrow{f_1} (x_1, y_1, -f)_{R_c} \xrightarrow{f_2} (x_2, y_2, -f)_{R_c} \xrightarrow{f_3} (c, l)_{R_i}, \quad (4.1)$$

where f_1 relates the ground point coordinates to its image location on the focal plane assuming an ideal acquisition system; f_2 accounts for distortions of light rays before they hit the focal plane due to the atmospheric refraction and lens defects; f_3 relates a coordinate on the focal plane in the camera geometry to its location in the image reference system.

f_1, f_2 , and f_3 relate to the interior and exterior orientations of the camera [67], as

described below.

4.3.1 Interior Orientation

The interior orientation (IO) establishes a mathematical model of the camera geometry. With the help of the camera calibration report, f_3 , a 2D affine transformation between the image coordinates and the camera coordinates, is determined using the fiducial marks location, and accounting for refinement of the principal point offset. In addition, this transformation corrects first-order film distortions (shrinkage or expansion) that occurred before the film was scanned. Higher-order film deformations are not corrected due to their non-systematic nature and, if severe, can limit the model validity. The radial symmetric lens distortions and atmospheric refraction are accounted for by f_2 . Other artifacts due to decentering lens distortions and non-flatness of the focal plane can be neglected. Notice that atmospheric refraction is altitude dependent, and the full determination of f_2 is obtained after defining f_1 during the exterior orientation.

4.3.2 Exterior Orientation

Once the IO defined, the exterior orientation (EO) of the camera is determined. It describes the position and angular orientation of the camera reference system, R_c , in the ground coordinates system, R_g , at the exposure time. The angular orientation is defined by three rotation angles ω, ϕ, κ , which may be seen as the roll, pitch, and yaw of the focal plane. The spatial position corresponds to the camera optical center coordinates, e.g., Easting, Northing, Altitude, in R_g . These six parameters are determined using space resection by collinearity. The well known collinearity principle states that a point on the ground, its corresponding image, and the optical center all lie on a straight line (i.e., A, a, and O aligned in Fig. 4.1). Formulating and solving the collinearity equation for at least three ground control points (GCPs), whose ground coordinates $(X, Y, Z)_{R_g}$ and image coordinates $(c, l)_{R_i}$ are known, allows determination of the six exterior orientation parameters. If more than three GCPs are available, the collinearity-derived equations are solved using a least-square adjustment [67]. f_1 is defined using these six parameters and the calibrated focal length of the camera.

4.3.3 Mapping Process

The mapping function is entirely defined from the IO and EO, and associates to any ground point $(X, Y, Z)_{R_g}$ its image coordinates $(c, l)_{R_i}$. Applied to all elements of a ground grid, with the altitude component read from the DEM, it defines the transformation matrices, containing the x and y coordinates of the pixels in the image to project. In practice, the ground resolution of the DEM is generally much lower than that of the images to orthorectify. This requires the DEM to be interpolated.

4.4 Resampling

The orthorectified images are constructed by resampling the raw images according to the transformation matrices. The ultimate task being the correlation of the resampled images, the challenge is to preserve the original information in the raw image and to avoid introducing bias. In theory, the ideal reconstruction kernel is the *sinc* kernel, but it is common practice to use the nearest neighbor, bilinear, or bicubic interpolations. These resampling techniques can corrupt the image information by introducing aliasing and bias the correlation [8]. Here we use a *sinc* kernel truncated to a length between 11 and 25 samples. The *resampling distances* [8], which characterize the width of the *sinc* lobes in the x and y directions, are determined from the transformation matrices, and represent the maximum absolute difference between adjacent pixel values in the matrices.

The construction of the projected image is then achieved by convolving the raw image with the *sinc* kernel at each (x, y) pair of the transformation matrices.

4.5 GCPs Selection and Co-Registration Optimization

4.5.1 GCPs Selection

GCPs are used to define the exterior orientation of an image, and their accuracy therefore affects the accuracy of the orthorectification. A common method consists in measuring in the field the ground coordinates of features clearly identifiable on the image to be orthorectified. This method is costly and might not be applicable easily depending on the area accessibility. The need for GCPs can be alleviated if an on-board kinematic GPS (KGPS) and inertial navigation unit (INU) are used to estimate directly the position and angular orientation of

the camera at exposure time [68]. The use of KGPS and INU have been common practice for the last couple of years. However, for more generality and to include older (pre-KGPS/INU) photographs, our approach assumes that the IO is not constrained from these techniques and that no field measurements of GCPs are available.

The objective of the GCPs' selection on the master image is to estimate an EO to obtain a well georeferenced master with minimum topographic distortions. This requires georeferencing the image to the DEM as precisely as possible. Based on feature recognition, and using external data such as a high-resolution map, or an already georeferenced image (SPOT, aerial image,...), tie points are selected. The document used for georeferencing provides the horizontal coordinates, and the vertical component is retrieved from the DEM. If no external data are available, the shaded DEM can be used to define GCPs. In this case, the DEM provides both horizontal and vertical coordinates, but this method suffers strong inaccuracies due to the usually large difference of resolution between the DEM and the image. However, GCPs optimization, explained in Section 4.5.2 allows for some refinement so that this approach generally yields good results. Furthermore, the use of a shaded DEM to determine GCPs is limited when the study area has smooth relief.

GCPs are selected on the slave image in order to co-register it as precisely as possible to the orthorectified master image. Slave GCPs are thus defined by selecting tie points between the orthorectified master and the raw slave, based on feature recognition. The georeferenced master provides the planimetric ground coordinates, and the altitude value is read from the DEM.

For our application, the measurement of coseismic ground deformation, it might not be possible to define GCPs outside the deformation zone to co-register the slave and master. The footprint of aerial photographs is typically on the order of a few kilometers, while the deforming zone of earthquakes large enough to produce ground ruptures (with magnitudes $M_w > 6.5$) is generally several tens of kilometers wide. As a consequence, selecting tie points between the orthorectified master and the slave may introduce systematic errors, since the slave point coordinates may have changed due to co-seismic deformation. In that case, the information on ground deformation at the scale of the area covered by the GCP is filtered out but the deformation at much smaller wavelength will still be retrieved, i.e., the fault trace, the fault offset, and the near-field deformation. Images with a larger footprint like SPOT (60×60 kms) generally contain areas far enough from the main deformation (i.e.,

away from the fault trace) where GCPs can be selected without introducing any significant errors (compared to the orthorectification geometric accuracy uncertainty).

If external data on ground deformation are available (e.g., field survey, GPS measures, SPOT measurements), it is then possible to correct for these long wavelength artifacts introduced by the GCPs that have sustained some coseismic displacement. In this case, tie points are selected as explained, and ground coordinates retrieved from the orthorectified master are corrected according to these external data. Alternatively, the theoretical displacements at the GCPs can be computed from some a priori earthquake source model, if available. The accuracy of the recovered deformations depends on the external data accuracy.

4.5.2 Co-Registration Optimization

Misregistrations between the orthorectified master and the orthorectified slave are unavoidable and can be reduced iteratively:

1. Start with GCPs derived from tie points selected between the orthorectified master and the slave images.
2. Estimate of Slave's External Orientation based on these GCPs.
3. Orthorectification of the Slave image, and correlation with the orthorectified master image.
4. At each GCP location, the GCP ground coordinates are corrected by the ground offset found between the master and slave orthorectified images.
5. Return to (2) with the updated GCPs coordinates. Iterate until corrections become negligible or stationary.

Practically, to reduce computation time, only patches centered around each GCP are orthorectified and correlated.

After optimization, the slave's GCPs are updated to provide a slave EO that will lead to well co-registered master and slave images at GCPs location. The quality of the co-registration is then generally sub-pixel. Moreover, this approach suppresses the need for a meticulous and time-consuming precise tie points selection. A manual, coarse selection is sufficient as the optimization adjusts their coordinates. Nevertheless, tie points must

be selected in areas where correlation has a good chance to succeed (good local texture), and where no obvious temporal change may bias the correlation (e.g., strong shadow, man-made changes). Residual mis-registration comes from all the artifacts, e.g., DEM error, uncorrected acquisition distortions, not accounted for during orthorectification.

GCPs optimization can also be applied to the master if its GCPs were to be determined from an already orthorectified image (e.g., a SPOT image or an aerial photograph). The shaded DEM can be used too, but is more subject to decorrelation due to its synthetic nature, and correlation is generally possible only in areas with rough topography.

It should be noted that the procedure assumes that the topography has not changed, so that the slave and master images can be orthorectified using the same DEM. This is only an approximation. Theoretically, one should rather use a pre- and post-earthquake DEM to orthorectify the pre- and post-earthquake images, respectively, to account for the change in topography. Given the uncertainties on the DEM values and georeferencing, which are generally large compared to the aerial photography resolution, it is better to use a single DEM: the orthorectification errors due to the DEM errors might be presumed to affect similarly the orthorectification of the master and slave images. We will see later that this approximation is a source of systematic errors that can be corrected.

4.6 Correlation

To measure precisely the relative offset between two images, several methods have been proposed in the literature. The one used in this study is based on phase correlation and described in [8]. For our application, the main requirements are that the correlation method is robust against noise, allows measurements with sub-pixel accuracy, and applies to relatively small correlation windows (typically 32×32 pixels).

The correlation is performed in two steps. The first step determines, at a multi-pixel scale, the shift between images from their correlation matrix. The second step refines the measurements at a sub-pixel scale by estimating the slope difference of the images' Fourier transform [8]. To reduce windowing artifacts in the Fourier transforms, patches are weighted with a Hanning window. Also, correlation is improved by applying a mask that filters out high frequencies.

Correlation is processed using sliding windows that scan the images (pre and post earth-

Table 4.1: Data references. Scans were obtained from the USGS and from a microdensitometer (MD) nominally designed for astronomy. CIR: Color Infra-Red.

Study Case	Date	NAPP Code	Film Type	Scan Origin	Res. (μm)
Landers	07/25/1989	1790-161	CIR	USGS	14, 21
				MD	10
	10/03/1995	6825-253	B/W	USGS	7, 14, 21
				MD	10
	06/01/2002	12498-144	CIR	USGS	14, 21
Hector Mine	07/25/1989	1790-210	CIR	USGS	21
	06/01/2002	12488-50	CIR	USGS	21

quake images in a seismotectonics context). Each correlation results in a measure of the offset in column direction, row direction, and a signal-to-noise ratio (SNR, ranging from 0 to 1 and assessing the measure quality). In case of a UTM projection, the measured offsets, in column and row, correspond directly to horizontal displacements along the East-West and North-South directions.

4.7 Application Case

In [65], the Kickapoo step over of the 1992 Landers, California, earthquake was studied successfully using USGS National Aerial Photography Program (NAPP) photos [69]. This program acquires images of the continental United States in a 5–7 year cycle. The aircraft altitude is around 20,000 feet (6100 m) and films are 9×9 inches, covering an area of slightly less than 10×10 km. The ground resolution is announced at 1 m while the film nominal resolution is about $10 \mu\text{m}$ corresponding to around 0.4 m on the ground. Michel and Avouac [65] used films scanned at $10 \mu\text{m}$ with a microdensitometer originally designed for astronomy with a theoretical positional accuracy of $0.6 \mu\text{m}$ and a root mean square error (rmse) of $0.2 \mu\text{m}$. However, errors of up to $1 \mu\text{m}$ in repetitiveness were observed, leading to ground errors of up to 4 cm. In practice, access to a microdensitometer is not always possible. To validate the methodology with more easily available data, we have studied the same case example using films scanned at $21 \mu\text{m}$ as delivered by the USGS (Table 4.1).

Regarding the DEM, we used the freely available SRTM DEM, with a ground resolution of 1 arc-second (~ 30 m). It has an absolute height accuracy of 16 m and a relative height

accuracy of 10 m. The absolute horizontal accuracy is 20 m and the relative horizontal accuracy is 15 m. These accuracies are quoted at 90% level [54]. The IO of the 1989 and 1995 images are established with the help of the camera calibration reports provided by the USGS. The 1995 image (post-earthquake) is co-registered first to the topography as the STRM mission was carried out in 2002 (post-earthquake). A shaded image of the DEM is generated (Fig. 4.2) with illumination parameters estimated from the 1995 image shadow pattern. Four GCPs are selected between the image and the shaded DEM. Planimetric and vertical coordinates are both obtained from the georeferenced DEM. Using patches of 250×250 pixels, GCPs are optimized according to 4.5.2. The average residual misregistration is evaluated to 2.4 m while the standard deviation residual is estimated to 18 m. This latter uncertainty is slightly higher than the 15 m relative horizontal accuracy of the SRTM DEM. More GCPs would have properly constrained the co-registration, but the limited topography in the image did not allow it. The 1995 EO is determined using the optimized GCPs and the IO. The image is then orthorectified and resampled on a 1 m resolution grid (UTM North Zone 11).

Five GCPs, quite distant from each other, are taken on one side of the fault between the orthorectified 1995 image and the 1989 image. Planimetric coordinates are obtained from the georeferenced 1995 orthorectified image, and altitude is read from the DEM. GCPs optimization is carried out with 256×256 pixel patches. After three iterations the optimization became stationary. The average residual misregistration is evaluated to 1 mm while the standard deviation residual is estimated to 35 cm. The 1989 image is orthorectified and resampled on the same grid.

Images are then correlated using a 64×64 pixel sliding window (64×64 m on the ground), with a 16 pixel step. The result of the correlation process is presented in Fig. 4.3, 4.5, and 4.6. The fault ruptures appear clearly as discontinuities in the displacement field. Horizontal fault slip vectors can then be easily measured from profiles run perpendicular to the fault trace (Fig. 4.4). As also shown in [65], the ruptures map and the fault slip vectors measured are in excellent agreement with the field investigation in [70]. To illustrate the potential of the technique we point to a secondary fault, mapped but not measured during the field investigations, which is both detected and measured from the aerial photographs (Fig. 4.3). The horizontal slip is estimated around 20 cm (one-fifth of the images' resolution), validating the sub-pixel change detection capability of the technique. In some areas,

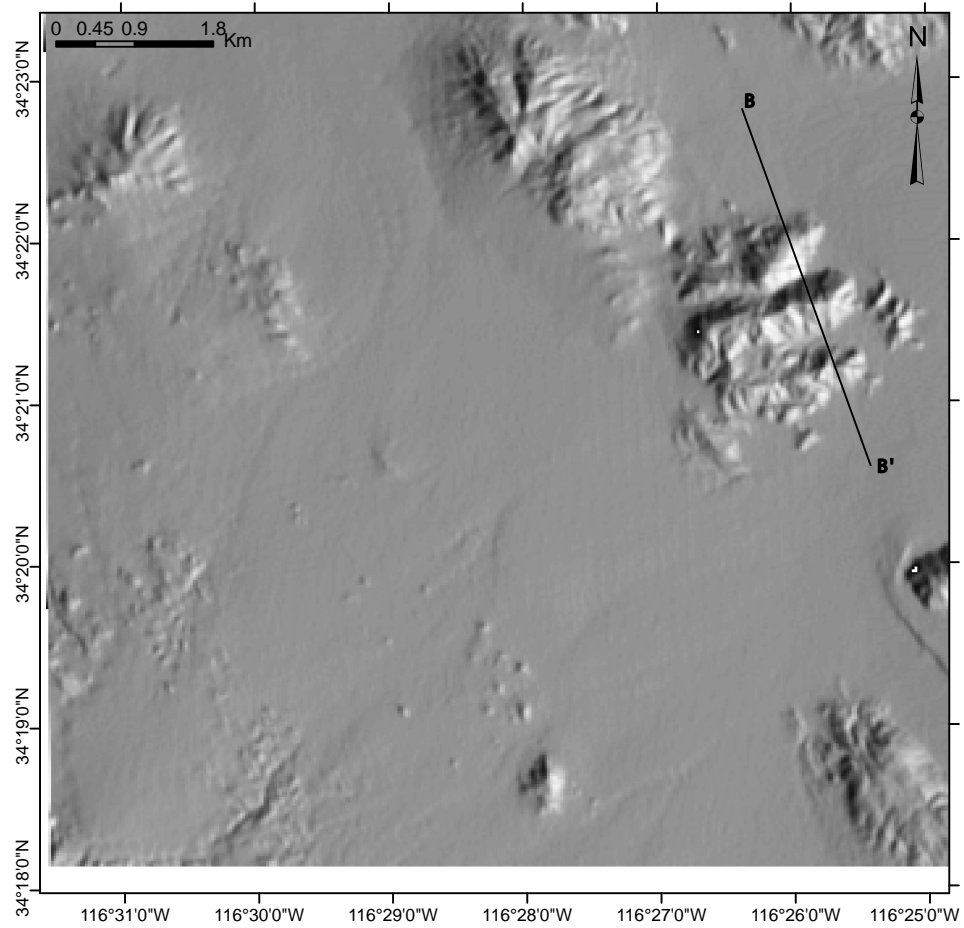


Figure 4.2: Shaded DEM of the study area. Profile BB' locates the profile on Fig. 4.5, and 4.10, and reported on Fig. 4.11.

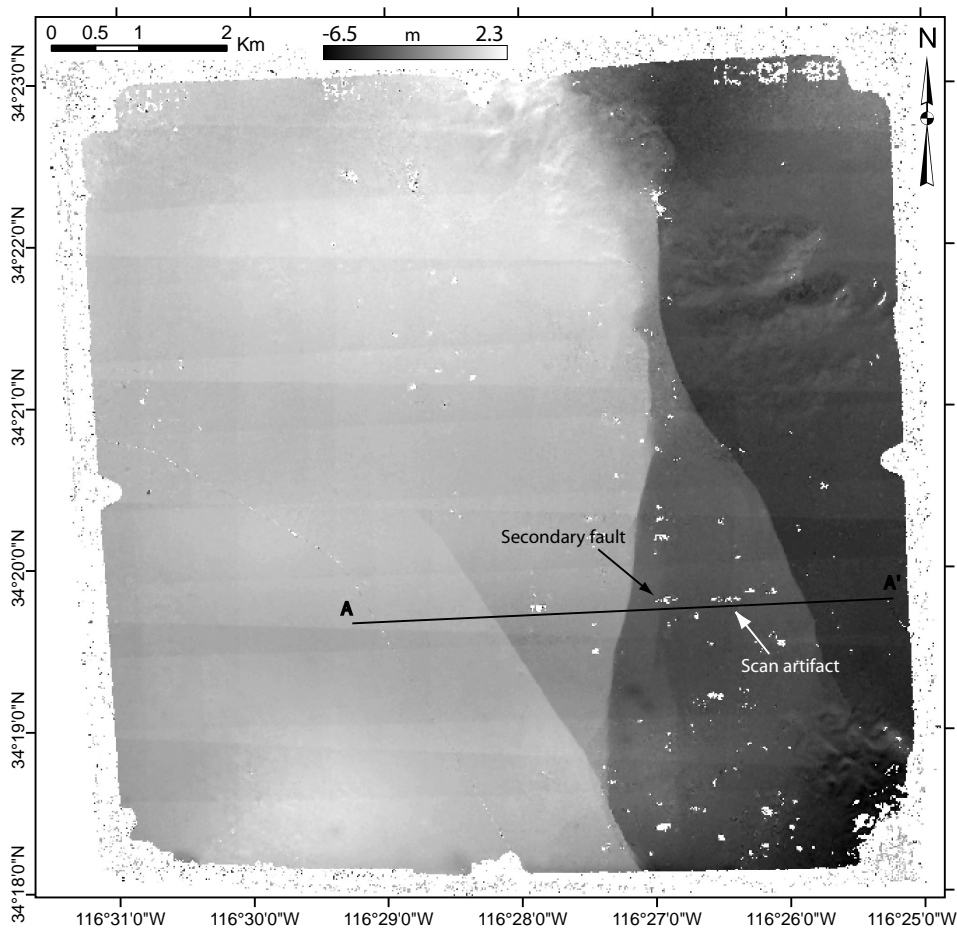


Figure 4.3: North/South component of the Landers 1989/1995 correlation map. Images are orthorectified on a 1 m grid and correlated using a 64×64 pixel window with a 16 pixel step. Positive displacement is toward the North. The fault profile clearly shows up, with secondary fault estimated at 20 cm. Film distortion and scan artifacts, with an amplitude of up 40 cm, are visible. Profile AA' is reported on Fig. 4.4.

correlation is lost leading to very small SNR or outliers. Only 0.3% of the total number of measurements fall in this category. Inspection of the decorrelation areas show that they result from man made changes (new or modified buildings), or coincide with area which are nearly translation invariant at the correlation window scale (sandy areas and straight isolated roads).

To assess the potential bias and error of the measurements, an image of 2002 is co-registered to the 1995 orthorectified image with 13 GCPs. The GCPs optimization, carried out with 256×256 pixels patches, converged after 4 iterations. The average residual misregistration is evaluated to 2 mm while the standard deviation residual is estimated to 30 cm.

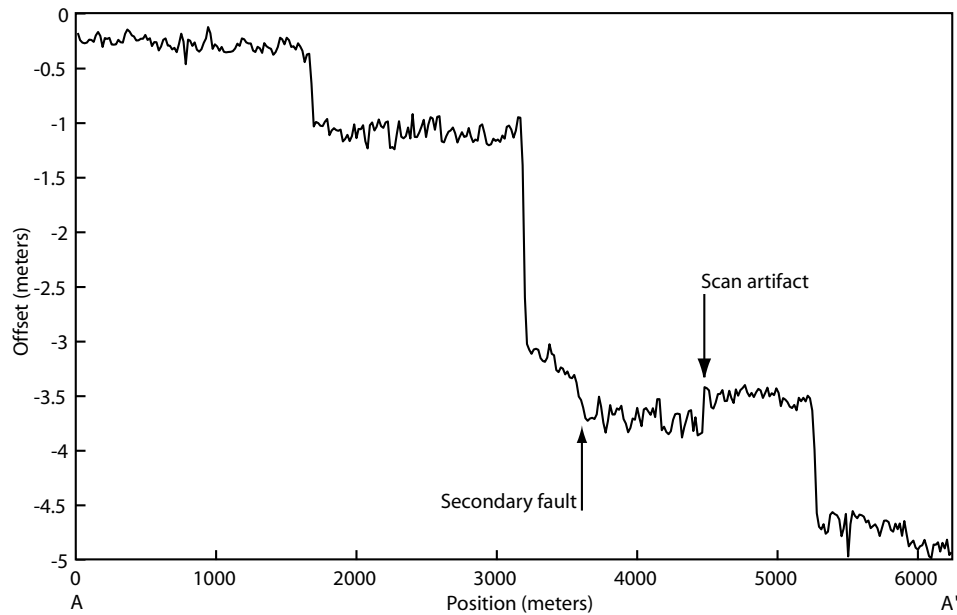


Figure 4.4: Profile from Fig. 4.3. Secondary fault with offset amplitude as low as 20 cm is detected and its location is indicated by a black arrow on Fig. 4.3. At around the same amplitude a scan artifact is also detected indicated by a white arrow on Fig. 4.3. The standard deviation of the measurements is 7 cm.

Results of the correlation are presented in Fig. 4.7 and 4.8. No significant ground deformation is expected given that the only large earthquake in the area over that period of time is the 1999, Mw 7.1, Hector Mine, California, earthquake which occurred about 30 km away from the study area. Locally, the measurement spread is Gaussian with a standard deviation of 7 cm. However, geometric artifacts mainly due to scan artifacts and film distortion cause the global measurement histogram to be not Gaussian with a spatially dependent distribution. The histogram is however centered at around zero, with a standard deviation of 25 cm, and a maximum amplitude of 1 m.

As seen in the East/West displacement field (Fig. 4.7), deformation is everywhere negligible except along the 1992 fault trace event where some small amount of displacement is detected. This deformation corresponds to right-lateral slip of about 10–15 cm. The possibility of a parallax effect due to a vertical uplift not accounted for in the DEM is discarded. Indeed, from Eq. 4.2, a 4 m up/down-lift would be necessary to cause a 15 cm horizontal parallax displacement. The displacement observed on the E-W component might be real and could correspond to aseismic slip triggered by the 1999, Hector Mine, earthquake, as

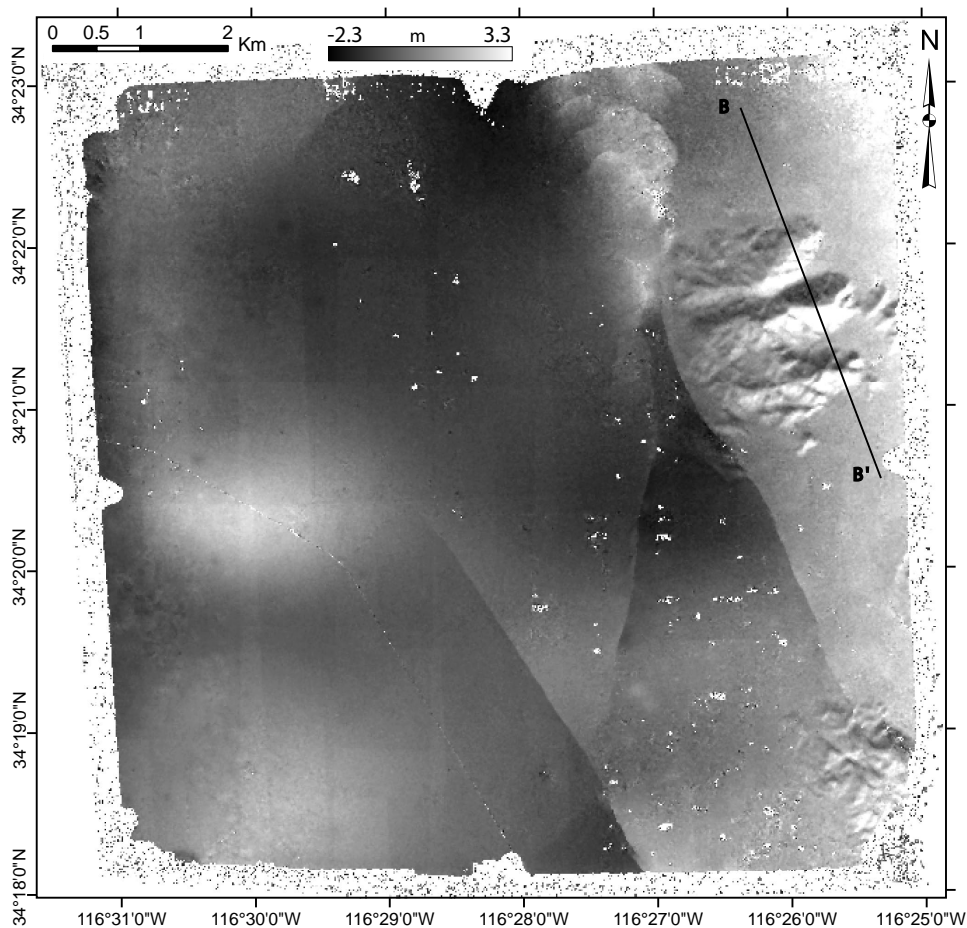


Figure 4.5: East/West component of the Landers 1989/1995 correlation map. Images are orthorectified on a 1 m grid and correlated using a 64×64 pixel window with a 16 pixel step. Positive displacement is toward the East. Topography and film artifacts are visible on the right and left side of the map respectively. Topography artifact is a parallax effect caused by the use of a single DEM for the 1989 and 1995 images although topography changed during the earthquake. Profile BB' is reported on Fig. 4.11.

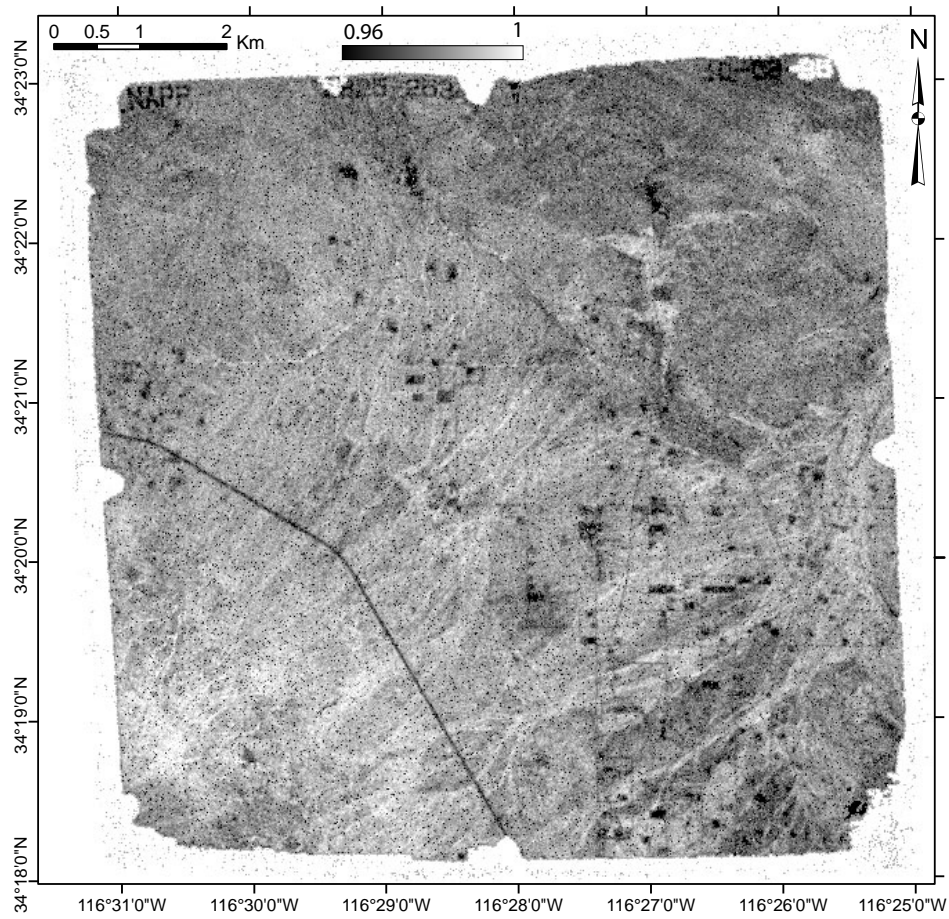


Figure 4.6: SNR component of the Landers 1989/1995 correlation map. A higher SNR indicates a better correlation. Roads are visible and get a low SNR due to the poor correlation algorithm convergence on translation invariant features [8]. Other areas of decorrelation include man made changes. The total amount of decorrelation accounts for 0.3% of the measurements.

reported on some other faults in [60] and discussed in [71]. However, this deformation does not show up in the North/South displacement field, possibly because it is obscured by the particularly strong scan artifacts on this component (Fig. 4.8).

4.8 DEM Artifacts

Topographic artifacts are seen on both 1989/1995 and 1995/2002 displacement maps, as suggested by the obvious correlation of the measured offsets with the shaded topography (Fig. 4.2, Fig. 4.5, and Fig. 4.7). The artifacts are most obvious on the 1989/1995 displacement field (Fig. 4.5) in the area of profile BB' where the relief is the roughest. A simple interpretation of this correlation is that the change of the topography due to co-seismic deformation cannot be ignored.

Assuming a perfect acquisition system and ignoring the film distortions, scan errors, and correlation bias, the effect of the change of the topography (Fig. 4.9) can be accounted for by writing:

$$\begin{cases} DX = \underbrace{(h - h_1) \times x_1/f_1 + u}_{a_x} + \underbrace{\Delta DEM(u, v) \times x_2/f_2}_{c_x} - \underbrace{(h - h_1 + dh) \times x_2/f_2}_{b_x} \\ DY = (h - h_1) \times y_1/f_1 + v + \Delta DEM(u, v) \times y_2/f_2 - (h - h_1 + dh) \times y_2/f_2 \end{cases} \quad (4.2)$$

where DX and u refer respectively to the real and measured displacements in the column direction. Y and v apply to the line direction. Subscripts 1 and 2 refer to the master and slave images. h , h_1 , H_1 , and dh represent respectively, the real altitude of a ground point, the DEM altitude at the ground point, the optical center altitude, and the vertical displacement of the ground point caused by the earthquake. f and x are the focal length and the camera coordinates of the ground point image. Rearranging Eq. 4.2 and using regular trigonometric equations we have:

$$\begin{cases} DX = (h - h_1) \left[\underbrace{\frac{x_2}{f_2} \left(\frac{H_2 - h - dh}{H_1 - h} - 1 \right)}_i - \frac{B_x + DX}{H_1 - h} \right] + \underbrace{\frac{x_2}{f_2} \Delta DEM(u, v)}_{ii} - \underbrace{\frac{x_2}{f_2} dh + u}_{iii} \\ DY = (h - h_1) \left[\frac{y_2}{f_2} \left(\frac{H_2 - h - dh}{H_1 - h} - 1 \right) - \frac{B_y + DY}{H_1 - h} \right] + \frac{y_2}{f_2} \Delta DEM(u, v) - \frac{y_2}{f_2} dh + v \end{cases} \quad (4.3)$$

where i represents the displacement induced by the DEM elevation error, taking into account

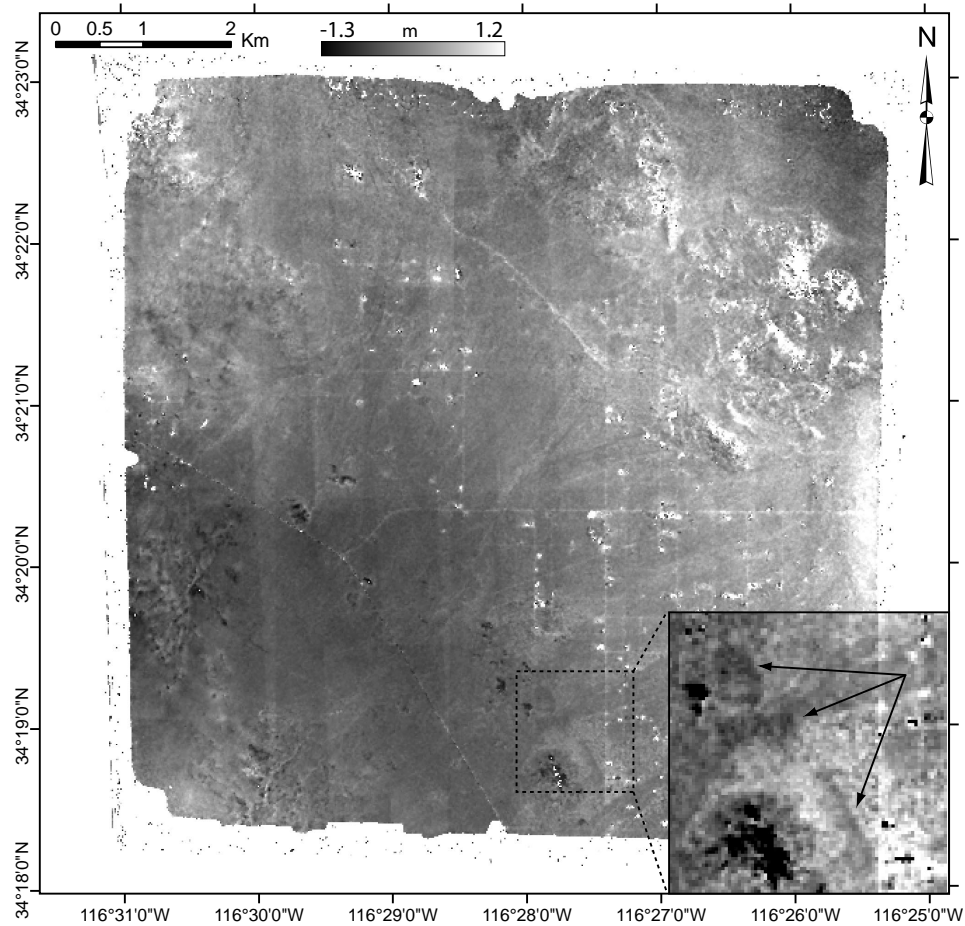


Figure 4.7: East/West component of the Landers 1995/2002 correlation map. Images are orthorectified on a 1 m grid and correlated using a 64×64 pixel window with a 16 pixel step. Inspection of decorrelation areas on topography revealed that shadowing difference is the cause. Some light scan artifacts are visible in the column directions. Black arrows indicate fault displacements with an amplitude estimated at around 10–15 cm. No clear explanation has been found yet. A parallax effect due to a vertical uplift not accounted for in the DEM seems hardly probable as 4 m of up/down lift would be necessary.

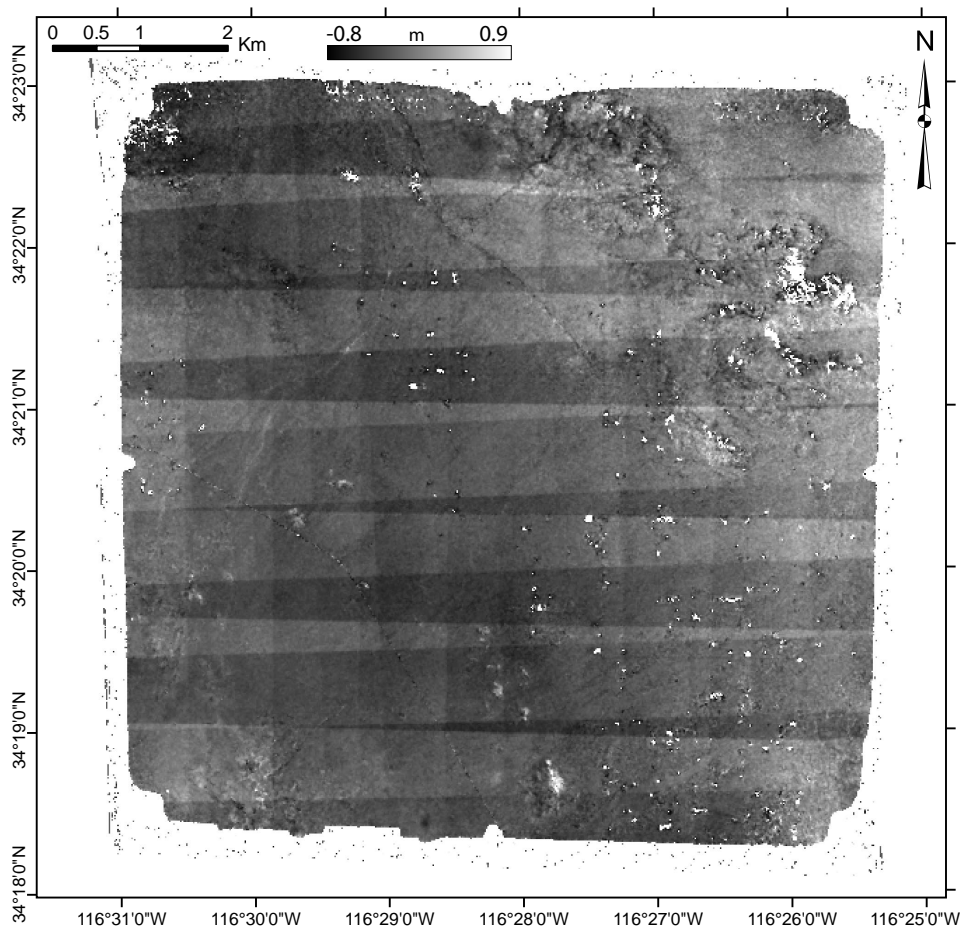


Figure 4.8: North/South component of the Landers 1995/2002 correlation map. Images are orthorectified on a 1 m grid and correlated using a 64×64 pixel window with a 16 pixel step. Strong scan artifacts are visible in the line direction but also in the column direction. They have an amplitude up to 40 cm, which is above the 20 cm fault detected in Fig. 4.3, and can limit the technique depending on their amplitude and location. Notice that the fault displacement detected in Fig. 4.7 does not appear here, although it may be masked by the strong scan artifacts.

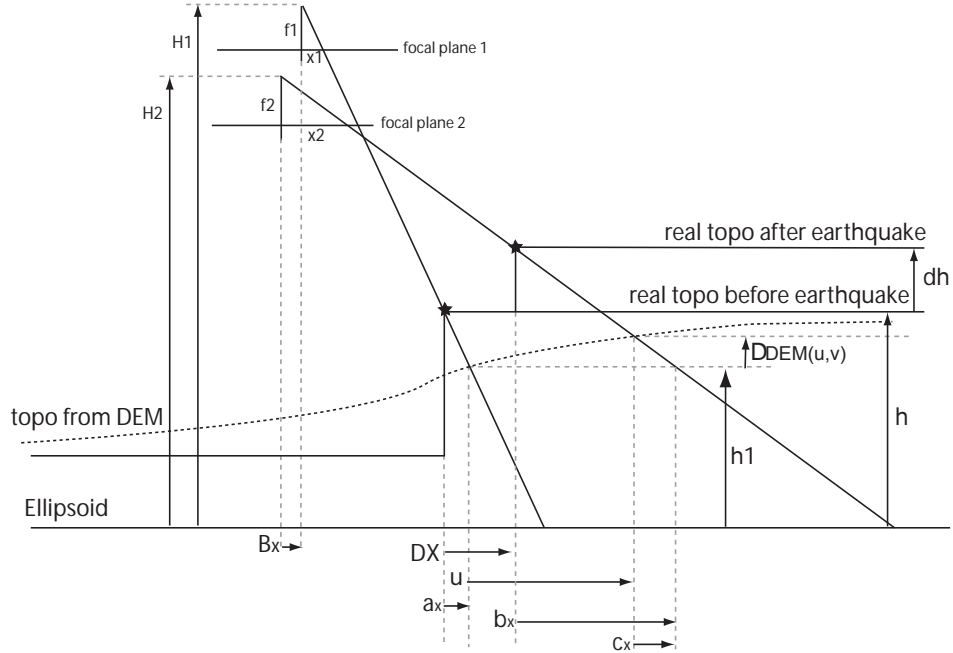


Figure 4.9: Geometry of the orthorectification and correlation measure in case of a unique DEM use (in one dimension). All other possible artifacts are considered null (film distortions, correlator bias, ...). DX and u represent the real and measured horizontal displacement, respectively, in the x direction.

the difference of exposure stations' location. It is the absolute DEM error ($h - h_1$) weighted by the stereoscopic parallax coefficient at the ground point considered. This coefficient is composed of an acquisition altitudes ratio, and the base/height ratio. *ii* represents the term originating from the approximation of the topography by the DEM. The corresponding artifacts are thus correlated to the topographic gradients and can then be easily identified. *iii* represents the horizontal offset resulting from a vertical displacement not accounted for when using a single DEM.

Field investigations have shown that vertical displacement in the Kickapoo area was small everywhere compared to the horizontal displacements [70]. *iii* can therefore be neglected. Moreover, from the EOs of the 1989 and 1995 images, optical centers are close enough that stereoscopic parallax effects are also negligible. Considering that the coseismic displacements are of at most a few meters, we then have $(B_x + DX) \ll H_1$. In addition, we have $H_1 \approx H_2$, so that *i* can be neglected. *i* is indeed estimated to at most 6 cm, assuming a DEM error of 20 m, in the upper range of estimated errors on the SRTM DEM. The real displacements given by Eq. 4.2 are then estimated by correcting the displacements

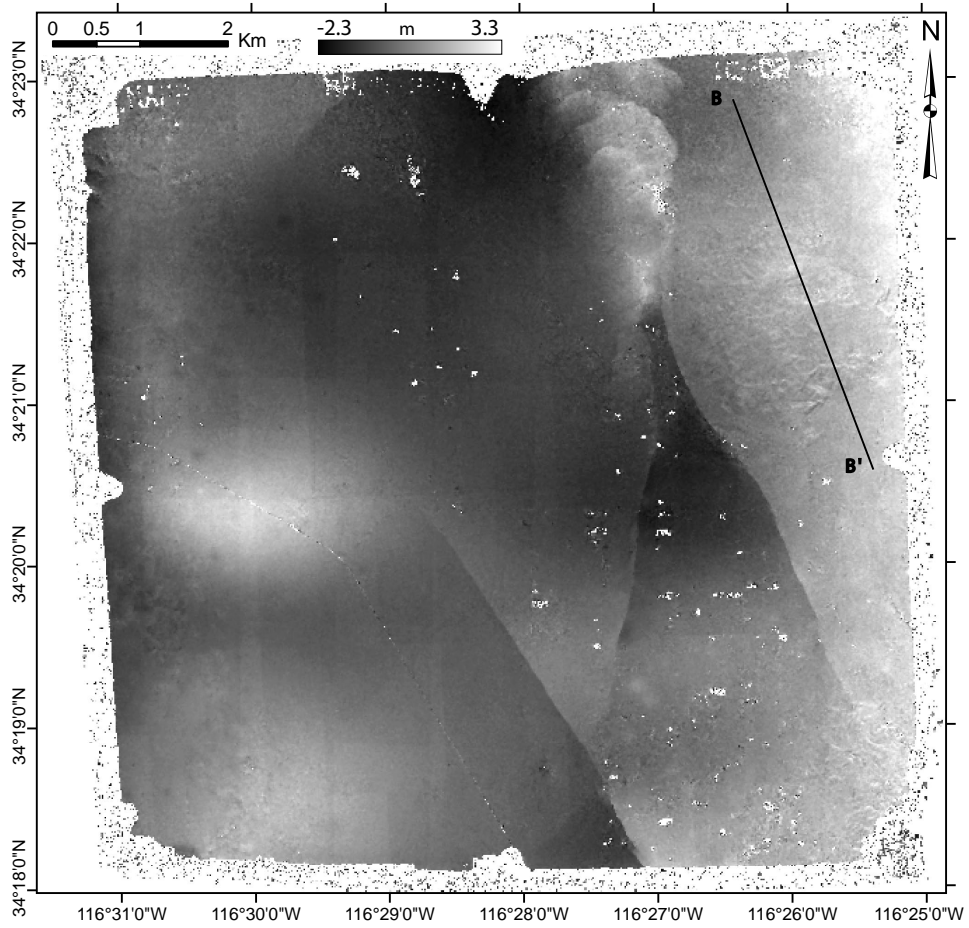


Figure 4.10: East/West component of the Landers 1989/1995 correlation map corrected for artifacts due to a single DEM use, according to Eq. 4.2. Profile BB' is reported on Fig. 4.11.

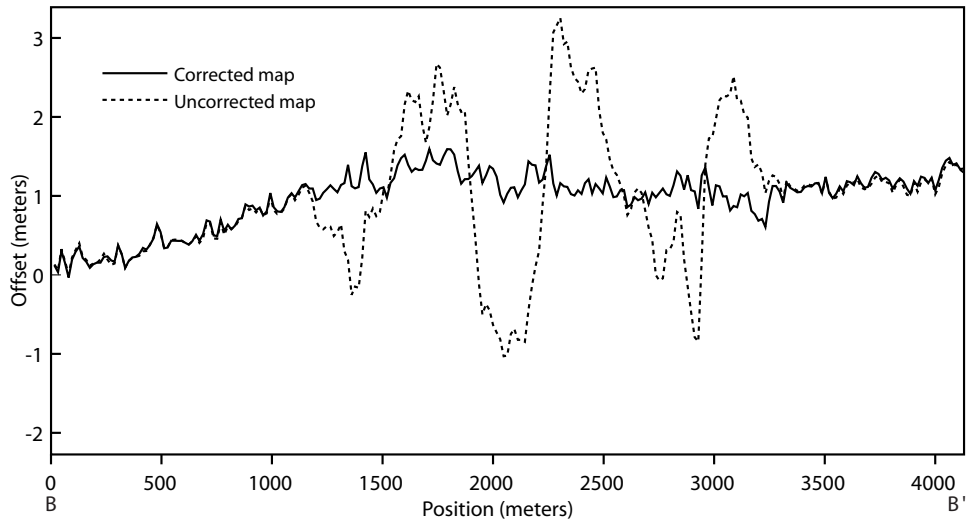


Figure 4.11: Profile BB' of the uncorrected (Fig. 4.5) and corrected (Fig. 4.10) East/West correlation map. Notice that artifacts are correlated to the topography (Fig. 4.2).

determined from the correlation map according to:

$$\begin{cases} u_{cor} = \Delta DEM(u, v) \times x_2 / f_2 + u \\ v_{cor} = \Delta DEM(u, v) \times y_2 / f_2 + v. \end{cases} \quad (4.4)$$

Using the apparent displacements estimated from the correlation map (u, v) , the DEM, and the slave image information, the corrected displacement field (u_{cor}, v_{cor}) can thus be retrieved. This correction is very effective in our case study: the topographic artifacts are no longer visible in Fig. 4.10, and Fig. 4.11. This simple procedure allows us to correct the correlation map from the artifacts induced by the use of a single DEM. Note that in the case of a significant vertical displacements the term *iii* in Eq. 4.2 cannot be neglected. In that case the measured offsets (u, v) are a linear combination of the horizontal and vertical displacements (DX, DY, dh) . All three components of displacements can be determined only if a second pair of images with a different viewing angle is available.

4.9 Scan

4.9.1 Scan Artifacts

In addition to topographic artifacts, scanning artifacts are visible in both 1989/1995 and 1995/2002 correlation maps (Fig. 4.5, 4.3, 4.7, 4.8) in North/South and East/West directions. The amplitude of the artifacts in the North/South (line) direction is higher and accounts for up to 40 cm on the ground.

To assess USGS digitized images quality, additional scans at different resolutions of the 1989 and 1995 films were obtained from the USGS (Table 4.1). Scanning was operated with a Zeiss Precision Scanner using a PHODIS Photogrammetric Image Processing System or a Leica Geosystems DSW600 Digital Scanning Workstation. Both instruments are attributed a positional accuracy rmse of $1.5\ \mu\text{m}$ (personal communication, USGS). We also used the microdensitometer (MD) scans of [65] of both 1989 and 1995 films.

The practical rmse ($1\ \mu\text{m}$) of the MD being inferior to the Leica and Zeiss scanners, the MD scans are considered as references. 1989 and 1995 USGS images were co-registered, wrapped, and correlated to the 1989 and 1995 MD images respectively. Apart from some long wavelength artifacts due to imprecision in co-registration and film distortions between films scanned by the USGS and the ones scanned with the MD, scan artifact patterns are easily recognizable (Fig. 4.12, 4.13).

The amplitude of the artifacts of the different scans are presented in Table 4.2. Artifacts in the offsets measured along the line and column directions are clearly visible, with larger amplitude found in the line direction. Scans at 7 and 14 μm provided different patterns but no better stability. The artifacts are smaller on the B/W scans than on the color-infrared (CIR) scans. Surprisingly, the 21 μm B/W scans are the less biased by the scanning artifacts.

The observed scan artifacts, which are much stronger than what the nominal characteristic of the scanners would suggest, may put a severe limitation on the technique depending on their amplitude and orientation relative to the signal to measure. However, the scan artifacts produce patterns that are easily identified and relevant information (map of surface ripples and surface fault slip) might be retrieved correctly from the correlation map using adequate care (Fig. 4.4).

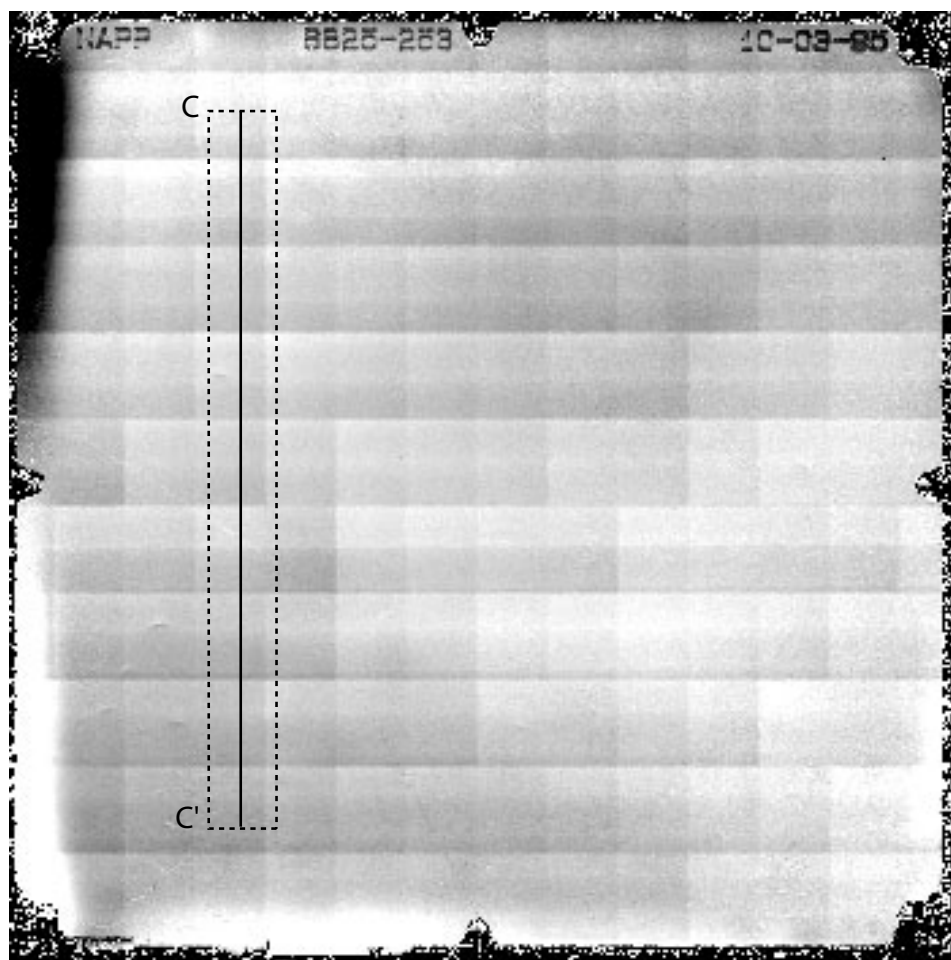


Figure 4.12: Line component of the MD/USGS scan correlation map. Scans of the 1995 photograph are obtained at $21\ \mu\text{m}$ from the USGS and at $10\ \mu\text{m}$ from a MD. MD scan is co-registered and wrapped onto the USGS scan using a sinc kernel for resampling. Correlation is processed using a 64×64 pixel window with a 32 pixel step. Scan artifacts are also visible on the column component but with smaller amplitude. Profile CC' is reported on Fig. 4.13. Other long wavelength deformations are due to film distortions and mis-registration.

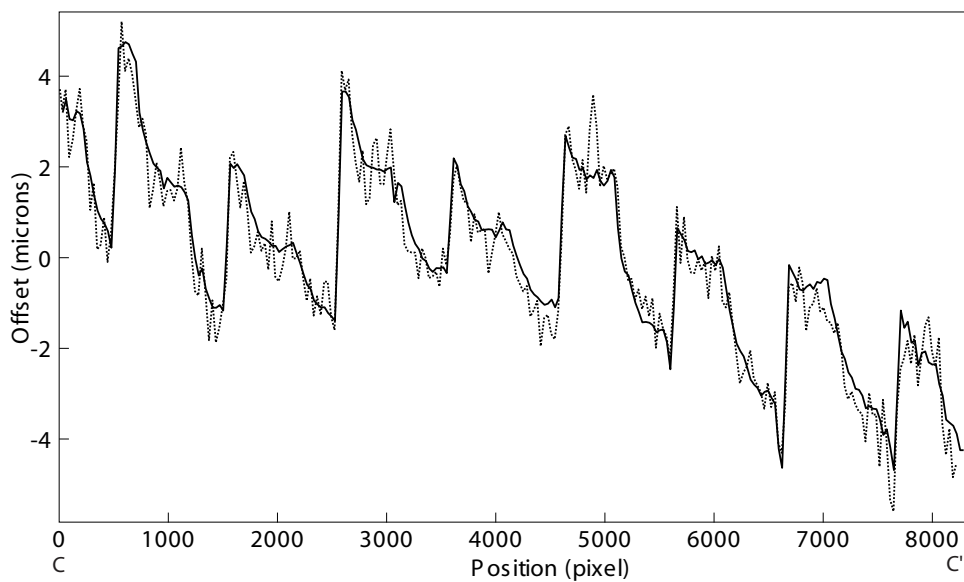


Figure 4.13: Profile CC' (Fig. 4.12) showing scan artifacts with amplitude up to $5\ \mu\text{m}$ (around 20 cm on ground) above the scanner specifications announced at $1.5\ \mu\text{m}$ rmse.

Table 4.2: USGS scans artifacts amplitude measured in row and column direction. Scans from the USGS are wrapped onto scan from an MD and correlated using a 64×64 pixels sliding window.

Year	Master Scan MD (μm)	Slave Scan USGS (μm)	Max Artifacts Row (μm)	Max Artifacts Column (μm)
1989	10	14	20	10
	10	21	8	4
1995	10	7	6	4
	10	14	6	4
	10	21	5	3

4.9.2 Scan Resolution

The photographs of the USGS NAPP program have a ground resolution estimated to be around 1 m. Scans at 10, 14, and 21 μm correspond to an average ground resolution of 40, 56, and 84 cm respectively. Comparison of coseismic ground deformation determined from scans at 10, 14, and 21 μm shows that there is no gain when the scanning resolution is improved, actually the quality of the measurement even degrades due to the stronger scan artifacts as discussed above.

For this particular study, a scan resolution close to the nominal image resolution is sufficient.

4.10 GCPs

4.10.1 GCPs—Absolute Accuracy

To assess the sensitivity of the technique to the choice and accuracy of GCPs, the 1995 aerial photograph was orthorectified with 4 different GCP sets:

- case 1—10 GCPs obtained from a field survey using a differential Real Time Kinematics (RTK) GPS, with an accuracy of few centimeters.
- case 2—10 GCPs optimized from a 10-m-ground-resolution orthorectified SPOT image (georeferenced with the SRTM DEM).
- case 3—4 GCPs optimized from the shaded SRTM DEM.
- case 4—4 GCPs carefully selected manually but not optimized from the shaded SRTM DEM. This case allows estimation of the performance of the orthorectification in the situation where a low-relief, hence a poorly contrasted, shaded DEM limits the correlation gain during the optimization.

Orthorectified images from case 2, 3, and 4 are correlated with the image from case 1, considered as the reference. Offsets found are characterized by long wavelength distortion with some high-frequency distortion correlated to the topography. Maximal misregistrations are 10 m, 18 m, and 25 m for case 1/2, case 1/3, and case 1/4, respectively. Case 2 and case 3 are within the DEM absolute horizontal accuracy (20 m), whereas case 4

is outside. Although the SPOT image was also coregistered with the DEM, case 2 absolute georeferencing is better than case 3. This is explained by the larger area and larger number of GCPs (20) used to coregister the SPOT image to the shaded DEM.

4.10.2 GCPs—Tectonic Signal Distortions

To assess the consequence of misregistrations on the measured displacement map, the 1989 slave image was co-registered and correlated with the 4 orthorectified images described in the previous section. The results were found to be similar regarding the mapping of the surface breaks and the determination of fault slip. However, the various cases yield deformation maps which differ at long wavelengths. In fact the major source of distortion at long wavelength is due to the assumption that the tie points between the master and slave images have the same geographic coordinates in the slave and master image, independently on the error on these coordinates. Tie points are indeed selected between the slave and the orthorectified master to co-register the two images. These tie points, converted to GCPs, are then optimized to refine the co-registration at a sub-pixel scale. The possible ground displacements at the locations of the GCPs location is then wrongly compensated. We illustrate this from NAPP aerial images of the 1999, Mw 7.1, Hector Mine, California, earthquake (Table 4.1). Pre- and post-earthquake images were processed using the methodology described above. Three slave GCPs were selected and optimized. The North/South displacement map is presented in Fig. 4.14. The horizontal displacement field is overlaid as vectors on the figure, together with the GCPs. The fault rupture is clearly visible. Its geometry and horizontal slip are in accordance with the field measurements [58]. As expected, displacement falls to zero at GCP locations. The co-registration compensates the real ground displacements at the GCPs and introduced long-wavelength distortion in the displacement map. Forcing the co-registration at GCPs locations, without accounting for the ground displacement at their location, thus introduces some long wavelength distortion of the displacement field, biasing measurements of ground displacement in the far-field.

This bias can be avoided if estimates of the ground displacements at the GCPs location are known and taken into account during the optimization. To demonstrate this point we used the displacement field determined at a larger scale from the correlation of SPOT images [8]. The SPOT images were co-registered using GCPs far away from the fault zone where coseismic displacement could be neglected. A subset of the North/South component

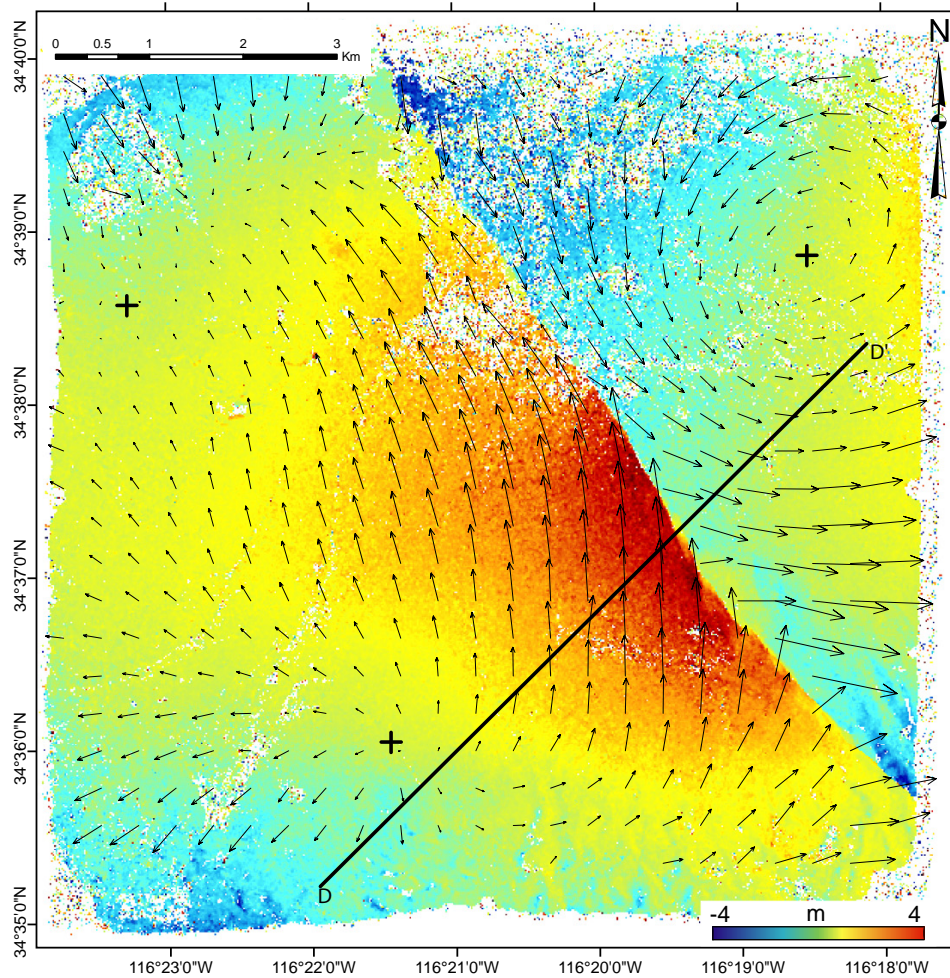


Figure 4.14: North/South component of the 1989/2002 correlation map of Hector Mine earthquake. Images are orthorectified on a 1 m grid and correlated using a 64×64 pixel window with a 16 pixel step. Three GCPs, located by the black crosses, are optimized to co-register the master and the slave without accounting for seismic ground displacement at their ground location. Overprinted arrow field is generated from the North/South and East/West correlation map, and represents the ground displacement field. Long wavelength distortions (vortex) are introduced to satisfy the master and slave co-registration. Profile DD' is reported on Fig. 4.15 and Fig. 4.17.

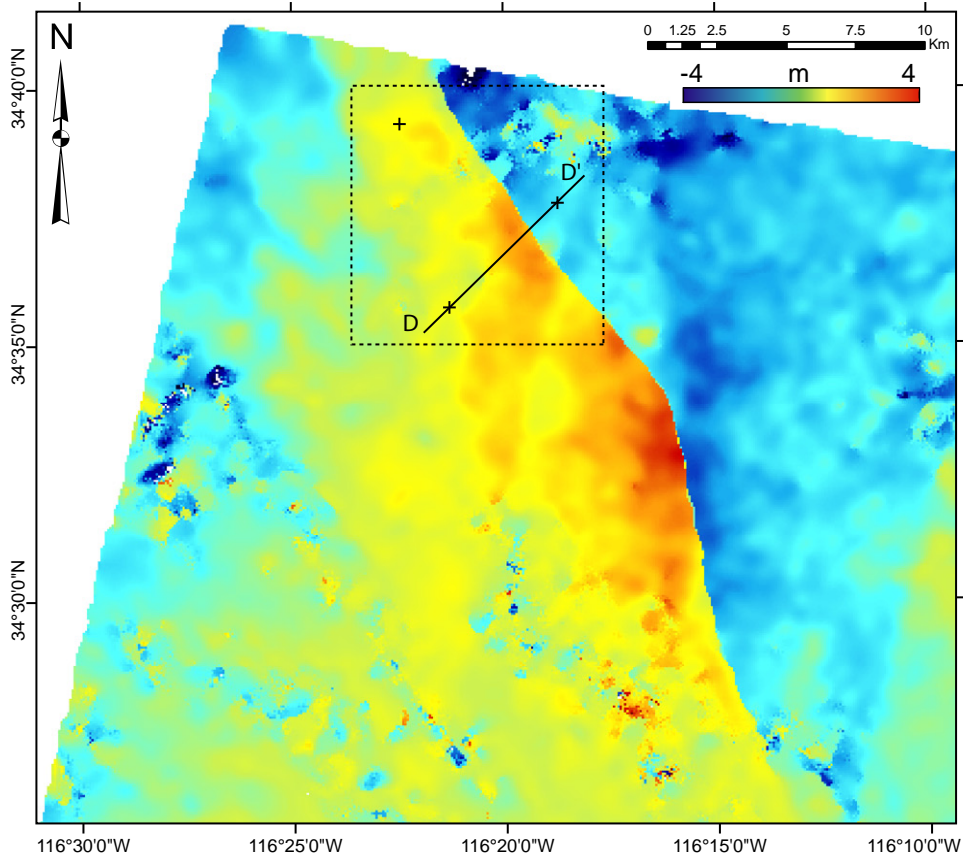


Figure 4.15: North/South component of the denoised SPOT correlation map of Hector Mine earthquake. Three GCPs located away enough from the fault to assume a null ground displacement are optimized to co-register the master and the slave. Images are orthorectified on a 10 m resolution grid and correlated using a 32×32 pixel window with a 8 pixel step. Positive displacement is toward the North. The raw correlation map is denoised by a technique preserving fault offset (personal communication, Leprince). The dotted square represents the aerial photograph footprint, and black cross indicates the location of the aerial photograph GCPs. Profile DD' is reported on Fig. 4.17.

of the displacement field measured from the SPOT image is shown in Fig. 4.15. The dashed square represents the aerial images footprint.

The aerial images were then processed taking into account the displacements measured from the SPOT images at the three GCPs used to co-register the slave with the orthorectified master (Fig. 4.15). The slave image is then registered to the tie points, which are assigned geographic coordinates determined from cross-correlation with the orthorectified master image, but shifted by the displacements determined from the SPOT image. The North/South component of the displacement obtained from this procedure is shown in Fig. 4.16. The fault geometry and horizontal slip value are identical to the ones from the

first process. The long wavelength component of the displacement field now matches the SPOT displacement field.

This procedure allows to measure ground displacement using images with different resolutions and different footprints in a common reference frame making mosaicking possible. Nevertheless, far-field ground deformation must be considered carefully, as film distortion, for example, manifests itself in the displacement map by deformation of similar frequency and amplitude see Fig. 4.17).

4.11 Conclusion

This study describes how the procedure originally developed to process optical satellite images, can be adapted to aerial photographs, taking into account the specific characteristics of this type of images. Orthorectification and georeferencing is achieved using the DEM only, without any other external data. The correlation of a master and a slave image taken before and after an earthquake yields offsets which primarily represent horizontal displacements. Some artifacts are introduced due to the use of a single DEM, but can be corrected in post-processing. The absolute georeferencing of the images is limited by the accuracy of the DEM georeferencing, and the slave and master images are co-registered with a sub-pixel accuracy of about $1/3$ of the pixel size. The limitation on the accuracy of the co-registration between master and slave images is due to film distortions, scan artifacts, and the assumption of no relative displacements of the tie points. This latter assumption can be reduced if the displacement at the tie points can be estimated independently (from other measurements or an a priori model of co-seismic ground deformation).

Better performances should be achieved in the future due to the development of digital aerial photography, and due to a better control on the images' geometry thanks to real-time kinematic GPS and Inertial Navigation Unit. In addition the technique is sensitive to temporal decorrelation such as those due to shadowing differences, man-made changes, changes of the vegetation cover, and clouds.

Despite these multiple sources of limitations, our study shows that this technique is extremely powerful to precisely map the fault trace, and to measure surface fault-slip and near-field ground deformation. The technique applies to ruptures with a minimum length of few kilometers and a minimum displacements of a few tens of centimeters. It should

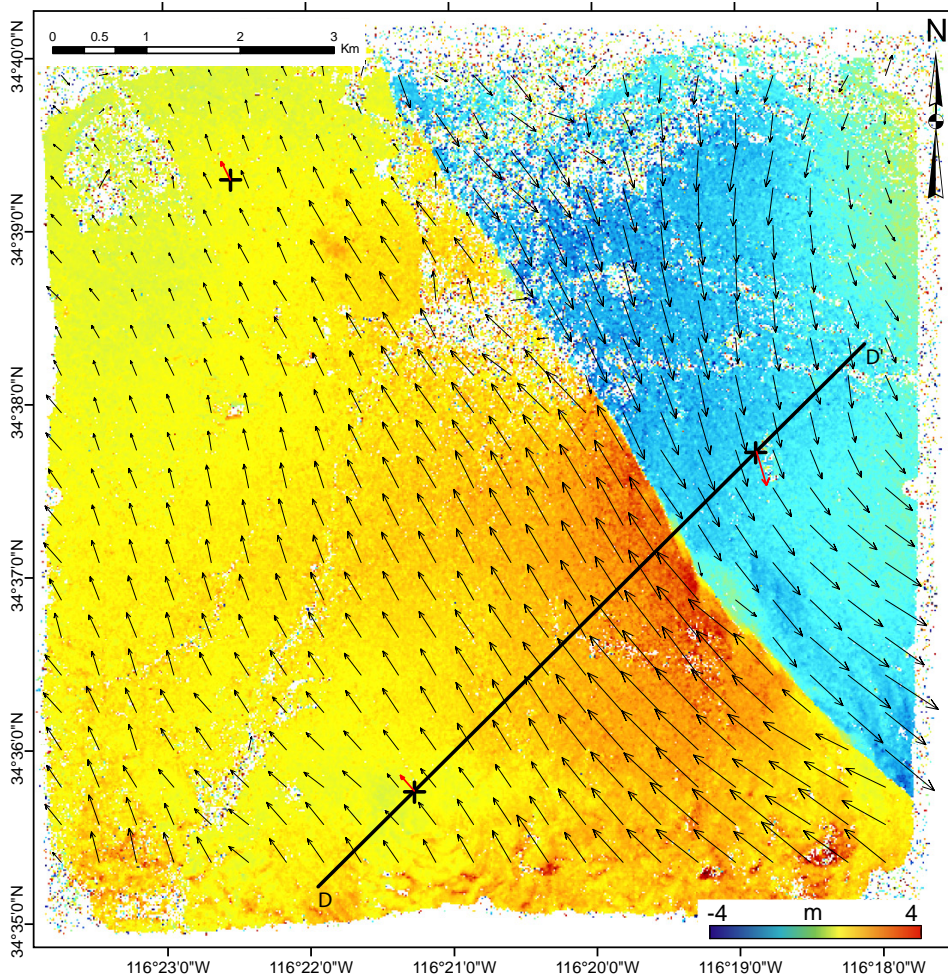


Figure 4.16: North/South component of the 1989/2002 correlation map of Hector Mine earthquake. Images are orthorectified on a 1 m grid and correlated using a 64×64 pixel window with a 16 pixel step. Three GCPs, located by the black crosses, are optimized to co-register the master and the slave while accounting for ground displacement at their ground location (red arrow) from SPOT measures (Fig. 4.15). Major long wavelength distortions present in Fig. 4.14 are removed. Only the long wavelength distortions caused by the SPOT correlation error may remain, along with those introduced by film distortions. Profile DD' is reported on Fig. 4.15 and Fig. 4.17.

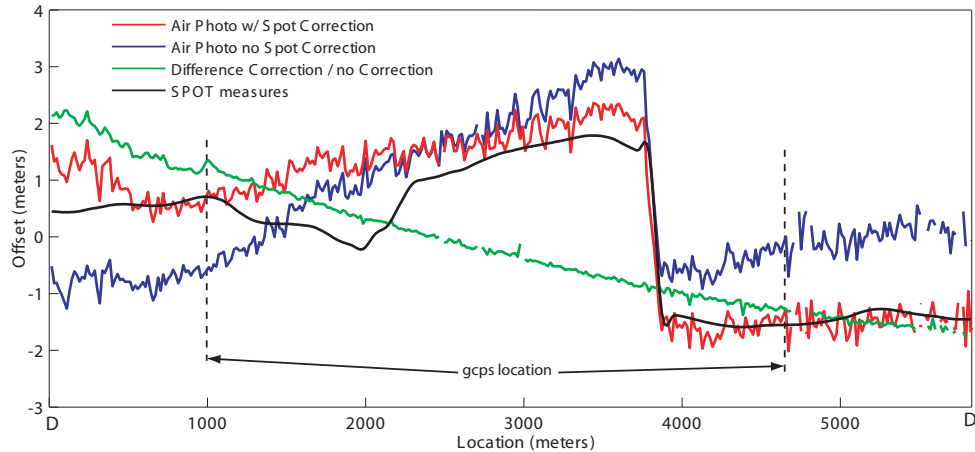


Figure 4.17: Profile from Fig. 4.14, Fig. 4.15, and Fig. 4.16. GCPs correction brings a 2nd order polynomial correction in each North/South and East/West directions. High-frequency signal (slip at the fault) is not affected, however.

thus be applicable to earthquakes breaking the surface with a moment magnitude exceeding about 6.5. This opens the possibility to reassess a number of past earthquakes for which aerial photography archives are available. Aerial photographs are less adapted to measuring ground deformation in the far-field, which will be best measured with optical satellite imagery (e.g., SPOT, ASTER) or interferometric synthetic aperture radar. Aerial photographs and these latter techniques are complementary as they provide unprecedented accuracy, respectively, in the near- and far-field measurements.

The algorithm of the processing chain are implemented in the software package COSI-Corr (ENVI module), complementing the satellite image processing package [8]. The software is available from the Caltech Tectonics Observatory website.

Chapter 5

Co-Registration of Optically Sensed Images and Correlation (COSI-Corr): an Operational Methodology for Ground Deformation Measurements

By Sébastien Leprince¹, François Ayoub², Yann Klinger³, and Jean-Philippe Avouac²

¹ Electrical Engineering Department, California Institute of Technology, Pasadena, California, USA

² Division of Geological and Planetary Sciences, California Institute of Technology, Pasadena, California, USA

³ Institut de Physique du Globe de Paris, 75005 Paris, France

Foreword— This chapter has been published under the reference S. Leprince, F. Ayoub, Y. Klinger, and J.P. Avouac, “Co-Registration of Optically Sensed Images and Correlation (COSI-Corr): an Operational Methodology for Ground Deformation Measurements,” *International Geoscience and Remote Sensing Symposium (IGARSS)*, vol. 6, Barcelona, Spain, July 2007, pp. 2700–2702. In this thesis, it is referred to as reference [72]. S. Leprince and F. Ayoub are responsible for the processing of the ASTER images according to the procedures described in Chapter 3, Appendix D, and that have been applied in Chapter 7. Y. Klinger provided the scans of the aerial images and processed them using

COSI-Corr under the guidance of F. Ayoub and S. Leprince, according to the procedures described in Chapter 4.

Recent methodological progress, Co-Registration of Optically Sensed Images and Correlation, outlined here, makes it possible to measure horizontal ground deformation from optical images on an operational basis, using the COSI-Corr software package. In particular, its sub-pixel capabilities allow for accurate mapping of surface ruptures and measurement of coseismic offsets. We retrieved the fault rupture of the 2005 Mw 7.6 Kashmir earthquake from ASTER images, and we also present a dense mapping of the 1992 Mw 7.3 Landers earthquake of California from the mosaicking of 30 pairs of aerial images.

5.1 Introduction

In addition to seismological records, the knowledge of ruptured fault geometry and coseismic ground deformations are key data to investigate the mechanics of seismic rupture. In principle, this information can be retrieved from sub-pixel correlation of pre- and post-earthquake remotely sensed optical images [5], as illustrated by earlier promising results [1], [10], [11]. However, this technique suffers from numerous limitations, mostly due to uncertainties on the imaging systems and on the platform attitudes. These uncertainties lead to unmodelled distortions and stereoscopic effects that are biasing the ground deformation measurements.

In this paper, we take advantage of a newly available technique that allows for precise correction of most of these limitations, and for accurate estimation of sub-pixel displacement between images [8]. This new technique, Co-Registration of Optically Sensed Images and Correlation (COSI-Corr), has been implemented in a software package and is freely available from the Caltech Tectonics Observatory website¹. Our goal is to show its ability to measure horizontal coseismic ground deformations. In particular, to complement the studies in [8] and [62], we investigate the use of ASTER (Advanced Spaceborne Thermal Emission and Reflection Radiometer) satellite and aerial images.

We first review the key steps that define the COSI-Corr methodology. Secondly, in complement to [9], we study two ASTER images bracketing the 2005, Mw 7.6 Kashmir

¹URL: http://www.tectonics.caltech.edu/slip_history/spot_coseis/

earthquake. Thirdly, in complement to [62] and [65], using 30 pairs of aerial photographs, we measure the horizontal coseismic ground displacement induced by the 1992, Mw 7.3 Landers earthquake of California. Finally, we open the discussion on new applications.

5.2 COSI-Corr Methodology

COSI-Corr proposes a methodology that allows for an automatic and precise orthorectification and co-registration of satellite or aerial images [8]. The procedure does not require external information such as GPS measurements of ground control points (GCPs), and is solely based on the knowledge of the topography and on the ancillary data provided with the observing platform (positions, velocities, attitude variations, and pointing directions for spacecrafts, or calibration reports for aerial photographs.) Sub-pixel change detection is then applied on the set of orthoimages produced.

The precise orthorectification procedure relies on the automatic generation of precise GCPs, which are generated such that the correction they imply on the viewing geometry of the observing platform allows for precise orthorectification and co-registration of the images. To make this process automatic and as bias-free as possible, the GCPs generation and the viewing geometry parameters are jointly optimized: we generate a precise set of GCPs from a raw image (slave), with respect to an already orthorectified image (master), by iteratively refining a rough selection of GCPs. Initial GCPs are derived from tie points roughly selected between the orthorectified master and the raw slave images. Image patches from the raw slave image are orthorectified and their mis-registration with the master orthoimage are estimated from correlation. A precise set of GCPs is produced when the mis-registration measured at each patch converges to a minimum. The GCPs generation is made independent of any external data by using a shaded image of the digital elevation model (DEM) as the first orthorectified master, and the first orthorectified image produced then becomes the master for subsequent slave images. This approach is applicable worldwide, taking advantage of the availability of accurate DEMs with global coverage (e.g., Shuttle Radar Topography Mission - SRTM).

Once a set of precise GCPs has been produced, we compute the inverse mapping matrices that associate ground coordinates with raw pixel coordinates. They define an irregular resampling grid in the raw image. To avoid the introduction of aliasing in the orthorectified

image, the irregular resampling problem is accounted for and the orthoimage is then built [8].

Horizontal ground displacements are retrieved from the sub-pixel correlation of the pre- and post-earthquake orthorectified images. Image correlation is achieved with an iterative, unbiased processor that estimates the phase plane in the Fourier domain [8]. This process leads to two correlation images, each representing one of the horizontal ground displacement components (East-West and North-South).

This methodology applies to any imaging system. Here, we apply it to pushbroom satellite images (ASTER), and to aerial images. In pushbroom imaging systems, all optical parts remain fixed during the acquisition, and the scanning is accomplished by the forward motion of the spacecraft. Each line in the image depends on the varying attitudes of the platform. In this case, COSI-Corr corrects the viewing parameters by linearly correcting the camera look directions to compensate for attitude drifts and sensor orientation uncertainties during image acquisition. In contrast, aerial photographs are images acquired from only one exposure. The geometric bias induced by the acquisition system is stationary and is compensated for using the traditional photogrammetric equations [62].

Raw images are wrapped onto the topography within the DEM resolution, and pairwise co-registered with a $\frac{1}{50}$ pixel accuracy, allowing for the measurement of horizontal fault offset with an accuracy on the order of $\frac{1}{20}$ of the pixel size [8].

5.3 The 2005, Mw 7.6 Kashmir Earthquake from ASTER Images

We report on the rupture of the Oct. 8, 2005, Mw 7.6 Kashmir earthquake from 15 m ASTER images acquired on Nov. 14, 2000 and on Oct. 27, 2005. A 30 m DEM produced from these ASTER images was used. Fig. 5.1 shows the North-South component of the ground offsets measured from correlation of the orthorectified and co-registered ASTER VNIR 3N images. This first analysis readily shows that the rupture reached the surface, although field evidence for fault ruptures was scant, and it provides a 70 km mapping of the fault geometry with an accuracy not achievable from field measurements. In addition to the coseismic signal, a wave pattern, running in the satellite along-track direction, reflects the undersampling of the satellite attitudes that therefore could not be accurately accounted for during orthorectification (we see here a pattern characteristic of unrecorded pitch variations,

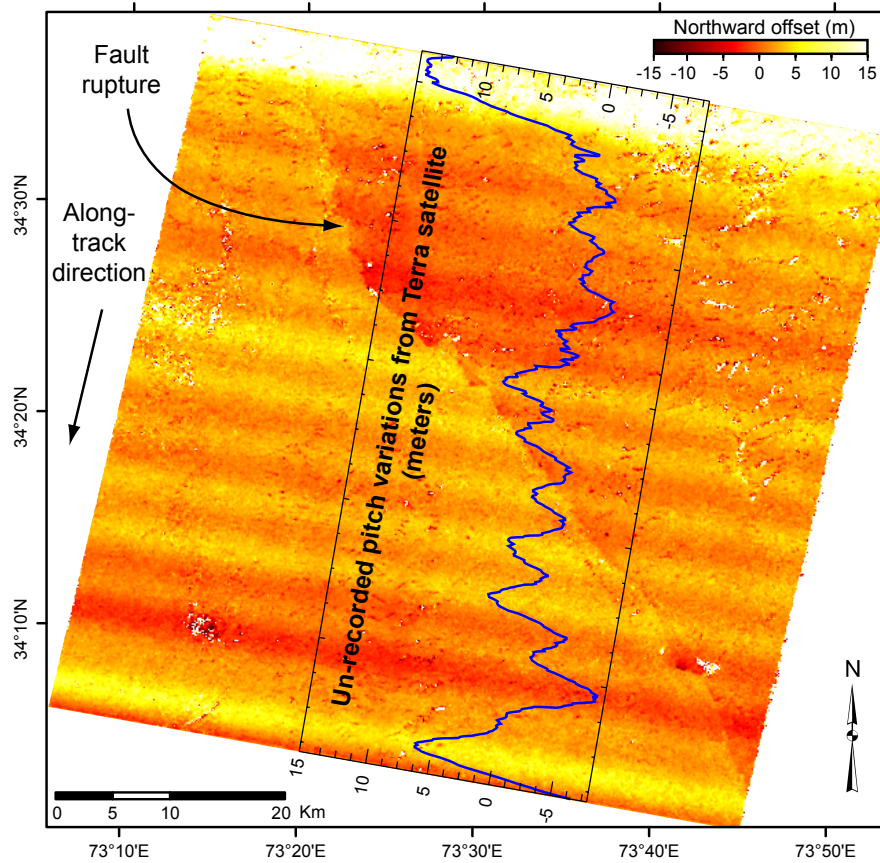


Figure 5.1: Northward component of the coseismic offset field from the 2005 Kashmir earthquake seen from ASTER images (positive to the North.) This correlation image was obtained with a sliding 32×32 pixel correlation window and 8 pixel step, leading to a ground resolution of 120 m. No measurement is assigned to white points, where correlation was lost. Correlation was lost mainly due to landslides or variation of the snow cover. The fault rupture is visible as a discontinuity in the offset field. A wave pattern, attributed to pitch variations, is biasing quantitative measurements.

a similar pattern on the East-West component reflected roll variations.) This pattern was removed from subtraction, in the across-track direction, of several profiles running in the along-track direction and not intersecting with the tectonic signal. This yields Fig. 5.2.

Fig. 5.2 allows us to quantify the horizontal coseismic ground displacement. The horizontal slip vector on the fault could be measured accurately from profiles running across the fault trace, including the fault-perpendicular component of horizontal displacements that could not be measured in the field [9]. Surface displacements indicate nearly pure thrusting with an average slip of about 5 m, peaking at 7 m.

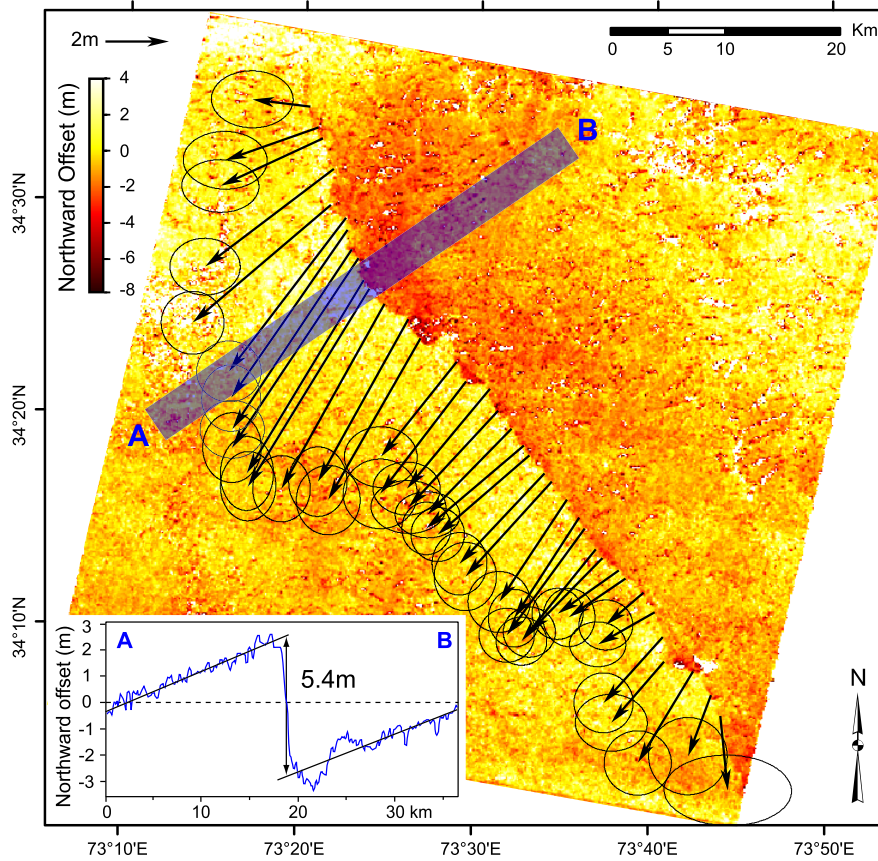


Figure 5.2: Northward component of the coseismic offset field from the 2005 Kashmir earthquake seen from ASTER images (positive to the North). Attitude variations were subtracted from Fig. 5.1. Arrows represent the horizontal surface fault slip. They are determined from linear least-square adjustment, on each side of the fault and on each NS and EW images, of stacked profiles running perpendicularly to the rupture. Profiles are stacked over a width of 6 km and a length of 18 km. Ellipses show the 95% confidence intervals. A longer profile highlights this procedure.

5.4 The 1992, Mw 7.3 Landers Earthquake from Aerial Photographs

Using aerial and satellite imagery, we studied the Mw 7.3 1992 Landers, California earthquake, which produced a 75 km surface rupture with an average right-lateral slip of 3 m. From the USGS–NAPP (U.S. Geological Survey - National Aerial Photography Program), 60 digitized photographs taken in 1989 and 1995 and covering the rupture were paired. Those images, announced at 1 m resolution, each have a footprint of slightly less than 10×10 km. In addition, a 5 m ground resolution 2002 SPOT 5 image and a displacement field of the area obtained from SPOT imagery, [1], were available. The 10 m NED DEM was used to account for the topography.

The SPOT 5 image, previously co-registered to the DEM and orthorectified on a 5 m resolution grid, was used as a common reference to register and orthorectify the aerial images from 1995, as they were both post-earthquake. Between 5 to 10 GCPs per image were selected and optimized with the SPOT 5 image [8], [62]. Optimizations were processed independently, although an improved method would jointly optimize the GCPs of all 1995 images using a bundle block adjustment. Images from 1995 were then orthorectified on a 1-m-resolution grid.

Tie points were selected between the 1995 orthorectified images and their corresponding images from 1989. However, in order to correctly co-register the images, ground displacement at the resulting GCPs locations had to be accounted for. Indeed, these GCPs, necessarily located in the near fault zone area due to the small footprint of aerial images, sustained some ground deformation. The possible ground displacement at the locations of the GCPs would then be incorrectly compensated if we did not account for it during the optimization. As seen in [62], this compensation would corrupt the deformation signal on long wavelengths, but would not affect the localization and slip of the fault. Nevertheless, the displacement map obtained from SPOT imagery was used as an estimate of the ground displacement at GCPs location.

GCPs from images of 1989 were optimized with their corresponding 1995 images as reference. At this stage, the use of a bundle block adjustment for the 1989 images would be difficult, as the best possible co-registration was needed between each image pair. Using a block bundle adjustment would minimize the global error over all pairs but would

introduce local mis-registration that would be perceived as ground displacement. Pairs of orthorectified images were then correlated using a sliding 64×64 m window.

A mosaic of the correlations is presented in Fig. 5.3. Most of the entire surface rupture was mapped, revealing small fault branches that were hardly recognized in the field.

5.5 Conclusion

We successfully applied the COSI-Corr methodology, newly developed, and processed two independent ASTER images, as well as 30 overlapping aerial image pairs. We precisely retrieved the horizontal coseismic displacement fields induced by the recent 2005 Kashmir earthquake, and by the 1992 Landers earthquake from USGS aerial archives.

COSI-Corr proves to be robust and offers an operational methodology to the measurement of horizontal ground deformations. In the case of earthquake studies, the possibility of accurately recovering the fault normal component, and the fact that the technique allows us to measure distributed deformation off the main fault trace, are of particular interest. The sub-pixel capability makes this technique suitable for many types of sensors and many other applications can be foreseen. The estimation of glacier flow velocities or sand dune migration rates are being investigated.

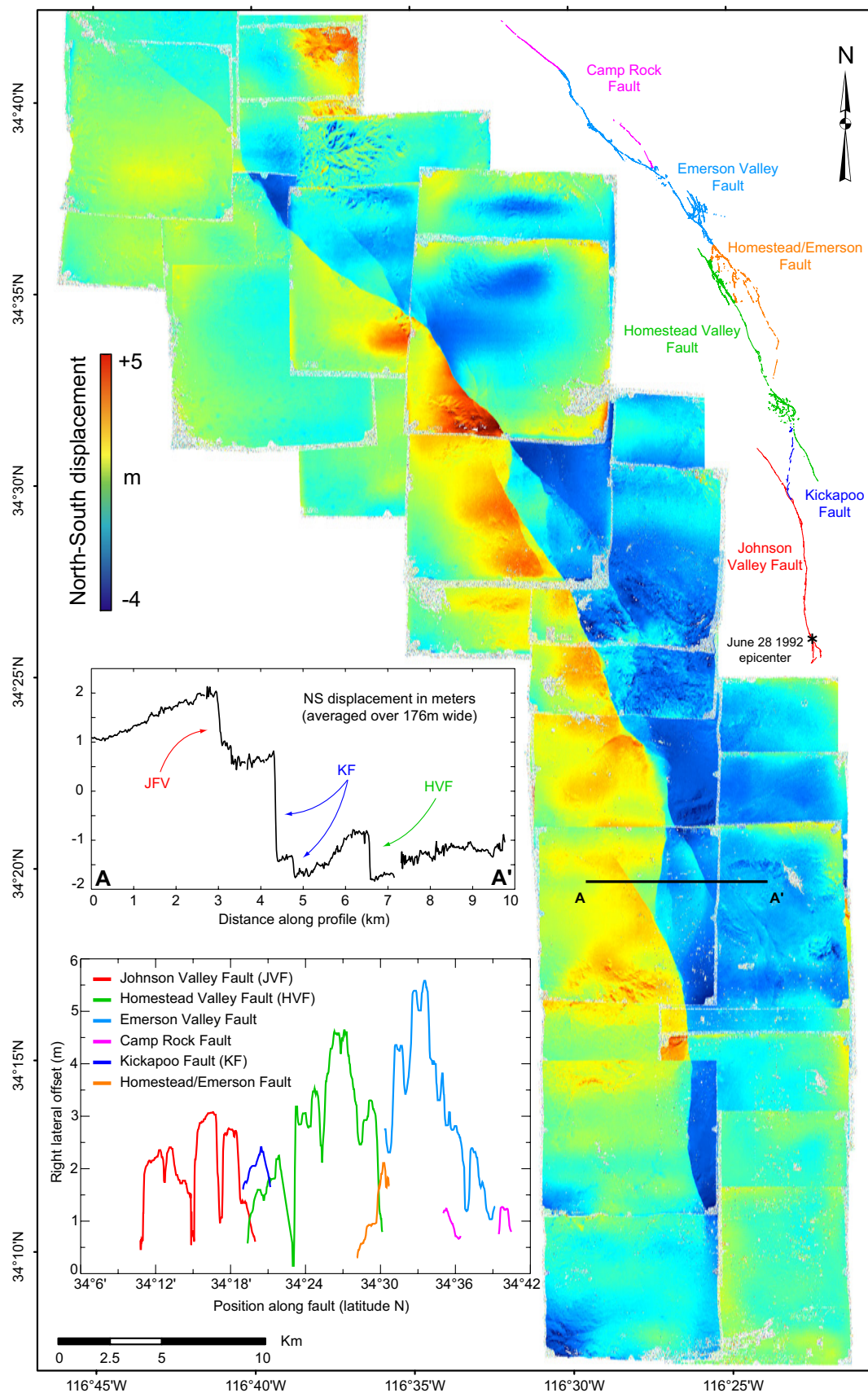


Figure 5.3: Northward component (positive to the North) of the coseismic offset field from the 1992, Mw 7.3 Landers earthquake of California. A mosaic of the North-South correlation images, issued from 30 USGS-NAPP 1989–1995 aerial image pairs, is shown. The mosaic covers most of the 75 km of the surface rupture, highlighting the strike-slip right-lateral nature of the event. The faults map is from [70]. The displacement map from SPOT imagery was of average quality and so was the correction brought on the GCPs. Hence, some long wavelength artifacts can still be seen, and film distortions also contribute to these artifacts. However, these long wavelength artifacts do not bias the measurement of the surface fault offsets [62].

Chapter 6

In-Flight CCD Distortion Calibration for Pushbroom Satellites Based on Subpixel Correlation

By Sébastien Leprince¹, Pablo Musé², and Jean-Philippe Avouac²

¹ Electrical Engineering Department, California Institute of Technology, Pasadena, California, USA

² Division of Geological and Planetary Sciences, California Institute of Technology, Pasadena, California, USA

Foreword— This chapter is in press under the reference S. Leprince, P. Musé, and J.P. Avouac, “In-Flight CCD Distortion Calibration for Pushbroom Satellites Based on Subpixel Correlation,” *IEEE Transactions on Geoscience and Remote Sensing*, (in press), 2008. S. Leprince is responsible for the geometrical analysis and modeling of the SPOT sensor, P. Musé provided expertise in minimization and polygon clipping problems, and J.P. Avouac is the project principal investigator.

We describe a method that allows for accurate in-flight calibration of the interior orientation of any pushbroom camera, and that in particular solves the problem of modeling the distortions induced by CCD misalignments. The distortion induced on the ground by

each CCD is measured using sub-pixel correlation between the orthorectified image to be calibrated and an orthorectified reference image that is assumed distortion-free. Distortions are modeled as camera defects, which are assumed constant over time. Our results show that in-flight interior orientation calibration reduces internal camera biases by one order of magnitude. In particular, we fully characterize and model the SPOT4-HRV1 sensor, and we conjecture that distortions mostly result from mechanical strain produced when the satellite was launched, rather than from effects of on-orbit thermal variations or aging. The derived calibration models have been integrated to the software package Co-registration of Optically Sensed Images and Correlation (COSI-Corr), freely available from the Caltech Tectonics Observatory website. Such calibration models are particularly useful in reducing biases in DEMs generated from stereo matching, and in improving the accuracy of change detection algorithms.

6.1 Introduction

Recent methodological advances have made it possible to accurately orthorectify and co-register pairs of optical satellite images, acquired from pushbroom systems, on an operational basis [8] [72]. The average co-registration accuracy is on the order of 1/50 of the pixel size, and associated with an accurate sub-pixel correlation technique, quantitative monitoring of Earth's surface deformations have become possible. For instance, the Co-registration of Optically Sensed Images and Correlation (COSI-Corr)¹ technique has been applied successfully to measure the horizontal coseismic displacement field induced by large earthquakes [1, 8–11, 19, 72], glacier flow [2, 4, 73], landslides [2], and sand dune migrations [74]. In each case, the accuracy on the horizontal displacement measured was on the order of 1/10 of the pixel size for individual measurements, and often better than 1/20 of the pixel size for measurements stacked over a swath.

At this level of accuracy, the ground deformation measurements are sensitive to any potential defect in the physical modeling of the satellite system. One recurring and troublesome issue has been the proper modeling of the internal orientation of pushbroom imaging satellites whose detector array is not composed of a single charge coupled device (CCD) line array, but rather of several line arrays combined together to form a longer single one. This

¹URL:http://www.tectonics.caltech.edu/slip_history/spot_coseis/

is for instance the case of the Satellite Pour l’Observation de la Terre (SPOT) satellites 1, 2, 3, and 4, where the panchromatic bands are acquired using four CCD line arrays of 1500 pixels each, combined together through an optical divider to form the complete equivalent 6000 pixels line scanning array [23].

Artifacts due to improper modeling of CCDs alignment are manifest in Fig. 6.1. This figure shows the displacement field measured from the sub-pixel correlation of a SPOT 4-HRV1 panchromatic image acquired in 1998, and a SPOT 2-HRV1 panchromatic image acquired in 2000, which were first precisely co-registered and orthorectified. These images cover the epicentral area of the Mw 7.1, Hector Mine earthquake, California, which struck in 1999, rupturing the Earth’s surface over a distance of about 60 km. Fig. 6.1 should then represent the measurement of the horizontal coseismic displacement field induced by this earthquake. The main rupture is indeed revealed and can be mapped in detail, but measurements seem biased by linear artifacts running in the satellites’ along-track direction. In areas where the coseismic deformation is negligible, biases corresponding to up to 1.6 m of ground displacement are measured. They are caused by the contribution of misaligned and distorted CCD line arrays of both satellites that were not modeled properly during orthorectification. A distortion-free, perfectly straight CCD line array model was indeed used.

In this paper, we describe a method that allows for in-flight calibration of the interior orientation of any pushbroom camera, and that in particular solves the problem of modeling the distortions induced by individual CCD misalignments. Our discussion and results are illustrated using pairs of panchromatic SPOT images. Section 6.2 presents a review of how the CCD distortion problem has been addressed thus far. In Section 6.3 we expose our calibration methodology, which is based on the measurement of the CCD-induced ground distortions using sub-pixel correlation, and on interpreting them as errors on the camera model. Internal orientation distortions are assumed constant over time and are measured with respect to an image that is assumed distortion-free. Section 6.4 presents the results obtained, while Section 6.5 discusses the performances and limitations of our calibration method.

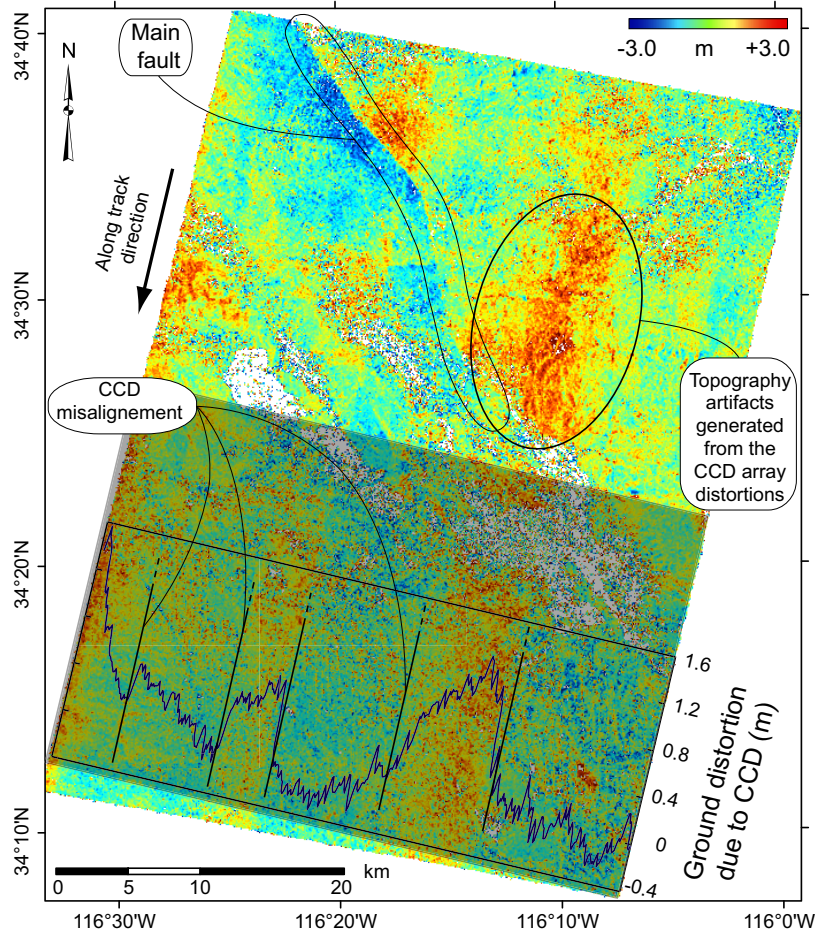


Figure 6.1: East-West component (eastward positive) of the displacement field measured over the Hector Mine area, California, using a 10 m panchromatic SPOT 4 image acquired on 08/17/1998, and a 10 m panchromatic SPOT 2 image acquired on 08/10/2000. Images were co-registered with the topography using the 1/3 arcsec, ~ 9 m, NED DEM from the USGS, co-registered together using automatic sub-pixel ground control points selection, and orthorectified on a 10 m UTM grid. Subpixel correlation was performed using 32×32 pixel correlation windows, sliding with a step of 8 pixels, yielding a displacement map sampled at every 80 m. This experiment is the same as the one depicted in Fig. 24 of [8]. The fault rupture, induced by the Mw 7.1, 1999 Hector Mine earthquake, is characterized as a discontinuity in the displacement field and accounts for up to 5.5 m of surface offset in this component. No measurement is assigned to white points, where correlation was lost due to drastic changes over alluvial areas, or because of sensor saturation on white sandy areas. Linear artifacts, running in the satellites along-track direction, betray the unmodeled distortions of the CCD arrays of each satellite. The dark box represents an area where the tectonic signal is assumed negligible with respect to the measurement noise (~ 70 cm). The superimposed graph shows the displacements within this box, averaged in the along-track direction. This stacked profile estimates the bias induced by the CCD distortions of both satellites. In flat topography areas (this is mostly the case in the dark box), induced ground distortions are up to 1.6 m. However, these also depend on the topography variations, as seen in the circled area, and as explained in Fig. 6.2.

6.2 Previous Work

To our knowledge, there exist very few authors in the open literature who have explicitly documented the problem of correcting the CCD distortions of pushbroom satellites. They all based their studies on the SPOT satellites, and are described below.

6.2.1 Benefiting from the Dual Acquisition System HRV1 and HRV2 on SPOT Satellites

In [75] and [50], Westin describes a procedure to explicitly calibrate the CCD distortions of the SPOT 1 satellite. SPOT 1, 2, and 4 satellites are equipped with two similar instruments, HRV1 and HRV2, that can acquire images simultaneously, and with different pointing angles thanks to their independent steering mirrors. Such acquisitions constitute stereo pairs with a base-to-height ratio equal to zero, and once projected on a common reference system (UTM), the local disparities are formulated as the superposition of the distortions from both instruments. Distortions from each instrument can be separated using at least three such pairs, each pair having a different incidence angle difference. This technique works well but is of limited practical use. One practical problem is that the HRV1 and HRV2 instruments are usually not acquiring scenes simultaneously, and finding at least three such stereo pairs from the SPOT archives is challenging. However, this problem could easily be overcome by a special order of images if the satellite is still running. Another more serious limitation is that this method applies only to satellites having two optical systems that can simultaneously image the same area. In other words, this formulation is only valid for SPOT satellites, whereas other satellites such as Quickbird, Ikonos, the IRS-1C satellite, etc..., which do not possess a duplicate of their optical instrument, but which also exhibit troublesome CCD distortions [76] [77], could benefit from a more general and versatile approach.

6.2.2 Along-Track Subtraction of Stacked Profiles

To correct CCD-induced distortions in a correlation image like the one shown in Fig. 6.1, one may be tempted to simply use post-processing tools to remove the apparent artifacts. Exact and tedious modeling of the distortions then becomes unnecessary. For instance, one could think of removing the CCD artifacts from Fig. 6.1 by subtracting, in the satel-

lites' along-track direction, stacked profiles taken where the displacement field is assumed to be zero. This is equivalent to subtracting the graph superimposed on Fig. 6.1 from the whole correlation image. Unfortunately this method, proposed in [1], has two major drawbacks. First, the correlation image must possess large areas where the ground displacement is negligible, which is impractical in the case of images spanning a large earthquake. Second, this stacking technique simply does not work because, as explained in Fig. 6.2, the CCD-induced distortions on the ground depend on the topography. Hence averaging non-constant ground distortions is meaningless. As an illustration, the circled artifacts in Fig. 6.1 cannot be canceled from stacks subtraction since they show obvious heterogeneities in the along-track direction. These parallax artifacts result from the CCD distortions and cannot be the result of the DEM vertical inaccuracy. The pre- and post-earthquake images have an incidence angle difference of 8.1° and the NED DEM has a vertical accuracy within ~ 3 m [78]. Consequently, the ground disparity induced by DEM parallax should not exceed 42 cm, and the ground disparities measured are comprised between 2–3 m. Hence the topography-dependent artifacts circled in Fig. 6.1 are indeed produced by the CCD distortions.

6.3 Proposed Methodology

6.3.1 Assumptions and Notations

In this study, we assume that artifacts observed in the correlation images are due to a combination of non-separable distortions from the optical system and the CCD elements, and they all can be modeled as positioning errors on the CCD elements' location in the focal plane [75]. For a given CCD element, the distortion is considered constant over the time of acquisition of an image. The acquisition time is about 9 s for a SPOT image. We will discuss the stationarity of CCD distortions over longer periods in Section 6.5.

To express our internal orientation model that accounts for the CCD and optical distortions, we use the internal orientation representation developed for the SPOT satellites, where each CCD element is associated with a particular look direction [23]. Notations are reported in Fig. 6.3.

The calibrated interior orientation of a slave image is derived from the correlation analysis between the slave image and a reference image that is assumed bias-free and perfectly

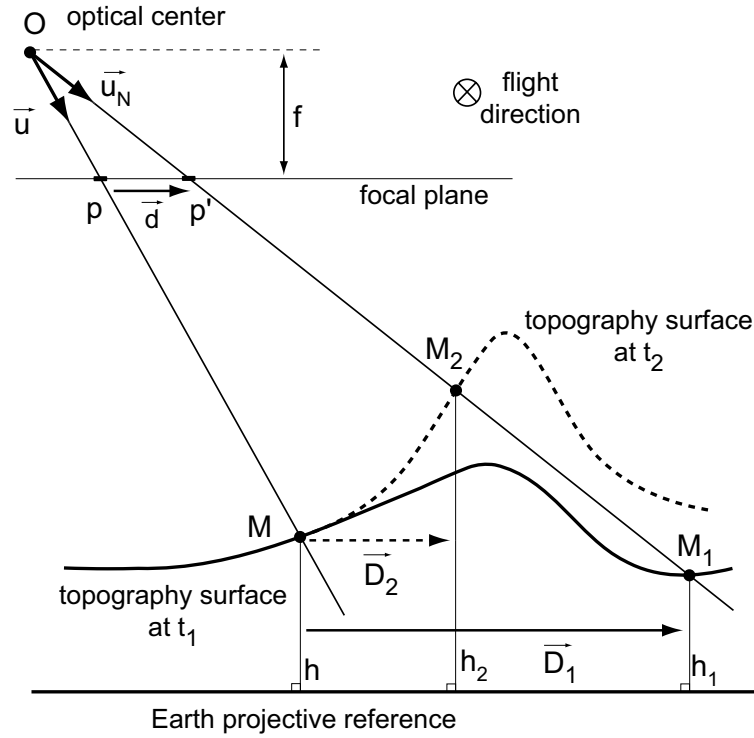


Figure 6.2: Assume that a particular pixel is thought to be imaging a scene from the position p in the satellite focal plane. Also assume that the optical system is sustaining some distortion, constant over time, that can be modeled as if this particular pixel p was in fact seeing the scene from the position p' in the focal plane. Call this distortion $\vec{d} = \vec{pp}'$. Then, orthorectify, co-register, and correlate the distorted image with a distortion-free reference image. If at a particular acquisition time t_1 , the topography of the scene is represented by the solid black line, then the ground disparity measured from correlation is \vec{D}_1 . Since \vec{d} is assumed constant over time, if the topography is instead represented by the dotted line at time t_2 , the ground disparity measured will be $\vec{D}_2 \neq \vec{D}_1$. Hence the ground disparities measured from the correlation of orthorectified images depend on the topography variations and cannot be averaged. This makes clear that CCD distortions must bias the production of digital elevation models from stereoscopic images [75]. The distortion in the focal plane \vec{d} is retrieved using the observed ground distortion. If at the time t_1 the pixel p sees the ground point M and the ground disparity \vec{D}_1 is measured, it means that the pixel p should have seen the ground point $M_1 = M + \vec{D}_1$, at elevation h_1 , instead. The problem of determining \vec{d} is therefore equivalent to determining the new camera unitary pointing vector \vec{u}_N of the pixel p , such that p sees the ground point M_1 when projected according to \vec{u}_N .

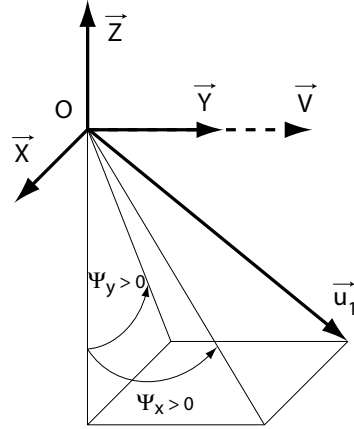


Figure 6.3: Each CCD element p in the focal plane is characterized by a pointing direction \vec{u}_1 , with origin the instrument's optical center O . These look directions are derived from the look angles (Ψ_x, Ψ_y) , such that $\vec{u}_1(p) = [-\tan \psi_y(p), \tan \psi_x(p), -1]^T / K$, and with K such that $\|\vec{u}_1(p)\|_2 = 1$, for all p . The set of look directions is fixed over a given acquisition and models the satellite interior orientation. It is given in the spacecraft body fixed reference system, also called the Navigation Reference Coordinate System. At nominal attitude when the satellite roll, pitch, and yaw are null angles, we have $\vec{Y} // \vec{V}$, $\vec{Z} // \vec{P}$, $\vec{X} = \vec{Y} \times \vec{Z}$, if \vec{P} and \vec{V} denote the satellite position and velocity vectors, respectively.

orthorectified. This reference image should largely overlap with the slave image to be calibrated. For example, it could be a mosaic of high-resolution aerial photographs orthorectified at the resolution of the slave image [79]. In this study, the reference image is a SPOT 5-HRG1 panchromatic image. The SPOT 5 sensor is composed of a single CCD line array that is accurately calibrated [79], and that has shown no detectable bias during correlation analysis [8]. The 1/3 arcsec (~ 9 m) NED digital elevation model (DEM) [78] is used for orthorectification purposes. Its resolution is thought to be sufficient to produce orthorectified images with negligible parallax effects if the images are free of modeling distortions.

6.3.2 Methodology

CCD distortions induce subtle disparities in the images that account for at most a small fraction of the pixel size. Therefore, the slave raw image should be perfectly orthorectified and co-registered with the reference, except for the CCD distortions that should be unambiguously measured. This is achieved thanks to accurate ground control points (GCPs), which correct for the satellite exterior orientation errors, and which are generated between the raw slave image and the orthorectified reference using sub-pixel correlation [8].

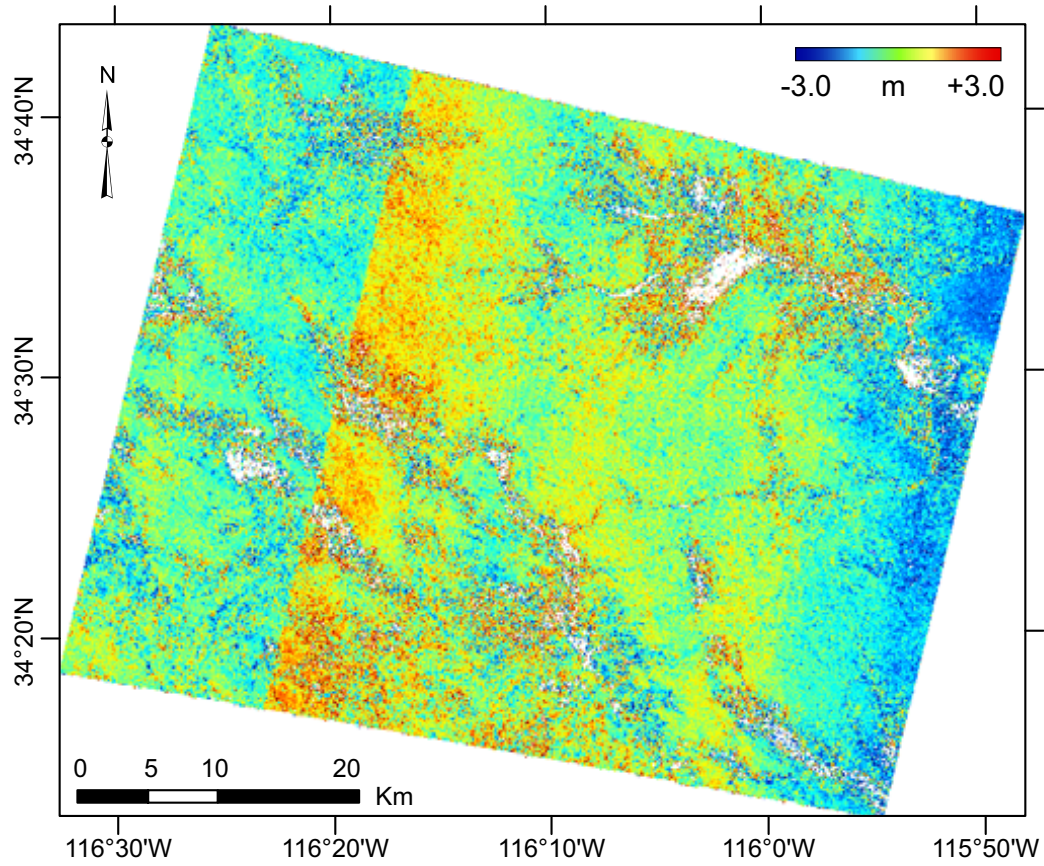


Figure 6.4: East-West component (eastward positive) of the disparity field measured from sub-pixel correlation of a reference SPOT 5 - HRG1 5 m panchromatic image acquired on 01/24/2003, and a slave SPOT 4 - HRV1 10 m panchromatic image acquired on 03/11/2000. Both images were orthorectified using the 1/3 arcsec NED DEM from the USGS. Thirty sub-pixel GCPs were used to tie the SPOT 5 image to the DEM, and 6 sub-pixel GCPs were used to tie both orthorectified images together [8]. Correlation analysis was performed on 32×32 pixel windows, sliding with a step of 8 pixels (80 m on the ground). Linear artifacts reveal the SPOT 4 CCD distortions.

The result of the correlation analysis between a SPOT 5 - HRG1 panchromatic reference image and a SPOT 4 - HRV1 slave image is shown in Fig. 6.4. The disparity field shows linear artifacts attributed to the SPOT 4 CCD distortions. No other biases are visible, meaning that precise orthorectification and co-registration have been achieved. In particular, the exterior orientation is satisfyingly modeled as no oscillating pattern is observed (typical for roll, pitch, or yaw variations residuals [72] [80]).

6.3.2.1 The Orthorectification Model

The orthorectification model, as detailed in [8], is of the form:

$$M(p) = O(p) + \lambda[T(p)R(p)\vec{u}_1(p) + \vec{\delta}(p)], \quad (6.1)$$

where:

- M is the point on the ground seen by the pixel p ,
- O is the position of the optical center in space when p was being acquired
- \vec{u}_1 is the interior look direction of the pixel p as defined in Fig. 6.3
- R is a 3D rotation matrix that accounts for the satellite roll, pitch, and yaw when p was being acquired
- T is a system reference change matrix from the orbital to the terrestrial coordinates system
- δ is the correction brought on the orthorectification model by the GCPs to ensure precise co-registration of the orthorectified slave and the reference images
- λ is some positive scaling number such that the ray defined by $O(p) + \lambda\vec{u}(p)$ intersects the topography surface as defined by the DEM at M .

GCPs are automatically derived with high accuracy by optimizing δ on some designated pixels of the raw image, called image control points (ICPs), such that orthorectified patches centered on those ICPs have an average co-registration with the reference image as accurate as possible, as measured using sub-pixel correlation.

In practice, we do not distinguish between the instrument optical center and the satellite center of mass, and δ is a linear correction on each of the X, Y, Z components of the terrestrial look direction $T(p)R(p)\vec{u}_1(p)$. Although δ has the potential of correcting any defect from both the interior and exterior orientations, the linear correction mostly corrects for attitude drifts of the satellite. We then next consider that δ corrects for any bias of the external orientation and that remaining biases are only due to distortions from the interior orientation, i.e., the CCD distortions.

Given a pixel p , the direct orthorectification model determines its projection M on the ground.

6.3.2.2 The Calibration

Given the orthorectification model, the following procedure, introduced in Fig. 6.2, is used to compute the calibrated look direction \vec{u}_N for all pixels in the slave image:

1. Call M the ground projection of the pixel p by the direct model orthorectification. Orthorectify the raw slave image onto a 32×32 pixel patch \mathbf{P} centered at M .
2. Compute the disparity \vec{D}_1 between \mathbf{P} and the orthorectified reference image using sub-pixel correlation.
3. Find $M_1 = M + \vec{D}_1$. Assign to M_1 its elevation h_1 according to the DEM.
4. Determine the new interior orientation look direction \vec{u}_N such that $M_1(p) = O(p) + \lambda_1 [T(p)R(p)\vec{u}_N(p) + \vec{\delta}(p)]$, for some $\lambda_1 > 0$, and under the constraint $\|\vec{u}_N(p)\|_2 = 1$.

This yields

$$\vec{u}_N(p) = R^T(p)T^T(p)\left(\frac{\overrightarrow{OM}_1}{\lambda_1} - \vec{\delta}(p)\right), \quad (6.2)$$

with λ_1 determined from the constraint $\vec{u}_N \cdot \vec{u}_N = 1$, which gives

$$\lambda_1 = \frac{\overrightarrow{OM}_1 \cdot \vec{\delta} - \sqrt{(\overrightarrow{OM}_1 \cdot \vec{\delta})^2 - (\|\vec{\delta}\|^2 - 1)\|\overrightarrow{OM}_1\|^2}}{\|\vec{\delta}\|^2 - 1}. \quad (6.3)$$

We indeed have $\lambda_1 > 0$ since $\|\vec{\delta}\|^2 < 1$. Physically, this means that the correction on the orthorectification model has a smaller magnitude than the pointing vector to be corrected. This should always be true when the satellite is imaging its specified ground target.

7. Iterate for all pixels in the raw slave image that overlap with the reference image. See Appendix E for details.

This procedure yields a calibration for each CCD element. It provides maximum redundancy because it is carried out for all lines in the raw image. Because pointing vectors (or look directions) are characteristic of the camera, they can be assumed constant over the image scanning time for a given CCD element, and they are ‘‘averaged’’ to give a more accurate

calibration. For a given CCD element, averaging all the pointing vectors \vec{u}_N^i means finding the unitary vector $\langle \vec{u}_N \rangle$ such that its direction is the mean direction of all unitary vectors \vec{u}_N^i . This is equivalent to finding $\langle \vec{u}_N \rangle$ that satisfies $\langle \vec{u}_N \rangle = \operatorname{argmin}_u \sum_i \|\vec{u} - \vec{u}_N^i\|^2$ for $\|\vec{u}\| = 1$. Equivalently, the spherical coordinates angles (θ_N, φ_N) of $\langle \vec{u}_N \rangle$ are the minimizers of

$$f(\theta, \varphi) = \sum_i (1 - \vec{u} \cdot \vec{u}_N^i), \quad (6.4)$$

$$\text{for } \vec{u} = (\sin \varphi \cos \theta, \sin \varphi \sin \theta, \cos \varphi)^T.$$

If we let A , B , and C denote the coordinates of the vector $\sum_i \vec{u}_N^i$ in the spacecraft body fixed reference system, i.e., $A = \sum_i \vec{u}_N^i \cdot \vec{X}$, $B = \sum_i \vec{u}_N^i \cdot \vec{Y}$, $C = \sum_i \vec{u}_N^i \cdot \vec{Z}$, we find

$$\theta_N = \arctan\left(\frac{B}{A}\right), \text{ and } \varphi_N = \arctan\left(\frac{A \cos \theta_N + B \sin \theta_N}{C}\right), \quad (6.5)$$

by equating the partial derivatives of $f(\theta, \varphi)$ to zero. For each CCD element, we can then determine a mean calibrated look direction $\langle \vec{u}_N \rangle$. In practice, to limit bias in the mean calibration, only calibration measurements resulting from a correlation with high signal-to-noise ratio, and with ground disparities comprised within a physical range of a few meters are used. At this point, the interior orientation of the satellite is fully calibrated and it is worth noting that no a priori knowledge on the camera parameters such as the focal length or the CCD sampling step in the focal plane have been used. The resulting calibration is therefore not biased even when these parameters are not known with enough accuracy.

We previously stated that the distortions of the optical system were primarily due to positioning errors of the CCD elements in the focal plane. Now that the camera interior orientation is calibrated, the focal plane distortions \vec{d} (see Fig. 6.2) can be determined by looking at the difference between the projection of the calibrated and non-calibrated look directions $\langle \vec{u}_N \rangle$ and \vec{u}_1 in the focal plane. We have:

$$\vec{d} = (d_x, d_y, 0)^T = p' - p = \frac{f}{r} \left[\frac{\langle \vec{u}_N \rangle}{|\langle u_N(z) \rangle|} - \frac{\vec{u}_1}{|u_1(z)|} \right], \quad (6.6)$$

where f is the instrument estimated focal length, r is the sampling step of the CCD array, and $u(z)$ is the Z component of \vec{u} , i.e., $u(z) = \vec{u} \cdot \vec{Z}$. For the SPOT 4 instrument, we used $r = 13 \mu\text{m}$ [23]. The exact value of the focal length varies slightly depending on authors, and we followed the recommendation of [75] using $f = 1084 \text{ mm}$. Fig. 6.5 shows each component,

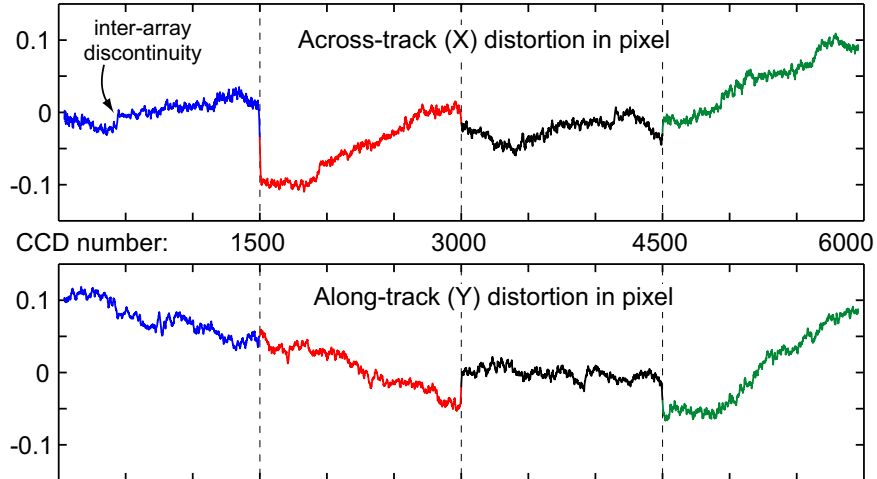


Figure 6.5: Measured distortions, in pixel, in the focal plane of the SPOT 4- HRV1 panchromatic sensor. The CCD line sensor is composed of four CCD line arrays of 1500 pixels each (vertical dotted lines). Discontinuities on the edges of each array reveal their misalignment. Both across-track and along-track distortions are measured with an uncertainty below 0.01 pixel rms. Distortions up to 0.12 pixel ($\sim 1.2\text{m}$ on the ground) are estimated. All 6000 pixels are calibrated, except for the first 43 and the last 40 pixels due to border effect in the correlation analysis. Distortion for these missing pixels were later linearly extrapolated from the nearest 150 distortions to provide a complete calibration of the sensor.

across-track d_x and along-track d_y , of the distortion \vec{d} measured in the focal plane of the SPOT 4- HRV1 panchromatic sensor. Discontinuities are clearly seen on the edge of each CCD array at pixel multiples of 1500. The uncertainty of this calibration model is better than 0.01 pixel rms, and shows significant CCD distortions even within each single CCD array.

Non-calibrated look angles (Ψ_x, Ψ_y) , defined in Fig. 6.3, relate to the non-calibrated interior orientation look directions \vec{u}_1 . In the same way, calibrated look angles (Ψ_x^N, Ψ_y^N) can be derived from the calibrated interior look direction $\langle \vec{u}_N \rangle$. Fig. 6.6 represents the difference between calibrated and non-calibrated look angles, in the polar plane defined by $(\Delta\Psi_x, \Delta\Psi_y)$, with $\Delta\Psi_x = \Psi_x^N - \Psi_x$, and $\Delta\Psi_y = \Psi_y^N - \Psi_y$, for all pixels p in the SPOT 4- HRV1 CCD sensor. This representation helps to visualize the kind of distortion that the CCD sensor suffers. On the first order, the clustering of each CCD array shows that discontinuities between arrays cause the worst defects. On a second order, the linearity in this polar plane of the points belonging to the CCD arrays 1, 2, and 4, shows internal rigid rotation of these arrays in the focal plane. On a third order, we can also point out inter-array discontinuities, as seen on the array 1. It is also visible in Fig. 6.5 around pixel

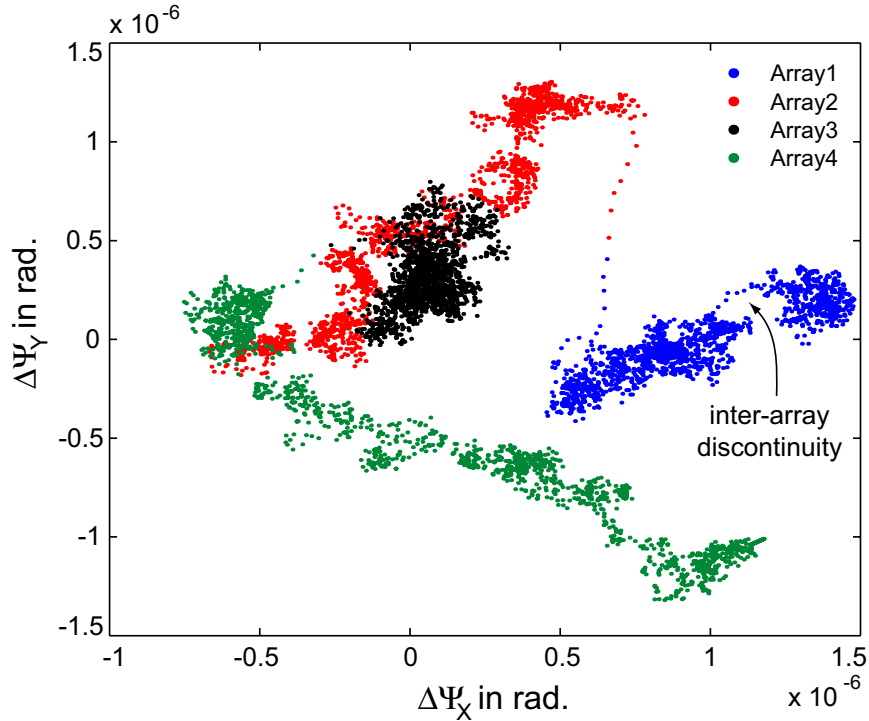


Figure 6.6: Polar representation of the differences between calibrated and uncalibrated interior orientation look directions. We define $\Delta\Psi_x = \Psi_x^N - \Psi_x$ and $\Delta\Psi_y = \Psi_y^N - \Psi_y$, where (Ψ_x, Ψ_y) and (Ψ_x^N, Ψ_y^N) are derived from the non-calibrated, \vec{u}_1 , and calibrated, $\langle \vec{u}_N \rangle$, interior orientation vectors. Each dot represents the look angle correction of a particular pixel. Colors are chosen to match those of Fig. 6.5. The clustering of the CCD arrays highlights the CCD arrays' misalignment in the focal plane, and the linear trend of the arrays 1, 2, and 4, shows that they are rotated in the focal plane. The CCD array 1 seems to be split into two clusters. The transition between these two clusters corresponds to the across-track discontinuity noticed in Fig. 6.5 around the pixel number 500. The width of the dot cluster representing the CCD array 4, about $0.1 \cdot 10^{-6}$ rad, is characteristic of the calibration uncertainty (not shown for clarity). At an altitude close to 830 km, this calibration allows for a geometric accuracy that is about 8 cm on the ground, or 1/125 of the pixel size.

number 500 in the across-track direction.

6.3.2.3 SPOT Steering Mirror and Correction Model

The SPOT interior orientation look directions \vec{u}_1 account for the modeling of the steering mirror [24]. Therefore, the correction devised above cannot be applied directly to another image from the same sensor, acquired with a different incidence angle. We need to introduce the rotation matrix R_M modeling the effect of the lateral steering mirror:

$$R_M = \begin{pmatrix} \cos(\Theta) & 0 & -\sin(\Theta) \\ 0 & 1 & 0 \\ \sin(\Theta) & 0 & \cos(\Theta) \end{pmatrix}, \quad (6.7)$$

where Θ is a rotation angle around the Y axis (Fig. 6.3). From the SPOT ancillary data, we compute $\Theta = (s - 48) \times 0.6^\circ$, where s is the step encoding the mirror rotation. We then define the correction model for the SPOT 1, 2, 3, and 4 satellites as:

$$\vec{d}u_0(p) = R_M^T \left[\langle \vec{u}_N(p) \rangle - \vec{u}_1(p) \right], \quad (6.8)$$

for all the 6000 pixels p constituting the line sensor. In our particular example, the slave SPOT 4-HRV1 panchromatic image has a mirror step $s = 46$, hence $\Theta = -1.2^\circ$. This allows us to propose a general correction model for this particular sensor, assuming that the CCD distortions do not change over time. To apply this correction to another image from the same sensor, say to the image I , we correct the given interior orientation look directions $\vec{u}_1(p)_I$, for all pixels p , according to:

$$\vec{u}_N(p)_I = \vec{u}_1(p)_I + R_{M_I} \vec{d}u_0(p), \quad (6.9)$$

where R_{M_I} is the mirror rotation matrix associated with the image I , which is assumed constant for a given image. No images are indeed acquired when the mirror is rotating, and a safety lag time is set to allow the mirror position to rest until potential oscillations become negligible [81].

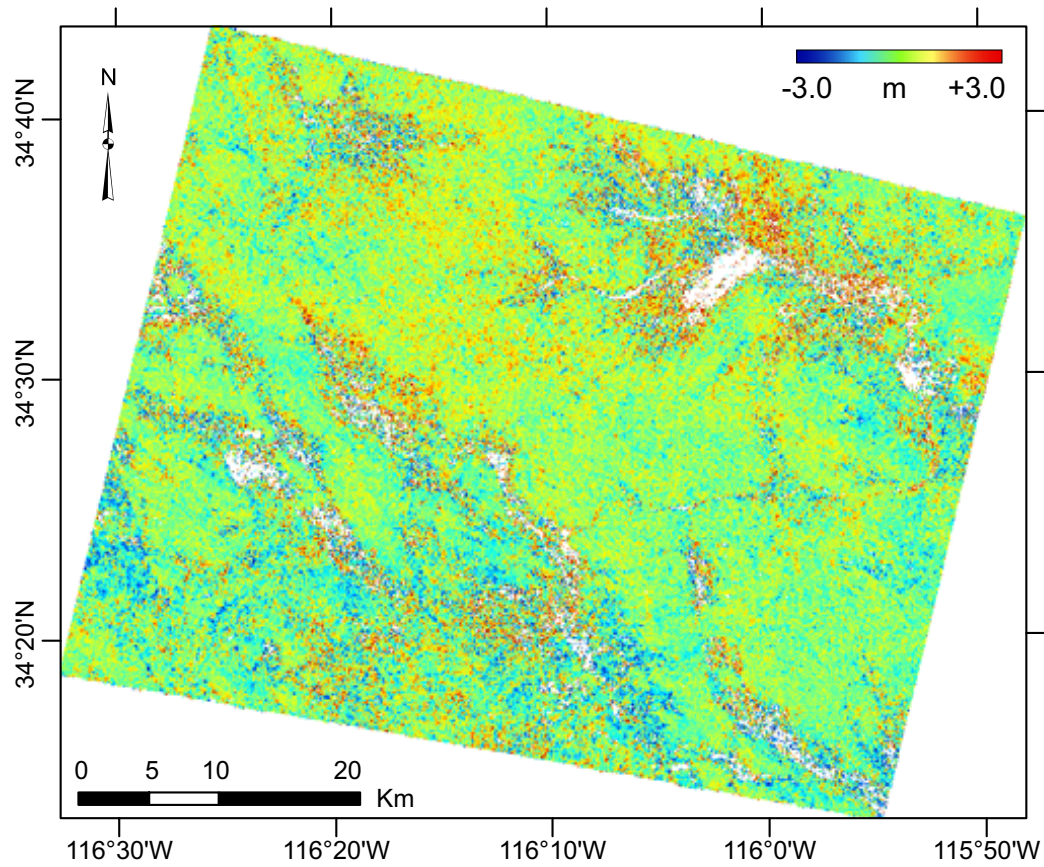


Figure 6.7: Same experiment as in Fig. 6.4, but the derived CCD correction model has been accounted for during orthorectification. The absence of visible bias related to the CCD distortions validates the methodology.

6.4 Results

Fig. 6.7 represents the correlation analysis between the SPOT 4 slave image when the interior orientation is corrected as described, and the SPOT 5 reference image. Compared with Fig. 6.4, it is clear that the CCD-induced distortions have been corrected well. This experiment validates the methodology presented and shows that the image from which the distortions are estimated is properly corrected. However, this experiment does not validate the way the mirror rotation is compensated. As the calibration model is used on the calibration image, the matrices R_M and R_{M_I} are identical, and they exactly compensate each other in the correction. Hence this experiment is insensitive to mirror rotation uncertainties.

Fig. 6.8 shows a more extended experiment and presents the same correlation analysis as in Fig. 6.1, but this time, the SPOT 4-HRV1 correction model that was estimated from the SPOT 4-HRV1 image of 2000, is applied to the SPOT 4-HRV1 pre-earthquake image of 1998. To obtain a complete distortion-free image, the SPOT 2-HRV1 sensor was also calibrated, using the same SPOT 5 reference image. No CCD artifacts remain, hence we can conclude that the CCD distortions, at least between 1998 and 2000, can be considered stationary. This is an encouraging result suggesting that a single calibration of a particular instrument can hold for several years.

In seismotectonic studies, fault slip measurements are important in understanding the mechanics of seismic ruptures [9–11]. They can be determined from the correlation analysis of pre and post-earthquake images by measuring the amplitude of discontinuities in profiles running perpendicularly through the fault. Thus far, it has been assumed that this procedure, which measures the relative displacement at the fault, is insensitive to artifacts from the imaging system. This is only true for artifacts whose wavelengths are much larger than the fault discontinuities, and this is unfortunately not the case with the CCD-induced distortions. In a particular setting where the fault is perpendicular to the satellite tracks, such measurements will not be biased, but if the CCD discontinuities are aligned with the fault offset, measurements will be inevitably corrupted. Fig. 6.9 compares the right lateral slip at fault from the offset field depicted in Fig. 6.1 and Fig. 6.8. The right lateral coseismic offset of the 1999 California Hector Mine earthquake is measured from the SPOT images before and after the CCD calibration is used. The discrepancy is up to 70 cm around kilometer 10, where one of the CCD artifact crosses the fault near longitude 116°16'W (see Fig. 6.1).

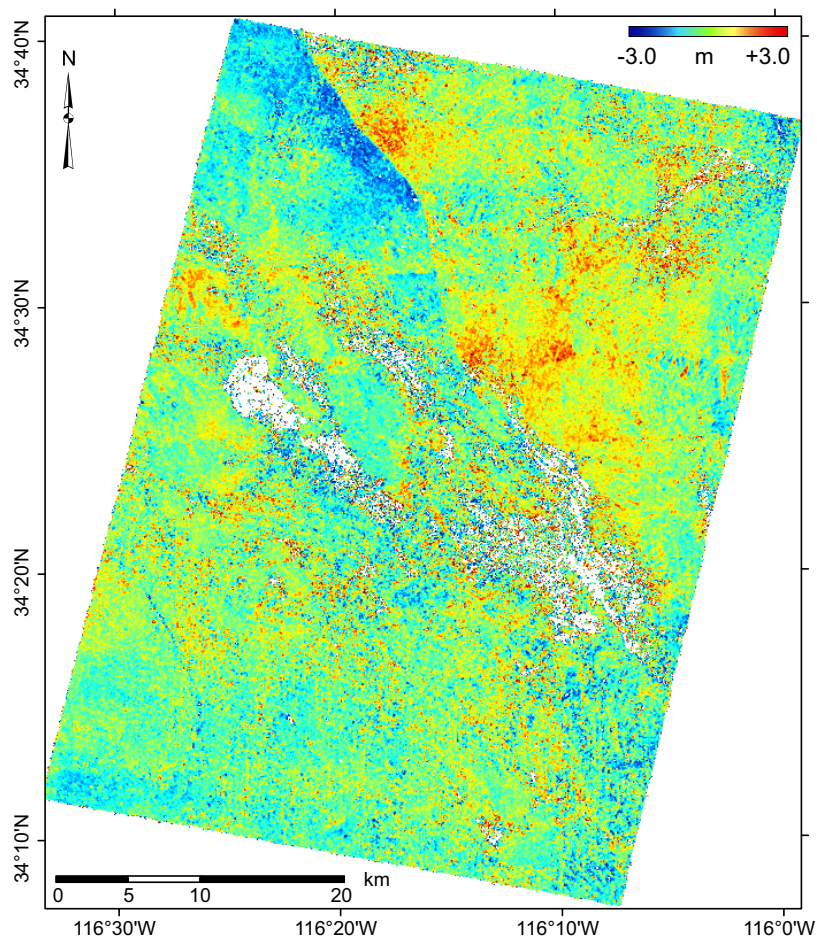


Figure 6.8: Same experiment as in Fig. 6.1, but the derived CCD correction model for both SPOT 4 and SPOT 2 images have been accounted for during orthorectification. Although the SPOT 4 sensor was calibrated from an image acquired in 2000, it is applied here on a 1998 pre-earthquake image. The absence of CCD artifacts suggests that the CCD distortions of this particular sensor are stationary over the years. We also notice that the topography-induced artifacts have disappeared. The proposed methodology should then improve the quality of DEMs produced from stereoscopic image pairs acquired from the instruments considered in this study.

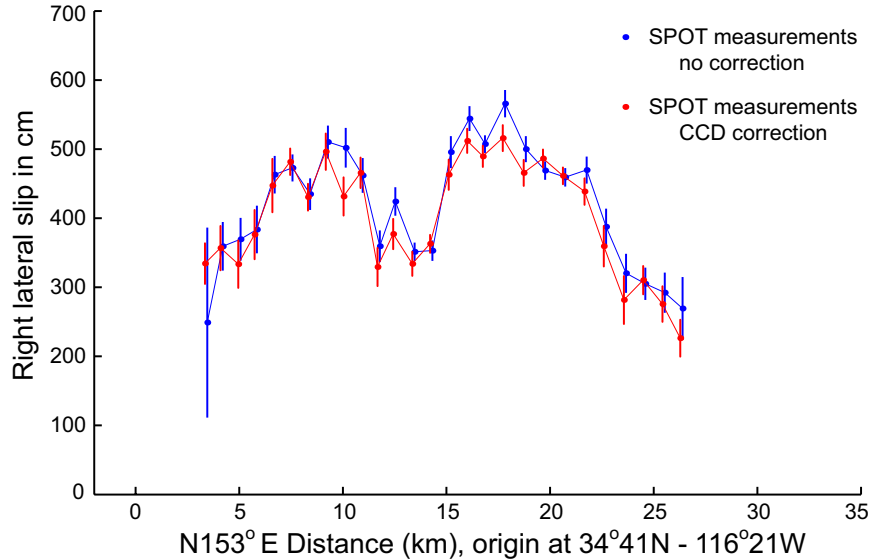


Figure 6.9: Comparison of the right lateral slip along the fault trace estimated from the correlation analysis from Fig. 6.1 and from Fig. 6.8. On this particular example, the CCD distortions induce up to 70 cm bias on the measured fault slip. Right lateral slip is determined by projecting the horizontal slip vectors along the fault strike. Horizontal slip vectors are measured from linear least-square adjustment, on each side of the fault and on each NS and EW images, of stacked profiles running perpendicularly to the rupture. Profiles are stacked over a width of 880 m and a length of 8 km.

This shows that the incorrect account for CCD distortions can lead to significantly biased measurements of fault slip. Thus, by correcting topographic and registration biases, the CCD calibration allows better accuracy of measurements in change detection applications.

6.5 Discussion and Conclusion

In this paper, we presented a methodology for in-flight calibration of the interior model of pushbroom satellites. This calibration mostly aims at correcting the CCD distortions which are the most common source of geometric artifacts encountered in these systems, and also any other stationary inaccuracies of the camera model. Interior orientation distortions are physically modeled as positioning errors on the location of the individual CCD elements, and must be properly accounted for during orthorectification. This methodology requires the use of a reference image, ideally orthorectified. The topography of the calibration site should then be known with high accuracy. In particular, we have presented the calibration of the SPOT 4- HRV1 panchromatic sensor, using a SPOT 5- HRG1 panchromatic image as

calibration reference. The test site was in California, where the $1/3$ arcsec (~ 9 m) NED DEM is available.

The effectiveness of the calibration process relies on two main assumptions regarding the stationarity of CCD distortions. It is first assumed that the CCD distortions are constant during the short acquisition time of the calibration image (typically <10 s). Corrections determined at each line can then be averaged to provide a more precise calibration. In some peculiar cases, it could be argued that some mirror oscillations during the acquisition could perturb the correction model, but, even if present, they in fact should be averaged to zero while averaging the corrections over all lines (high-frequency oscillations [81]). This first assumption is thus very likely to be valid. The strength of a particular calibration is its ability to be applied to images other than the image it has been derived from. However, doing so is only valid if the CCD distortions are constant over much longer periods (typically a few years), which is the second assumption made here. In the study presented, we applied successfully the correction derived from a 2000 image to a 1998 image. Also investigated but not shown here [82], the same calibration model was applied to acquisitions from 2004 and 2006. These images were acquired at different latitudes, i.e., 12°N instead of 34°N for the California image used to derive the calibration, and at different seasons (summer vs. winter), hence under different orbital conditions. In all these investigations, residual distortions were at most 0.02 pixel. This residual is higher than the expected calibration accuracy detailed (~ 0.005 – 0.01 pixel), but should be compared to the distortion errors when the calibration was not used, i.e., up to 0.12 pixel. The discrepancy, however, observed between the expected and the measured calibration accuracy can be explained by several factors:

- Already discussed, the CCD distortions may not stay perfectly constant over long periods, and the calibration derived from the 2000 image may not be entirely valid from 1998 to 2006.
- The reference SPOT 5 image may exhibit some CCD distortions [83], and the NED DEM used for orthorectification is not ideal either. Hence our ortho-reference image certainly does not allow for a perfect calibration.
- Three years separate the SPOT 5 reference image from the SPOT 4 image from which the calibration is determined. Decorrelations related to land cover changes are visible

in the correlation analysis of Fig. 6.4, and image-dependent biases may be present in the resulting calibration. For example, shadows on topographic features can bias the correlation analysis if the images are acquired at different seasons [8]. This could be minimized by averaging several calibrations derived from independent sets of images. Short acquisition periods between the reference and the calibration images should also be sought to minimize potential decorrelations.

- The mirror rotation of the calibration image is compensated for to derive a general calibration model, and then the mirror rotation of the image to be calibrated is accounted for to apply the correction. Mirror rotation angles are discretized every 0.6° , and these uncertainties add up to the final calibration inaccuracy. Again, averaging calibration models determined from sets of independent images should minimize the correction uncertainties.

Despite all these limitations, our results show that in-flight interior orientation calibration is beneficial, reducing internal camera biases by about one order of magnitude. Further work is still needed to better understand the cause and the time variability of the focal plane distortions, but we have shown that in the case of the SPOT 4-HRV1 panchromatic sensor, most of the CCD distortions could be thought of as stationary errors for periods as long as eight years, even on different orbits. This fact suggests that distortions may mostly result from mechanical effects during the satellite launch that later remained, and that effects of on-orbit thermal variations on the satellite structure may only account for a more negligible part. Therefore, in-flight interior orientation calibration is meaningful and should be generalized on all pushbroom systems designed to offer satisfying geometrical accuracy for, e.g., DEM generation and change detection applications.

The calibration models for the SPOT 2 and the SPOT 4 HRV1 panchromatic sensors described in this paper have been integrated to the free software package COSI-Corr (Co-registration of Optically Sensed Images and Correlation), developed with IDL (Interactive Data Language) and integrated in ENVI (Environment for Visualizing Images). This software is available from the Caltech Tectonics Observatory website (<http://www.tectonics.caltech.edu/>).

This study validates that the CCD elements of optical sensors are subject to positioning errors on the order of $1/10$ of the pixel size. Images acquired by such sensors are therefore not exactly regularly sampled. Most orthorectification procedures rely on inverse orthorec-

tification modeling where a regular grid on the ground is back-projected in the satellite image plane. The orthoimage is produced by resampling the raw image, assumed regularly sampled, at the grid points back-projected in the image plane. This formulation is thought to produce rigorously built orthoimages while avoiding the problem of irregular resampling posed by the direct orthorectification modeling [8]. Because raw images cannot be assumed strictly regularly sampled anymore, our study finally suggests that a more explicit account of the irregular resampling problem, as treated in [84] for instance, might help to further improve the quality of orthorectified images.

Chapter 7

The 2005, Mw 7.6 Kashmir Earthquake: Sub-Pixel Correlation of ASTER Images and Seismic Waveforms Analysis

By Jean-Philippe Avouac¹, François Ayoub¹, Sébastien Leprince¹, Ozgun Konca¹, and Don V. Helmberger¹

¹ Tectonics Observatory, Geology and Planetary Science Division, California Institute of Technology, Pasadena, California, USA

Foreword— This chapter has been published under the reference J.P. Avouac, F. Ayoub, S. Leprince, O. Konca, and D.V. Helmberger, “The 2005, Mw 7.6 Kashmir earthquake, rupture kinematics from sub-pixel correlation of ASTER images and seismic waveforms analysis,” *Earth and Planetary Science Letters*, vol. 249, no. 3–4, pp. 514–528, 2006. In this thesis, it is referred to as reference [9]. J.P. Avouac provided the global seismo-tectonic analysis of the study, while F. Ayoub and S. Leprince contributed in providing measurements of the co-seismic displacements using ASTER images. The technique described in Chapter 3 for SPOT images has been extended to ASTER images, as described in Appendix D, and integrated into COSI-Corr. O. Konca and D.V. Helmberger contributed in providing the seismological analysis and in deriving joint modeling of surface coseismic displacements and seismic waveforms.

We analyze the Mw 7.6 Kashmir earthquake of October 8, 2005, using sub-pixel correlation of ASTER images to measure ground deformation, and modeling seismic waveforms. The surface rupture is continuous over a distance of 75 km and cuts across the Hazara syntaxis, reactivating the Tanda and the Muzaffarabad faults. North of Muzaffarabad the surface rupture coincides approximately with the MBT, on the southwestern flank of the syntaxis, although the two faults have opposite dip angles. The rupture terminates abruptly at the hairpin turn of the MBT showing a strong structural control. The fault offset is 4 m on average and peaks to 7 m northwest of Muzaffarabad. The rupture lasted about 25 s and propagated updip and bi-laterally by 2 km/s, with a rise time of 2–5 s. The shallowness and compactness of the rupture, both in time and space, provides an explanation for the intensity of destructions. This kind of analysis could be achieved as soon as a post-earthquake image is available, and would provide key information for early assessment of damages. The study sheds some light on seismic hazard in the Himalaya, and raises concern regarding the possibility of a repetition of the 1555 event which presumably ruptured the Himalayan front south of the Kashmir basin and may have reached a magnitude $M_w > 8$.

7.1 Introduction

The Mw 7.6 earthquake, which struck Northern Pakistan and Kashmir on October 8, 2005, claimed a minimum of 80,000 lives. This is to-date the most devastating earthquake to have occurred along the Himalayan arc. Some earthquakes in the twentieth century have probably approached or exceeded Mw 8, in particular the 1934 Bihar-Nepal and the 1905 Kangra earthquakes [85], but they did not cause as many casualties as the 2005 event (Fig. 7.1). This is a sad reminder that seismic vulnerability has risen critically over the last few decades due to the growth of the population in the region and probably insufficient awareness of seismic hazard [86, 87]. Here, we report investigations of ground deformation in the epicentral area using optical images and measure the fault rupture by combining this information with an inversion of teleseismic body-waves. Our analysis of this particular event brings important information on the characteristics of Himalayan earthquakes, sheds some light on the active tectonics of the western syntaxis, and opens the way to a new approach for early assessment of damages.

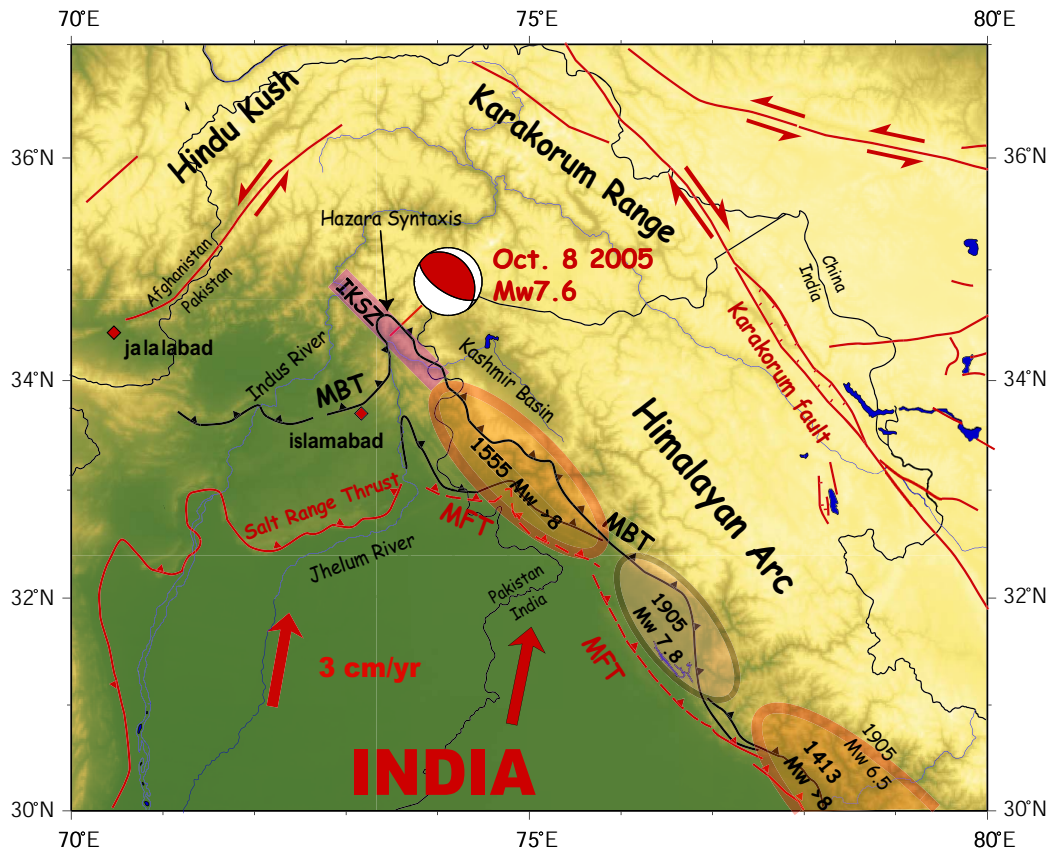


Figure 7.1: Tectonic setting of the October 8 2005 Kashmir earthquake. Rupture areas of major Himalayan earthquakes documented from historical studies [85] and paleoseismic investigations [88]. Shaded ellipses show estimated locations of ruptures in 1413, 1555 and 1905. Major active faults, modified from Yeats et al [89] and [88], are shown in red. Dashed lines indicate approximate location of blind thrust faults. Velocity of peninsular India relative to stable Eurasia computed from the Euler pole of the Indian plate determined by Bettinelli et al. [90]. MFT: Main Frontal Thrust fault. MBT: Main Boundary Thrust fault. IKSZ: Indus Kohistan Seismic Zone [91].

7.2 Remote Sensing Analysis

We measured ground deformation in the epicentral area from the sub-pixel correlation of ASTER images acquired on November 14, 2000, and October 27, 2005 (Fig. 7.2). We use a new procedure [8] adapted from a previous approach that had been designed specifically for processing SPOT images [1] and which has been applied to a few events [10,11,19,20,63]. A similar approach has been recently applied to ASTER images on the Kokoxili earthquake, yielding mitigated results [92]. The images are orthorectified on a common 15-m-resolution grid using a DEM computed from a stereo pair of ASTER images. Offsets are then measured from the local cross-correlation of the two orthorectified images. Uncertainties on the imaging system, in particular on the satellite orbit and attitude, and on the topography can lead to apparent offsets unrelated to ground deformation. The satellite viewing parameters are optimized to minimize these artifacts. This process partially removes the deformation at long wavelengths, which trade off with satellite viewing parameters, but significantly enhances the performance of the sub-pixel correlation technique for the measurements of deformation at short wavelengths [8]. The resulting offset field is therefore a reliable measurement of ground displacement at shorter wavelengths (typically a few kilometers). Our measurements reveal a clear discontinuity which can be traced over a distance of about 75 km in the offset field both on the north-south (Fig. 7.2) and east-west (Fig. 7.3) components.

Despite the five year interval between the two images, the correlation is good, except at locations where major landslides were triggered by the earthquake (Fig. 7.4). We analyzed a second pair of ASTER images to evaluate the possible continuation of the rupture to the southeast. The resolution on the measurement of ground displacements is not as good as for the first pair because the two images were taken in different seasons (in April and November) and do not correlate as well (Fig. 7.5). The fault trace can not be traced beyond the area covered by the first pair of images. The horizontal slip vector on the fault can be measured accurately from profiles run across the fault trace (Fig. 7.2). The discontinuity is sharp, with deformation localized within a zone no wider than a few hundred meters. It clearly indicates that the rupture reached the surface, as confirmed by field investigation [93] (see also <http://www.geo.oregonstate.edu/people/faculty/yeatsr.htm>, personal communication from Paul Tapponnier) and inspection of high-resolution optical images (personal communication

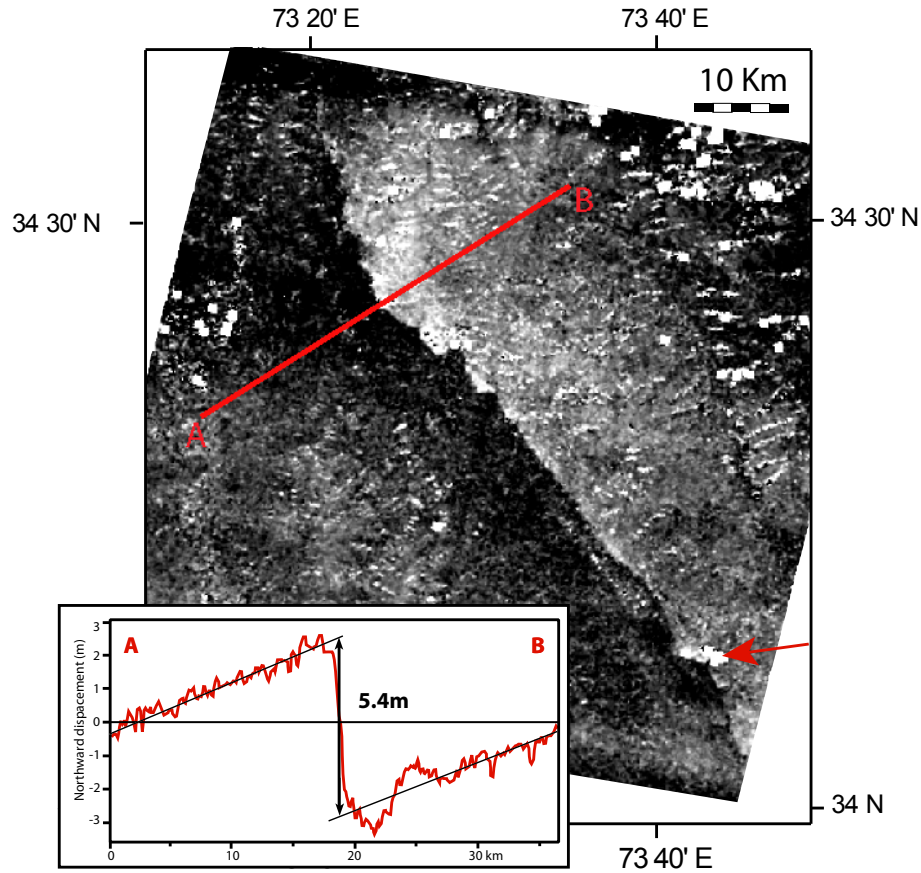


Figure 7.2: Displacements measured from sub-pixel correlation of ASTER images. Northward ground displacements (white to the south, black to the north), determined from the correlation of ASTER images, with a 15 meter ground resolution, taken on November 14, 2000 (AST_L1A.003:2003527667), and October 27, 2005 (AST_L1A.003:2031572195). The incidence view is 8.6° for both images. The correlation image was obtained with a sliding 32×32 pixel correlation window and 8 pixel step. Ground resolution on the correlation image is 120 m. No measurement is assigned to white points, where the correlation is lost or where outliers (where the measured ground displacement was found to exceed 10 m) have been filtered out. Correlation is lost mainly due to landslides or variation of the snow cover. For example, the red arrow points to an area where the correlation is lost due a major landslide. Outliers are mostly due to shadowing effects. Inset: Profile of the NS component of ground displacement obtained by stacking all measurements within a 9-km-wide swath centered on profile AB.

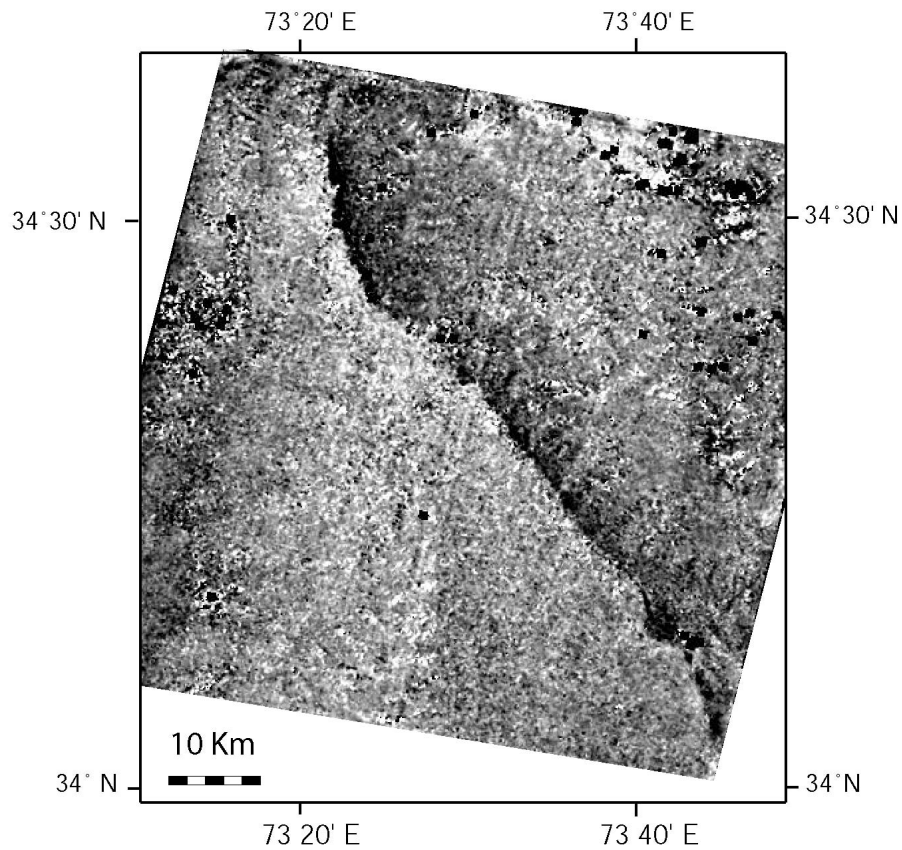


Figure 7.3: E-W ground displacements measured from sub-pixel correlation of ASTER images. E-W ground displacements (white to the east, black to the west), determined from the correlation of ASTER images taken on November 14, 2000, and October 27, 2005. The image was obtained with a 32×32 correlation window and 8 pixel step.

from Laurent Bollinger). Along the northern termination of the rupture, near Balakot, field investigations have revealed a fold scarp rather than clear ground ruptures [93]. The displacement field measured from our technique shows a rather clear discontinuity in this area suggesting that, even there, the rupture must have reached very close to the surface. Along the upper Jhelum valley the fault trace is remarkably linear and follows the northeastern flank of the valley for about 30 km north of Muzaffarabad along the previously mapped Tanda fault [94](Fig. 7.6). The fault trace curves and becomes more irregular where it joins the Muzaffarabad fault and cuts across the Kunhar valley. The irregularity of the fault trace to the north is mainly due to the roughness of the topography. The spatial variation of intersection of the fault trace with the topography shows a northeast dip angle. The fault trace makes a “v” where it cuts across a topographic ridge south-east of the upper Jhelum river valley (box in Fig. 7.6). From this geometry the near surface dip angle is inferred to be about 10° . The fault’s complexity across the Neelum river valley probably corresponds to a tear fault connecting the Muzaffarabad and the Tanda faults.

Horizontal slip vectors were determined about every 2 km along the fault trace from the discontinuity of ground displacement measured along profiles run across the fault (Fig. 7.7). The amplitude of the horizontal slip vector reaches a maximum of 7.15 ± 0.4 m about 10 km northwest of Muzaffarabad (Fig. 7.7). We observe a local minimum at the junction between the Tanda and the Muzaffarabad faults. Surface slip varies quite significantly along the Muzaffarabad fault and tapers abruptly at the northern end of the rupture with a steep gradient of about one meter per kilometer over a distance of about 5 km. Along the straight fault segment of the Tanda Fault the horizontal slip is nearly constant, around 4 ± 0.8 m. As the rupture approaches its crossing of the Upper Jhelum river, slip diminishes to just 1.5 m, again at a rate of about one meter per kilometer. In the hills further south, slip magnitude rises as high as 3.5 m, but has much more variability. The rupture is nearly pure dip-slip, as the azimuth of horizontal slip motion is on average $N41^\circ E$ —nearly perpendicular to the $138^\circ E$ average strike of the fault trace.

7.3 Seismological Analysis

The Harvard CMT solution, determined from the modeling of the long period surface waves, yields a northeast dipping fault plane striking $N133^\circ E$, with a rake of 123° , and a dip an-

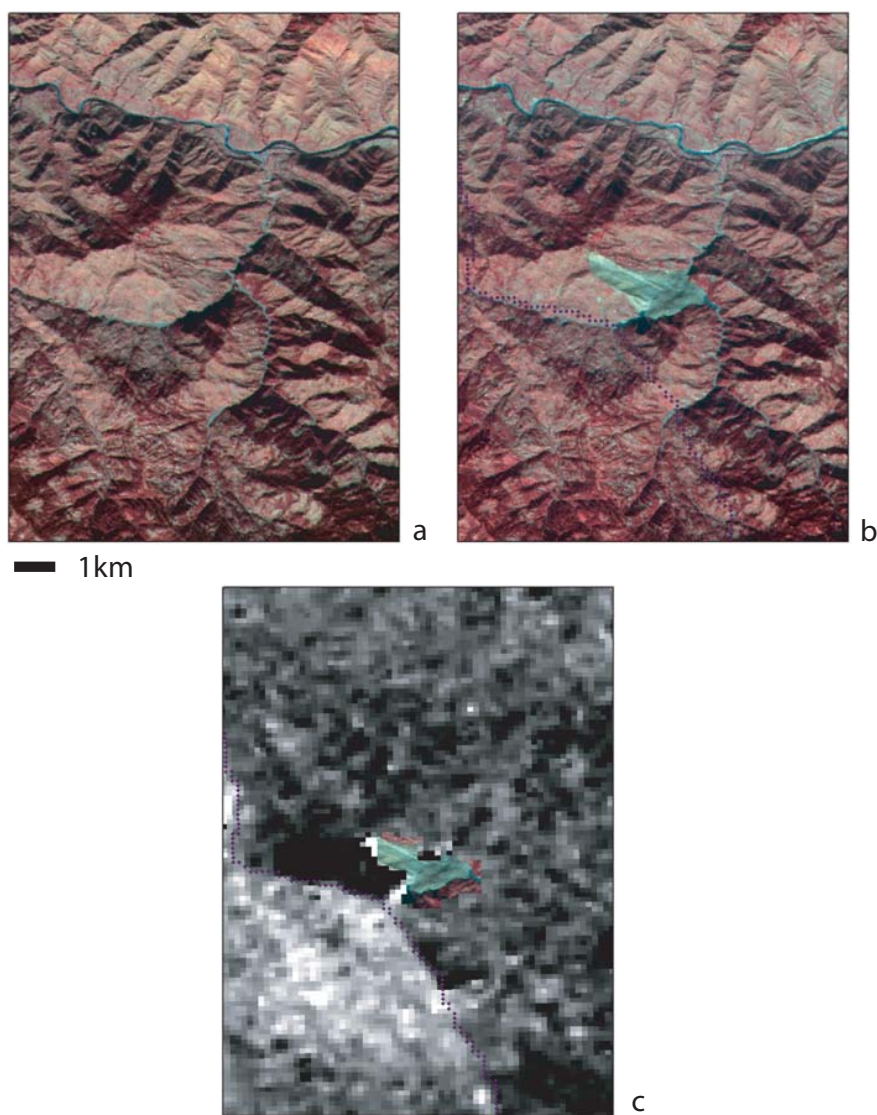
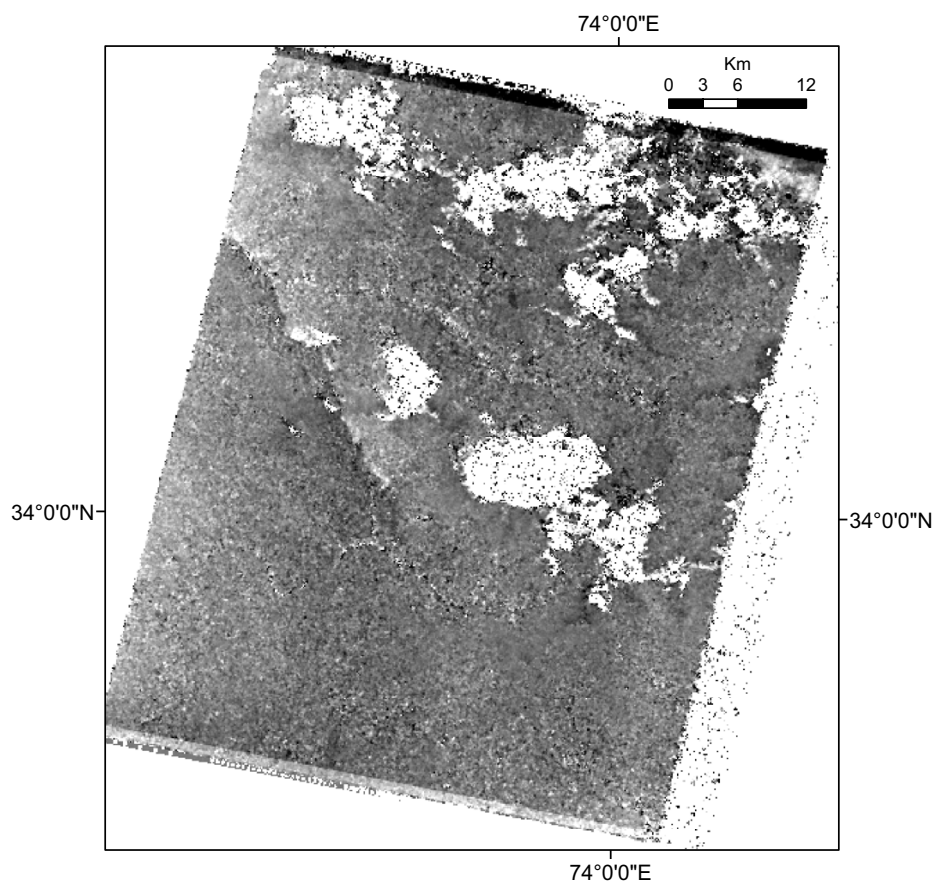


Figure 7.4: Example of decorrelation due to landsliding. Close up view of a landslide area on the ASTER image taken on November 14 2000 (a) and October 27 2005 (b) The landslide shows up in green in b and corresponds closely to the area where correlation is lost. Other ASTER views of this landslide processed by Eric Fielding are accessible at (<http://earthobservatory.nasa.gov/NaturalHazards/>), and field pictures by Bob Yeats at <http://www.geo.oregonstate.edu/people/faculty/yeatsr.htm>. Blue dots follow the fault trace mapped from the discontinuity in the offset field.



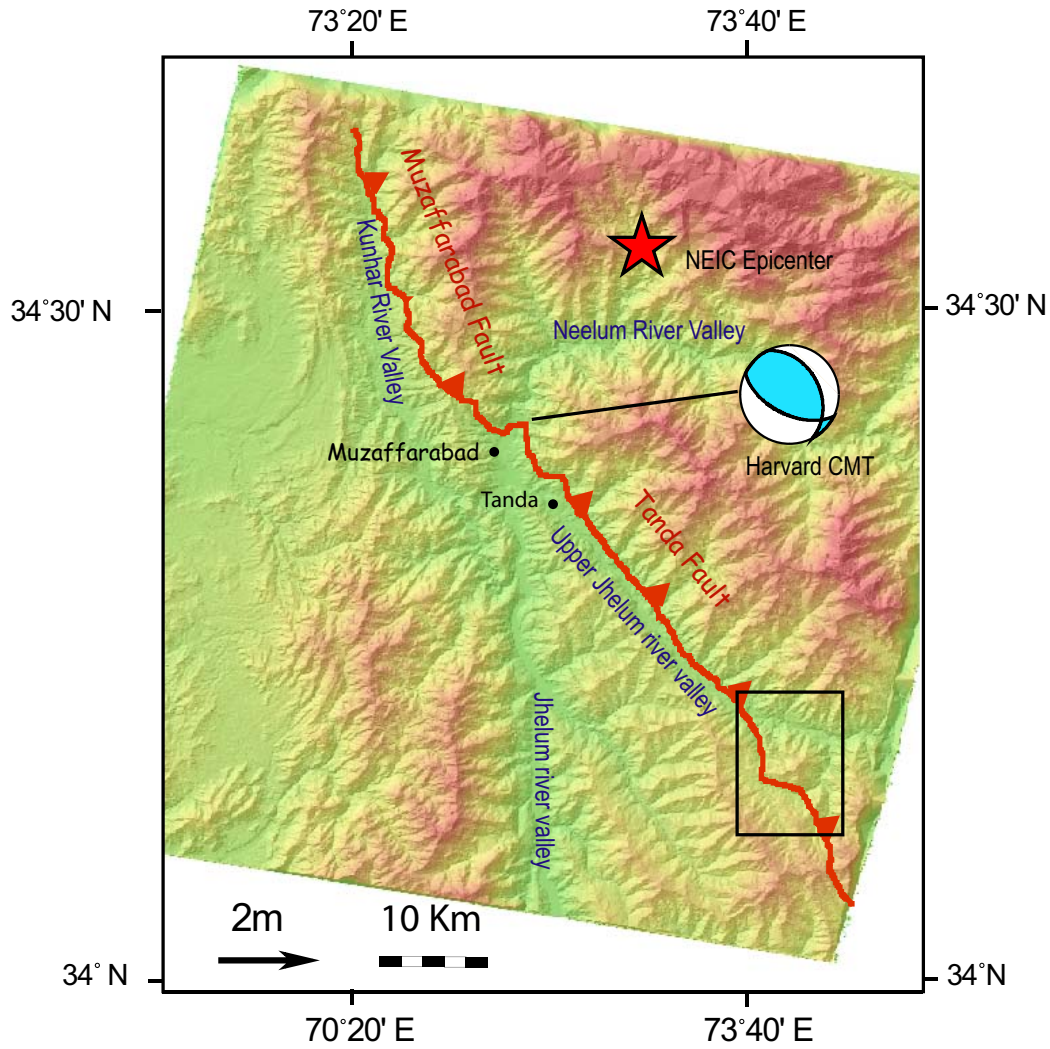


Figure 7.6: Surface fault trace mapped from the discontinuity of the offset field (Fig. 7.3 and Fig. 7.4). The rupture geometry across the Neelum River and south of the Jhelum river valley (Box) indicates a shallow, 10° , dip angle near the surface.

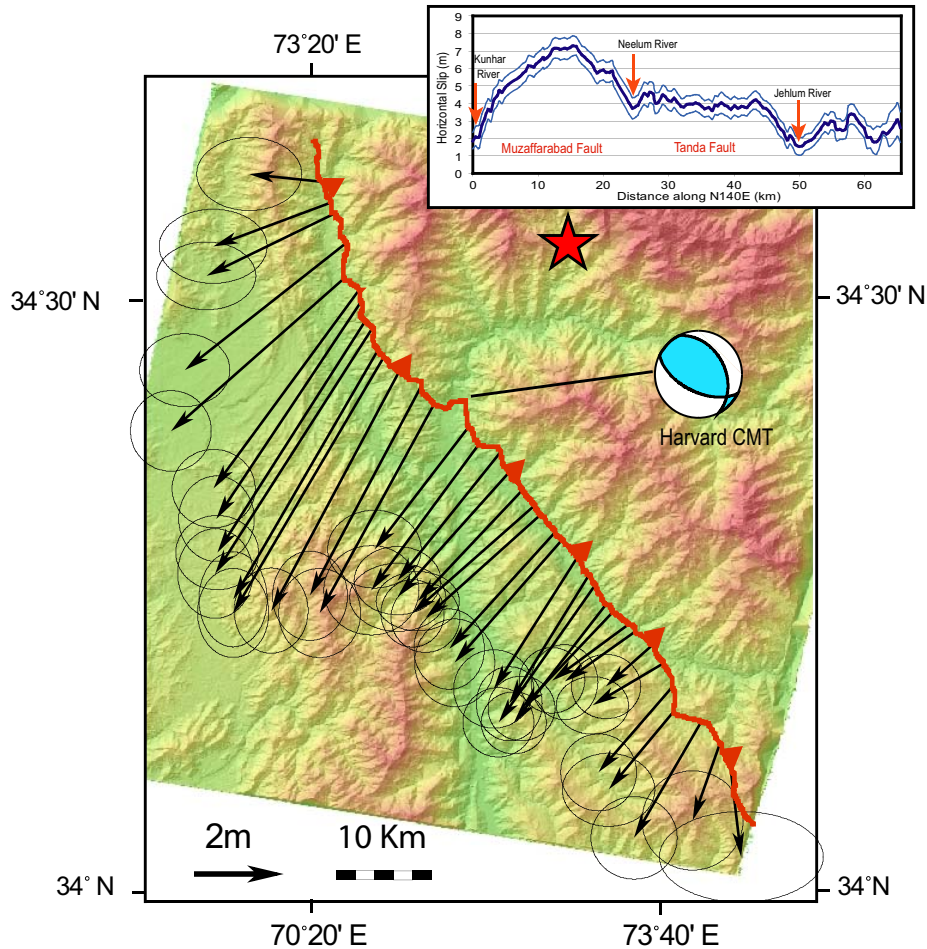


Figure 7.7: Surface fault slip. Horizontal slip vectors at about 2 km spacing along the fault trace, measured from the discontinuity of E-W and N-S ground displacement measured at the fault on 18-km-long, 6-km-wide profiles run perpendicular to the fault. NS and EW offsets at the fault are measured from linear least-squares adjustment on each side of the fault. Ellipses show 2-sigma uncertainties on each measurement. Inset: Surface fault slip and 1-sigma uncertainty projected along N140°E. Each measurement is determined from the offset at the fault of the N-S and E-W component of the offset field measured along 18-km-long and 6-km-wide profiles.

gle of 40° (<http://www.seismology.harvard.edu/CMTsearch>) (Fig. 7.6). The corresponding seismic moment is 2.94×10^{20} N.m. Given the relatively shallow hypocentral depth, the dip angle is not well constrained from the long period surface waves. For comparison, the focal mechanism determined by the USGS from body waves indicates a fault strike of 133°E , a rake of 140° , and a dip angle of 29° (<http://neic.usgs.gov>). These source parameters are consistent with the $\text{N}138^\circ$ fault strike determined in our study and imply a somewhat larger strike-slip component of slip than the surface slip vectors determined from the remote sensing analysis. A finite source model has also been obtained from the inversion of the teleseismic body waves by Parsons et al. [95]. This model assumes a single planar fault segment striking 108°E and dipping 31° to the northeast and a nucleation point at the USG epicenter. The model shows two distinct asperities about 30 km apart, with the nucleation point in between, and at depth shallower than about 10 km. Our measurements suggest a different fault geometry, and the slip distribution at the surface does not show two distinct asperities. We have determined a finite source model from the modeling of teleseismic waveforms, in the 0.01–1 Hz frequency band, following the procedure of Ji et al. [96]. Fault geometry with two fault segments, a 60-km-long southern segment striking 320° , and a 15 km long northern segment striking 343° , was constructed based on the observed surface break derived from our remote sensing analysis. These two segments approximately coincide with the Tanda and the Muzaffarabad faults, respectively. The slip vectors on the subfaults closest to the surface were constrained to fit the surface slip measurements to within 2-sigma. We thus assume that all of the measured slip at the surface occurred during the seismic phase, ignoring the possibility that some of it would be due to shallow afterslip over the first 3 weeks following the earthquake. In the absence of near fault continuous geodetic measurements, we cannot test this hypothesis. We selected a set of P-wave records providing the best possible coverage in azimuth and distance (Fig. 7.8). We tested various dip angles between 25° and 40° and found that the polarity of the P and S wave first motions were best adjusted with a dip angle of 29° , consistent with the USGS determination. We used the USGS epicenter, which is accurate to about 20 km, to estimate the rupture initiation depth. Given the fault geometry, as defined from the fault trace at the surface and the best-fitting dip angle, this assumption implies a hypocentral depth of 11 km. The best-fitting model shows a simple source with a relatively compact high-slip zone spanning the Tanda and Muzaffarabad faults and mostly updip of the nucleation point

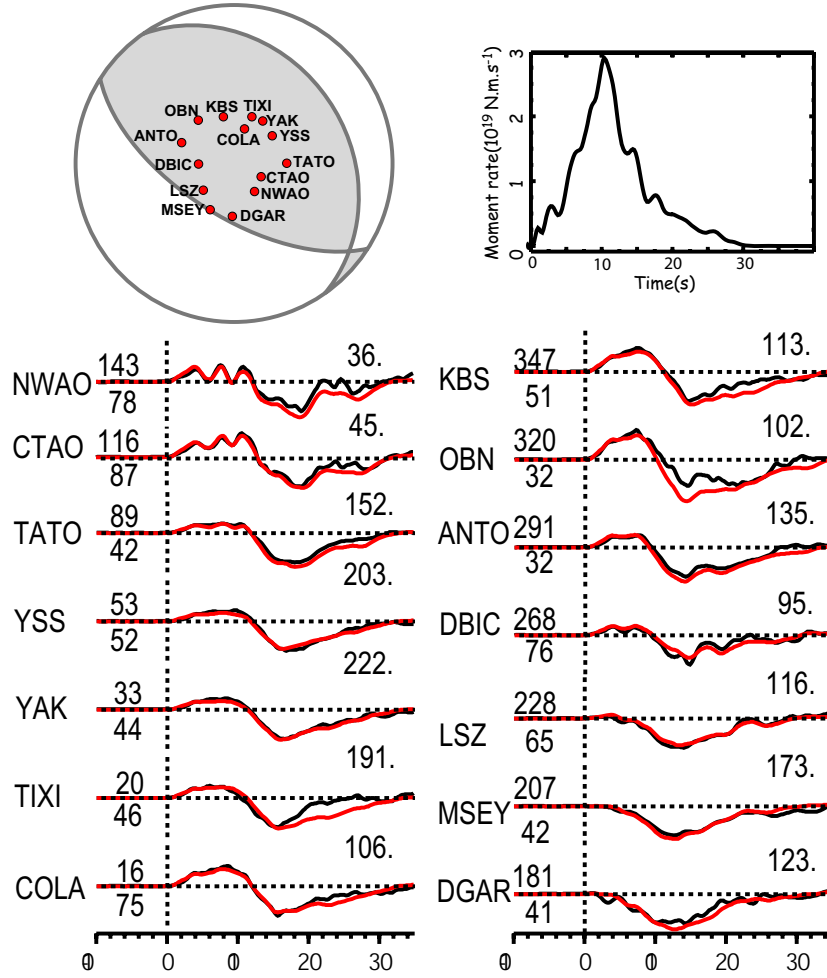


Figure 7.8: Modeling of teleseismic waveforms (P waves) using the source model derived from the joint inversion of waveforms and surface slip. Measured (black) and modeled (red) seismograms. The location and the stations with respect to the focal mechanism representation of the finite source model is shown on top left. The moment release time function is shown on top right.

(Fig. 7.9). The preferred model has a nearly constant rupture velocity of about 2 km/s and a short rise time between 2 s and 5 s (Fig. 7.8). Forcing rise times to be longer than 5 s degrades the solution (the misfit to the waveforms increases from 17.5% to 20.8%), despite the trade-off with rupture velocity. The focal mechanism representation of our finite source model is close to the Harvard CMT (Fig. 7.9), and the released moment is 2.82×10^{20} N.m, only 4% smaller. This shows that our source model is consistent with the source model derived from the surface waves.

We have also determined a source model by inverting the teleseismic waveforms only, i.e., without any constraints on surface slip, but with the fault geometry derived from the

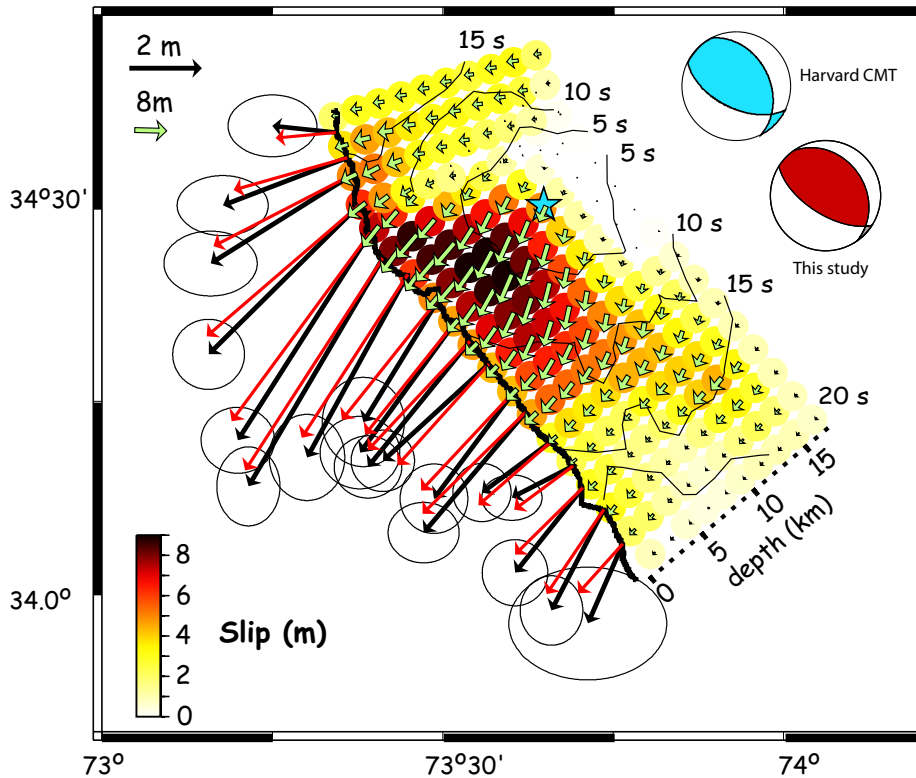


Figure 7.9: Slip distribution derived from the seismic waveforms and surface slip distribution. Modeled slip distribution and isochrones showing the rupture kinematics obtained from the modeling of teleseismic bodywaves. The fault geometry consists of two planar fault segments following the fault trace, subdivided in the horizontal and downdip direction in 2 km by 3 km cells. The star shows the location of the nucleation points, on the fault plane, assumed to coincide with the USGS epicenter ($34.493^{\circ}\text{N}, 73.629^{\circ}\text{E}$). Seismic waveforms and surface displacements are computed in a layered half space with a 1-D crustal model interpolated from CRUST2.0 [97]. Horizontal slip vectors measured along the surface fault trace (black arrows with 2-sigma uncertainty ellipses) are compared to the theoretical displacements (red arrows) computed using the method of Xie and Yao [98]. Green arrows show slip vectors on the fault plane at depth. The double-couple component of the seismic moment tensor computed from the summation of the seismic moment of each subfault of our model (red) is compared with the Harvard CMT (blue).

surface fault trace. The solution is similar to that obtained from the joint inversion, showing a higher amplitude strong asperity roughly at the same location (Fig. 7.10). This source model yields a moment release that underestimates the Harvard CMT solution by 12%, and the misfit to the seismic waveforms is equivalent (17.8%) to that obtained from the model ignoring the constraints on surface slip. The predicted surface slip vectors systematically underestimate the measurements. Therefore, shallow slip is clearly underestimated in this model. The main reason is that the seismological waveforms are not very sensitive to slip at shallow depth (less than 2–3 km), where the elastic moduli are assumed low, because it doesn't contribute much to the seismic moment release. The slip distribution at shallow depth in the joint inversion is thus highly constrained by the surface measurements, while the slip distribution at depth more than about 5 km is constrained primarily by the seismic data. The slip distribution obtained from the joint inversion shows a good consistency between the slip distribution at depth and near the surface, except along the northern fault portion where the quite shallow slip is required only to fit the surface fault slip.

We have also tested the sensitivity of the source model to the assumed location of the epicenter. For example, we show in Fig. 7.11 the solution obtained by moving the nucleation point 12 km to the northwest relative to that determined by the USGS. This particular position was tested to check the shallowness of the slip distribution along the northern portion of the fault. The solution yields about the same fit to the waveforms and surface measurements (Fig. 7.11). The main difference is that more slip at depth on the Muzaffarabad fault segment is now inferred. The high slip patch there, with about 14 m of slip at 5–10 km depth, is required for the seismic rupture to be still essentially bilateral, despite the position of the nucleation being close to the northern termination of the fault. The models obtained from seismological inversion are thus quite sensitive to the assumed position of the epicenter and fault geometry. Two robust features are that the rupture was confined to relatively shallow depth, less than about 10 km, and was bilateral. It turns out that the source model obtained assuming that the USGS epicenter is correct (Fig. 7.4) is relatively satisfying, in particular because the slip distribution is not too patchy, showing a consistent pattern near the surface, where it is constrained from our ASTER measurements, and at depth, where it is constrained from the seismic data. The source models derived from the inversion of the seismic waveforms with account for the correct location and geometry of the fault are in fact a good first-order approximation. Such models would probably be

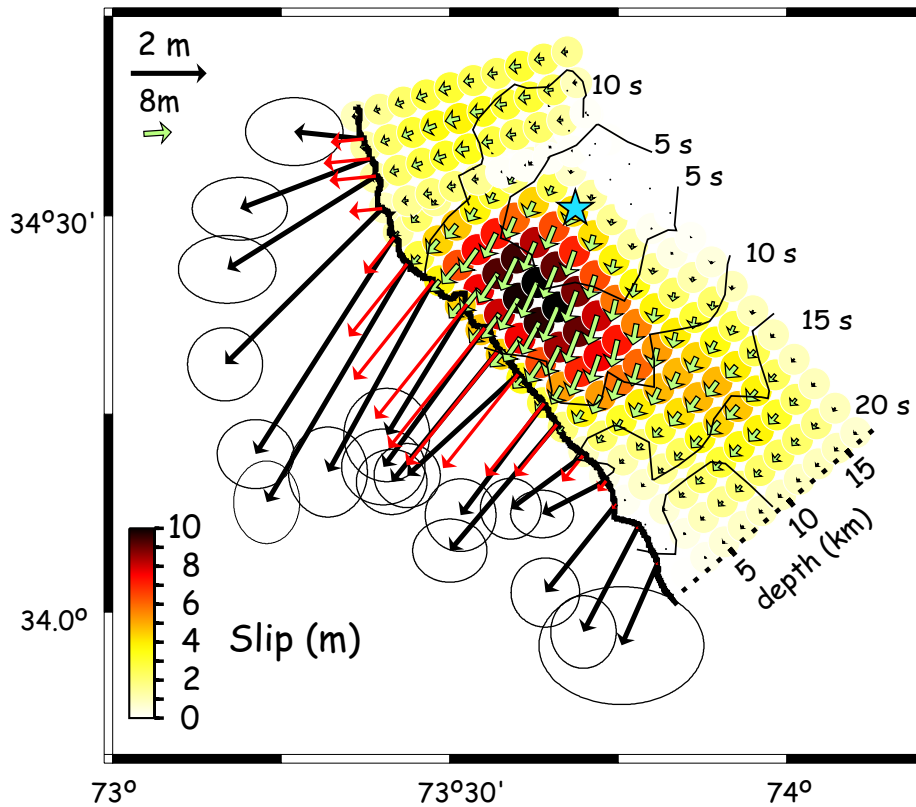


Figure 7.10: Slip distribution derived from the modeling of seismic waveforms without constraints on surface slip. Modeled slip distribution and isochrons showing the rupture kinematics obtained from the modeling of teleseismic bodywaves. Horizontal slip vectors measured along the surface fault trace (black arrows with 2-sigma uncertainty ellipses) are compared to the theoretical displacements (red arrows) computed using the method of Xie and Yao [98]. Green arrows show slip vectors on the fault plane at depth. The fault geometry is the same as in Fig. 7.3. The released moment is 2.59×10^{19} N.m, about 12% less than the value associated with the Harvard CMT solution.

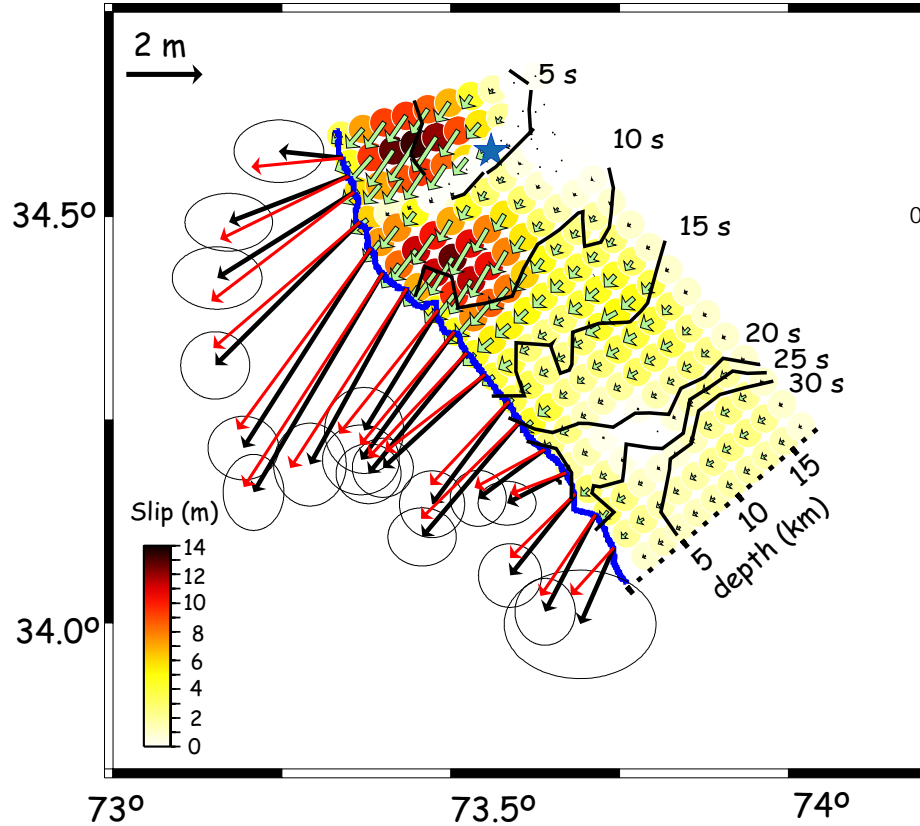


Figure 7.11: Slip distribution derived from the seismic waveforms and surface slip distribution assuming an epicenter 12 km northwest of that determined by the USGS. Modeled slip distribution and isochrones showing the rupture kinematics obtained from the modeling of teleseismic body waves. The fault geometry consists of two planar fault segments following the fault trace, subdivided in the horizontal and downdip direction in 2 km by 3 km cells. The star shows the location of the nucleation points, on the fault plane, at 34.58°N, 73.56°E.

enough for a reliable early assessment of nearfield effects.

7.4 The 2005 Kashmir Earthquake in Its Neotectonic Setting

The 2005, Mw 7.6 Kashmir earthquake occurred at the western extremity of the Himalaya, where the arc joins the Karakorum, Pamir, and Hindu Kush ranges (Fig. 7.1). The physiography of the range, as well as geological structures define a syntaxis, called the Hazara syntaxis (or Kashmir-Hazara syntaxis), outlined by the hairpin turn of the Main Boundary thrust fault (MBT) [99]. The MBT is a major fault bounding the Himalayan range that has thrust metasediments of the Lesser Himalaya over the Tertiary molasse of the Himalayan foreland [100] (Fig. 7.1). Active deformation in the area results from the 31 mm/yr north-

ward indentation of the northeastern Indian Peninsula into Eurasia [90] (Fig. 7.1). Along the northwestern Himalaya a fraction of that convergence, estimated to about 14 mm/yr [101], is absorbed by thrusting perpendicular to the range. The most active thrust fault under the Himalaya is generally thought to be the Main Frontal Himalayan Thrust fault (MFT) which marks the emergence at the surface of the Main Himalayan thrust fault (MHT), which is the basal decollement beneath the Himalayan orogenic wedge [102]. Between the Hazara syntaxis and about 76°E, the MHT is mostly blind as slip tapers below fault-tip folds [89, 91]. The MHT has produced very large recurrent earthquakes with magnitudes possibly as high as Mw 8.8, as documented from paleoseismic investigations: along the Himalayan foothills in Nepal, there is evidence for a 17+5/-3 m slip event around 1100 AD at locations separated by 240 km along strike [103]; evidence for a similar event were also found in the Kumaon and Garhwal Himalaya and dated to around 1413 A.D [88]. The loose chronological constraints are such that this rupture could correspond to the historical earthquake of 1505 AD (personal communications by Tom Rockwell and Bob Yeats) (Fig. 7.1). Four major earthquakes with magnitudes close to Mw 8 occurred along the Himalaya between 1897 and 1950 [85] but none of these earthquakes was associated with a surface break. In particular, the Mw 7.8, 1905 Kangra event, which occurred along the Himalayan front southeast of Kashmir Basin and presumably ruptured the MHT but which did not reach the surface [104] (Fig. 7.1). The largest historical event in the northwestern Himalaya occurred in 1555 A.D. Historical accounts report evidence for liquefaction and major geomorphic effects mostly in the Pir Panjal Range south of the Kashmir Basin [105] (<http://asc-inia.org/gq/1555kashmir>). This event may have ruptured some of the active faults mapped within the Kashmir basin itself [89] but rupture of the decollement beneath the Basin and the Pir Panjal Range seems more plausible to us. The magnitude of that earthquake remains conjectural. Given the reported effects, which suggest that MMI intensities reached XII, and the 2 month duration over which aftershocks were felt, a magnitude larger than 8 is probable [85] (Fig. 7.1). Monitoring by a local seismic network around the Hazara syntaxis has revealed an alignment of seismicity, which is called the Indus-Kohistan Seismic Zone (IKSZ, Fig. 7.1) [91]. The IKSZ strikes parallel to the northwestern Himalaya, but extends beyond the Hazara syntaxis. This seismicity extends northwestwards the belt of seismic activity that follows the front of the entire Himalayan arc [106, 107]. This is an indication that northwest trending Himalayan basement structures extend beyond the

syntaxis and that the change in the strike of the MBT is a rather superficial feature, probably related to the infracambrian salt [91]. Along the central-Nepal Himalaya the belt of seismicity has been shown to mark the downdip end of the locked portion of the MHT where interseismic stress accumulation is highest [107,108]. It has been deduced that large earthquakes break the MHT updip of this seismic zone.

7.5 Discussion

7.5.1 Performance of the Sub-Pixel Correlation of Optical Images

Despite the 5 year time difference between the two ASTER images, their sub-pixel correlation has provided a detailed description of the surface slip distribution with an accuracy not achievable by other techniques. Near the near fault zone, our technique performs better than SAR interferometry because the coherence of SAR is often lost due to too high strain or the effect of ground shaking, or because the fringe rate exceeds the limit of one pixel-per-fringe. Cross-correlation of SAR amplitude is an alternative approach [61] which has been successfully applied to this particular earthquake [109,110], but the accuracy is not as good as what we have obtained with optical images regarding the details of the rupture geometry and the measurement of surface slip. The correlation of SAR amplitude images does however provide constraints on the vertical component of displacements which are not accessible from optical images. Compared to field investigations, our technique provides the two components of horizontal surface slip, whereas the component of displacement normal to the fault trace is generally not measurable in the field, and also, it takes into account deformation off the main fault trace that is generally missed during field surveys.

7.5.2 Characteristics of the Seismic Rupture

The 2005 Kashmir earthquake appears to be a simple shallow crustal event with a relatively compact slip distribution, a standard sub-shear rupture with a rather short rise time. The updip propagation of the rupture together with its steep dip angle and shallow distribution of slip must have contributed to the heavy damages in the nearfield. This event shares some similarities with the 1999, Chichi Mw 7.6 earthquake, for which a well-constrained slip model has also been obtained from the joint analysis of geodetic and seismic waves [111] and which ruptured a thrust fault along the western foothills of Taiwan in a tectonic setting

very similar to that along the Himalayan front. In both cases, the rupture nucleated on the bottom edge of the asperity, and was restricted at depth shallower than about 15 km on relatively steep thrust faults. The shallow depth of the slip distribution is consistent with the view that deformation becomes dominantly aseismic at depth greater than about 15 km due to the transition from stick-slip to stable frictional sliding as temperature rises above 250–300°C [112,113]. The short rise time of just 2–5 s is also a characteristic of both the Kashmir and the Chichi events, and seems typical of intracontinental events as shown from other case examples of joint inversion of seismic waveforms and geodetic data [96,114–116]. By comparison, subduction events have similar rupture velocities, but seem to be characterized by much longer rise times, and hence produce less severe ground shaking [117]. Finally, we notice that the earthquake nucleated near the junction between the Tanda and the Muzaffarabad faults.

7.5.3 Relation to Known Active Faults and Geological Structures

The 2005 Kashmir earthquake ruptured major faults including fault segments along the Tanda and Muzaffarabad faults which had already been identified and mapped as an active fault [94, 118] (note that the whole rupture is referred to as the Balakot-Bagh fault by Parsons et al. [95] and the Geological Survey of Pakistan). Geomorphic evidence for activity of the Tanda fault is clear too; well developed triangular facets bound the northeastern flank of the valley; the topography northeast of the valley is systematically higher and more rugged than on the southwestern side of the valley; rivers—in particular the Neelum River—are systematically more entrenched into the hanging wall. Evidence for recent activity along the Muzaffarabad fault is more subtle: some triangular facets are apparent on the east of the Kunhar valley (Fig. 7.6); also, the topography is higher on the eastern side of the Kunhar valley. This is the opposite of what one would expect given that the eastern side consists of the Murree molasse, a formation much more readily erodable than the Proterozoic metasediments on the western side of the valley. It is interesting to note that the Muzaffarabad fault which has thrust the Murree formation and underlying Precambrian limestones and shales over Proterozoic formations, parallels the MBT [119] (Fig. 7.12) but has the opposite sense of motion and dip. This is consistent with the observation of a recent reversal of the sense of motion on the MBT [118]. It illuminates Armbruster et al.’s observations that recent deformation cuts across the syntaxis [120]. The fact that

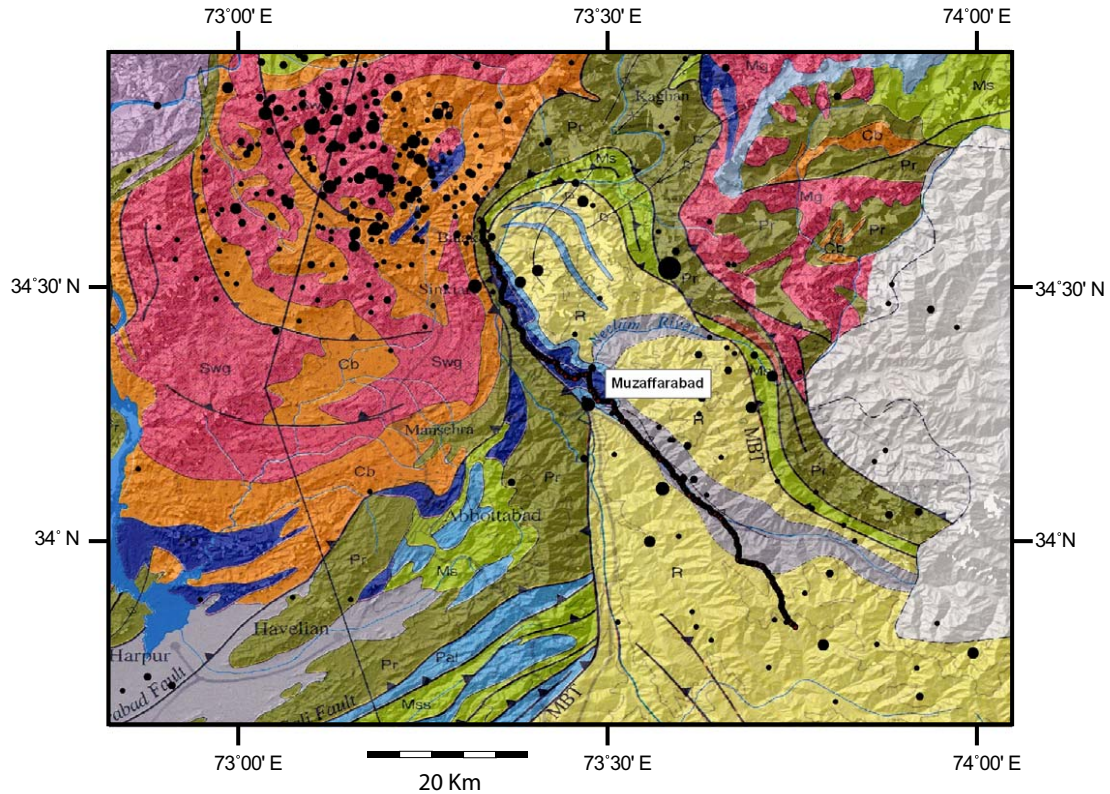


Figure 7.12: Comparison of ruptured fault trace with bedrock geology. Geological map from Searle et al. [119]. Black dots show aftershocks up to December 31, 2006, with $m_b > 4$. The fault rupture coincides with the Muzaffarabad fault [118] northwest of Muzaffarabad. Southeast of Muzaffarabad, along the upper Jhelum river valley, it has reactivated the Tanda fault [94]. The fault thrusts Precambrian limestone and shales (Pz, shown in blue) over Tertiary molasse of the Murree formation (R, shown in yellow) or over Proterozoic schists (Pr, shown in green). The Muzaffarabad fault parallels the Murree thrust, which is a segment of the Main Boundary Thrust (MBT), but has as sense of motion opposite to the long term geological motion. Southwest of Muzaffarabad the fault cuts through the Murree formation.

surface ruptures along the Muzaffarabad fault parallel the MBT and terminate abruptly at the hairpin turn of the MBT is a clear indication for a strong structural control of the earthquake rupture. We also observe that the surface slip is relatively uniform along the straight fault segment along the Upper Jhelum river, suggesting that variability of the slip and geometric complexity are correlated and decrease with cumulative geological offset [121]. It is noteworthy that the aftershock activity does not correlate well with the extent of the surface ruptures and was particularly intense beyond the abrupt northern termination of rupture (Fig. 7.12), along the IKSZ.

7.5.4 Importance of Out-of-Sequence Thrusting for Seismic Hazard Along the Himalayan Arc

The 2005 Kashmir earthquake might be compared to the most recent damaging earthquakes along the Himalaya, the Ms 7.1 Uttarkashi earthquake of 1991 [122] and the Ms 6.6 Chamoli earthquake of 1999 [123] which both occurred in the Garhwal Himalaya. Both earthquakes were caused by the rupture of blind thrust faults dipping about 10° to the north, probably on the deep portion of the MHT. In contrast, the Kashmir earthquake was not on the basal detachment. Instead it occurred on a relatively steep fault that splays upward from it, like probably the 1974 Pattan earthquake [124]. One might wonder whether such out-of-sequence thrust events, potentially much more damaging than the Chamoli or Uttarkashi earthquakes, should be expected elsewhere along the Himalaya. Evidence for brittle faulting along the front of the high range have been reported elsewhere, in particular in the Nepal Himalaya, showing that out-of-sequence thrusting can indeed occur [125] possibly as a response to locally enhanced erosion [126]. However, for the Nepal Himalaya it can be argued that such out-of-sequence thrust events must be rare. Indeed, the observation that the geological slip rate of the MFT [127] is not significantly different from the geodetic convergence rate across the central Nepal Himalaya [90], implies that most of the shortening is localized on the MHT, probably as a result of repeated $M > 8$ large earthquakes. Elsewhere along the arc the situation might be different. However, it might be that the particular setting of the Kashmir event near the western syntaxis makes out-of-sequence thrust events more frequent than along the main stretch of the Himalayan arc. Thrust faulting within the orogenic wedge might be the mechanism by which the wedge maintains its critical slope in response to the particularly rapid erosion rates in the Hazara syntaxis [128] and eventually to spreading of the thrust sheet due to aseismic creep along the basal detachment.

7.5.5 Return Period of Major Earthquakes Across the Himalaya of Kashmir and Himachal Pradesh

The average slip on the fault patch ruptured by the 2005 Kashmir earthquake is 4.2 m. If the geodetically determined 14 mm shortening rate across the range were accommodated by the repetition of such earthquakes, their return period along this particular segment of the arc would be about 300 yr. Given the 600 km length of the stretch of the Himalayan arc

between the Hazara syntaxis and Dehra Dun (corresponding to the area pictured in Fig. 7.1), the return period of such events over the whole area would be about 30 to 40 years. The historical catalogue is well short of such events. It seems therefore likely that shortening across the northwestern Himalaya is primarily the result of less frequent but significantly larger events, the 1555 A.D. event being one of these. Stress redistribution during the Kashmir event must have increased the stresses on the major thrust faults south-east of the Hazara syntaxis and therefore increased the probability of a new seismic rupture in the Himalaya of Kashmir and Himachal. By contrast this event does not seem to have increased the probability of an earthquake along the Salt Range Thrust [95], even more so if the Salt Range thrust is creeping aseismically due to the Infracambrian salt layer at the base of the thrust sheet [91], but this idea remains to be tested from geodetic measurements.

7.6 Conclusion

The Kashmir 2005 earthquake is the first modern earthquake in the Himalaya to produce documented surface rupture. Despite the complex geological setting associated with the Hazara syntaxis, the slip pattern and source kinematics are relatively simple. This earthquake occurred along the seismicity belt which follows the front of the high range all along the arc, but it departs from previous events with similar magnitudes since it was caused by rupture of a steeply dipping thrust fault that broke all the way to the surface. The 2005 Kashmir event shows that seismic hazard related to out-of-sequence thrusting in the Himalaya can be devastating and should not be overlooked, although major events along the MHT seem much more probable. The 2005 earthquake must have increased the probability of rupture along the MHT or possible out-of-sequence thrust faults along the Himalayan front to the south east, with the possible repetition of events such the 1555 AD earthquake. The death toll in such an event would probably be even larger than in 2005. This should be a major concern for the growing population living in the region.

This study, carried out with 15-m-resolution images taken 5 years apart, demonstrates the potential of optical imagery as a complement to seismology for the analysis of large earthquakes. A global coverage already exists thanks to the SPOT and ASTER programs, and there is no doubt that high-quality optical imagery, with metric or submetric resolution, will be available in the future. This warrants that the approach described here will be

applicable to future large earthquakes. Well-constrained source models, and some estimate of near-field effects, could be produced a couple of hours after the images are available.

Chapter 8

Glacier-Surface Velocities in Alpine Terrain from Optical Satellite Imagery—Accuracy Improvement and Quality Assessment

By Dirk Scherler¹, Sébastien Leprince², and Manfred R. Strecker¹

¹ Institut für Geowissenschaften, Universität Potsdam, 14415 Potsdam, Germany

² Electrical Engineering Department, California Institute of Technology, Pasadena, California, USA

Foreword— This chapter has been submitted with the reference D. Scherler, S. Leprince, and M. R. Strecker, “Glacier-surface velocities in alpine terrain from optical satellite imagery—accuracy improvement and quality assessment”, *Remote Sensing of Environment*, 2008. In this thesis, it is referred to as reference [129]. D. Scherler is responsible for the data manipulation and interpretation. S. Leprince provided his expertise to analyze the quality of the measurements and to determine the sources of possible bias. M. R. Strecker is the project principal investigator.

The worldwide retreat of mountain glaciers has important consequences for the water, the food, and the power supply of large and densely populated areas in South and Central Asia. Successful mitigation of the hydrological impacts on societies as well as as-

sessing glacier-related hazards requires large scale monitoring of glacier dynamics. However, detailed glaciological data from this region are lacking, due to its size and its difficult accessibility. We have applied a novel technique for precise orthorectification, co-registration, and sub-pixel correlation of Advanced Spaceborne Thermal Emission and Reflection Radiometer (ASTER) satellite imagery to derive surface velocities of high Asian glaciers. The described approach allows for the correction of offsets due to attitude effects and sensor distortions, as well as elevation errors if an SRTM-based DEM was used for orthorectification. After post-processing, the error on the displacements is on the order of 2–4 m per correlation. Translated into annual velocities, this error is reduced (increased) when the correlated images are more (less) than a year apart. Through application of a filtering procedure and several quality tests, the consistency of the results can be validated to provide confidence in the remotely sensed velocity measurements, despite the lack of ground control. This novel approach allows fast, easy, and economically viable acquisition of detailed glaciological data in areas of difficult access, and provides means for large-scale monitoring of glaciers in high mountainous terrain.

8.1 Introduction

Global warming causes the retreat of glaciers in many mountainous regions [130], and even the most optimistic scenarios for future temperature change involve glacier retreat over many decades to come [131]. This has important consequences for the global hydrological cycle, particularly in climatic threshold areas characterized by water stress. For example, the water, the food, and the power supply of densely populated regions in South and Central Asia are to a large degree dependent on snow and glacier melt water [132–134]. Successful mitigation of the hydrological changes and their impacts on society therefore poses a pressing challenge, calling for large-scale monitoring of glaciers, and for better understanding of glacier dynamics [135–137]. Because of the large size and difficult accessibility of high mountainous terrain, especially in Asian orogens, remote sensing techniques provide a means of efficient data acquisition. For example, satellite images have been used to track the shrinkage of glaciers [138–140]; analyze and monitor supraglacial lakes [141]; determine the equilibrium line altitude [142], and estimate annual mass balances of glaciers [143]. The flow velocity of glaciers, which can be measured through remote sensing, is a crucial variable to

determine ice discharge [3, 12, 144, 145]. For many applications it is necessary to accurately co-register and, if possible, orthorectify the satellite images. However, this is problematic especially in steep mountainous terrain where accurate digital elevation models (DEMs) are often unavailable. As a result, flow velocities of alpine glaciers are still not routinely measured [146]. COSI-Corr is a new application, which provides the opportunity to precisely orthorectify and co-register optical satellite imagery [8], and thus allows measurement of glacier-surface velocities even in difficult, virtually inaccessible terrain.

Here, we evaluate the potential and limits of COSI-Corr to measure glacier-surface velocities in alpine terrain with optical satellite imagery, and we provide guidelines to improve the accuracy of the measurements and to assess their quality without available ground-truth data. This includes correction of offsets in the displacement maps due to attitude effects or due to elevation-errors from the DEM. The methodological principles are applicable to optical satellite imagery in general and are demonstrated here using Advanced Spaceborne Thermal Emission and Reflection Radiometer (ASTER) imagery in the Himalaya and Karakoram. Furthermore, we discuss recommended acquisition conditions as well as typical problems and how to minimize errors.

We have investigated several glaciers from two Himalayan regions: Khumbu in Nepal and Garhwal in India. First, we demonstrate the methodological principles on the relatively slow Khumbu glacier at Mount Everest. Second, we investigate and model displacement errors induced by systematic elevation errors in the SRTM-based DEM, at the Gangotri glacier group, Garhwal. In a further step, the recent velocity history of Gangotri glacier, situated in the headwaters of the Ganges, is analyzed to demonstrate the capabilities and limits of the method to monitor glacier dynamics.

8.2 Remote Sensing of Glacier-Surface Velocities

Measuring glacier-surface velocities can be accomplished through either field studies or remote-sensing techniques [147]. The advantages of direct field-based measurements are the high accuracy and arbitrary temporal resolution. However, observations over long periods involve frequent revisits of the survey points, which can only be located on the accessible parts of a glacier, resulting in very spatial coverage. In contrast, remote sensing-based measurements provide the opportunity to achieve large and possibly complete spatial coverage

even in isolated, remote areas. Currently, three methods are commonly employed to derive glacier-surface velocities: interferometry of synthetic aperture radar (SAR) imagery, SAR feature-tracking, and cross correlation of optical satellite images. These approaches have their strengths and limitations [4], which we briefly address below.

Velocity measurements by interferometry of SAR imagery (InSAR) may achieve high accuracies, but require that coherence between the images is not lost due to modification of the glacier surface by, e.g., melting or snowfall [148]. Further problems arise when the deformation or displacement gradient is larger than the dimensionless ratio of pixel size to wavelength of the radar signal, i.e., 3×10^{-3} in the case of ERS. Given these limitations and the orbital paths of the available satellites, InSAR-derived velocity measurements are typically constrained to time spans of 1, 3, or 6 days [149,150]. Thus, the obtained velocity data may be representative only for the observation period and an extrapolation to annual velocities may be meaningless. Furthermore, it is likely that high atmospheric water content introduces a considerable atmospheric contribution to the phase delay [151,152]. Additional errors may arise when converting the InSAR-derived line-of-sight velocity to a 3-dimensional velocity vector using assumptions about the direction of flow, e.g., in the direction of the steepest slope and/or parallel to the surface [153,154]. In the case of valley glaciers, the steepest-slope assumption may occasionally fail and cause large errors, as shown in [153] and [146]. Furthermore, if the glacier is not in steady state, substantial vertical velocities may introduce errors on the horizontal velocity components [155]. Finally, in order to obtain absolute displacement values, the ambiguous phase signal needs to be unwrapped, which may be problematic in some cases [146,148].

Feature tracking in SAR imagery [148,156,157] is similar to cross correlation of optical satellite imagery [158,159]. The basic approach is to track features from one scene to another and to calculate their velocity given the temporal separation and the measured linear displacement. In this technique, however, the influence of “streak errors”, which are probably related to ionospheric effects [160,161], may cause problems when analyzing low velocities. Another major drawback of SAR imagery in steep mountainous terrain is the high incidence angle of the sensor, which may inhibit visibility of the target glacier [146], and which also implies using very accurate DEMs to correctly orthorectify the measurements. Deriving reliable horizontal velocities is thus difficult.

The detail and accuracy of the measurements, when using optical imagery, is largely

limited by the ground resolution of the sensor and by the ability to precisely co-register satellite images acquired at different dates. The latter task is usually the most difficult and has led to inaccuracies on the order of one pixel, i.e., 15 m if ASTER imagery were used [162, 163]. When using a rigorous orthorectification model [164], severe distortions may arise from an inaccurate DEM, which is a common problem in mountainous regions. Additional errors commonly occur due to changes in the satellite attitude during scanning of the images [1]. An optical sensor like ASTER has an incidence angle close to nadir and thus provides the possibility to accurately orthorectify the image. However, a common drawback of optical imagery is the dependency on cloud-free conditions.

In summary, velocity measurements by InSAR are most appropriate for analyzing very short time scales, i.e., days, or where extrapolation to longer time scales is justified, e.g., in ice sheet studies [161]. Feature tracking in SAR imagery and cross correlation of optical imagery is more appropriate for analyses over longer periods. Although limited by cloud cover during image acquisition, cross correlation of optical imagery provides a quick and efficient way of measuring glacier surface velocities. In order to achieve the measurement accuracy required to infer, e.g., annual velocity variations, the measurements should be devoid of any systematic errors, filtered to exclude miscorrelations, and checked for their consistency with regard to flow features on the glacier surface.

8.3 Methods and Data

We have processed 25 ASTER images to derive glacier-surface velocities from different regions in the Himalaya and Karakoram. Table 8.1 presents the images analyzed in this study, along with details on the acquisition parameters. Although we generally avoided scenes with heavy cloud and snow cover, we included a number of less optimal scenes to test their suitability for velocity measurements.

In the following section we present a method to (1) derive glacier-surface velocities from optical satellite imagery and improve the accuracy of the results, and to (2) filter the results and check the quality without ground-truth data. The different steps are organized in two work flows (see Fig. 8.1). The first group of tasks comprises orthorectification, co-registration, and correlation of the satellite imagery, followed by post-processing of the correlation results using COSI-Corr. COSI-Corr is a new software package that was orig-

Table 8.1: List of the ASTER scenes used in this study. All given data were extracted from the metadata of the images. The orientation measures the angle between the along-track direction and North in a clockwise direction. The images that were used as the master images in the co-registration procedure are marked with a star (*). The listed cloud cover is from the images metadata and generally overestimates the true cloud cover.

Region	Granule ID	Date [yyyy-mm-dd]	Sun azim. [deg]	Sun elev. [deg]	Incidence angle [deg]	Orientation [deg]	Cloud Cover [%]
Khumbu	ASTL1A 0009280513510312080	2000-09-28	155.78	57.51	-2.870	9.26	63
Case study 1	ASTL1A 0010140513270106251	2000-10-14	161.76	52.29	0.022	9.26	70
	ASTL1A 0112200502290201111	2001-12-20	160.96	36.18	0.025	9.26	43
	ASTL1A 0210040500380210261	2002-10-04	152.76	54.87	-2.829	9.26	49
	ASTL1A 0211210500340212070	2002-11-21	162.48	40.26	-0.041	9.26	36
	ASTL1A 0301080500160303170	2003-01-08	157.48	36.44	-0.030	9.26	48
	ASTL1A 0310230459290311050	2003-10-23	158.65	48.60	0.019	9.26	25
	ASTL1A 0410090458390410220	2004-10-09	154.41	52.87	0.022	9.26	72
	ASTL1A 0410250458240411040	2004-10-25	158.11	47.51	-2.873	9.26	77
	ASTL1A 0411100458190411210	2004-11-10	160.38	42.70	-1.480	9.26	55
	ASTL1A 0511130458410511190	2005-11-13	161.12	41.93	0.022	9.26	47
	* ASTL1A 0511290458400512020	2005-11-29	161.18	38.58	-0.019	9.26	45
	ASTL1A 0512060504390512090	2005-12-06	162.41	37.35	8.588	9.31	76
	ASTL1A 0512150458320512180	2005-12-15	160.27	36.29	0.016	9.26	43
	ASTL1A 0602010458090602040	2006-02-01	151.87	39.99	-2.876	9.26	40
	ASTL1A 0701190459340701220	2007-01-19	154.56	37.74	-2.867	9.26	67
Garhwal	ASTL1A 0109090542130109210	2001-09-09	149.10	60.91	5.699	9.56	52
Case study 2	ASTL1A 0310100529250310220	2003-10-10	156.13	49.64	-5.727	9.56	44
	ASTL1A 0310100529340310220	2003-10-10	155.70	50.21	-5.727	9.51	13
	ASTL1A 0407240529140408100	2004-07-24	116.65	68.37	-8.586	9.56	40
	ASTL1A 0508190534580508220	2005-08-19	133.17	65.31	5.729	9.56	87
	ASTL1A 0510150528360510180	2005-10-15	157.07	47.74	-8.583	9.56	69
	ASTL1A 0609230535100609260	2006-09-23	151.63	55.82	2.878	9.56	52
	* ASTL1A 0610090534580610120	2006-10-09	158.14	50.61	5.729	9.56	62
	ASTL1A 0611100535050611130	2006-11-10	163.20	40.39	2.873	9.56	57

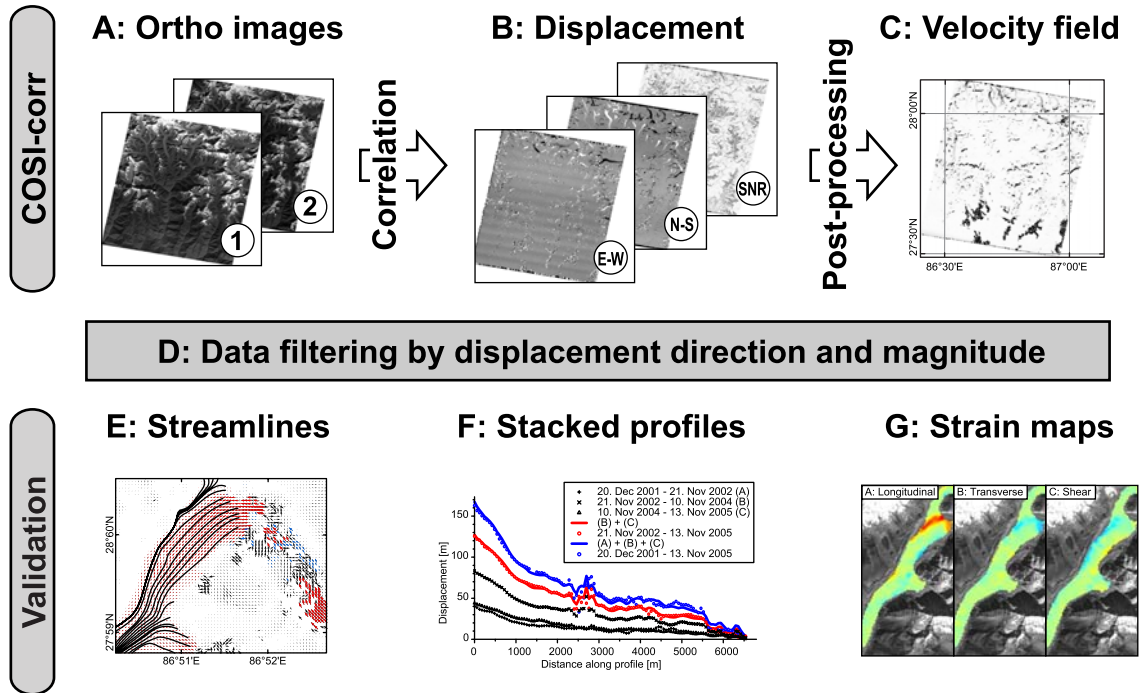


Figure 8.1: Processing chain of the applied method to derive accurate glacier surface velocities. The first work flow comprises the orthorectification and co-registration of multitemporal satellite images (A), their correlation (B), and post-processing (C) to improve the accuracy of the displacement measurements. These steps were done using ENVI and COSI-Corr. The correlation results are filtered (D) and checked for their consistency using streamlines (E), stacked profiles (F), and strain maps (G) in the second work flow.

inally developed for the detection of coseismic displacement [2, 8] (available for download from the Caltech Tectonics Observatory website, <http://www.tectonics.caltech.edu>). The software package is an IDL-based module for the remote sensing platform ENVI© by RSI. The application allows processing of aerial as well as satellite imagery from the SPOT, ASTER, and Quickbird sensors. A detailed description of the methodological background and COSI-Corr can be found in [8], and applications in [2] and [9]. The outcome of COSI-Corr are E-W and N-S displacement maps across the overlapping part of the orthoimages, and a signal-to-noise ratio map providing information on the quality of the measurements. The second group of tasks is related to data filtering and quality assessment of the results. In case of more than one correlation, i.e., more than two orthoimages, further steps may help comparison and combination of the acquired data.

8.3.1 Orthorectification, Co-Registration, and Sub-Pixel Correlation of Satellite Images Using COSI-Corr, Application to Mountain Glaciers

The orthorectification procedure relies on the automatic generation of ground control points (GCPs). A precise set of GCPs is generated from a raw image (slave), with respect to an already orthorectified image (master), by iteratively refining a rough selection of GCPs. Initial GCPs are derived from tie points roughly selected between the orthorectified master and the raw slave image. Image patches from the raw slave image are orthorectified and their misregistrations with the master image are estimated from correlation. A precise set of GCPs is produced when the misregistration measured at each patch converges to a minimum. Generating the GCPs is independent of any ground data by using a shaded image of the DEM as the first orthorectified master. The first orthorectified image produced will then become the new master for subsequent slave images. This approach is globally applicable, taking advantage of the availability of DEMs with global coverage, such as from the Shuttle Radar Topography Mission (SRTM). However, the DEM needs to be free of voids, which is a common problem in mountainous terrain. Smaller gaps can be safely interpolated using standard methods while larger patches should be replaced with other data sources, as described in numerous studies [165, 166]. Alternatively, SRTM tiles from many mountainous regions in the world, where most of the largest data voids have been patched with data from topographic maps, is publicly available from Jonathan de Ferranti (<http://www.viewfinderpanoramas.org>). Such DEMs have been used in this study.

Once a set of precise GCPs has been produced, the mapping matrices that associate ground coordinates with raw pixel coordinates are computed. They define the resampling grid from the raw image to the orthorectified image (Fig. 8.1A). Special care is brought to the resampling operation in order to avoid the introduction of aliasing in the orthorectified image.

Horizontal ground displacements are retrieved from the sub-pixel correlation of multi-temporal orthorectified images (Fig. 8.1B). Image correlation is achieved with an iterative, unbiased processor that estimates the phase plane in the Fourier domain. This process leads to two correlation images, each representing one of the horizontal ground displacement components (East-West and North-South) and to a signal-to-noise-Ratio (SNR) for each measurement, assessing the confidence of the results. In a typical process, images are

wrapped onto the topography within the DEM resolution, and co-registered in pairs with $1/50$ – $1/20$ pixel accuracy, allowing for the measurement of horizontal offsets with accuracy on the order of $1/20$ – $1/10$ of the pixel size.

All data produced for this study have been obtained using ASTER band 3N 15-m-resolution images. To allow the measurement of large displacements without losing resolution on the displacement fields, the COSI-Corr multiscale correlation analysis was performed using 128-down to 32-pixel window sizes. Steps of 4 pixels between adjacent correlations yielded ice flow velocity maps sampled at every 60 m.

An important feature of COSI-Corr is the possibility to accurately orthorectify and co-register an unlimited number of satellite images on a common grid, which can be derived from a DEM. This allows simultaneous analysis of the kinematic and topographic data.

8.3.2 Post-Processing Procedures

8.3.2.1 Removal of Residual Attitude Effects

Data on the roll, pitch, and yaw of the satellite during image acquisition come with the imagery’s metadata, and are accounted for during orthorectification. However, the ASTER sensor does not sample the attitude information frequently enough to allow for full compensation of image distortions [80]. As a result, the correlation maps of two orthoimages show wave artifacts in the across-track direction of the image. A gentle long wavelength distortion in the along-track direction is attributed to focal plane distortions, e.g., spherical aberration from the optical system or distortion of the CCD sensor [167]. Such systematic distortions can be removed within COSI-Corr (Fig. 8.1C). The ability to remove these artifacts depends on the fraction of visible, stable ground (i.e., ground that does not involve any glacier flow) in the two orthoimages. Generally, the higher the amount of stable and visible ground, the better the possibilities of removing attitude effects. However, distortions resulting from attitude effects may be obscured when other errors are present, e.g., due to inaccurate DEMs.

8.3.2.2 Removal of DEM-Related Errors

Although COSI-Corr was explicitly designed for correlating satellite images irrespective of their incidence angles, different incidence angles may lead to distortions in the orthorecti-

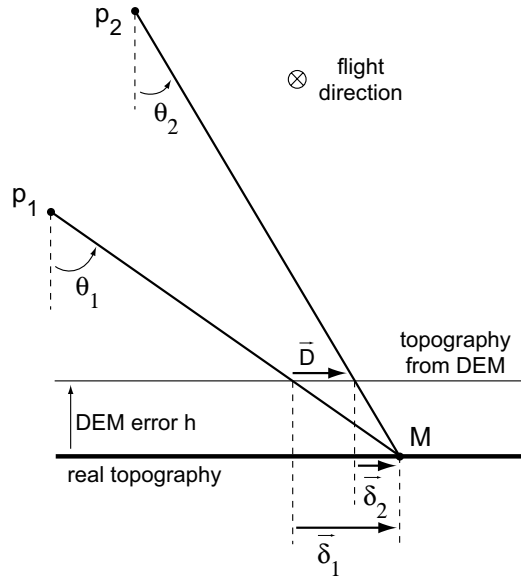


Figure 8.2: Effect of DEM error on displacement measurements. Assume a pixel p_1 from an image I_1 acquired at a date t_1 sees the ground point M . Assume a pixel p_2 from an image I_2 acquired at a date t_2 sees the same point M on the ground, and that both images are orthorectified and co-registered according to a DEM with an elevation error h . For simplicity, it is assumed that locally, around the ground point M , the topography and the elevation error are well approximated by constants. θ_1 and θ_2 are the angles between the line of sight of the pixels p_1 and p_2 , and the vertical. When the orthorectified images I_1 and I_2 are correlated, a disparity D , induced by the elevation error h , is measured. We have $D = \delta_1 - \delta_2$, i.e., $D = h(\tan(\theta_1) - \tan(\theta_2))$. In the case of ASTER images, we assume that all pixels have a comparable sight angle that is well approximated by the instrument incidence angle.

fication in case of an inaccurate DEM. These distortions are transferred in the correlation procedure to the displacement maps. Errors are most prominent in the E-W displacement because the ASTER sensor is inclined only in the across-track direction and the orbital path of the carrying satellite TERRA is only a few degrees off north. The measured ground disparity D is related to the incidence angles of the correlated scenes, θ_1 and θ_2 , and to the elevation error of the DEM, h , by

$$D = h(\tan(\theta_1) - \tan(\theta_2)), \quad (8.1)$$

and increases with the difference in incidence angles and the elevation error of the DEM (see Fig. 8.2). As the SRTM data is the principal source for DEMs in many studies, it is useful to assess any systematic errors that can be modeled to improve the accuracy of the

displacement measurements. It has been shown in earlier studies that the elevation error of the SRTM-based DEMs contains a component which linearly increases with terrain slope, and another one which depends on terrain aspect [168–170]. The dependency on terrain aspect is presumably related to the orbital path of the Space Shuttle and to the look direction of the antenna [168]. Accordingly, elevations of foreslopes (i.e., with a northwesterly aspect) are generally underestimated and elevations of backslopes (i.e., with a southeasterly aspect) are generally overestimated. Because COSI-Corr delivers orthoimages, and correlation maps are well co-registered with the DEM used for orthorectification, the ground disparities can be compared to the topography to produce a model for correcting the displacement errors. We found that the residual displacement error, ε , can be estimated with the model

$$\varepsilon = K \cdot s \cdot \cos(a + \varphi) + z, \quad (8.2)$$

where s is the slope of the topography surface, a is the topography aspect, and K , φ , and z are constants to be determined from, e.g., a least-squares procedure. In all cases we investigated, φ was around 1.3 rad, i.e., 75 degrees, which implies that the largest offsets occur at aspects of around 105 and 285 degrees (see Table 8.2). K can be interpreted as the maximum offset among all aspects, per slope radian. In this study, the absolute value of K , for the E-W displacement, was always around 13 m/rad, i.e., about 23 cm per degree slope angle. The last term, z , is not related to the DEM-error but may be regarded as the mean error due to attitude effects. This term could be set to zero if the correlation results, after correcting for DEM-error effects, allow removal of the attitude effects with the destriping tool in COSI-Corr. In some cases, as we will show later, this is not possible due to residual noise in the correlation map which stems from (1) inaccurate slope and aspect values, and (2) erroneous sampling of miscorrelations or moving ground for estimating the parameters K and φ . Before fitting Eq. (8.2) to the displacement, aspect, and slope data, we used a signal-to-noise ratio threshold of 0.99 and a data range between -20 m and +20 m for E-W and -10 m and +10 m for N-S displacement to minimize noise and erroneous sampling.

8.3.3 Data Filtering

Once all systematic errors have been removed, the measurements should be filtered to exclude miscorrelations and to identify reasonable correlations that may be obscured between

Table 8.2: Details on the error evolution during post-processing of the correlations used in the study of the recent velocity history of Gangotri glacier. Correlations with high differences in incidence angles showed higher errors than usual due to inaccuracies in the SRTM-based DEM that was used for orthorectification. When the differences in incidence angles were low, corrections of DEM-induced errors were not necessary. Residual offsets were determined from all displacement data in a range between -10 m and +10 m. Thus, slow moving glacier ice has also unwillingly been sampled and the residual offset estimates should be regarded as upper bounds.

Correlation details					Residual offset [m]						Parameters for the correction model		
Ortho1	Ortho2	Time span [a]	Inc. angle diff. [deg]		Raw		DEM corr.		Attitude corr.		K [m/deg]	φ [deg]	z [m]
					mean	std	mean	std	mean	std			
Aug 05	Sep 06	1.08	2.85	E-W	-1.14	3.76	\	\	-0.25	3.39	\	\	\
				N-S	1.72	4.24	\	\	-0.75	3.72	\	\	\
Aug 05	Oct 06	1.17	0.00	E-W	-0.74	3.92	\	\	-0.07	3.50	\	\	\
				N-S	-0.20	4.34	\	\	-0.04	3.73	\	\	\
Aug 05	Nov 06	1.25	2.86	E-W	-1.02	4.11	\	\	-0.10	3.68	\	\	\
				N-S	-1.06	4.43	\	\	-0.22	3.99	\	\	\
Jul 04	Oct 05	1.25	0.00	E-W	0.20	3.70	\	\	0.04	3.49	\	\	\
				N-S	-0.06	3.98	\	\	-0.02	3.60	\	\	\
Jul 04	Aug 05	1.08	14.32	E-W	0.13	5.25	0.11	4.45	-0.07	4.07	-0.239	63.59	-1.07
				N-S	1.46	4.16	0.11	3.49	0.19	3.18	0.048	68.48	0.08
Oct 03	Jul 04	0.75	2.86	E-W	-1.41	4.19	\	\	0.12	3.37	\	\	\
				N-S	1.34	3.56	\	\	0.31	3.28	\	\	\
Oct 03	Aug 05	1.84	11.46	E-W	1.59	5.18	0.18	5.03	0.23	4.84	-0.214	78.21	-4.58
				N-S	0.17	4.57	0.14	4.54	0.38	4.25	0.043	86.78	-0.04
Oct 05	Oct 06	1.00	14.31	E-W	0.09	5.25	-0.01	4.55	-0.04	4.37	-0.244	71.33	-1.02
				N-S	0.12	3.58	0.05	3.48	\	\	0.045	86.48	0.00
Oct 05	Sep 06	0.92	11.46	E-W	-0.17	5.31	0.07	4.97	0.04	4.61	-0.238	70.75	0.24
				N-S	-0.74	3.80	-0.09	3.77	-0.02	3.59	0.049	78.63	0.95
Oct 05	Nov 06	1.08	11.46	E-W	0.09	5.37	0.01	4.84	-0.01	4.43	-0.232	73.26	-0.32
				N-S	0.21	3.733	0.11	3.48	0.23	3.42	0.056	59.63	-0.16
Oct 03	Oct 06	3.00	11.46	E-W	1.41	5.09	0.13	4.45	\	\	-0.224	72.84	-3.54
				N-S	0.07	3.67	0.11	3.27	\	\	0.037	76.67	-0.04
Sep 01	Oct 03	2.08	11.43	E-W	-1.56	5.07	-0.06	3.61	0.00	3.49	0.253	69.16	3.97
				N-S	-0.03	4.115	-0.03	2.85	-0.01	2.81	-0.044	76.62	-0.10
Sep 01	Aug 05	3.95	0.03	E-W	1.05	4.02	\	\	0.30	3.27	\	\	\
				N-S	0.11	4.23	\	\	-0.22	3.27	\	\	\

miscorrelated patches (Fig. 8.1D). Excluding measurements with a low signal-to-noise ratio is a starting point to quickly filter the displacement maps. However, not all miscorrelated points are excluded from this procedure, and we have found that in addition, a simple directional filter is very efficient in getting rid of most remaining miscorrelations [162]. This was done by defining the flow direction from flow features on the glacier surface in the orthoimages and allowing for some deviation, e.g., of up to 20° . A further filter is applied to the magnitude of the displacement to acknowledge that velocities do not change abruptly, but rather gradually. However, both filter procedures need to be applied with variable parameters (e.g., directions, sizes, and thresholds) on different patches of the glacier and thus require some manual tuning. Overlaying the displacement field in form of vector arrows on one of the orthoimages helped to identify whether the results were consistent with the flow features on the glacier surfaces. We designed an interface in MATLAB[®] that allows for a quick definition of thresholds and patch sizes to apply the filters.

8.3.4 Quality Assessment and Validation Techniques

The lack of ground-truth velocity measurements by means of differential GPS, for example, hampers simple evaluation of remotely sensed measurements in most cases. Yet, in order to assess the quality of the measurements, we designed a number of tests to check the consistency of the results with regard to the displacement direction, magnitude, and their gradients. These include (1) a test of the displacement direction by using the displacement field to construct streamlines, i.e., displacement paths, which can be checked against flow features on the glacier surface in the orthoimages (Fig. 8.1E); (2) a test of the magnitude of displacement by comparing the sum of incremental displacement measurements (e.g., the addition of displacements measured from images between 2001–2002, 2002–2003 and 2003–2004) with a displacement measurement over the complete observation period (i.e., 2001–2004) (Fig. 8.1F); and (3) a check of the displacement gradients by overlying the orthoimages with strain rate maps calculated from the displacement data (Fig. 8.1G), using the method by Nye [171] as shown in studies by Bindschadler et al. [172]. For the calculation of strain rates, only filtered displacement values have been used and small gaps in the displacement maps have been linearly interpolated. Furthermore, in order to suppress small-scale dynamics and noise in the strain rates, the displacement maps have been smoothed with a 5×5 pixel convolution filter [172]. An error estimation of the strain-rate

calculations was performed by bootstrapping ($n = 1000$) the calculations using the E-W and N-S displacements with added uncertainties. The uncertainties have been randomly drawn from a normal distribution described by the residual error over stable ground. The resulting strain-rate maps describe the longitudinal, transverse, and shear strain rates over the glacier surface. The reference frame is the local flow direction. With this suite of tests, we determined whether the correlation procedure was stable and we produced consistent results that are supported by flow features on the glacier surface.

8.4 Study Area

Currently, approximately 115,000 km² of mountainous terrain are glacierized in South and Central Asia [173], making this region the largest glacierized continental area outside the polar regions. Despite the great number of glaciers in the Himalaya and Karakoram and their important role for water supply to the region, glaciological data are surprisingly limited. The available measurements of glacier areas and mass-balance calculations have shown that glaciers in the Asian highlands are generally retreating [173,174], in some cases at high rates—like the Parbati glacier in India, retreating at almost 52 m/yr [175]. However, some glacier advances have been observed in the eastern Himalaya and the Karakoram, where this has been linked to increasing precipitations [176], and/or decreased summer temperatures [177,178].

Because of the low latitudinal position between 27 and 37° N, Himalayan glaciers usually occur at elevations of more than 4 km. The largest glaciers of the region are found in the Karakoram, where some descend to elevations of less than 3 km. Such descent to relatively low altitudes are commonly thought to be driven by a high amount of supraglacial debris cover that shields the ice from ablation, lowering accumulation-area ratios compared to debris-free glaciers [179]. The debris cover is an important feature for deriving surface velocities from optical satellite imagery, as it creates and preserves pronounced surface morphology over relatively long timescales [180]. However, the correlation procedure tends to fail when illumination conditions are grossly different between scenes.

The climatic conditions along the Himalayan arc are characterized by important differences [181]. The easternmost Himalaya receives large amounts of rainfall throughout the year, delivered by the Indian monsoon in summer and the East Asian monsoon during win-

ter. Hence, frequent cloud cover limits the choice of suitable satellite scenes. Moisture supply in the central Himalaya is dominated by the Indian summer monsoon, although winter snow fall may reach considerable amounts at higher elevations [182]. Towards the western end of the Himalaya, and in the Karakoram and Hindukush, the influence of the Indian summer monsoon decreases, and winter precipitation by the Westerlies increases. Additionally, a strong north-south rainfall gradient prevails across the entire Himalaya due to orographically forced precipitation of monsoonal moisture [181]. Thus, the Asian highlands are characterized by different climatic sectors that control the cloud-cover characteristics and the suitability of satellite scenes to derive glacier-surface velocities.

In our study we have chosen the Mount Everest region, Khumbu, in the Nepalese Himalaya, and the Gangotri glacier group, Garhwal, in the Indian Himalaya. We selected these sites because they hold abundant glaciers of different sizes that are important water resources [183], and some of them, due to recent down-wasting, are prone to catastrophic outburst flooding [184,185], making them prime targets for monitoring strategies. The high elevation sectors in both regions experience moderate wet monsoonal climate, with more influence of the Westerlies in Garhwal.

8.5 Results

In this section, we first present the results from a full orthorectification and correlation procedure on a set of ASTER images from the Mount Everest region, in the Nepalese Himalaya. This case study details the techniques to improve the measurement accuracy, to filter the results, and to test for their consistency. Additionally, the data from individual correlations are compared and combined to enhance the spatial coverage of glacier velocities. The second case study from Garhwal in the Indian Himalaya deals with the effects of DEM-errors on velocity measurements. After correcting for these errors, an examination of the recent velocity history of the Gangotri glacier is performed to demonstrate the capabilities and limits of the method to detect velocity variations.

8.5.1 Case Study 1: Khumbu Himal, Nepal

Fig. 8.3 shows an ASTER orthoimage from the Mount Everest region, acquired in November 2004, and a displacement map produced by correlation with another orthoimage from

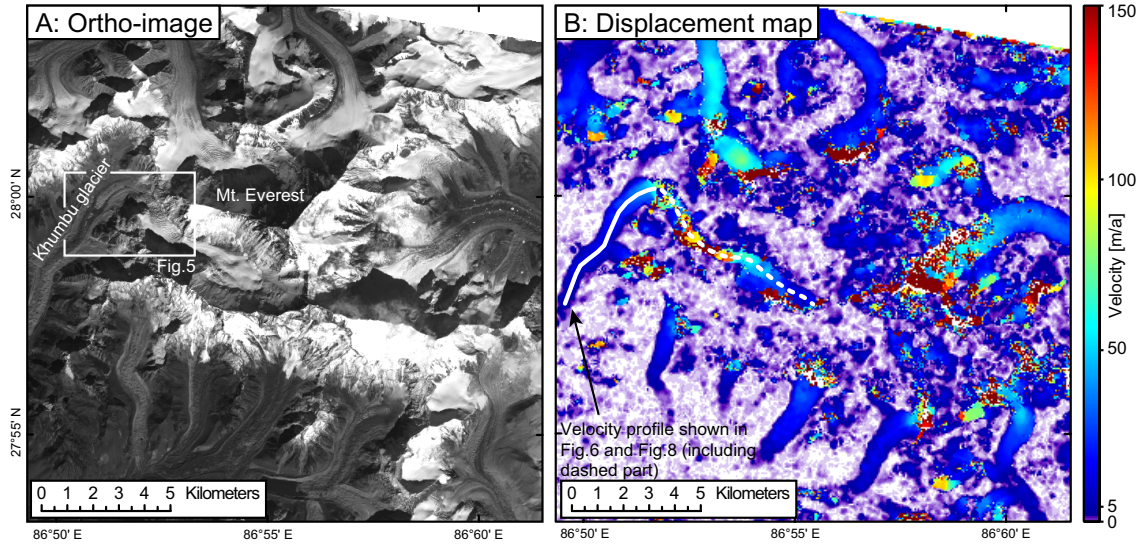


Figure 8.3: Ortho-image (A) acquired on Nov. 10th 2004 and displacement map (B) from the Mount Everest region, Nepal. The displacement map was produced by correlating the orthoimage in (A) with another orthoimage acquired on Nov. 29th 2005. Displacement values are normalized to annual velocities. The subset in A is shown in Fig. 8.5 and the velocity along the profile in B is displayed in Fig. 8.6 (short profile) and Fig. 8.8 (long profile).

November 2005. The acquisition setting of both ASTER scenes with identical near vertical incidence angles, similar shading, absence of clouds, and only limited snow cover, provide ideal conditions for orthorectification and correlation (see Table 8.1).

8.5.1.1 Accuracy Improvement

Well-identifiable stripes in the E-W displacement map are due to attitude variations and are a first sign of low noise and successful orthorectification (Fig. 8.4). The stripes have been removed with the COSI-Corr destriping-tool. This has improved the accuracy of the measurements as is shown in Fig. 8.4. Before the correction, the residual displacement in the E-W direction, as measured from all data points lying within -10 m to $+10\text{ m}$, had a mean value of -0.63 m and a standard deviation of 3.16 m . After removing the distortions in the line direction of the image, the residual displacement decreased to a mean value of $-0.11 \pm 2.52\text{ m}$. Further removal of the more gentle distortion in the column direction improved the accuracy only somewhat to a mean of $-0.05 \pm 2.41\text{ m}$. Most likely, optimal results from the destriping procedure would have been achieved if the destriping model had been defined using stable ground only. However, this would be a laborious task, and

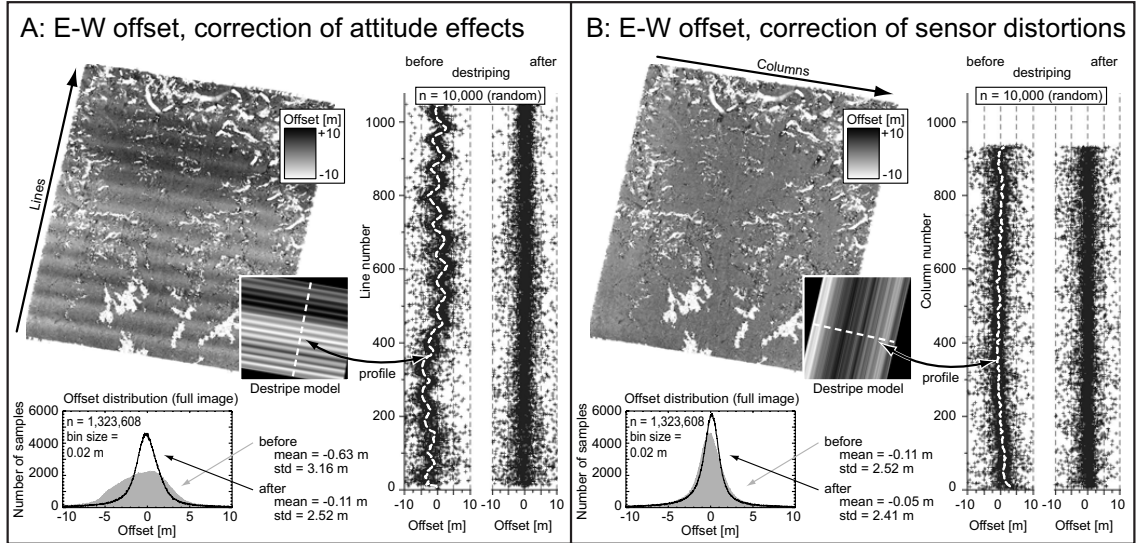


Figure 8.4: Correction of attitude effects (A) and sensor distortions (B) in the E-W displacement component of the correlation shown in Fig. 8.3B. The correction models for destriping are produced by calculating the mean residual offset in the column- (A) and in the line-direction (B) of the image. The residual offsets are determined from stable ground, i.e., no glaciers, by discarding all displacements with absolute values of more than 10 m. Even though slow moving glaciers will not be discarded this way, their share among the entire population of offsets is small. While the scatter plots depict the individual offsets of a randomly sampled set of 10,000 pixels, the histograms show the entire population arranged in 0.02 m offset bins. Note that the residual mean offset and its standard deviation after correction in (A) equals the values before correction in (B).

we found that simply thresholding the displacement map to a range that encompasses the undulations due to attitude effects, e.g., -10 m to $+10$ m, works well enough to remove any systematic undulations. Indeed, most of the glaciers have moved by more than 10 m during our study period, and most of the ice-flow related measurements can be discarded from simple thresholding.

8.5.1.2 Filtering

After removal of obvious systematic distortions in the displacement images, the displacement measurements over the glacier area have been filtered to eliminate miscorrelations. This approach is used on Khumbu glacier (N27.9806, E86.8766), which is an intermediate-sized glacier (16.5 km length) located southwest of Mount Everest. Based on an analysis by Luckman et al. [180], the lowermost 2 km of the glacier appears to be stagnant.

As was already apparent in the displacement map in Fig. 8.3B, the correlation procedure

failed in certain parts of the glacier and returned erroneous displacements (see Fig. 8.5). This is particularly the case in the steep portions of the glacier where the velocity gradient, and thus deformation of the glacier surface, is large. Another problem that may not be apparent at first sight is artificial displacement due to moving shadows [4]. If the sun angles are different in the scenes to be correlated, the correlation procedure will possibly detect the shifting shadows and record an artificial displacement. This effect is observable in the shaded regions of Fig. 8.5, where the arrows indicate an apparent northward displacement. In order to exclude such miscorrelations, we have filtered the data over the area of the glacier as described in Section 8.3.3. The result of the filter procedure in the central part of Khumbu glacier is shown in Fig. 8.5. Most of the obvious erroneous vectors have been discarded using the directional filter (black arrows). The magnitude filter discarded another group of displacement vectors that were pointing in the correct direction, but showed anomalously high or low displacement values (green arrows). In this case, we applied the filters on patches of up to 1 km^2 , depending on changes in flow direction and magnitude, and allowed for $\pm 20^\circ$ deviation from the defined flow direction. The magnitude filter was applied more variably according to nearby, well-identifiable velocities, usually within a range of $\pm 30 \text{ m/a}$. Clearly, unless filtering is performed very carefully with tight thresholds and on small patches, erroneous results may survive and correct results may be discarded, e.g., some displacement vectors at the edges of Khumbu glacier in Fig. 8.5. However, the proportion of these cases among the entire population of retrieved data points is usually very small, even if the filtered patches are relatively large.

8.5.1.3 Quality Assessment

With a set of filtered displacement vectors, we are able to assess the quality of our measurements by testing the consistency between different correlations and with regard to the appearance of the glacier in the orthoimages.

The first consistency test using streamlines is applied on the lower part of Khumbu glacier, which has good and continuous data coverage (Fig. 8.5). The streamlines agree quite well with the flow features on the glacier surface seen in the orthoimage. In the lower part of Khumbu glacier the streamlines are narrowed, due to the confluence with a tributary glacier. A minor mismatch of the streamlines coming from the tributary glacier and the banding on the glacier surface (hardly visible in the figure) does not appear to

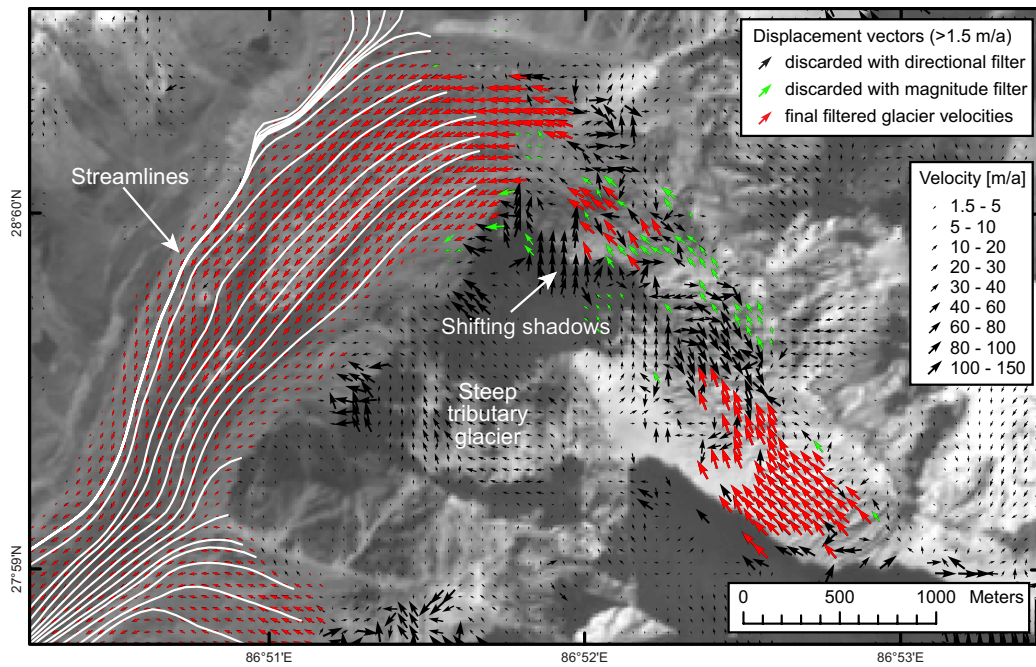


Figure 8.5: Velocity field of the central part of Khumbu glacier derived from correlation shown in Fig. 8.3B. Ortho-image in the background is from Nov. 10th 2005. Black arrows depict displacements of more than 1.5 m/a. Through filtering the data by direction, most miscorrelations are discarded. Further filtering by magnitude removed data points pointing in the right direction, but that showed anomalously high or low velocities (green arrows). The red arrows depict the final filtered velocity vectors that are consistent with flow features on the glacier surface. Streamlines are shown in white and were constructed using the retrieved velocity vectors. Note the steep tributary glacier in the center of the image which shows relatively consistent motion downslope towards Khumbu glacier. Although it appears that these two glaciers are connected, lateral moraines between them are seen in the orthoimage, and they provide argument against a link. Therefore, we excluded the tributary glacier from further analysis.

be an artifact, as it is observable in all other correlations. Instead, the mismatch appears to reflect a relative increase in ice discharge from this tributary compared to the upper Khumbu glacier.

For the second consistency test we used four orthoimages from the years 2001, 2002, 2004, and 2005 (see Table 8.1). An example from the lower part of Khumbu glacier is given in Fig. 8.6. For this profile, the raw, unfiltered data have been used to show the good agreement over most parts of the profile. The displacements derived between 2002 and 2004, and all time spans encompassing this period, show some suspicious velocity variations in the center of the profile. From visual inspection it was found that these variations are due to the enlargement of a supraglacial pond, where the retreat of the bounding cliffs caused the impression of reduced velocity at the up-glacier side and increased velocity at the down-glacier side of the pond. The stacked profiles show that the magnitudes of the displacement measurements agree very well in the upper part of the profile but contain larger scatter in the lower part, where surface degradation through melting is higher. Furthermore, at lower displacement values, the distorting influence of noise increases, especially with regard to the displacement direction. These poor quality data have been excluded using the filter procedure. One should note that the measured displacements are always straight and may thus be underestimated if the true displacement path was curved. However, as the magnitudes of the displacement vectors are generally small compared to the local curvatures of the flow, the displacement paths are well approximated linearly. Problems may appear when measuring flow in strong bends over longer time spans.

For the third consistency test, we calculated strain rates from the displacement field and examined its compatibility with regard to the glacier surface, e.g., the occurrence of crevasses. However, in the central part of the Khumbu glacier where crevasses are formed, the correlation failed and this check was therefore impossible. Nevertheless, an examination of the pattern of strain rates still allows identification of unexpected displacement gradients. Fig. 8.7 shows the components of the calculated surface strain rate over Khumbu glacier and the error in longitudinal strain rates. While most of the glacier is characterized by moderately low strain rates, some areas stand out with much higher strain rates. First, in the highest parts on Khumbu glacier where the velocity data were retrieved, the glacier considerably slows down, which causes high values of negative strain rates, i.e., shortening rates. This happens just below a steep part along the glacier profile, where numerous

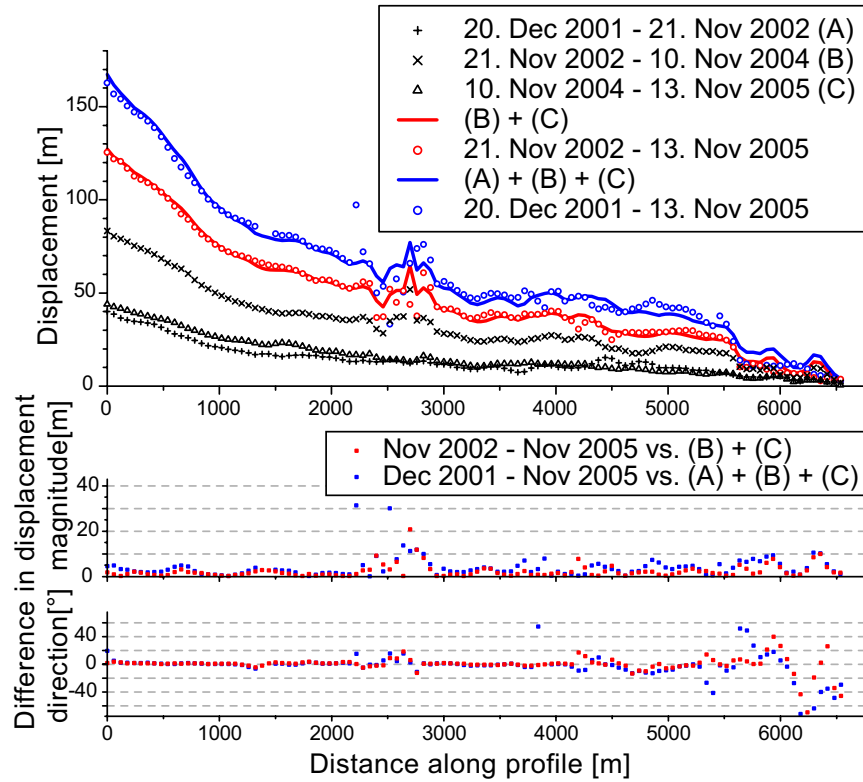


Figure 8.6: Stacked displacement profiles from the lower part of Khumbu glacier (see Fig. 8.3B for footprint). The data points depict the displacement over the time span given in the legend text. The red line (blue line) is the sum of the 2 (3) displacements denoted by + and × (and Δ). The red (blue) circles depict the displacement measured over the same time periods as covered by the red (blue) lines. The overall good correspondence provides confidence in the reliability of the individual measurements.

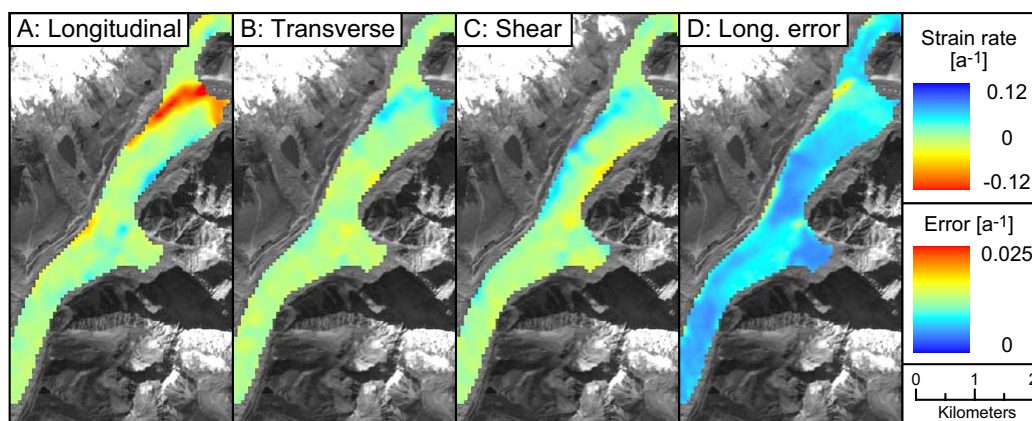


Figure 8.7: Longitudinal (A), transverse (B), and shear (C) strain rate maps and the error on the longitudinal strain rate (D) over Khumbu glacier derived from the filtered velocity vectors shown in Fig. 8.5. The distribution and magnitude of transverse and shear strain rate errors look similar to the longitudinal strain rate error and are not shown. See text for details on the calculation of the strain rates and strain rate error. Note large negative longitudinal and positive transverse strain rates, indicative of deceleration and lateral spreading at the confluence with a tributary glacier at the northern edge of the covered area.

crevasses have formed, and presumably closed again. Second, approximately half a kilometer west, along-flow shortening reaches a peak at the confluence with a tributary glacier coming from the north. When looking at the velocity vectors and streamlines in Fig. 8.5 and at the transverse strain rates in Fig. 8.7, it is apparent that ice near the edge of Khumbu glacier has divergent flow towards the tributary glacier. Consequently, the tributary ice, which flows with velocities of less than 3 m/a near the confluence, is being pushed aside and not incorporated into the main ice stream of Khumbu glacier. Therefore, the contribution of ice from the tributary glacier appears to be reduced, which causes Khumbu glacier to expand laterally. Newly formed crevasses with a NW-SE orientation that can be seen in high-resolution satellite images (e.g., in Google Earth©), support this conclusion.

In the upper part of the covered area of Khumbu glacier, shear-strain rates at the glacier margins are high and of opposite signs, as would be expected. In the lower part, where surface velocities as well as velocity gradients across the width of the glacier are low, shear-strain rates are lower too. The error on the longitudinal strain rates (Fig. 8.7D) is the highest in the regions of low velocities, as the flow direction is strongly affected by the uncertainties, which results in considerable scatter of the velocity gradients. The errors on the transverse and shear-strain rates are similar to that of the longitudinal-strain rates, and therefore not shown.

8.5.1.4 Data Combination: Continuous Velocity Profile from Khumbu Glacier

Because most correlation maps contain patches where the procedure failed or returned erroneous data, it may be useful to combine the results from several correlations to enhance the spatial coverage across a glacier. The quality assessment of the velocity measurements at Khumbu glacier has shown that our analysis is consistent between different data sets and also with regard to flow features on the glacier surface. Furthermore, a comparison of the filtered velocity measurements (not shown) has yielded very similar results throughout the observation period, from 2001 to 2007. Thus, in order to arrive at a continuous velocity profile of Khumbu glacier, we extracted the displacement data of all correlations we performed along a profile that extends from the highest point in the accumulation zone, down to the toe of the glacier (Fig. 8.3B). We applied the aforementioned filter procedure with the same parameters, to all displacement maps simultaneously, to extract only the meaningful data points from our profile. Fig. 8.8 shows the original raw data (A), the filtered and averaged data (B) and the standard deviation of the raw and filtered data from all correlations (C). A large data set of 22 displacement maps enabled us in this case to produce a relatively well-constrained velocity profile, even though the results of the correlations are not equally good over the whole glacier. Especially the lower part is very consistent and the standard deviation among data points of different displacement maps is well below 5 m/a. The central part shows the largest scattering of velocities and most data points have been discarded during filtering. There, the glacier flows over steep topography, and attains high velocities and strain rates, which cause the development of crevasses. Thus, strong surface modifications between the images complicate the correlation procedure.

It should be emphasized that the combination of velocity measurements from different time periods is only possible when the glacier shows no signs of velocity change over the period of observation. This condition has to be examined, e.g., using velocity profiles, before compiling the data.

8.5.2 Case Study 2: Garhwal Himalaya, India

The Gangotri glacier group is situated in western Garhwal, India, and forms part of the headwaters of the Ganges. The Gangotri glacier is, with more than 30 km length, one of the largest glaciers in the Indian Himalaya. We have obtained 9 ASTER scenes covering a

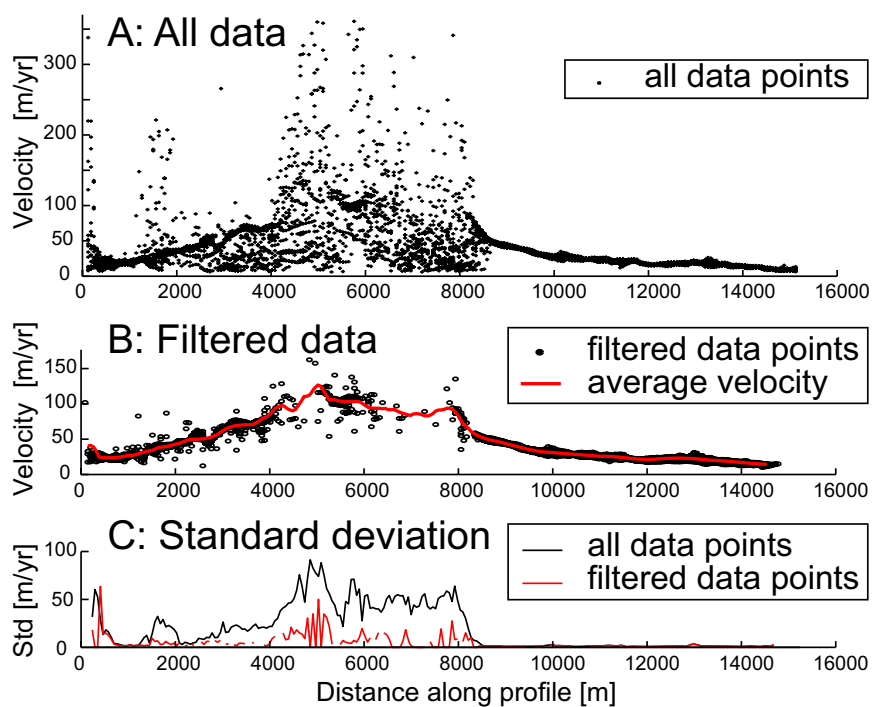


Figure 8.8: Continuous velocity profile of Khumbu glacier derived from 22 correlations. While all data points (A) show considerable scatter in the central and upper part, the filtered data points (B) display less scatter, as is shown in the plot of the standard deviation (C) of the data points from the different correlations.

period from September 2001 to November 2006 (see Table 8.1). Unfortunately, almost half of the scenes were acquired with incidence angles of -5.7 degrees and less, while the other half have incidence angles of 5.7 degrees and more. Thus, many correlations are characterized by incidence angle differences of more than 11 degrees. These angle differences, along with inaccuracies of the SRTM-based DEM, caused additional errors on the displacement measurements on the order of up to 10 m. Below, we present the results from modeling and removing these errors and we provide an analysis of the recent velocity history of the Gangotri glacier to document the accuracy limit. Note that the presented error description and modeling is related to our use of an SRTM DEM specifically, as we observe the bias of the SRTM DEM, scaled by a function of the incidence-angle difference (see Eq. (8.1)). The error modeling may be applied to all correlation results of orthoimages produced with SRTM-based DEMs, but the fitting parameters are specific to each correlation.

8.5.2.1 Correcting for DEM-related distortions

Fig. 8.9 depicts the E-W displacement over Gangotri glacier and adjacent areas, derived from a correlation of orthoimages from October 2003 and October 2006 (see Table 8.1). The difference in incidence angles between the orthoimages is 11.5 degrees. In Fig. 8.9A it is seen how displacement errors over stable ground produce an artificial shading effect, which highlights the dependence of the elevation error on terrain aspect. The variation of the mean E-W and N-S offsets with terrain aspect and slope angle is given in Fig. 8.10. We modeled the offsets using equation (2), with $K = -12.817$ m/rad, $\varphi = 1.271$ rad, and $z = -3.54$ m for the E-W component and $K = -2.111$ m/rad, $\varphi = 1.338$ rad, and $z = -0.04$ m for the N-S component, determined from least-squares adjustment. The applied correction improved the measurement accuracy to the degree that the attitude effect became visible (Fig. 8.9). However, in this case we were not able to further correct the attitude effects more precisely as described in Section 8.3.2.1, due to a high level of noise and a too small fraction of stable, correlated ground that could be used for destriping. Thus, the negative z value in the E-W component represents the mean attitude effect which was biased towards higher values in the upper part of the image where more stable, correlated ground was present. The correction improved the mean residual errors determined from all displacement values between -10 m and $+10$ m, from 1.41 ± 5.1 m (errors are 1σ) to 0.13 ± 4.4 m for the E-W component, and from 0.07 ± 3.7 m to 0.11 ± 3.3 m for the N-S component. Better results

can be obtained when destriping is possible (Table 8.2). Nevertheless, given that distortions from DEM-errors increase linearly with slope angle, the impact on derived glacier velocities is only small as glaciers mostly occur on low-gradient terrain. This is shown in Fig. 8.9C, which depicts the surface velocities of Gangotri and the adjacent Chaturangi glaciers along profiles from different correlations. A measurement from September 2001 to August 2005, with no difference in incidence angle is used as a reference, even though natural velocity variations may occur. However, these should be rather small due to the length of the observation period. The profile plots show that the difference between the velocity from the uncorrected and corrected correlation (October 2003–October 2006) is small and almost not visible. Furthermore, the velocity measurements from the corrected correlation and the correlation from September 2001 to August 2005, yield very similar values. Even though differences in mean residual offsets exist (Table 8.1), these are rather small and within the error of any single correlation when comparing annual velocities. Note that the length of the observation period allowed accurate measurements of surface velocities of less than 10 m/a in the lower part of Chaturangi glacier (Fig. 8.9).

The results from the error-modeling and removal of other correlations used in this study are given in Table 8.2. At incidence angle differences of more than 10 degrees, DEM-induced errors were visible, modeled, and removed. In most cases it was possible to correct the displacement maps for attitude effects after removal of the DEM-induced errors. The residual errors on the corrected displacement measurements, determined from stable ground with offsets in the range of -10 m to +10 m, are similar to the residual errors on correlations with low incidence angle differences. Thus, the error removal was successful.

8.5.2.2 Data Comparison: Recent Velocity History of the Lower Part of the Gangotri Glacier

Velocity measurements from the correlations presented in Table 8.2 were used to investigate the recent velocity history of Gangotri glacier. We picked a profile along the central flow line of the glacier and plotted the annual velocity with the associated errors, given as shaded areas around some of the measurements, in Fig. 8.11.

Over most of the profile, the annual velocity from October 2003 to July 2004 was faster than during the period from July 2004 to October 2005 (Fig. 8.11A). The difference is greater than the combined error of the measurements and is therefore significant. Interestingly,

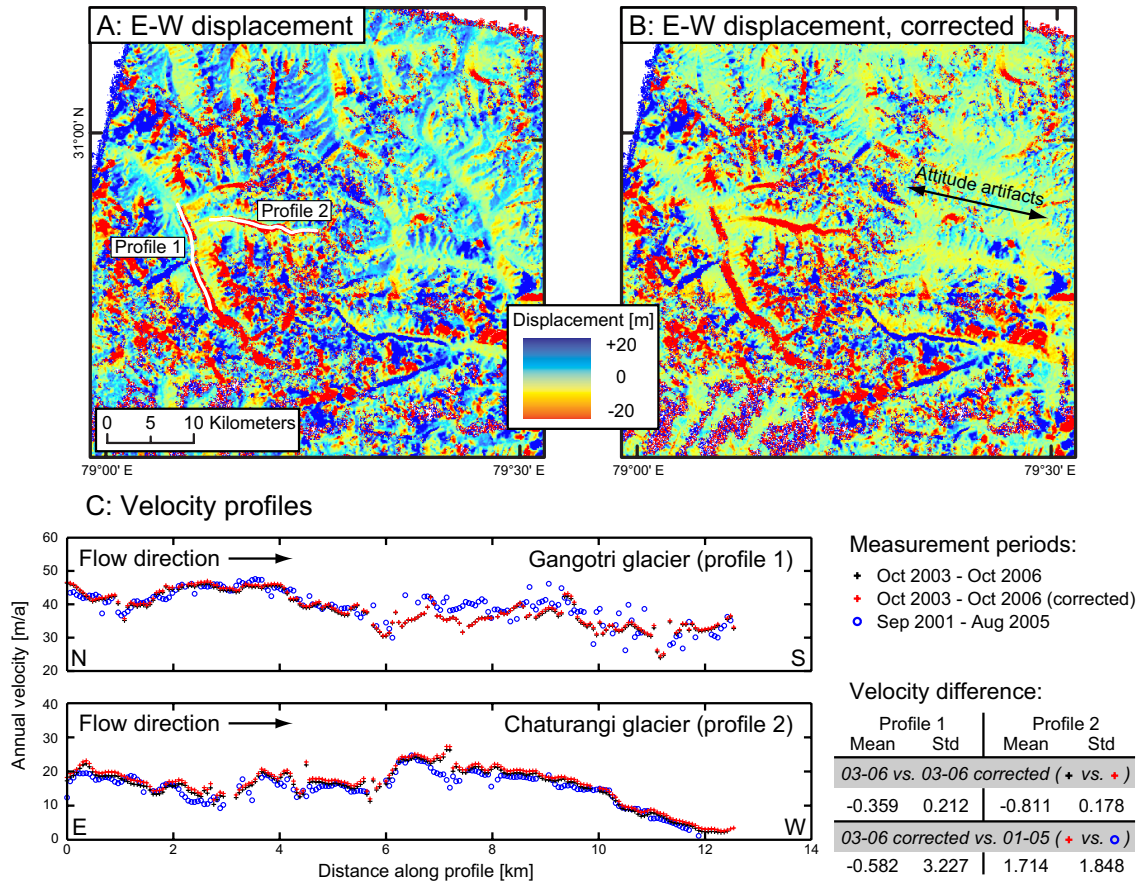


Figure 8.9: Uncorrected (A) and corrected E-W displacement map (B) over the Gangotri glacier group derived from correlation of orthoimages acquired on Oct. 10, 2003, and Oct. 9, 2006. The color-coding applies to pixels with displacement values in between +20 m and -20 m and pixels with values outside this range are given the last color of the respective side of the color bar. The aspect dependence of the SRTM-based DEM-error produces an artificial hill shade effect in (A). After correction of DEM-induced offsets, distortions due to attitude artifacts become visible (B). Velocity profiles of the Gangotri and Chaturangi glaciers are shown in (C). For comparison, the uncorrected and corrected velocity measurements from the period 2003–2006 are plotted together with velocity measurements from the period 2001–2005, where topography-related artifacts are absent as the incidence angles during acquisition of the images were similar (see Table 8.2). The differences between all three data sets are small as the glaciers flow over low-gradient terrain and the DEM-induced error increases with terrain slope.

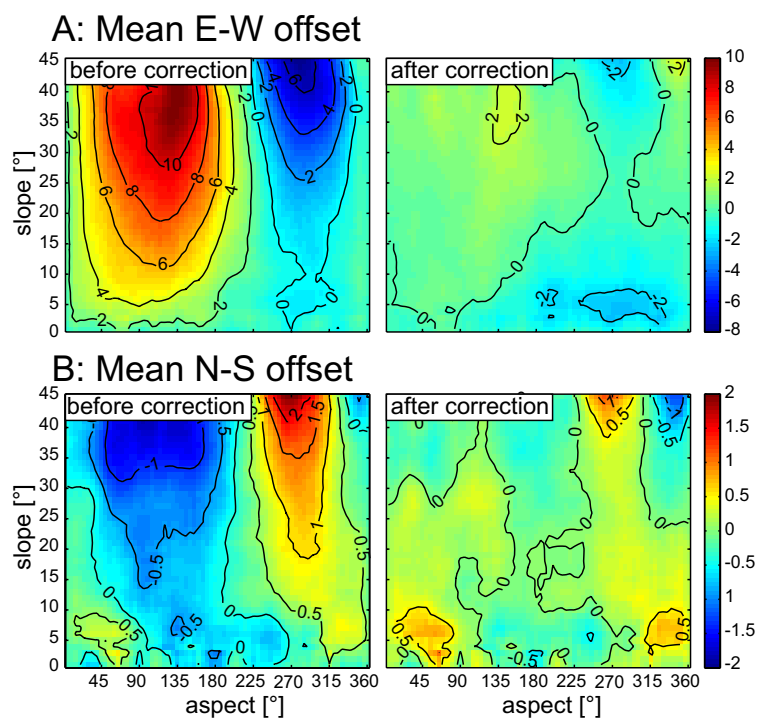


Figure 8.10: Mean E-W (A) and N-S offset (B) from the correlation of the Oct 2003 and Oct 2006 orthoimages from the Gangotri glacier group (see Table 8.1) as a function of slope angle and aspect. The mean offsets were determined from the E-W and N-S displacement values ranging between -20 m and +20 m, and -10 m and +10 m, respectively. Slope angles were sampled in 1 degree intervals and aspect in 5 degree intervals. The resulting distribution was smoothed with a 5×5 convolution filter. At slope angles of more than 45 degrees (not shown), fewer data points lead to more scatter.

the difference vanishes in the lowermost part of the glacier. The annual velocity from October 2003 until August 2005 rests in between the analyzed periods, as would be expected. However, whether or not this velocity difference is a true decrease in ice discharge over time or an effect of the sampled period, e.g., a seasonal effect, is not clear from this analysis.

In order to elucidate the role of the seasonal coverage of the observation periods, we investigated annual velocities over different periods within one hydrological year, although only available from 2005 to 2006. Fig. 8.11B depicts a less obvious, but still visible difference in annual velocity when comparing a time period starting in August 2005 with one starting in October 2005. Velocities from August 2005 to October 2006 appear faster than velocities from October 2005 to October 2006. Although the difference is larger than the combined errors only at some places along the profile, the similar observations from two correlations in each time period lend additional credibility to the results. Importantly, the occurrence of the velocity difference spatially coincides with the larger velocity difference observed in the earlier time periods in Fig. 8.11A.

The main difference in seasonal coverage between the presented observation periods with slower and faster surface velocities is the extension of the slow velocity observations into the third quarter of the year, i.e., over late July to early October in the first case (Fig. 8.11A) and over late August to early October in the second case (Fig. 8.11B). Hence, the flow velocity during this time of the year appears to be relatively slower compared to the average velocity during the rest of the year. The larger velocity difference in the first case (Fig. 8.11A) can be explained if periods of slower velocities extend from July to October in both years, 2004 and 2005. Therefore, we conclude that the measured difference in annual velocities from 2003 to 2005 may be due to the same reason as for the observed difference in velocity during the period from 2005 to 2006. Nevertheless, we still do not know if this is a seasonal, i.e., annually reoccurring, effect or the result of individual speed-up events.

Several studies on alpine glaciers as well as outlet glaciers of ice sheets have shown that glacier flow velocities can vary over daily to annual time scales [186–190]. Such variations have commonly been attributed to melt-water-induced changes in the subglacial hydrology that lead to variations in the speed of basal sliding. For example, Zwally et al. [188] documented an annual increase in summertime flow velocity at Swiss Camp, near the edge of the west-central Greenland Ice Sheet, which was concurrent with melting days and stopped as soon as temperatures dropped below zero again. Importantly, after each period of enhanced

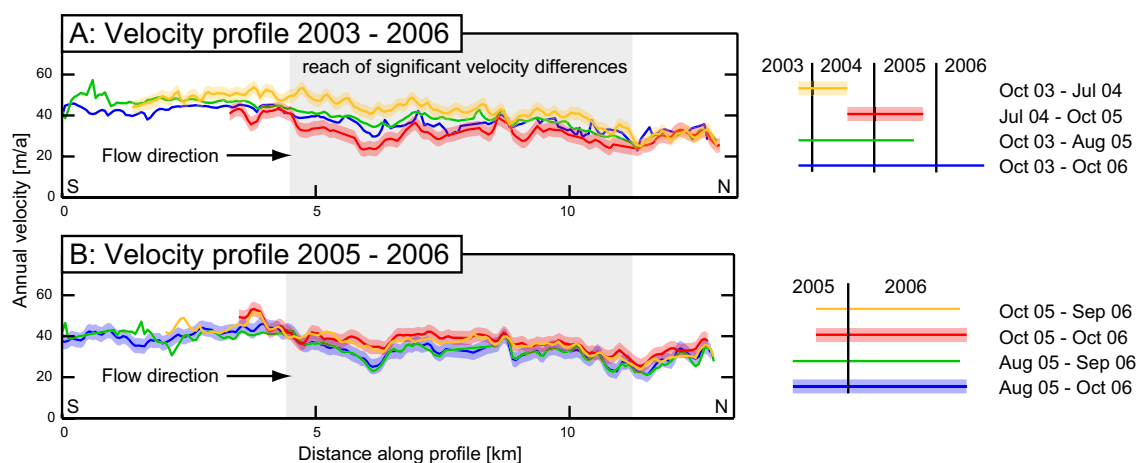


Figure 8.11: Recent velocity history of the lower part of Gangotri glacier derived from correlation of orthoimages from the years 2003 to 2006. The shaded rims around selected profiles give the one-sigma error range, calculated from the residual offsets (see Table 8.2). (A) shows the annual velocity during the period 2003 to 2006. Significant differences exist between the 2003–2004 and 2004–2005 data sets over the reach marked by a gray background. (B) shows the annual velocity from different observation periods from 2005 to 2006. Even though of lower magnitude, a similar velocity difference is visible over the same reach as in A. The footprint of the parofile is shown as Profile 1 in Fig. 8.9A.

flow, the flow velocity dropped to a level that was slower than the average winter-time velocity. A similar behavior has been observed at many mountain glaciers that often show the highest flow velocities during spring to early summer and before maximum ablation and proglacial stream discharge occurs [191–193].

Such phenomena may explain the observed variations in flow velocity of the Gangotri glacier. During early summer, velocities may be higher as temperatures are high and melting occurs. However, melting declines from August to October, and flow velocities may reach slower than average levels. In fact, meteorological studies [194] have shown that (1) longest sunshine hours and highest evaporation at the terminus of Gangotri glacier occur during May, June, and September; (2) high temperatures prevail from at least May until August and drop dramatically during September; (3) most rainfall, hence, cloudiness occurs from July to September. Furthermore, discharge measurements close to the terminus of Gangotri glacier show a gradual increase in discharge until July/August followed by a gradual decrease [183]. Therefore, we speculate that following peak melting and discharge in July/August, flow velocities decrease to slower than average levels. Hence, the observed decrease in average annual velocity from 2003 to 2005 may be the result of the observation

period and may not reflect an overall decrease in flow velocity and ice discharge.

8.6 Discussion

Our analysis of glacier dynamics using combined ASTER imagery and COSI-Corr shows that this methodology is well suited to derive accurate, low-cost glacier-surface velocity measurements from remote regions where ground instrumentation is costly and difficult to implement. Below, we discuss the quality of the obtained measurements as well as associated errors, and we compare our approach with other methods and optical sensors. Finally, we evaluate the opportunities of this technique for glacier-monitoring applications.

8.6.1 Measurement Errors

All data in this study are given as horizontal glacier-surface velocities or displacements. Data have not been converted to surface-parallel velocities. This can be easily achieved with the DEM used for orthorectification, as the topographic and kinematic data are well co-registered. In order to reach high accuracy at this step, the local slope should be calculated from a smoothed along-flow topographic profile. However, such conversion does not account for the emergence velocity, which is the vertical velocity due to accumulation and ablation [154].

In the two case studies we estimated the residual errors on the measurements by analyzing the distribution of offsets with absolute values of less than 10 m. This means that “slow” moving ice is being erroneously sampled, hence skewing the distribution to higher offsets. Applying an additional threshold of 0.99 to the signal-to-noise ratio map usually limits the data used to low-relief areas. This results in much lower residual offset values on the order of zero mean and a standard deviation of 1 m. However, as we cannot assume that the residual errors on measurements of moving glaciers can be characterized by stable ground with high SNR values, we applied the rather conservative error estimation without using a drastic SNR threshold. Hence, the errors presented in this study should be regarded as upper bounds on the one-sigma errors. For synoptic comparisons, it is convenient that measurements over time periods of more than one year reduce the error on annual velocities and average out short-term velocity variations.

The second case study highlights issues associated with inaccurate topographical data.

As in many regions worldwide, the most accurate DEM available to date for high mountainous terrain is based on SRTM data, and such problems occur frequently. Importantly, our method presents a novel way to model and to correct for the resulting displacement errors. However, at slope angles greater than ~ 45 degrees, the model does not fit the offset data as well as at lower angles, due to large scatter and insufficient data points. Fortunately, glaciers occupy mostly low-gradient terrain, where such topography-related errors are small, providing good possibilities to correct them. Furthermore, an advantage of ASTER imagery over most other sensors is that the incidence angle of the 3N band (VNIR), which should be used for velocity measurements, is always close to nadir, hence assuring small topographic errors.

8.6.2 Comparison with Field-Based Velocity Measurements

We do not know of any ground-truth measurements from the glaciers we considered in the case studies to validate our measurements. However, some measurements from Chhota Shigri glacier, Himachal Pradesh, Indian Himalaya [195], and from Baltoro glacier, Karakoram, Pakistan [196], have been published and may provide a basis for comparison.

In Fig. 8.12 we plotted the respective velocity measurements against measurements we derived from ASTER imagery and COSI-Corr. The data agree reasonably well in the case of Chhota Shigri glacier (Fig. 8.12A). The available ASTER images for that glacier do not provide optimal conditions due to cloud cover and changing snow cover conditions, but some scenes allow determination of surface velocities. A problem in comparing the data sets is that the localities where the velocity data has been obtained are not identical. Despite these difficulties, some natural variability, and the generally low velocities, which increase the relative error, the results obtained with ASTER imagery and COSI-Corr are satisfying.

In the case of Baltoro glacier (Fig. 8.12B), the difference between the remote sensing and the GPS-data are large. However, this difference appears to be a true effect related to seasonal velocity variations [196]. The GPS campaign recorded the velocity of Baltoro glacier during short periods of up to 11 days in summer 2004. Our data, and the velocity data by Mayer et al. [196] obtained from optical satellite imagery, show much slower velocities, even though the general shape of the velocity profiles resemble each other. They give an error estimate of ~ 20 m/a for their satellite-derived measurements. Furthermore, as the authors also used LANDSAT imagery for these measurements, the error is likely to

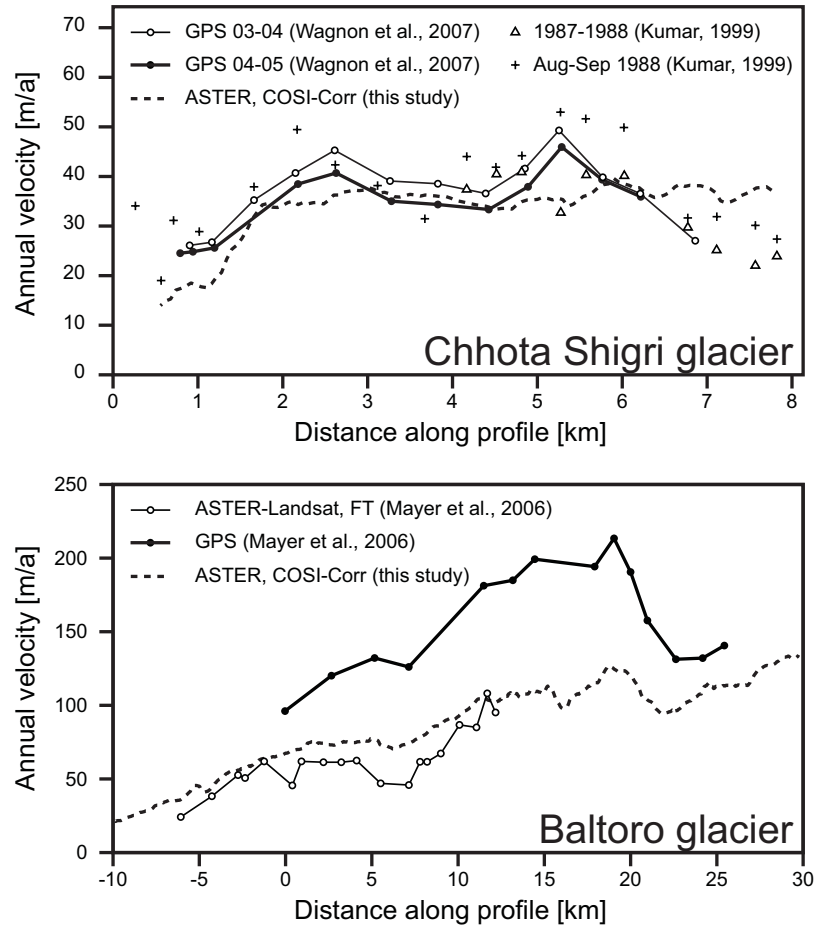


Figure 8.12: Comparison of GPS-derived velocity measurements with measurements obtained from COSI-Corr using ASTER imagery on Chhota Shigri glacier, Indian Himalaya (A), and Baltoro glacier, Karakoram, Pakistan (B). See text for discussion.

be higher due to the imaging technique of the LANDSAT sensor, as discussed below.

In summary, the GPS-based velocity measurements from Chhota Shigri support our remotely derived measurements, while the measurements conducted on Baltoro glacier highlight the importance of seasonal velocity variations. Such variations can be efficiently explored using optical satellite imagery, as the analysis of the velocity history of Gangotri glacier demonstrates. Furthermore, extrapolating InSAR-derived velocity measurements from such glaciers may grossly over- or underestimate annual mean velocities.

8.6.3 Comparison with SAR-Derived Velocity Measurements

When comparing our velocity measurements of Khumbu glacier with those obtained by Luckman et al. [180] using InSAR and feature tracking, important differences emerge. First,

the SAR-derived data show significant scatter over most of the profile, which is not seen in our data. Second, the measurements obtained from feature tracking and interferometry over two time periods each, differ considerably between techniques and also between two periods using one technique. As we did not see any significant annual velocity variations throughout our observation period, we do not expect this glacier to have varied in velocity, but rather the methods to have produced inaccurate estimates. In fact, the absolute errors associated with the InSAR-derived measurements, given by Luckman et al. [180], often exceed the velocity itself. Problems with InSAR in the lower parts of the analyzed glaciers are acknowledged by these authors and more confidence is put on the data obtained from feature tracking. Luckman et al. [180] have also analyzed Kangshung glacier on the eastern slopes of Mt. Everest. In this area, they obtained results that are much more consistent with our data. However, the errors given by the authors are quite high, and on average reach 50% of the absolute velocity. These errors are thus too high to reliably detect velocity changes and assign them to natural causes and not to measurement problems.

8.6.4 Other Optical Sensors

Apart from ASTER, other satellite imagery as well as aerial photos, can also be used with COSI-Corr to measure ground displacement [8]. Satellite pour l'Observation de la Terre (SPOT) imagery in particular has proven useful in deriving glacier-surface velocities [2,4]. Compared to ASTER, SPOT images come with a more accurate attitude description (attitude variations are sampled at a higher rate), and do not usually require the correction of attitude effects in the displacement maps. However, as the incidence angles in SPOT images can be high, DEM-induced errors in steep terrain may cause larger distortions.

It is not possible to accurately process satellite images from the Landsat Thematic Mapper (TM) or Enhanced Thematic Mapper+ (ETM+). This is due to the unknown attitude variations of the satellite and the imaging system. Whereas SPOT and ASTER are pushbroom sensors, i.e., they scan across-track lines of 60 km instantaneously, TM and ETM+ sample the ground along 16 across-track lines of 185 km (this is a whiskbroom system). Hence, attitude variations do not only occur in the along-track direction, but also in the across-track direction, which makes their removal virtually impossible.

8.6.5 Implications for Glacier Monitoring

The suitability, global coverage, and low cost of ASTER scenes make this imagery a viable option among other alternatives to conduct large-scale and long-term monitoring campaigns of remote glacial systems [137]. In comparison with other sensors, the use of ASTER imagery provides reliable results, as inherent problems with attitude effects and inaccurate DEMs can be solved. However, when investigating glaciers flowing with velocities on the order of less than 50–100 m/a, for example, feature tracking methods using optical imagery, as in this study, or SAR imagery, or a combination of both [157], are indicated. Also, when dense cloud cover limits the availability of optical imagery, as for example in the per-humid eastern Himalaya, SAR-imagery may be the only option, even though errors due to changing atmospheric conditions may be quite high. Finally, if the considered glacier is rapidly deforming, correlation over longer time spans can be difficult, and if optical images with a short temporal separation are not available, SAR-studies may be more useful.

8.6.5.1 Image Acquisition Details

When looking for available imagery covering a region of interest, several important principles should be kept in mind.

First, cloud cover should be low. However, when the master image has been successfully orthorectified, all other slave images require only three tie points to be accurately co-registered. Thus, even cloudy images with 3 patches (approx. 3 km×3 km in size) of stable ground can be accurately co-registered. Importantly, thin, partly transparent clouds do not pose a problem. Therefore, even though cloud cover restricts the use of optical imagery to derive glacier-surface velocities, in many cases, images with even 50% of cloud cover or more can be used, as long as the glacier of interest is visible.

Second, images with grossly different snow-cover characteristics, such as winter and summer scenes, are problematic to correlate. The problem is not the snow cover itself, but the difference. That is why images from the same season usually work well, whether with or without snow cover. As the degree of snow cover is usually not identical between two images, parts on the glacier where the correlation procedure obtained poor results or failed are commonly encountered. Such data gaps may be filled with another correlation if images are present and the velocity did not change, as in the case of Khumbu glacier in the first

case study.

Third, in images with high gains, the snow-covered areas are saturated and therefore do not allow for any correlation. Fortunately, this is not often the case for ASTER data, as the commonly used 3N band has a rather narrow spectral bandwidth (760–860 nm). In contrast, SPOT imagery is often characterized by the high gains and broader spectral bandwidth of the panchromatic sensor (500–730 nm), then leading to saturations. For this reason, many of the earlier SPOT images, when high mountainous terrain was not among the main target areas of satellite-data acquisitions, have high gains and are useless for velocity measurements over snow-covered areas. In contrast, more recent SPOT5 imagery is now adapted and provides images with lower gains over snow-covered mountains.

Fourth, snow cover and any other kind of surface modification complicate the correlation procedure. This applies directly to the resolvable time span and measurable velocities. When velocities are high, shorter time spans between the orthoimages lead to better results. For example, a surging glacier, which may flow at rates of several hundred meters per year, requires a narrow temporal separation of the images. When velocities are low, a longer temporal separation of the images is preferred, if surface degradation by melting or down-wasting does not interfere. Time spans exceeding one year also reduce the residual error when normalizing the results to annual velocities. For instance, we succeeded in measuring annual velocities of ~ 10 m/a on glaciers with little surface degradation in Garhwal.

8.6.5.2 Further Potential of COSI-Corr in Glaciological Applications

A high accuracy in the orthorectification and co-registration of temporally separated images is key to numerous change-detection studies. For instance, the ability to measure the shrinkage and retreat rates of glaciers stands or falls with the accuracy of the orthorectification and co-registration of the imagery [197].

In our case studies, we were able to make excellent use of the accurate co-registration between the orthoimages and the DEM. This allows the simultaneous analysis of the reflectance, kinematic, and topographic data sets, to detect and to model the DEM-induced errors in the displacement measurements. As the flow and surface expression of glaciers is to a large degree dependent on topography, the combination of the data sets holds insightful potential for studying glacier dynamics.

Furthermore, satellite-derived glacier velocities and associated strain rates yield the

potential for tuning numerical glacier models [146]. This may provide unique opportunities for modeling studies to be applied in regions where detailed glaciological data from field studies are limited or lacking, as in the Himalaya or Karakoram.

8.7 Conclusions

In this study we have used the new application COSI-Corr to orthorectify, co-register and correlate ASTER satellite imagery and derive glacier surface velocities. We have shown how to minimize residual offsets on the displacement measurements due to attitude effects, and have presented a way to detect, model, and correct for additional offsets induced by elevation errors of the SRTM-based DEM. Additionally, we developed techniques to check the quality and consistency of the results despite lack of ground control. The achieved measurement accuracies allowed for detection of seasonal velocity variations of 10–20 m/a in the lower part of the Gangotri glacier, Garhwal, India.

If the glacier surface velocities are stable over several years, the results of individual correlations may be combined to enhance the spatial coverage across a glacier, as was shown at Khumbu glacier, Nepal. This is particularly useful for synoptic studies aiming at continuous velocity profiles or maps from glaciers over large areas.

Furthermore, the accurate co-registration of the orthoimages, the displacement maps, and the DEM used for orthorectification, provides the possibility to investigate links between surface features on the glacier, glacier dynamics, and topography. This may prove useful for modeling studies that require tuning to recent conditions.

Therefore, our approach presents a method to efficiently monitor glacier-surface velocities at low cost and over large areas. This is important in light of global warming and the need for water management plans to take account of shrinking glaciers.

Chapter 9

Conclusion

9.1 Advances

This thesis has demonstrated that optically sensed images, acquired by either satellite or airborne sensors, can effectively be used to measure horizontal ground displacements. Accurately measuring ground displacements requires both an accurate co-registration of the images, and an accurate correlation technique. The stereoscopic effects induced by the viewing differences of the images, the attitude effects due to the platform motion in space, and the camera biases have to be properly corrected for to achieve accurate co-registration of image pairs. This was achieved thanks to a physical formalization of the sensor geometry, which takes into account acquisition errors before images are reprojected (see Chapter 3). Co-registering pairs of images indeed involves reprojecting the images in a common distortion-free geometry, and it was chosen to reproject them on the ground, warped onto the topography, to produce high-accuracy orthorectified images. This approach facilitates the co-registration of images acquired by different sensors, with possibly different resolutions (see Chapter 2). Reprojecting the images involves a resampling operation that should be carefully designed to avoid the introduction of aliasing in the orthorectified images, which biases the correlation. In addition, the correlation technique, which serves as the ground displacement measuring tool, has to be robust against noise to deliver reliable measurements even in challenging situations. This complete processing chain has been implemented in a software package, Co-registration of Optically Sensed Images and Correlation (COSI-Corr), freely available from the Caltech Tectonics Observatory website¹. On average, images can be registered with accuracy around 1/50 to 1/20 of the pixel size, allowing local ground dis-

¹URL:http://www.tectonics.caltech.edu/slip_history/spot_coseis/

placements to be measured with accuracy better than 1/10 of the pixel size. This technical advance is particularly useful for seismo-tectonic studies since, when combined with seismic waveform modeling, it can help describe in some detail the seismic faulting process (see Chapter 7). It has been shown that measurements of surface rupture from optical aerial and satellite images compare well with field measurements, and that they have, in addition, the potential of measuring off-fault distributed slip (Chapters 3 and 4, see also [73]). Optical imagery measurements can therefore provide the envelope of the slip distribution on a ruptured fault, allowing for the study of rupture velocity variations during an earthquake [198].

The COSI-Corr methodology has also proved to be robust and valuable to measure a variety of surface processes such as surface displacements due to glacier flow and landslides (Chapter 2). Methods to estimate and to correct for topography artifacts due to the lack of resolution of currently available digital elevation models (DEM) have been proposed, now making the correlation of optical images the method of choice to monitor temperate glaciers (Chapter 8). Not shown in this manuscript but also validated, the correlation of optical images has also proved valuable to monitor sand dune migrations [74], and rifting processes [82]. Applications requiring fine co-registration of multi-spectral bands, like vegetation monitoring, can also benefit from the techniques described. Spectral bands of multi-spectral images are traditionally co-registered in the satellite geometry, neglecting stereoscopic effects and platform attitude variations between bands, often leading to poor registration, which limits the range of application of multi-spectral images. The COSI-Corr methodology would provide orthorectified and well co-registered multi-spectral image bands.

COSI-Corr is already used for a wide range of applications: researchers from nearly 200 different institutions have downloaded it over the past year. Two provisional patents have been filed, the first one regarding the fundamental processing chain described in Chapter 3 (reference CIT-5067-P, filed on 01/18/2008), and the second one regarding the in-flight calibration of optical sensors described in Chapter 6 (reference CIT-5091-P filed on 02/20/2008).

9.2 Limitations and Perspectives

The correlation of optical satellite and aerial images has a vast potential to answer quantitative questions related to change detection applications that have been left dormant until now, but this technique also exhibits limitations. The main contribution of this thesis is that it clearly identifies and builds the elements of a global processing chain, which defines a rigorous framework to the correlation of optical images. The quality of the correlation results can therefore be studied in light of this processing chain, making it possible to separate errors due to data quality, or due to the choice of the algorithms implemented, for instance. Limitations can be separated into four categories and further improvements are proposed to limit their influence.

9.2.1 Limitations Due to Image Content

Limitations due to image content are the most easily identified, and are typically responsible for most of the decorrelations. Drastic temporal changes between images due to changes in cloud cover, snow cover, vegetation cover, due to anthropic modifications (construction or destruction of buildings and roads, for instance), or due to new alluvial processes are frequently encountered in remotely sensed images, limiting the ability of the correlation procedure to measure ground displacements. Most of these changes usually coincide with seasonal variations, and correlating images from different seasons is therefore usually more challenging. Seasonal variations can also induce changes in shadowing differences, biasing the correlation results because shadow displacements can be mistaken for ground displacements in rough terrain configurations. The correlation is also usually lost on areas that are, at the scale of the correlation window, translation invariant. Correlation over straight and isolated roads can then be lost, as well as correlation over areas of constant radiometry such as lakes and water reservoirs. Areas of high reflectance induce sensor saturation and forces our methodology to fail as well. This is often the case on icy areas and white sandy desert areas. All these drastic changes can also limit the co-registration capabilities, because accurate co-registration between image pairs is obtained by iteratively reducing the relative displacement between registration patches selected on stable ground. If many drastic changes are present in the images to analyze, registration points might be difficult to select, making the whole processing chain less reliable. Being aware of these limitations

usually allows selection of images from commercial catalogs that are the most likely to yield satisfying analysis. For instance, rough mountainous areas where snow and cloud cover change rapidly, where shadow length and orientation can be very different between seasons, and where the dynamical range of images can be high–up to the sensor saturation–may provide images that are among the most challenging to analyze. Despite these many challenges, it has been shown that the correlation of optical satellite images is the tool of choice to monitor temperate glaciers, and that careful selection of images can overcome most of these limitations (Chapter 8).

9.2.2 Limitations Due to Ancillary Data Quality

Less reliable analysis are obtained when the ancillary data used for processing are not accurate. We define here ancillary data in broader terms than it was given in the main body of this manuscript, designating by it all data needed to accurately apply the COSI-Corr methodology to a pair of images, with the exception of the actual images. These include the DEM, the satellite position, velocity, the attitude variations (roll, pitch, yaw) when acquiring the images, and the camera model. The most common source of errors due to ancillary data are stereoscopic artifacts induced by the lack of resolution of currently available DEM, emphasized by the difference of the incidence angle of the images. When using a DEM with coarse resolution, i.e., when the DEM resolution is less than a third of the image resolution, topographic artifacts can be minimized by selecting images with similar incidence angles. This solution is however not always possible and may put severe constraints on images' availability. It has therefore been shown that in some cases, and in particular when using the Shuttle Radar Topography Mission (SRTM) DEM, topography artifacts could be modeled and removed from displacement maps, therefore unbiasing the measurements (Chapter 8). This technique could be extended to correct for DEM errors, then correcting the inaccuracy directly at the source. Directly correcting inaccurate ancillary data has been demonstrated by devising a scheme for in-flight calibration of pushbroom cameras (Chapter 6). Uncertainties on the camera model can produce inaccurate orthorectified images, leading to systematic biases in displacement maps (and also in DEMs derived from stereo-matching), as has been evidenced and corrected for with the SPOT sensors. The same camera calibration technique would benefit most of the pushbroom systems, and could easily be extended even to aerial frame cameras. Finally, the sampling rate and ac-

curacy at which platform attitudes are recorded is of prime importance to avoid oscillating bias patterns in displacement maps. For instance, studies using ASTER images suffer from such artifacts due to the low recording rate of the spacecraft attitude, and only a simple destripping method has been proposed to mitigate this problem (Chapter 5). Further work should be directed toward complete attitude reconstruction using the differential variations observed between spectral bands. The ASTER spectral bands indeed scan the same scene with a small lag time, and high-frequency attitude reconstruction could be foreseen using cross-correlation techniques between the spectral bands of a given image [80].

9.2.3 Limitations Due to Image Quality

Image quality is a very broad term and in this section we are focusing on the effects of quantization and aliasing, which we have found to be significant factors in potentially limiting the precision of displacement measurements.

Sub-pixel displacements imply very subtle radiometric variations of the images, and this information can be easily altered if the quantization is too coarse. All the images used in this study were quantified by the acquisition system using only 8 bits per pixel. Investigations not shown in this study have concluded that improving quantification from 8 to 12 bits/pixel could reduce the noise level of the displacement measurements by a factor of 2. The newer satellites such as Quickbird, Worldview-1, or the future Pleiades, offer higher quantization depth, ranging from 10 to 12 bits/pixel. Better precision on the ground displacement measurements are therefore expected in the near future.

Imaging satellite systems are designed to offer sharp images of the ground, yielding to the resolution race that we are currently witnessing in the space industry. For instance, the Worldview-1 satellite, launched in 2007, offers a 50 cm ground resolution, and the two Pleiades satellites, planned for 2010 and 2011, will offer a 70 cm ground resolution. Sharp images are obtained when the frequency components near the image Nyquist frequency contribute to a non-negligible amount of the image energy. This is practically implemented by designing the cut-off frequency of the optical system to be well beyond the Nyquist frequency of the sensor. Unfortunately, these images, designed to visually satisfy most users, are highly aliased. For instance, it is not rare for the optical cut-off frequency to be more than 4 times larger than the sensor's Nyquist frequency. This design concept clearly limits the ability of phase correlation techniques, and maybe other quantitative techniques as well,

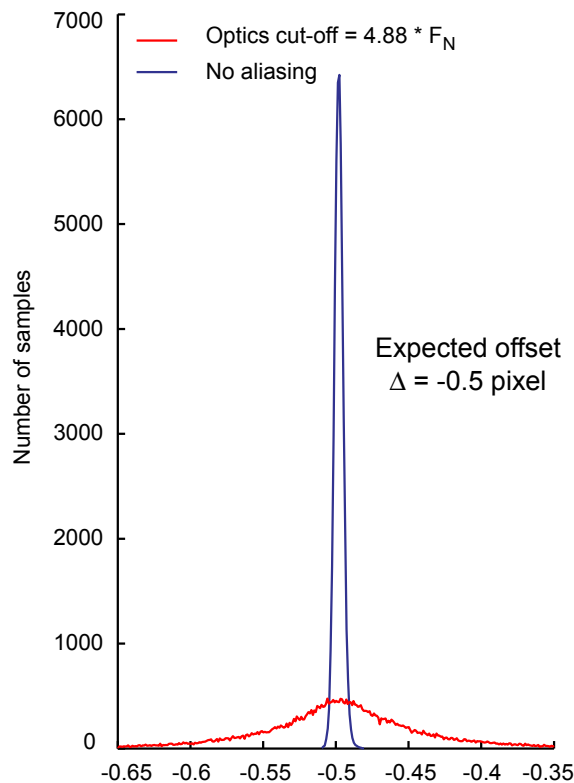


Figure 9.1: Loss in correlation precision by introduction of aliasing. Pairs of shifted low-resolution 10 m images have been simulated from a 1 m resolution aerial image. Low resolution images have been down-sampled assuming the optical cut-off frequency matches the CCD Nyquist frequency. The optical system is assumed ideal, with no obstruction, and noise-free. The optical cut-off frequency has been changed by varying the entrance pupil diameter of the simulated telescope, but in practice, it could simply be achieved through defocusing. Some studies have also shown that changing the bias substrate voltage of back-illuminated CCD sensors could produce a similar effect [199]. Generated images have been correlated using 32×32 pixel windows. Histograms of correlation measurements from shifted aliasing-free images appear in blue. The half pixel displacement introduced is retrieved with $\sigma = 0.002$ pixel. The red curve corresponds to the same experiment, but this time the optical cut-off frequency is 4.88 times the CCD Nyquist frequency, therefore introducing aliasing in the down-sampled and shifted images. This design is equivalent to choosing the width of the main lobe of the optical point spread function to be of the size of a CCD cell. It leads to sharp images and it is a common design option [200]. This case would also closely simulate the SPOT 1–4 sensors if a perfect imaging system were assumed. Using these aliased images, the displacement introduced is recovered with uncertainty $\sigma = 0.07$ pixel. It is interesting to note that this uncertainty is not far from the uncertainty noticed in practical applications.

to deliver accurate measurements. For instance, optical system simulations have concluded that such aliased images could induce a degradation of the displacement noise level by one order of magnitude when comparing with images produced by a band-limited optical design (see Fig. 9.1). The acquisition of band-limited, i.e., necessarily blurry, images therefore seems to be the logical choice to allow quantitative analysis of images. As demonstrated by the SPOT 5, 2.5 m Supermode scheme, which acquires nearly band-limited images, sharp images can be “visually restored” through deconvolution techniques [201, 202]. In addition to measurement noise, aliasing in the images can contribute, under specific conditions, to the type of wave artifacts observed in Fig. 3.20. Further work is needed to formally understand how aliasing biases phase correlation techniques, but this phenomenon has already been observed, though not explained, when a coarse resampling kernel was used to orthorectify images [1].

9.2.4 Limitations Due to Chosen Processing Strategy

Ground displacements are measured using a phase correlation technique that locally assumes rigid block translation. Although we have not found this to be a major limitation, there exist cases where this assumption can be observed to fail, at least partially. Across a fault for instance, when each part of the fault has moved in opposite directions, the SNR of the correlation is usually significantly smaller than elsewhere, due to the deviation from the rigid model assumption (see Chapter 4). When topographic artifacts are present due to DEM lack of resolution, the distortions induced are clearly not linear and the correlation also appears to have lower SNR. This remark should question classical techniques for deriving DEM from stereo image matching. Since stereo matching is usually done using correlation methods on locally rigid block translations, it is clear that a scheme where the topography is iteratively measured and compensated for would yield better accuracy as the rigid block model becomes more valid at each iteration.

The phase correlation technique derived has proved to be satisfyingly robust against noise in many practical situations. However, studying the formulation proposed from a Bayesian inverse-problem point of view, it is possible to show that this formulation is equivalent to attributing the observation uncertainty to the displacement to be measured at each frequency, rather than attributing a noise model to the image radiometry. In other words, the formulation proposed finds the best translation between image patches assuming noise-

free images, among translations at several frequencies, assumed to belong to a Gaussian-like distribution. The adaptive masking technique helps to mitigate the images noise-free assumption, but further studies are required to formally prove which noise model is best suited for image correlation analysis.

Correlation is performed on patches, and it can be considered that each correlation measurement provides an average translation over the image patches being analyzed. If we had access to the fully resolved displacement field encoded within a pair of images, we could then think of our measurements as being the fully resolved displacement field convolved by the correlation window. Deriving displacement fields with higher spatial accuracy could therefore be investigated through deconvolution of the correlation maps. This is a possible improvement that is left for further studies.

Another limitation concerns the orthorectification scheme. The inverse orthorectification model has been chosen in Chapter 3 to facilitate a rigorous resampling of the orthoimages. This model assumes that, at least locally, images are regularly sampled in the image plane. According to the study of Chapter 6, it is clear that because of the CCD distortions of pushbroom satellites, this assumption cannot hold everywhere. Therefore, an explicit formulation of the irregular resampling problem could be useful in some cases. For example, a formulation inspired by the study in [84] could be sought, eliminating at the same time the limitation of a separable resampling kernel. High frequencies in the orthoimages could then be recovered, and more accurate ground displacements could be retrieved if a solution to the aliasing bias in the correlation process can be found. Further studies are needed to overcome these limitations.

Finally, this thesis has presented a powerful technique to derive surface displacement fields from optically sensed images. It has proved accurate in many different applications, and the solutions proposed have been found well adapted to the applications for which they have initially been designed, i.e., the measurement of localized events such as earthquakes. However, because the technique proves robust and accurate, and given the large amount of optical images being continuously acquired by satellite and airborne programs, potential applications are growing. The continuous monitoring of natural phenomena therefore seems to be the logical path for further applications. For instance, precisely studying the impact of global warming on sea-level rise and freshwater supply to populations would require no less than the continuous monitoring of most glaciers on Earth. At this scale, a fully

automated processing would be absolutely necessary to handle very large data sets. In the procedure described in Chapter 3, one should remember that although accurate GCPs are automatically generated, patches where they will appear are manually selected. This step, which may take from 10 to 30 min per image, is driven by the necessity to control the a priori information on the stable ground areas present in the images to analyze. For earthquake studies, GCPs should be generated away from the near fault zone, and for glacier studies, GCPs should not lie on the moving glacierized ground. Completely suppressing manual intervention seems to be a particularly difficult task, but would be mandatory to envision continuous monitoring of large areas. For glacier studies for instance, one could think of automatically detecting glacierized areas to identify the best locations where GCPs should be generated. Continuous monitoring is still a step away from today, but we feel that this thesis has greatly contributed to reducing the size of that step.

Appendix A

Direct Model Orthorectification, Using a DEM

Let M_0 be the ground point at elevation h_0 obtained from direct model orthorectification of a given look angle \vec{u}_3 . Using a DEM, the point M , seen from \vec{u}_3 , that belongs to the topography surface, is approximated from the following algorithm:

$$i = 0$$

$$h_0 = h_{\text{start}}$$

$$M_0 = M \text{ computed at elevation } h_0$$

repeat

$$i = i + 1$$

$$h_i = h(M_{i-1}) \text{ from DEM}$$

$$M_i = M \text{ computed at elevation } h_i$$

until $\|M_i - M_{i-1}\| \leq d_{\text{min}}$.

d_{min} is set for a precision of 1 cm. Convergence is usually reached after 2 iterations. h_{start} is set to zero when the process is first started, then the exit value of the previous computed point is used. The DEM is interpolated at the location M_i using bi-cubic interpolation.

Appendix B

TPSS Algorithm Applied to the Inverse Orthorectification Problem

Calling R_x and R_y the nominal image ground resolution in the Easting and Northing directions, the best image sub-pixel coordinates $\mathbf{m} = (x^*, y^*)$ that minimize Φ , eq. (3.7), are given by the following TPSS [30] algorithm:

$$\mathbf{m}_{-1} = (x_0 - 1, y_0 + \varepsilon)^t$$

$$\mathbf{m}_0 = (x_0, y_0)^t$$

$$\mathbf{g}_{-1} = (R_x, R_y)^t$$

$$h = 10^{-2}/R_y$$

$$\Phi_0 = \Phi(x_0, y_0)$$

$$k = 0$$

repeat

$$\mathbf{g}_k = \begin{pmatrix} \frac{\Phi(x_k+h, y_k) - \Phi(\mathbf{m}_k^t)}{h} \\ \frac{\Phi(x_k, y_k+h) - \Phi(\mathbf{m}_k^t)}{h} \end{pmatrix}$$

$$\Delta \mathbf{m} = \mathbf{m}_k - \mathbf{m}_{k-1}$$

$$\Delta \mathbf{g} = \mathbf{g}_k - \mathbf{g}_{k-1}$$

$$\alpha_k = \Delta \mathbf{m}^t \cdot \Delta \mathbf{m} / \Delta \mathbf{m}^t \cdot \Delta \mathbf{g}$$

$$\mathbf{m}_{k+1} = \mathbf{m}_k - \alpha_k \cdot \mathbf{g}_k$$

$$\Phi_{k+1} = \Phi(\mathbf{m}_{k+1}^t)$$

$$k = k + 1$$

until $|\Phi_k - \Phi_{k-1}| \leq p^2$.

At the first grid point, $\mathbf{m}_0 = (x_0, y_0)^t$ is set to an arbitrary position in the raw image. For all others, the result of the previous optimization is used for initialization. Starting conditions for the gradient \mathbf{g}_{-1} are difficult to set up since one cannot guess the correct sign but the proposed initialization works well in practice. We used $\varepsilon = 10^{-9}$. The value of h may be critical. It has to be as small as possible to give the derivation a good accuracy but should not be too small so that interpolation of satellite attitude remains meaningful. We have found that h should depend on the raw image resolution. p sets the minimum orthorectification accuracy. For a centimeter accuracy ($p = 10^{-2}$) convergence is reached with an average of 3 iterations.

Appendix C

TPSS Algorithm Applied to the Phase Correlation Minimization Problem

If $\mathbf{m} = (\Delta_x, \Delta_y)$ represents the displacement to be estimated, the algorithm is described as follows:

$$\mathbf{m}_{-1} = (\Delta_{x_0} - 0.1, \Delta_{y_0} - 0.1)^t$$

$$\mathbf{g}_{-1} = \begin{pmatrix} \sum_{\omega_x} \sum_{\omega_y} W(\omega_x, \omega_y) \\ \sum_{\omega_x} \sum_{\omega_y} W(\omega_x, \omega_y) \end{pmatrix}$$

$$k = 0$$

repeat

$$\mathbf{g}_k = \begin{pmatrix} \sum_{\omega_x} \sum_{\omega_y} \frac{\partial \varphi_{\Delta_k}(\omega_x, \omega_y)}{\partial \Delta_x} \\ \sum_{\omega_x} \sum_{\omega_y} \frac{\partial \varphi_{\Delta_k}(\omega_x, \omega_y)}{\partial \Delta_y} \end{pmatrix}$$

$$\Delta \mathbf{m} = \mathbf{m}_k - \mathbf{m}_{k-1}$$

$$\Delta \mathbf{g} = \mathbf{g}_k - \mathbf{g}_{k-1}$$

$$\alpha_k = \Delta \mathbf{m}^t \cdot \Delta \mathbf{m} / \Delta \mathbf{m}^t \cdot \Delta \mathbf{g}$$

$$\mathbf{m}_{k+1} = \mathbf{m}_k - \alpha_k \cdot \mathbf{g}_k$$

$$k = k + 1$$

until $|\mathbf{m}_k - \mathbf{m}_{k-1}| \leq (p, p)$.

with:

$$\frac{\partial \varphi_{\Delta}(\omega_x, \omega_y)}{\partial \Delta_x} = 2W(\omega_x, \omega_y)\omega_x$$

$$\begin{aligned} & [Q_R(\omega_x, \omega_y) \sin(\omega_x \Delta_x + \omega_y \Delta_y) - \\ & Q_I(\omega_x, \omega_y) \cos(\omega_x \Delta_x + \omega_y \Delta_y)] \end{aligned}$$

and

$$\frac{\partial \varphi_{\Delta}(\omega_x, \omega_y)}{\partial \Delta_y} = 2W(\omega_x, \omega_y)\omega_y$$

$$\begin{aligned} & [Q_R(\omega_x, \omega_y) \sin(\omega_x \Delta_x + \omega_y \Delta_y) - \\ & Q_I(\omega_x, \omega_y) \cos(\omega_x \Delta_x + \omega_y \Delta_y)], \end{aligned}$$

where Q_R and Q_I are defined as in Section 3.4.5.2. p sets the stop-condition for the convergence. We have chosen $p = 10^{-3}$ so that displacements in each direction are estimated with an accuracy of at least 10^{-3} pixel. The initialization of the algorithm, given by $(\Delta_{x_0}, \Delta_{y_0})$ is described in Section 3.4.5.5.

Appendix D

Application to ASTER Images

Position, velocity, sight vectors, and attitude angles of the imaging system during image acquisition are provided with raw (level 1A) ASTER images in ancillary data [203]. These parameters constitute the ASTER viewing geometry. The ASTER sight vectors are equivalent to the SPOT look directions \vec{u}_2 .

Geometrical-axes conventions between SPOT and ASTER systems are different: X and Y axes are swapped and the Z axis is inverted. Taking into account these conventions and from the attitude angles provided it is therefore possible to retrieve the look directions \vec{u}_1 for ASTER images by inversion of eq. (3.4). ASTER ancillary data are then translated onto SPOT variables. We have done so in a pre-processing step and 15 m raw ASTER images have been successfully processed from the complete chain proposed. Systematic oscillations in the correlation images with an amplitude of 5–6 m and a periodicity of 4.8 km have revealed the lack of accuracy and sampling density of the ASTER attitude data. Subtracting stacks across correlation images have allowed removal of most of these attitude artifacts to produce a high-quality displacement field between pairs of images [9]. The natural noise of such correlation images has been estimated to be around 2 m in each North/South and East/West component.

Appendix E

Determining the Overlap Between the Slave and the Reference Images

To avoid unnecessary computations during calibration, it is crucial to determine beforehand the region in the raw slave image, which, once projected on the ground, will overlap with the orthorectified reference image. This can be accomplished automatically, with the following algorithm:

1. Extract the ground coordinates (UTM) of the four corners of the orthorectified reference image. This defines a convex 4-polygon, P_1 .
2. Determine the ground coordinates (UTM) of the raw slave image corners using the direct orthorectification model. This defines a second 4-polygon P_2 in the orthorectified domain.
3. Compute the intersection of the interior of these two 4-polygons. This can be solved using Sutherland-Hodgman's polygon clipping algorithm [204]. The intersection is a new polygon P_3 in the orthorectified domain.
4. Map P_3 from the orthorectified domain to the geometry of the raw slave image. This is done by applying the inverse orthorectification model on each vertex of P_3 .
5. The projection of P_3 in the raw slave image plane is assumed to be the polygon, P_4 , delimited by the inverse projection of the P_3 vertices. P_4 is then shrunk by the size of the correlation window that will be used during calibration to avoid edge effects, producing the polygon P_5 . Distortions are then estimated for all pixels in the raw slave image that are contained within the P_5 polygon.

Bibliography

- [1] N. Van Puymbroeck, R. Michel, R. Binet, J.-P. Avouac, and J. Taboury, “Measuring earthquakes from optical satellite images,” *Applied Optics*, vol. 39, no. 20, pp. 3486–3494, 2000.
- [2] S. Leprince, E. Berthier, F. Ayoub, C. Delacourt, and J. P. Avouac, “Monitoring earth surface dynamics with optical imagery,” *Eos, Transactions, American Geophysical Union*, January 1st 2008.
- [3] T. Scambos, M. Dutkiewicz, J. Wilson, and R. Bindschadler, “Application of image cross-correlation to the measurement of glacier velocity using satellite image data,” *Remote Sensing of Environment*, vol. 42, no. 33, pp. 177–186, 1992.
- [4] E. Berthier, H. Vadon, D. Baratoux, Y. Arnaud, C. Vincent, K. Feigl, F. Remy, and B. Legresy, “Surface motion of mountain glaciers derived from satellite optical imagery,” *Remote Sensing of Environment*, vol. 95, no. 1, pp. 14–28, 2005.
- [5] R. Crippen and R. Blom, “Measurement of subresolution terrain displacements using Spot panchromatic imagery,” in *International Geoscience and Remote Sensing Symposium (IGARSS)*, vol. 3, June 1991, pp. 1667–1670.
- [6] A. Kääb, “Monitoring high-mountain terrain deformation from repeated air- and spaceborne optical data: examples using digital aerial imagery and ASTER data,” *ISPRS Journal of Photogrammetry and Remote Sensing*, vol. 57, no. 1–2, pp. 39–52, 2002.
- [7] C. Delacourt, P. Allemand, B. Casson, and H. Vadon, “Velocity field of the ’La Clapiere’ landslide measured by the correlation of aerial and QuickBird satellite images,” *Geophysical Research Letters*, vol. 31, no. L15619, 2004.

- [8] S. Leprince, S. Barbot, F. Ayoub, and J. P. Avouac, "Automatic and precise orthorectification, co-registration and sub-pixel correlation of satellite images, application to ground deformation measurements," *IEEE Transactions on Geoscience and Remote Sensing*, vol. 45, no. 6, pp. 1529–1558, 2007.
- [9] J. P. Avouac, F. Ayoub, S. Leprince, O. Konca, and D. Helmberger, "The 2005, Mw 7.6 Kashmir earthquake, rupture kinematics from sub-pixel correlation of ASTER images and seismic waveforms analysis," *Earth and Planetary Science Letters*, vol. 249, no. 3-4, pp. 514–528, 2006.
- [10] S. Dominguez, J.-P. Avouac, and R. Michel, "Horizontal coseismic deformation of the 1999 Chi-Chi earthquake measured from SPOT satellite images; implications for the seismic cycle along the western foothills of central Taiwan," *Journal of Geophysical Research*, vol. 108, no. B2, 2003.
- [11] Y. Klinger, R. Michel, and R. King, "Evidence for a barrier model from Mw7.8 Kokoxili (Tibet) earthquake slip-distribution," *Earth and Planetary Science Letters*, vol. 242, pp. 354–364, 2006.
- [12] E. Rignot and P. Kanagaratnam, "Changes in the velocity structure of the Greenland ice sheet," *Science*, vol. 311, no. 5763, pp. 986–990, 2006.
- [13] J. Malet, A. Auzet, O. Maquaire, B. Ambroise, L. Descroix, M. Estves, J. Vandervaere, and E. Truchet, "Soil surface characteristics influence on infiltration in black marls: application to the Super-Sauze earthflow (southern Alps, France)," *Earth Surface Processes and Landforms*, vol. 28, pp. 547–564, 2003.
- [14] C. Squarzoni, C. Delacourt, and P. Allemand, "Nine years of spatial and temporal evolution of the La Valette landslide observed by SAR interferometry," *Engineering Geology*, vol. 68, no. 1–2, pp. 53–66, 2003.
- [15] J. Townshend, C. Justice, C. Gurney, and J. McManus, "The impact of misregistration on change detection," *IEEE Transactions on Geoscience and Remote Sensing*, vol. 30, no. 5, pp. 1054–1060, 1992.

- [16] N. Bryant, A. Zobrist, and T. Logan, "Automatic co-registration of space-based sensors for precision change detection and analysis," in *International Geoscience and Remote Sensing Symposium (IGARSS)*, vol. 2, July 2003, pp. 1371–1373.
- [17] X. Dai and S. Khorram, "Effects of image misregistration on the accuracy of remotely sensed change detection," *IEEE Transactions on Geoscience and Remote Sensing*, vol. 36, no. 5, pp. 1566–1577, 1998.
- [18] H. Vadon and D. Massonnet, "Earthquake displacement fields mapped by very precise correlation. Complementarity with radar interferometry," in *International Geoscience and Remote Sensing Symposium (IGARSS)*, vol. 6, Honolulu, HI, USA, July 2000, pp. 2700–2702.
- [19] R. Binet and L. Bollinger, "Horizontal coseismic deformation of the 2003 Bam (Iran) earthquake measured from SPOT-5 THR satellite imagery," *Geophysical Research Letters*, vol. 32, no. 2, 2005.
- [20] R. Michel and J.-P. Avouac, "Deformation due to the 17 August 1999 Izmit, Turkey, earthquake measured from SPOT images," *Journal of Geophysical Research*, vol. 107, no. B4, 2062, 2002.
- [21] C. Schiek, "Terrain change detection using ASTER optical satellite imagery along the Kunlun fault, Tibet," Master's thesis, University of Texas at El Paso, 2004. [Online]. Available: http://www.geo.utep.edu/pub/schiek/Cara.Schiek_Master_Thesis.pdf
- [22] D. Massonnet, M. Rossi, C. Carmona, F. Adragna, G. Peltzer, K. Feigl, and T. Rabaute, "The displacement field of the Landers earthquake mapped by radar interferometry," *Nature*, vol. 364, pp. 138–142, July 1993.
- [23] *SPOT User's Handbook*, SPOT Image Corporation, 1897 Preston White Dr., Reston, VA 22091-4368, 1990.
- [24] S. Riazanoff, *SPOT Satellite Geometry Handbook*, SPOT Image, 5 rue des Satellites, 31030 Toulouse Cedex 4, France, January 2002.
- [25] Z. Altamini, P. Sillard, and C. Boucher, "ITRF 2000: A new release of the International Terrestrial Reference Frame for earth sciences applications," *Journal of Geophysical Research*, vol. 107, no. B10, 2002.

- [26] J. Snyder, *Map Projections—A Working Manual*, ser. U.S. Geological Survey Professional Paper 1395. Government Printing Office, 1987.
- [27] T. Westin, “Precision rectification of SPOT imagery,” *Photogrammetric Engineering and Remote Sensing*, vol. 56, no. 2, pp. 247–253, 1990.
- [28] L. Chen and L. Lee, “Rigorous generation of digital orthophotos from SPOT images,” *Photogrammetric Engineering and Remote Sensing*, vol. 59, no. 5, pp. 655–661, 1993.
- [29] Y. El-Manadili and K. Novak, “Precision rectification of SPOT imagery using the direct linear transformation model,” *Photogrammetric Engineering and Remote Sensing*, vol. 62, no. 1, pp. 67–72, 1996.
- [30] J. Barzilai and J. Borwein, “Two-point step size gradient methods,” *IMA Journal of Numerical Analysis*, vol. 8, pp. 141–148, 1988.
- [31] R. Keys, “Cubic convolution interpolation for digital image processing,” *IEEE Transactions on Acoustics, Speech, and Signal Processing*, vol. 29, no. 6, pp. 1153–1160, 1981.
- [32] A. Oppenheim, R. Schaffer, and J. Buck, *Discrete-Time Signal Processing*, 2nd ed. Upper Saddle River, NJ: Prentice Hall, 1999.
- [33] P. P. Vaidyanathan, *Multirate Systems and Filter Banks*. Upper Saddle River, NJ: Prentice Hall, 1993.
- [34] B. Zitová and J. Flusser, “Image registration methods: a survey,” *Image and Vision Computing*, vol. 21, no. 11, pp. 977–1000, 2003.
- [35] H. Foroosh, J. Zerubia, and M. Berthod, “Extension of phase correlation to subpixel registration,” *IEEE Transactions on Image Processing*, vol. 11, no. 3, pp. 188–200, 2002.
- [36] W. Hoge, “A subspace identification extension to the phase correlation method [mri application],” *IEEE Transactions on Medical Imaging*, vol. 22, no. 2, pp. 277–280, 2003.

- [37] H. Stone, M. Orchard, C. Ee-Chien, and S. Martucci, "A fast direct Fourier-based algorithm for subpixel registration of images," *IEEE Transactions on Geoscience and Remote Sensing*, vol. 39, no. 10, pp. 2235–2243, 2001.
- [38] H. Carfantan and B. Rouge, "Estimation non biaisée de décalages subpixelaire sur les images SPOT," in *Colloque GRETSI*, Toulouse, France, September 2001.
- [39] J. Goodman, *Introduction to Fourier Optics*, 2nd ed. McGraw Hill, 1996.
- [40] A. Leon-Garcia, *Probability and Random Processes for Electrical Engineering*, 2nd ed. Addison Wesley, 1994.
- [41] C. Knapp and G. C. Carter, "The generalized correlation method for estimation of time delay," *IEEE Transactions On Acoustics, Speech, and Signal Processing*, vol. 24, no. 4, pp. 320–327, 1976.
- [42] G. H. Golub and C. F. V. Loan, *Matrix Computations*, 2nd ed. The Johns Hopkins University Press, 1989.
- [43] J. Manton, R. Mahony, and Y. Hua, "The geometry of weighted low-rank approximations," *IEEE Transactions on Signal Processing*, vol. 51, no. 2, pp. 500–514, 2003.
- [44] D. Field, "Relations between the statistics of natural images and the response properties of cortical-cells," *Journal of the Optical Society of America - A*, vol. 4, no. 12, pp. 2379–2394, 1987.
- [45] D. Tolhurst, Y. Tadmor, and T. Chao, "Amplitude spectra of natural images," *Ophthalmic and Physiological Optics*, vol. 12, no. 2, pp. 229–232, 1992.
- [46] A. van der Schaaf and J. van Hateren, "Modeling the power spectra of natural images: Statistics and information," *Vision Research*, vol. 36, no. 17, pp. 2759–2770, 1996.
- [47] C. Latry and B. Rouge, "Optimized sampling for CCD instruments: the Supermode scheme," in *International Geoscience and Remote Sensing Symposium (IGARSS)*, vol. 5, July 2000, pp. 2322–2324.
- [48] (2003) SPOT satellite technical data. SPOT Image. [Online]. Available: <http://www.spotimage.fr>

- [49] C. Jayles and M. Costes, “Ten centimeters orbits in real-time on-board of a satellite, DORIS/DIODE current status,” *Acta Astronautica*, vol. 54, no. 5, pp. 315–323, 2004.
- [50] T. Westin, “Interior orientation of SPOT imagery,” in *XVIIIth ISPRS Congress, Commission I*, I. S. for Photogrammetry and R. Sensing, Eds., vol. 29, Washington, D.C., 1992, pp. 193–198.
- [51] M. Sveldow, C. McGillem, and P. Anuta, “Image registration: Similarity measure and preprocessing method comparisons,” *IEEE Transactions on Aerospace and Electronic Systems*, vol. 14, no. 1, pp. 141–149, 1978.
- [52] W. Pratt, “Correlation techniques of image registration,” *IEEE Transactions on Aerospace and Electronic Systems*, vol. 10, no. 3, pp. 353–358, 1974.
- [53] N. Dodgson, “Quadratic interpolation for image resampling,” *IEEE Transactions on Image Processing*, vol. 6, no. 9, pp. 1322–1326, 1997.
- [54] (2000) Shuttle radar topography mission. JPL-NASA. [Online]. Available: <http://www2.jpl.nasa.gov/srtm/statistics.html>
- [55] X. Li and H. Gotze, “Tutorial: Ellipsoid, geoid, gravity, geodesy, and geophysics,” *Geophysics*, vol. 66, no. 6, pp. 1660–1668, 2001.
- [56] *Caltech Online Catalog*. [Online]. Available: http://www.data.scec.org/catalog_search/date_mag_loc.php
- [57] M. Simons, Y. Fialko, and L. Rivera, “Coseismic deformation from the 1999 Mw 7.1 Hector Mine, California, earthquake as inferred from InSAR and GPS observations,” *Bulletin of the Seismological Society of America*, vol. 92, no. 4, pp. 1390–1402, 2002.
- [58] J. A. Treiman, K. J. Kendrick, W. A. Bryant, T. K. Rockwell, and S. F. McGill, “Primary surface rupture associated with the Mw 7.1 16 October 1999 Hector Mine earthquake, San Bernardino County, California,” *Bulletin of the Seismological Society of America*, vol. 92, no. 4, pp. 1171–1191, 2002.
- [59] G. Peltzer, F. Crampé, and P. Rosen, “The Mw 7.1, Hector Mine, California earthquake: surface rupture, surface displacement field, and fault slip solution from ERS

- SAR data,” *C. R. Acad. Sci. Paris, Earth and Planetary Sciences*, vol. 333, pp. 545–55, 2001.
- [60] Y. Fialko, M. Simons, and D. Agnew, “The complete (3-D) surface displacement field in the epicentral area of the 1999 Mw 7.1 Hector Mine earthquake, California, from space geodetic observations,” *Geophysical Research Letters*, vol. 28, no. 16, pp. 3063–3066, 2001.
- [61] R. Michel, J. P. Avouac, and J. Taboury, “Measuring near field coseismic displacements from SAR images: application to the Landers earthquake,” *Geophysical Research Letters*, vol. 26, no. 19, pp. 3017–3020, 1999.
- [62] F. Ayoub, S. Leprince, and J. P. Avouac, “Measuring co-seismic ground deformation from aerial photography using COSI-Corr,” *ISPRS Journal of Photogrammetry and Remote Sensing*, submitted 2007.
- [63] K. Feigl, F. Sarti, H. Vadon, S. McClusky, S. Ergintav, P. Durand, R. Bürgmann, A. Rigo, D. Massonnet, and R. Reilinger, “Estimating slip distribution for the Izmit mainshock from coseismic GPS, ERS-1, RADARSAT, and SPOT measurements,” *Bulletin of the Seismological Society of America*, vol. 92, no. 1, pp. 138–160, 2002.
- [64] Y. Klinger, X. W. Xu, P. Tapponnier, J. V. der Woerd, C. Lasserre, and G. King, “High-resolution satellite imagery mapping of the surface rupture and slip distribution of the m-w similar to 7.8, 14 November 2001 Kokoxili earthquake, Kunlun Fault, northern Tibet, China,” *Bulletin of the Seismological Society of America*, vol. 95, no. 5, pp. 1970–1987, 2005.
- [65] R. Michel and J. P. Avouac, “Coseismic surface deformation from air photos: The Kickapoo step over in the 1992 Landers rupture,” *Journal of Geophysical Research*, vol. 111, no. B03408, 2006.
- [66] E. Berthier, Y. Arnaud, D. Baratoux, C. Vincent, and F. Rémy, “Recent rapid thinning of the “Mer de Glace” glacier derived from satellite optical images,” *Geophysical Research Letters*, vol. 31, no. L17401, 2004.
- [67] P. R. Wolf and B. A. Dewitt, *Elements of Photogrammetry with Applications in GIS*. 3rd ed. McGraw Hill, 2000.

- [68] K. P. Schwarz, M. A. Chapman, M. E. Cannon, and P. Gong, "An integrated INS/GPS approach to the georeferencing of remotely sensed data," *Photogrammetric Engineering and Remote Sensing*, vol. 56, no. 12, 1993.
- [69] (1987) National aerial photography program. USGS. [Online]. Available: <http://edc.usgs.gov/guides/napp.html>
- [70] K. Sieh, L. Jones, E. Hauksson, K. Hudnut, D. Eberhart-Phillips, T. Heaton, S. Hough, K. Hutton, H. Kanamori, A. Lilje, S. Lindvall, S. McGill, J. Mori, C. Rubin, J. A. Spotila, J. Stock, H. Thio, J. Treiman, B. Wernicke, and J. Zachariasen, "Near-field investigations of the landers earthquake sequence, april to july, 1992," *Science*, vol. 260, pp. 171–176, 1993.
- [71] W. X. Du, L. R. Sykes, B. E. Shaw, and C. H. Scholz, "Triggered aseismic fault slip from nearby earthquakes, static or dynamic effect?" *Journal of Geophysical Research - Solid Earth*, vol. 108, no. B2, 2003.
- [72] S. Leprince, F. Ayoub, Y. Klinger, and J. P. Avouac, "Co-registration of optically sensed images and correlation (COSI-Corr): an operational methodology for ground deformation measurements," in *International Geoscience and Remote Sensing Symposium (IGARSS)*, vol. 6, Barcelona, Spain, July 2007, pp. 2700–2702.
- [73] M. Taylor, S. Leprince, J. P. Avouac, and K. Sieh, "Detecting co-seismic displacements in glaciated regions: An example from the great November 2002 Denali earthquake using SPOT horizontal offsets," *Earth and Planetary Science Letters*, in press, 2008.
- [74] S. Leprince, E. Berthier, F. Ayoub, C. Delacourt, and J. P. Avouac, "Monitoring Earth surface dynamics with optical imagery," American Geophysical Union, Fall Meeting, San Francisco, December 2007.
- [75] T. Westin, "Inflight calibration of SPOT CCD detector geometry," *Photogrammetric Engineering and Remote Sensing*, vol. 58, no. 9, pp. 1313–1319, 1992.
- [76] E. Baltsavias, Z. Li, and H. Eisenbeiss, "DSM generation and interior orientation determination of IKONOS images using a testfield in Switzerland," in *ISPRS Workshop High-Resolution Earth Imaging for Geospatial Information*, I. S. for Photogrammetry and R. Sensing, Eds., Hannover, Germany, 2005.

- [77] K. Jacobsen, "Calibration of optical sensors," in *ISPRS Commission I, International Calibration and Orientation Workshop EuroCOW 2006*, I. S. for Photogrammetry and R. Sensing, Eds., Castelldefels, Spain, 2006.
- [78] "National Elevation Dataset," U.S. Geological Survey. [Online]. Available: <http://ned.usgs.gov/>
- [79] R. Gachet, "SPOT5 in-flight commissioning: inner orientation of HRG and HRS instruments," in *XXth ISPRS Congress, Commission I*, I. S. for Photogrammetry and R. Sensing, Eds., vol. 35, Istanbul, Turkey, 2004.
- [80] Y. Teshima and A. Iwasaki, "Correction of attitude fluctuation of Terra spacecraft using ASTER/SWIR imagery with parallax observation," *IEEE Trans. Geosci. Remote Sens.*, vol. 46, no. 1, pp. 222–227, 2008.
- [81] E. Breton, A. Bouillon, R. Gachet, and F. Delussy, "Pre-flight and in-flight geometric calibration of SPOT5 HRG and HRS images," in *ISPRS Commission I Symposium, Pecora 15/Land Satellite Information IV Conference*, I. S. for Photogrammetry and R. Sensing, Eds., Denver, CO, USA, 2002.
- [82] I. Barisin, S. Leprince, J. P. Avouac, B. Parsons, and T. Wright, "Deformation measurement for the September 2005 AFAR rifting event from sub-pixel correlation of spot images," American Geophysical Union, Fall Meeting, San Francisco, December 2007.
- [83] A. Bouillon, E. Breton, F. D. Lussy, and R. Gachet, "SPOT5 HRG and HRS first in-flight geometry quality results," in *Proceedings of SPIE - Sensors, Systems, and Next-Generation Satellites VI*, vol. 4881, 2003, pp. 212–223.
- [84] A. Almansa, B. Rougé, and S. Jaffard, "Irregular sampling in satellite images and reconstruction algorithms," in *35th Congres National d'Analyse Numrique (CANUM03)*, June 2003.
- [85] R. Bilham, "Earthquakes in India and the Himalaya: tectonics, geodesy and history," *Annals of Geophysics*, vol. 47, no. 2-3, pp. 839–858, 2004.
- [86] R. Bilham, V. Gaur, and P. Molnar, "Earthquakes: Himalayan seismic hazard," *Science*, vol. 293, no. 5534, pp. 1442–1444, 2001.

- [87] J. Jackson, "Fatal attraction: living with earthquakes, the growth of villages into megacities, and earthquake vulnerability in the modern world," *Philos. Trans. R. Soc. Lond. A*, vol. 364, p. 19111925, 2006.
- [88] S. Kumar, S. Wesnousky, T. Rockwell, R. Briggs, V. Thakur, and R. Jayangondaperumal, "Paleoseismic evidence of great surface rupture earthquakes along the Indian Himalaya," *Geophysical Research Letters*, vol. 111, no. B03304, 2006.
- [89] R. Yeats, T. Nakata, A. Farah, M. Mizra, M. Pandey, and R. Stein, "The Himalayan frontal fault system," *DeJong and Farah, Editors, Geodynamics of Pakistan, Geological Survey of Pakistan: Seismicity of the Hazara Arc in Northern Pakistan: Decollement vs. Basement Faulting, Annales Tectonicae Special Issue Supplement to Volume VI*, p. 8598, 1992.
- [90] P. Bettinelli, J. Avouac, M. Flouzat, F. Jouanne, L. Bollinger, P. Willis, and G. Chitraka, "Plate motion of India and interseismic strain in the Nepal Himalaya from GPS and DORIS measurements," *Journal of Geodesy*, vol. 80, no. 8-11, pp. 567–589, 2006.
- [91] L. Seeber, J. Armbruster, and R. Quittmeyer, "Seismicity and continental collision in the Himalayan arc," *In: H.K. Gupta and F.M. Delany, Editors, ZagrosHindukushHimalaya: Geodynamic Evolution 3, Geodynamic Series, American Geophysical Union, Washington*, p. 215242, 1981.
- [92] C. Schiek and J. Hurtado, "Slip analysis of the Kokoxili earthquake using terrain-change detection and regional earthquake data," *Geosphere*, vol. 2, no. 3, pp. 187–194, 2006.
- [93] R. Yeats and A. Hussain, "Surface features of the Mw 7.6, 8 October 2005 Kashmir earthquake, northern Himalaya, Pakistan: Implications for the Himalayan front," Seismological Society of America (SSA) meeting, San Francisco, CA, 2006.
- [94] T. Nakata, H. Tsutsumi, S. Khan, and R. Lawrence, "Active faults of Pakistan," Research Center for Regional Geography Hiroshima University, Hiroshima, Japan, p. 141, 1991.

- [95] T. Parsons, R. Yeats, Y. Yagi, and A. Hussain, "Static stress change from the 8 October, 2005 $M = 7.6$ Kashmir earthquake," *Geophysical Research Letters*, vol. 33, no. L06304, pp. 1192–1207, 2006.
- [96] C. Ji, D. Wald, and D. Helmberger, "Source description of the 1999 Hector Mine, California, earthquake, part I: Wavelet domain inversion theory and resolution analysis," *Bulletin of the Seismological Society of America*, vol. 92, no. 4, pp. 1192–1207, 2002.
- [97] C. Bassin, G. Laske, and G. Masters, "The current limits of resolution for surface wave tomography in North America," *Eos, Transactions, American Geophysical Union*, 2000.
- [98] X. Xie and Z. Yao, "A generalized reflection-transmission coefficient matrix method to calculate static displacement field of a dislocation source in a stratified half space," *Chin. J. Geophys.*, vol. 32, p. 191205, 1989.
- [99] P. Treloar, M. Coward, A. Chambers, C. Izatt, and K. Jackson, *Thrust geometries, interferences anti rotations in the Northwest Himalaya*, ser. Thrust Tectonics. K.R. McCaiy (Ed.) Chapman and Halt, London, UK, 1992.
- [100] A. Gansser, *Geology of the Himalayas*. Interscience Publishers, London, 1964.
- [101] P. Banerjee and R. Bürgmann, "Convergence across the northwest Himalaya from GPS measurements," *Geophysical Research Letters*, vol. 29, no. 13, 2002.
- [102] M. Hauck, K. Nelson, L. Brown, W. Zhao, and A. Ross, "Crustal structure of the Himalayan orogen at $\sim 90^\circ$ east longitude from project INDEPTH deep reflection profiles," *Tectonics*, vol. 17, no. 4, p. 481500, 1998.
- [103] J. Lavé, D. Yule, S. Sapkota, K. Basant, C. Madden, M. Attal, and R. Pandey, "Evidence for a great medieval earthquake (approximate to 1100 AD) in the Central Himalayas, Nepal," *Science*, vol. 307, no. 5713, pp. 1302–1305, 2005.
- [104] K. Wallace, R. Bilham, F. Blume, V. Gaur, and V. Gahalaut, "Surface deformation in the region of the 1905 Kangra $M_w = 7.8$ earthquake in the period 18462001," *Geophysical Research Letters*, vol. 32, no. L15307, 2005.

- [105] R. Iyengar, D. Sharma, and J. Siddiqui, "Earthquake history of India in medieval times," *Indian J. Hist. Sci.*, vol. 34, 1999.
- [106] J. Baranowski, J. Armbruster, L. Seeber, and P. Molnar, "Focal depths and fault plane solutions of earthquakes and active tectonics of the Himalaya," *Journal of Geophysical Research*, vol. 89, no. B8, p. 69186928, 1984.
- [107] M. Pandey, R. Tandukar, J. Avouac, J. Lave, and J. Massot, "Interseismic strain accumulation on the Himalayan crustal ramp (Nepal)," *Geophysical Research Letters*, vol. 22, no. 7, p. 751754, 1995.
- [108] L. Bollinger, J. Avouac, R. Cattin, and M. Pandey, "Stress buildup in the Himalaya," *Journal of Geophysical Research*, vol. 109, no. B11405, 2004.
- [109] S. Fujiwara, M. Tobita, H. Sato, S. Ozawa, H. Ue, M. Koaarai, H. Nakai, M. Fujiwara, H. Yurai, T. Nishimura, and F. Hayashi, "Satellite data gives snapshot of the 2005 Pakistan earthquake," *Eos, Transactions, American Geophysical Union*, 2006.
- [110] E. Pathier, E. Fielding, T. Wright, R. Walker, B. Parsons, and S. Hensley, "Displacement field and slip distribution of the 2005 Kashmir earthquake from SAR imagery," *Geophysical Research Letters*, vol. 33, no. L20310, 2006.
- [111] C. Ji, D. Helmberger, T.-R. Song, K.-F. Ma, and D. Wald, "Slip distribution and tectonic implications of the 1999 Chi-Chi, Taiwan earthquake," *Geophysical Research Letters*, vol. 28, no. 3, p. 43794382, 2001.
- [112] J. P. Avouac, "Mountain building, erosion and the seismic cycle in the Nepal Himalaya," In: R. Dmowska, Editor, *Advances in Geophysics*, Elsevier, Amsterdam, 2003.
- [113] C. Scholz, *The Mechanics of Earthquakes and Faulting*. Cambridge University Press, New York, 1990.
- [114] B. Hernandez, F. Cotton, and M. Campillo, "Contribution of radar interferometry to a two-step inversion of the kinematic process of the 1992 Landers earthquake," *Journal of Geophysical Research. Solid Earth*, vol. 104, no. B6, pp. 13 083–13 099, 2004.

- [115] C. Ji, K. Larson, Y. Tan, K. Hudnut, and K. Choi, “Slip history of the 2003 San Simeon earthquake constrained by combining 1-Hz GPS, strong motion, and teleseismic data,” *Geophysical Research Letters*, vol. 31, no. L17608, 2004.
- [116] B. Delouis, D. Giardini, P. Lundgren, and J. Salichon, “Joint inversion of InSAR, GPS, teleseismic, and strong-motion data for the spatial and temporal distribution of earthquake slip: application to the 1999 Izmit mainshock,” *Bulletin of the Seismological Society of America*, vol. 92, no. 1, pp. 278–299, 2002.
- [117] A. Konca, V. Hjorleifsdottir, T. Song, J. Avouac, D. Helmberger, C. Ji, K. Sieh, R. Briggs, and A. Meltzner, “Rupture kinematics of the 2005, Mw 8.6, nias-simeulue earthquake from the joint inversion of seismic and geodetic data,” *Bulletin of the Seismological Society of America*, vol. 97, no. 1, pp. S307–S322, 2007.
- [118] J. Calkins, T. Offield, S. Abdullah, and S. Ali, *Geology of the southern Himalaya in Hazara, Pakistan and adjacent areas*, ser. U.S. Geological Survey Professional Paper 716-C. Government Printing Office, Washington, D.C., 1975.
- [119] M. Searle, M. Khan, M. Jan, J. DiPietro, K. Pogue, D. Pivnik, W. Sercombe, C. Izatt, P. Blisniuk, P. Treloar, M. Gaetani, and A. Zanchi, “Geological map of north Pakistan (western Himalaya, Salt Ranges, Kohistan, Karakoram, Hindu Kush),” 1996.
- [120] J. Armbruster, L. Seeber, and K. Jacob, “Northwestern termination of Himalayan mountain frontactive tectonics from microearthquakes,” *Journal of Geophysical Research, Solid Earth*, vol. 83, no. B1, pp. 269–282, 1978.
- [121] S. Wesnousky, “Seismicity as a function of cumulative geologic offset: some observations from southern California,” *Bulletin of the Seismological Society of America*, vol. 80, no. 5, pp. 1374–1381, 1990.
- [122] F. Cotton, M. Campillo, A. Deschamps, and B. Rastogi, “Rupture history and seismotectonics of the 1991 Uttarkashi, Himalaya earthquake,” *Tectonophysics*, vol. 258, no. 1, pp. 35–51, 1996.
- [123] K. Rajendran, C. Rajendran, S. Jain, C. Murty, and J. Arlekar, “The Chamoli earthquake, Garhwal Himalaya: field observations and implications for seismic hazard,” *Current Science*, vol. 78, no. 1, pp. 45–51, 2000.

- [124] W. Pennington, "A summary of field and seismic observations of the Pattan earthquake 28 december 1974," *In: A. Farah and K.A. DeJong, Editors, Geodynamics of Pakistan, Geological Survey of Pakistan (1989)*, p. 143147, 1989.
- [125] T. Nakata, "Active faults of the Himalaya of India and Nepal," *In: L.L. Malinconico Jr. and R. Lillie, Editors, Tectonics of the Western Himalayas Special Paper, Geol. Soc. of America*, vol. 232, p. 243264, 1989.
- [126] K. Hodges, C. Wobus, K. Ruhl, T. Schildgen, and K. Whipple, "Quaternary deformation, river steepening, and heavy precipitation at the front of the Higher Himalayan ranges," *Earth Planet. Sci. Lett.*, vol. 220, no. 3-4, p. 379389, 2004.
- [127] J. Lavé and J. Avouac, "Active folding of fluvial terraces across the Siwaliks Hills, Himalayas of central Nepal," *Journal of Geophysical Research*, vol. 105, no. B3, pp. 5735–5770, 2000.
- [128] P. Zeitler, P. Koons, M. Bishop, C. Chamberlain, D. Craw, M. Edwards, S. Hamidullah, M. O. Jan, M. A. Khan, M. U. K. Khattak, W. Kidd, R. Mackie, A. Meltzer, S. Park, A. Pécher, M. Poage, G. Sarker, D. Schneider, L. Seeber, and J. Shroder, "Crustal reworking at Nanga Parbat, Pakistan: metamorphic consequences of thermal-mechanical coupling facilitated by erosion," *Tectonics*, vol. 20, no. 5, pp. 712–728, 2001.
- [129] D. Scherler, S. Leprince, and M. R. Strecker, "Glacier-surface velocities in alpine terrain from optical satellite imagery - accuracy improvement and quality assessment," *Remote Sensing of Environment, Submitted*, submitted 2008.
- [130] J. Oerlemans, "Quantifying global warming from the retreat of glaciers," *Science*, vol. 264, no. 5156, pp. 243–245, 1994.
- [131] S. Solomon, D. Qin, M. Manning, Z. Chen, M. Marquis, K. Averyt, M. Tignor, and H. M. (Eds.), "Climate change 2007: The physical science basis," Contribution of Working Group I to the Fourth Assessment Report of the Intergovernmental Panel on Climate Change, Cambridge: Cambridge University Press, 2007.

- [132] A. Karim and J. Veizer, "Water balance of the Indus river basin and moisture source in the Karakoram and western Himalaya: Implications from hydrogen and oxygen isotopes in river water," *Journal of Geophysical Research*, vol. 107, no. D18, 2002.
- [133] M. Winiger, M. Gumpert, and H. Yamout, "Karakorum-Hindukush-western Himalaya: assessing high-altitude water resources," *Hydrological Processes*, vol. 19, pp. 2329–2338, 2005.
- [134] M. Parry, O. Canziani, J. Palutikof, P. van der Linden, and C. H. (Eds.), "Climate change 2007: Impacts, adaptation and vulnerability," Contribution of Working Group II to the Fourth Assessment Report of the Intergovernmental Panel on Climate Change. Cambridge: Cambridge University Press, 2007.
- [135] W. Haeberli, J. Cihlar, and R. G. Barry, "Glacier monitoring within the global climate observing system," *Annals of Glaciology*, vol. 31, pp. 241–246, 2000.
- [136] W. Haeberli, M. Hoelzle, F. Paul, and M. Zemp, "Integrated monitoring of mountain glaciers as key indicators of global climate change: the European Alps," *Annals of Glaciology*, vol. 46, pp. 150–160, 2007.
- [137] J. S. Kargel, M. J. Abrams, M. P. Bishop, A. Bush, G. Hamilton, H. Jiskoot, A. Kääh, H. H. Kieffer, E. M. Lee, F. Paul, F. Rau, B. Raup, J. F. Shroder, D. Soltesz, D. Stainforth, L. Stearns, and R. Wessels, "Multispectral imaging contributions to global land ice measurements from space," *Remote Sensing of Environment*, vol. 99, pp. 187–219, 2005.
- [138] F. Paul, A. Kääh, M. Maisch, and T. K. W. Haeberli, "The new remote-sensing-derived Swiss glacier inventory: I. methods," *Annals of Glaciology*, vol. 34, pp. 355–361, 2002.
- [139] S. J. S. Khalsa, M. B. Dyurgerov, T. T. Khromova, B. H. Raup, and R. G. Barry, "Space-based mapping of glacier changes using ASTER and GIS tools," *IEEE Transactions on Geoscience and Remote Sensing*, vol. 42, no. 19, pp. 2177–2183, 2004.
- [140] V. B. Aizen, V. A. Kuzmichenok, A. B. Urazakov, and E. M. Aizen, "Glacier changes in the Tien Shan as determined from topographic and remotely sensed data," *Global and Planetary Change*, vol. 56, no. 3–4, pp. 328–340, 2007.

- [141] R. L. Wessels, J. S. Kargel, and H. H. Kieffer, "Aster measurement of supraglacial lakes in the Mount Everest region of the Himalaya," *Annals of Glaciology*, vol. 34, pp. 399–408, 2002.
- [142] A. Rabatel, J. P. Dedieu, and C. Vincent, "Using remote-sensing data to determine equilibrium-line altitude and mass-balance time series: validation on three French glaciers, 1994-2002," *Journal of Glaciology*, vol. 51, no. 175, pp. 539–546, 2005.
- [143] E. Berthier, Y. Arnaud, R. Kumar, S. Ahmad, P. Wagnon, and P. Chevallier, "Remote sensing estimates of glacier mass balances in the Himachal Pradesh (Western Himalaya, India)," *Remote Sensing of Environment*, vol. 108, no. 3, pp. 327–338, 2007.
- [144] R. M. G. H. Engelhardt, B. Kamb, and R. M. Frolich, "Satellite radar interferometry for monitoring ice sheet motion: Application to an antarctic ice stream," *Science*, vol. 262, no. 5139, pp. 1525–1530, 1993.
- [145] I. Joughin, W. Abdalati, and M. Fahnestock, "Large fluctuations in speed on Greenland's Jakobshavn Isbrae glacier," *Nature*, vol. 432, no. 7017, pp. 608–610, 2004.
- [146] E. Trouvé, G. Vasile, M. Gay, L. Bombrun, P. Grussenmeyer, T. Landes, J. M. Nicolas, P. Bolon, I. Petillot, A. Julea, L. Valet, J. Chanussot, and M. Koehl, "Combining airborne photographs and spaceborne sar data to monitor temperate glaciers: Potentials and limits," *IEEE Transactions on Geoscience and Remote Sensing*, vol. 45, no. 4, pp. 905–924, 2007.
- [147] B. Hubbard and N. F. Glasser, *Field Techniques in Glaciology and Glacial Geomorphology: Glacier mass balance and motion (pp. 179-216)*. Chichester: Wiley, 2005.
- [148] T. Strozzi, A. Luckman, T. Murray, U. Wegmüller, and C. L. Werner, "Glacier motion estimation using sar offset-tracking procedures," *IEEE Transactions on Geoscience and Remote Sensing*, vol. 40, no. 11, pp. 2384–2391, 2002.
- [149] D. Massonnet and K. L. Feigl, "Radar interferometry and its application to changes in the earth's surface," *Reviews of Geophysics*, vol. 36, no. 4, pp. 441–500, 1998.

- [150] I. Joughin, R. Kwok, and M. Fahnestock, "Estimation of ice-sheet motion using satellite radar interferometry: method and error analysis with application to Humboldt Glacier, Greenland," *Journal of Glaciology*, vol. 42, no. 142, pp. 564–575, 1996.
- [151] R. Goldstein, "Atmospheric limitations to repeat-track radar interferometry," *Geophysical Research Letters*, vol. 22, pp. 2517–2520, 1995.
- [152] B. Puysegur, R. Michel, and J. P. Avouac, "Tropospheric phase delay in interferometric synthetic aperture radar estimated from meteorological model and multispectral imagery," *Journal of Geophysical Research*, vol. 112, no. B05419, 2007.
- [153] K. E. Mattar, P. W. Vachon, D. Geudtner, A. L. Gray, I. G. Cumming, and M. Brugman, "Validation of alpine glacier velocity measurements using ers tandem-mission sar data," *IEEE Transactions on Geoscience and Remote Sensing*, vol. 36, no. 3, pp. 974–984, 1998.
- [154] N. Reeh, J. J. Mohr, S. N. Madsen, H. Oerter, and N. S. Gundestrup, "Three-dimensional surface velocities of Storstrommen glacier, Greenland, derived from radar interferometry and ice-sounding radar measurements," *Journal of Glaciology*, vol. 49, no. 165, pp. 201–209, 2003.
- [155] N. Reeh, S. N. Madsen, and J. J. Mohr, "Combining sar interferometry and the equation of continuity to estimate the three-dimensional glacier surface-velocity vector," *Journal of Glaciology*, vol. 45, no. 151, pp. 533–538, 1999.
- [156] R. Michel and E. Rignot, "Flow of glacier Moreno, Argentina, from repeat-pass shuttle imaging radar images: Comparison of the phase correlation method with radar interferometry," *Journal of Glaciology*, vol. 45, no. 149, pp. 93–100, 1999.
- [157] I. Joughin, "Ice-sheet velocity mapping: a combined interferometric and speckle-tracking approach," *Annals of Glaciology*, vol. 34, pp. 195–201, 2002.
- [158] B. K. Lucchita and H. M. Ferguson, "Antarctica: Measuring glacier velocity from satellite images," *Science*, vol. 234, no. 4779, pp. 1105–1108, 1986.
- [159] R. A. Bindshadler and T. A. Scambos, "Satellite-image-derived velocity field of an antarctic ice stream," *Science*, vol. 252, no. 5003, pp. 242–252, 1991.

- [160] L. Gray, K. Mattar, and G. Sofko, “Velocity and flux of the filchner ice shelf and its tributaries determined from speckle tracking interferometry,” *Geophysical Research Letters*, vol. 27, no. 10, pp. 1451–1454, 2000.
- [161] I. Joughin, T. Slawek, R. Bindshadler, and S. F. Price, “Changes in west Antarctic ice stream velocities: Observation and analysis,” *Journal of Geophysical Research*, vol. 107, no. B11, 2002.
- [162] A. Kääh, “Combination of SRTM3 and repeat ASTER data for deriving alpine glacier flow velocities in the Bhutan Himalaya,” *Remote Sensing of Environment*, vol. 94, pp. 463–474, 2005.
- [163] L. Stearns and G. Hamilton, “A new velocity map for Byrd Glacier, East Antarctica, from sequential ASTER satellite imagery,” *Annals of Glaciology*, vol. 41, pp. 71–76, 2005.
- [164] T. Toutin, “Review article: Geometric processing of remote sensing images: models, algorithms and methods,” *International Journal of Remote Sensing*, vol. 25, no. 10, pp. 1893–1924, 2004.
- [165] E. Luedeling, S. Siebert, and A. Buerkert, “Filling the voids in the SRTM elevation model - a TIN-based delta surface approach,” *ISPRS Journal of Photogrammetry and Remote Sensing*, vol. 62, no. 4, pp. 283–294, 2007.
- [166] R. E. Crippen, S. J. Hook, and E. J. Fielding, “Nighttime ASTER thermal imagery as an elevation surrogate for filling SRTM DEM voids,” *Geophysical Research Letters*, vol. 34, no. L01302, 2007.
- [167] S. Leprince, P. Musé, and J. P. Avouac, “In-flight CCD distortion calibration for push-broom satellites based on subpixel correlation,” *IEEE Transactions on Geoscience and Remote Sensing*, in press, 2008.
- [168] B. Bourguin and N. Baghdadi, “Assessment of C-band SRTM-DEM in a dense equatorial forest zone,” *Comptes Rendus Geoscience*, vol. 337, no. 14, pp. 1225–1234, 2005.
- [169] Y. Gorokhovich and A. Voustianiouk, “Accuracy assessment of the processed SRTM-based elevation data by CGIAR using field data from USA and Thailand and its

- relation to the terrain characteristics,” *Remote Sensing of Environment*, vol. 104, no. 4, pp. 409–415, 2006.
- [170] T. Toutin, “Impact of terrain slope and aspect on radargrammetric DEM accuracy,” *ISPRS Journal of Photogrammetry and Remote Sensing*, vol. 57, no. 3, pp. 228–240, 2002.
- [171] J. F. Nye, “A method of determining the strain-rate tensor at the surface of a glacier,” *Journal of Glaciology*, vol. 3, no. 25, pp. 409–419, 1959.
- [172] R. A. Bindschadler, P. L. Vornberger, D. D. Blankenship, T. A. Scambos, and R. Jacobel, “Surface velocity and mass balance of ice streams D and W, West Antarctica,” *Journal of Glaciology*, vol. 42, no. 142, pp. 461–475, 1996.
- [173] M. B. Dyurgerov and M. F. Meier, “Glaciers and the changing earth system: A 2004 snapshot,” *Occasional Paper No. 58*, p. http://instaar.colorado.edu/other/download/OP58-dyurgerov_meier.pdf, 2005.
- [174] P. A. Mayewski and P. A. Jeschke, “Himalayan and Trans-Himalayan glacier fluctuations since AD 1812,” *Arctic and Alpine Research*, vol. 11, no. 3, pp. 267–287, 1979.
- [175] A. V. Kulkarni, B. P. Rathore, S. Mahajan, and P. Mathur, “Alarming retreat of Parbati glacier, Beas basin, Himachal Pradesh,” *Current Science*, vol. 88, no. 11, pp. 1844–1850, 2005.
- [176] S. Liu, D. Shangguan, Y. Ding, H. Han, C. Xie, Y. Zhang, J. Li, J. Wang, and G. Li, “Glacier changes during the past century in the Gangrigabo mountains, southeast Qinghai-Xizang (Tibetan) plateau, China,” *Annals of Glaciology*, vol. 43, pp. 187–193, 2006.
- [177] K. Hewitt, “The Karakoram anomaly? glacier expansion and the ‘elevation effect’, Karakoram Himalaya,” *Mountain Research and Development*, vol. 25, no. 4, pp. 332–340, 2005.
- [178] H. J. Fowler and D. R. Archer, “Conflicting signals of climatic change in the upper Indus basin,” *Journal of Climate*, vol. 19, no. 17, pp. 4276–4293, 2006.

- [179] D. I. Benn, M. P. Kirkbride, L. A. Owen, and V. Brazier, "Glaciated valley landsystems," *In: Evans, D.J.A. (Ed.), Glacial Landsystems (pp. 372-404). London: Hodder Arnold., 2003.*
- [180] A. Luckman, D. Quincey, and S. Bevan, "The potential of satellite radar interferometry and feature tracking for monitoring flow rates of Himalayan glaciers," *Remote Sensing of Environment*, vol. 111, pp. 172–181, 2007.
- [181] B. Bookhagen and D. W. Burbank, "Topography, relief, and TRMM-derived rainfall variations along the Himalaya," *Geophysical Research Letters*, vol. 33, no. L08405, 2006.
- [182] T. J. Lang and A. P. Barros, "Winter storms in the Central Himalayas," *Journal of the Meteorological Society of Japan*, vol. 82, no. 3, pp. 829–844, 2004.
- [183] P. Singh, U. K. Haritashya, N. Kumar, and Y. Singh, "Hydrological characteristics of the Gangotri glacier, central Himalayas, India," *Journal of Hydrology*, vol. 327, no. 1-2, pp. 55–67, 2006.
- [184] D. A. Cenderelli and E. E. Wohl, "Peak discharge estimates of glacial lake outburst floods and "normal" climatic floods in the Mount Everest region Nepal," *Geomorphology*, vol. 40, pp. 57–90, 2001.
- [185] R. Kattelmann, "Glacial lake outburst floods in the Nepal Himalaya: a manageable hazard flood management in India," *In: Natural Hazards 28, [Mirza, M.N.Q, A.Dixit and Ainun Nishat (eds.)], Kluwer Academic Publishers, Dordrecht*, pp. 145–154, 2003.
- [186] R. Bindschadler, W. D. Harrison, C. F. Raymond, and R. Crosson, "Geometry and dynamics of a surge-type glacier," *Journal of Glaciology*, vol. 18, no. 79, pp. 181–194, 1997.
- [187] G. H. Gudmundsson, A. Bassi, M. Vonmoos, A. Bauder, and U. H. F. M. Funk, "High-resolution measurements of spatial and temporal variations in surface velocities of Unteraargletscher, Bernese Alps, Switzerland," *Annals of Glaciology*, vol. 31, pp. 63–68, 2000.

- [188] H. J. Zwally, W. Abdalati, T. Herring, K. Larson, J. Saba, and K. Steffen, "Surface melt-induced acceleration of Greenland ice-sheet flow," *Science*, vol. 297, no. 5579, pp. 218–222, 2002.
- [189] R. S. Anderson, S. P. Anderson, K. R. MacGregor, E. D. Waddington, S. O'Neel, C. A. Riihimaki, and M. G. Loso, "Strong feedbacks between hydrology and sliding of a small alpine glacier," *Journal of Geophysical Research*, vol. 109, no. F03005, 2004.
- [190] T. C. Bartholomaus, R. S. Anderson, and S. P. Anderson, "Response of glacier basal motion to transient water storage," *Nature Geoscience*, vol. 1, pp. 33–37, 2008.
- [191] I. C. Willis, "Intra-annual variations in glacier motion: a review," *Progress in Physical Geography*, vol. 19, no. 1, pp. 61–106, 1995.
- [192] A. C. Fountain and J. S. Walder, "Water flow through temperate glaciers," *Reviews of Geophysics*, vol. 36, no. 3, pp. 299–328, 1998.
- [193] J. T. Harper, N. F. Humphrey, W. T. Pfeffer, and B. Lazar, "Two modes of accelerated glacier sliding related to water," *Geophysical Research Letters*, vol. 34, no. L12503, 2007.
- [194] P. Singh, U. K. Haritashya, and N. Kumar, "Meteorological study for Gangotri Glacier and its comparison with other high altitude meteorological stations in central Himalayan region," *Nordic Hydrology*, vol. 38, no. 1, pp. 59–77, 2007.
- [195] P. Wagnon, A. Linda, Y. Arnaud, R. Kumar, P. Sharma, C. Vincent, J. G. Pottakkal, E. Berthier, A. Ramanathan, S. I. Hasnain, and P. Chevallier, "Four years of mass balance on Chhota Shigri Glacier, Himachal Pradesh, India, a new benchmark glacier in the western Himalaya," *Journal of Glaciology*, vol. 53, no. 18, pp. 603–611, 2007.
- [196] C. Mayer, A. Lambrecht, M. Belò, C. Smiraglia, and G. Diolaiuti, "Glaciological characteristics of the ablation zone of Baltoro glacier, Karakoram, Pakistan," *Annals of Glaciology*, vol. 43, pp. 123–131, 2006.
- [197] D. K. Hall, K. J. Bayr, W. Schöner, R. A. Bindshadler, and J. Y. L. Chien, "Consideration of the errors inherent in mapping historical glacier positions in Austria from the ground and space (1983-2001)," *Remote Sensing of Environment*, vol. 86, pp. 566–577, 2003.

- [198] A. O. Konca, S. Leprince, J. P. Avouac, and D. V. Helmberger, “Rupture process of 1999, Mw 7.1 Duzce earthquake from joint analysis of SPOT, GPS, InSAR, strong-motion and teleseismic data,” *Bulletin of the Seismological Society of America*, Submitted, 2008.
- [199] A. Karcher, C. J. Bebek, W. F. Kolbe, D. Maurath, and V. P. M. U. M. Wagner, “Measurement of lateral charge diffusion in thick, fully depleted, back-illuminated CCDs,” *IEEE Transactions on Nuclear Science*, vol. 51, no. 5, pp. 2231–2237, 2004.
- [200] V. Samson, F. Champagnat, and J. F. Giovannelli, “Point target detection and sub-pixel position estimation in optical imagery,” *Applied Optics*, vol. 43, no. 2, pp. 257–263, 2004.
- [201] P. Dh er et e and B. Roug e, “Image de-blurring and application to SPOT5 THR satellite imaging,” in *International Geoscience and Remote Sensing Symposium (IGARSS)*, vol. 1, Toulouse, France, July 2003, pp. 318–320.
- [202] S. Durand, F. Malgouyres, and B. Roug e, “Image deblurring, spectrum interpolation and application to satellite imaging,” *ESAIM: Control, Optimisation and Calculus of Variations*, vol. 5, pp. 445–475, 2000.
- [203] *ASTER User’s Guide, Part I-II*, Earth Remote Sensing Data Analysis Center, 2001.
- [204] I. Sutherland and G. Hodgman, “Reentrant polygon clipping,” *Commun. ACM*, vol. 17, no. 1, pp. 32–42, 1974.